

Model-Based Condition Monitoring and Power Management  
for Rechargeable Electrochemical Batteries

By

Taesic Kim

Presented to the Faculty of  
The Graduate College at the University of Nebraska  
In Partial Fulfillment of Requirements  
For the Degree of Doctor of Philosophy

Major: Interdepartmental Area of Engineering,  
(Computer Engineering-Computer Science)

Under the Supervision of Professors Wei Qiao and Liyan Qu

Lincoln, Nebraska

May, 2015

UMI Number: 3700290

All rights reserved

INFORMATION TO ALL USERS

The quality of this reproduction is dependent upon the quality of the copy submitted.

In the unlikely event that the author did not send a complete manuscript and there are missing pages, these will be noted. Also, if material had to be removed, a note will indicate the deletion.



UMI 3700290

Published by ProQuest LLC (2015). Copyright in the Dissertation held by the Author.

Microform Edition © ProQuest LLC.

All rights reserved. This work is protected against unauthorized copying under Title 17, United States Code



ProQuest LLC.  
789 East Eisenhower Parkway  
P.O. Box 1346  
Ann Arbor, MI 48106 - 1346

# Model-Based Condition Monitoring and Power Management for Rechargeable Electrochemical Batteries

Taesic Kim, Ph.D.

University of Nebraska, 2015

Advisers: Wei Qiao and Liyan Qu

Rechargeable multicell batteries have been used in various electrical and electronic systems, e.g., renewable energy systems, electric-drive vehicles, commercial electronics, etc. However, there are still concerns about the reliability and performance degradation of rechargeable batteries caused by low thermal stability and the aging process. A properly designed battery management system (BMS) is required for condition monitoring and control of multicell batteries to ensure their safety, reliability, and optimal performance. The goal of this dissertation research was to develop a novel BMS for rechargeable multicell batteries.

First, this research developed high-fidelity battery models for online condition monitoring and power management of battery cells. The battery models were capable of capturing the dynamic circuit characteristics, nonlinear capacity and nonlinear open-circuit voltage effects, hysteresis effect, and temperature effect of the battery cells.

Second, this research developed a novel self-X, multicell battery design. The proposed multicell battery can automatically configure itself according to the dynamic load/storage demand and the condition of each cell. The proposed battery can self-heal from failure or abnormal operation of single or multiple cells, self-balance from cell state

imbalances, and self-optimize to improve energy conversion efficiency. These features were achieved by a highly efficient cell switching circuit and a high-performance condition monitoring and control system.

Moreover, this research developed several model-based condition monitoring algorithms based on the proposed battery models. First, a particle swarm optimization-based parameter identification algorithm was developed to estimate the impedance and state of charge (SOC) of batteries using the proposed hybrid battery model. Second, an algorithm combining a regression method for parameter identification, a sliding-mode observer for SOC estimation, and a two-point capacity estimation method were proposed. In addition, an electrical circuit with hysteresis model-based condition monitoring algorithm was proposed. It systematically integrates: a fast upper-triangular and diagonal recursive least square for online parameter identification, a smooth variable structure filter for SOC estimation, and a recursive total least square for maximum capacity and state of health estimation. These algorithms provided accurate, robust condition monitoring for lithium-ion batteries. Due to the low complexity, the proposed second and third algorithms are suitable for the embedded BMS applications.

## ACKNOWLEDGEMENTS

First of all, I would like to give my sincere appreciation and gratitude to my advisor, Dr. Wei Qiao, for his encouragement, assistance, and unwavering guidance in the technical and personal aspects of my studies.

I am very grateful to my co-advisor, Dr. Liyan Qu, for her constructive review and comments to my dissertation as well as my supervisory committee members, Drs. Jerry L. Hudgins and Steve Goddard, for their valuable suggestions, reviews of my dissertation, cheerful comments, and the consideration shown to me. I also would like to express my gratitude to Dr. Dean Patterson for his advice and consideration.

I am also grateful to Dr. Zafer Sahinoglu and Dr. Yebin Wang at Mitsubishi Electric Research Laboratories (MELR) for giving me the opportunity to intern at the prestigious industrial research lab to learn how to apply control theories to design practical battery management systems. With their help and support, I have made great progress in my research of battery condition monitoring algorithms.

I would like to thank all of my colleagues, Dr. Xiang Gong, Dr. Yue Zhao, Mr. Dingguo Lu, Ms. Ting Dai, Mr. Jianwu Zeng, Mr. Zhe Zhang, Mr. Chun Wei, Mr. Ze Wang, Mr. Cong Ma, and Mr. Daiyun Ha in the Power & Energy Systems Laboratory for their friendship and discussions in the development of this research.

I would also give my thanks to my congress members in the Korean Church of Omaha and all of my friends in Lincoln and Omaha.

Most of all, I would like to thank my wife, Dr. Jeong Soon Lee, my lovely daughter, Dana, my parents, and my family members, for their steadfast devotion, love, encouragement, motivation, and prayer throughout my pursuit of the doctoral degree.

Financial support from the following institutions/organizations is gratefully acknowledged:

- National Science Foundation, USA (CAREER Award ECCS-0954938 and Grant IIP-1414393)
- Federal Highway Administration, USA
- University of Nebraska-Lincoln
- IEEE Industry Applications Society
- IEEE Power and Energy Society
- IEEE Power Electronics Society
- IEEE Control Systems Society

*To my wife, Jeong Soon Lee; my daughter, Dana; my parents, Gujung Kim and Soonsun Kang; my sister Sunmi; and my brother, Taejin for their love and support.*

## Table of Contents

|  |             |
|--|-------------|
| <b>Acknowledgements .....</b>                              | <b>iv</b>   |
| <b>List of Abbreviations and Symbols .....</b>             | <b>xii</b>  |
| <b>List of Figures.....</b>                                | <b>xxiv</b> |
| <b>List of Tables .....</b>                                | <b>xxx</b>  |
| <b>Chapter 1: Introduction .....</b>                       | <b>1</b>    |
| 1.1 Motivation for the Work .....                          | 1           |
| 1.2 Goal and Objectives of the Research .....              | 3           |
| 1.3 Outline of Dissertation .....                          | 5           |
| <b>Chapter 2: Literature Review.....</b>                   | <b>6</b>    |
| 2.1 BMS .....  | 6           |
| 2.2 Hardware of a BMS.....                                 | 7           |
| 2.3 Software of a BMS.....                                 | 9           |
| 2.4 Battery Modeling.....                                  | 11          |
| 2.5 Condition Monitoring Algorithms .....                  | 15          |
| 2.5.1 Model Parameter Identification.....                  | 16          |
| 2.5.2 State of Charge Estimation.....                      | 18          |
| 2.5.3 State of Health Estimation .....                     | 21          |
| 2.5.4 State of Power and State of Function Estimation..... | 22          |
| <b>Chapter 3: Battery Modeling.....</b>                    | <b>25</b>   |

|   |           |
|---|-----------|
| 3.1 Hybrid Battery Model .....  | 25        |
| 3.2 Enhanced Hybrid Battery Model.....  | 29        |
| 3.2.1 Related Works.....  | 29        |
| 3.2.1.1 Nonlinear Capacity and Nonlinear OCV effect .....                           | 29        |
| 3.2.2 Simple Expression of KiBaM .....  | 32        |
| 3.2.3 The Enhanced Hybrid Battery Model .....                                       | 34        |
| 3.2.3.1 Runtime SOC Prediction Module .....   | 35        |
| 3.2.3.2 Electrical Circuit Battery Model .....                                      | 36        |
| 3.2.4 Model Parameter Extraction.....   | 37        |
| 3.2.4.1 Runtime SOC Prediction Module Parameters.....                               | 38        |
| 3.2.4.2 Electrical Circuit Model Parameters .....                                   | 42        |
| 3.2.5 Model Validation.....   | 51        |
| 3.3 Electrical Circuit with Hysteresis Battery Model .....                          | 59        |
| 3.4 Chapter Summary.....  | 62        |
| <b>Chapter 4: Self-X Multicell Battery Design.....</b>                              | <b>63</b> |
| 4.1 Self-X Multicell Battery Module Design.....                                     | 63        |
| 4.1.1 Cell Switching Circuit.....   | 65        |
| 4.1.2 Module Management System (MMS).....   | 70        |
| 4.2 Self-X Multicell Battery System Design for EVs and PHEVs .....                  | 76        |
| 4.2.1 Control and Protection for Each Module of Self-X Multicell Battery System ... | 78        |

|  |            |
|--|------------|
| 4.2.2 Master Battery Management System .....                                       | 80         |
| 4.3 A Bidirectional DC/DC Converter for Multicell Batteries .....                  | 82         |
| 4.3.1 Series-Connected, Self-Reconfigurable Multicell Battery Pack .....           | 83         |
| 4.3.2 The Bidirectional DC/DC Converter with the Unified CCAV Control Scheme       | 84         |
| 4.4 Validation .....   | 88         |
| 4.4.1 Module-Level Self-Healing .....  | 88         |
| 4.4.2 Module-Level Self-Balancing .....  | 93         |
| 4.4.3 System-Level Simulation with a DC/DC Converter .....                         | 95         |
| 4.4.4 Bidirectional DC/DC Converter Simulation .....                               | 98         |
| 4.4.5 Efficiency Analysis for Cell Switching Circuit .....                         | 102        |
| 4.5 Chapter Summary .....  | 106        |
| <b>Chapter 5: Particle Swarm Optimization-Based Electrical Parameter and SOC</b>   |            |
| <b>Estimation .....</b>  | <b>107</b> |
| 5.1 Hybrid Battery Model for Model-Based Condition Monitoring .....                | 108        |
| 5.2 Electrical Parameter Identification by PSO .....                               | 109        |
| 5.3 SOC Estimation and Compensation .....  | 112        |
| 5.4 Validation .....   | 114        |
| 5.5 Chapter Summary .....  | 119        |
| <b>Chapter 6: Simplified Hybrid Battery Model-Based, Real-Time Impedance, SOC,</b> |            |
| <b>and SOH Estimation .....</b>  | <b>120</b> |

|   |  |     |
|---|--|-----|
| 6.1   | Parameter Identification by MWLS Method.....   | 122 |
| 6.2   | Real-Time SOC Estimation by ADSMO .....  | 124 |
| 6.3   | Real-Time SOC Estimation and Compensation.....   | 126 |
| 6.5   | SOH Estimation by Two-Point Method.....  | 127 |
| 6.6   | Validation.....  | 128 |
| 6.7   | Chapter Summary.....   | 132 |
| <br>  |  |     |
| <b>Chapter 7: An Electrical Circuit with Hysteresis Battery Model-Based Real-Time</b> |  |     |
| <b>Impedance, SOC, and SOH Estimation..... 133</b>                                    |  |     |
| 7.1   | The Electrical Circuit with Hysteresis Battery Model-Based- Condition Monitoring Strategy..... | 133 |
| 7.2.  | Impedance Estimation by FUDLRS.....  | 134 |
| 7.3   | SOC Estimation by SVSF .....   | 141 |
| 7.4   | SOH Estimation by RTLS.....  | 144 |
| 7.5   | Validation.....  | 149 |
| 7.5.1   | Simulation Studies.....  | 149 |
| 7.5.2   | Experimental Studies.....  | 155 |
| 7.6   | Chapter Summary.....   | 161 |
| <br>  |  |     |
| <b>Chapter 8: Conclusions, Contributions, and Recommendations for Future Research</b> |  |     |
| <b>..... 162</b>  |  |     |
| 8.1.  | Conclusions of This Dissertation .....   | 162 |

8.2. Contributions of This Dissertation ..... 163

8.3 Recommendations for Future Research ..... 165

**Bibliography ..... 167**

**Appendix..... 183**

## LIST OF ABBREVIATIONS AND SYMBOLS

|                  |   |
|------------------|---|
| ADSMO            | Adaptive discrete-time sliding mode observer              |
| Ah               | Ampere-hour   |
| ANN              | Artificial neural network                                 |
| BMS              | Battery management system                                 |
| CAN              | Controller area network                                   |
| CCAV             | Constant current adaptive voltage                         |
| CCCV             | Constant current constant voltage                         |
| C.C.             | Constant current  |
| CCM              | Continuous conduction mode                                |
| C-rate           | Current rate  |
| C.R.             | Constant resistor   |
| DC               | Direct current  |
| DEKF             | dual extended Kalman filter                               |
| EF               | Exponential forgetting                                    |
| EKF              | Extended Kalman filter                                    |
| EV               | Electric vehicle  |
| FUDRLS           | Fast upper-triangular and diagonal recursive least square |
| HV               | High-voltage  |
| I <sup>2</sup> C | Inter-integrated circuit communication                    |
| IC               | Integrated circuit  |
| ISVSF            | Iterative smooth variable structure filter                |
| I-V              | Current-voltage   |

|        |   |
|--------|---|
| KiBaM  | Kinetic battery model                             |
| LS     | Least square                                      |
| LV     | Low-voltage                                       |
| MBMS   | Master battery management system                  |
| MOSFET | Metal-oxide-semiconductor field-effect transistor |
| MMS    | Module management system                          |
| MWLS   | Moving window least square                        |
| OCV    | Open-circuit voltage                              |
| P.C.   | Pulsed current                                    |
| PCB    | Printed circuit board                             |
| PDE    | Partial differential equation                     |
| PHEV   | Plug-in hybrid electric vehicle                   |
| PID    | Proportional-integral-derivative                  |
| PSO    | Particle swarm optimization                       |
| RC     | Resistor-capacitor                                |
| RLS    | Recursive least square                            |
| RMSE   | Root mean square error                            |
| RTLS   | Recursive total least square                      |
| SEI    | Solid electrolyte interface                       |
| SMO    | Sliding mode observer                             |
| SOC    | State of charge                                   |
| SOH    | State of health                                   |
| SOP    | State of power                                    |

|       |  |
|-------|--|
| SOF   | State of function  |
| SPKF  | Sigma-point Kalman filter  |
| SVD   | Singular value decomposition                                       |
| SVSF  | Smooth variable structure filter                                   |
| TLS   | Total least square   |
| UDRLS | Upper-triangular and diagonal factorization recursive least square |
| VF    | Variable forgetting  |
| VLSI  | Very-large-scale integration                                       |
| WF    | Weighting factor   |

---

|                   |  |
|-------------------|--|
| $a_0 \sim a_{19}$ | Coefficients of the empirical equations of the runtime SOC prediction module parameters and OCV of enhanced hybrid battery model |
| $b_0$ and $b_1$   | Notations of linearized OCV  |
| $b_s$ and $c_s$   | Stochastic quantities  |
| $c$               | Capacity ratio of KiBaM  |
| $c_1$             | Cognition learning rate of particles   |
| $c_2$             | Social learning rate of particles  |
| $C_{available}$   | Available capacity of a battery cell in As   |
| $C_d$             | Double-layer capacitance in F  |
| $C_{ij}$          | The $j$ th battery cell in bank $i$  |
| $C_{max}$         | Maximum capacity of a battery cell in Ah   |
| $C_{max\_new}$    | Maximum capacity of a new battery cell in Ah   |
| $C_{sd}$          | Short-term diffusion capacitance in F  |

|                              |   |
|------------------------------|---|
| $C_{SVSF}$                   | Linearized measurement matrix of SVSF                   |
| $C_{unavailable}$            | Unavailable capacity of a battery cell in As            |
| $C_{usable}$                 | Usable capacity of a battery cell in As                 |
| $\hat{C}_{max}$              | Estimated maximum capacity of a battery cell in As      |
| $diag$                       | Diagonal function                                       |
| $d_1, d_2, \text{ and } d_3$ | Parameters of running time-averaged estimation          |
| $D$                          | Duty cycle of DC/DC converter                           |
| $D_0$                        | Zero current duty cycle of DC/DC converter              |
| $D_{ij}$ and $D_i$           | Zener diodes  |
| $D_{new}$                    | New diagonal matrix                                     |
| $D_{old}$                    | Old diagonal matrix                                     |
| $\bar{D}$                    | Diagonal weighting matrix                               |
| $e$                          | Posterior voltage estimation error of FUDRLS in V       |
| $E$                          | Time-average expression of $e(k)^2$ in $V^2$            |
| $e_{z,k k}$                  | Posteriori measurement error of SVSF at time $k$ in V   |
| $e_{z,k+1 k}$                | Measurement error of SVSF at time $k$ in V              |
| $e_{z,k+1 k+1}$              | Posteriori measurement error of SVSF at time $k+1$ in V |
| $f(\cdot)$                   | value function with respect to $\Delta SOC_b$           |
| $G_1$ and $G_2$              | Gate control signal of DC/DC converter                  |
| $h_1$ and $h_2$              | The heights of the two wells in KiBaM                   |
| $H(i_B)$                     | $\exp(-\rho i_B T_s)$                                   |
| $I_{ABS}$                    | Minimum charge/discharge current of the battery in A    |
| $i_B$                        | Current of a battery cell in A                          |

|              |   |
|--------------|---|
| $I_{br}$     | Current of a battery bank in A                                    |
| $I_B$        | Battery pack current of DC/DC converter in A                      |
| $I_{B\_REF}$ | Reference battery current of DC/DC converter in A                 |
| $I_{cr}$     | Current of the each battery cell in a battery bank in A           |
| $I$          | Normalized battery current in C-rate in C                         |
| $I_d$        | Demand current of a battery system in C                           |
| $I_D$        | A vector of constant discharge current rate in C                  |
| $I_{DMAX}$   | Maximum current of power MOSFET in A                              |
| $i_{rated}$  | Rated current ( i.e., 1C) in C                                    |
| $I_L$        | Average inductor current in A                                     |
| $k_B$        | Number of series banks to be used                                 |
| $k$          | Discrete time index   |
| $k_1$        | Beginning time of SOH estimation period in s                      |
| $k_2$        | End time of SOH estimation period in s                            |
| $k'$         | Constant related to the diffusion rate of KiBaM                   |
| $K_{FUDRLS}$ | Kalman gain of FUDRLS   |
| $K_{LV}$     | Correction factor for low temperature                             |
| $K_{VOC}$    | Correction coefficient of the temperature effect in OCV-SOC curve |
| $l$          | SMO gain of the switching control vector                          |
| $L(I_D)$     | Vector of the end of discharge times corresponding to $I_D$ in s  |
| $n_a$        | Number of usable cells in a bank                                  |
| $N$          | Number of particles in a swarm                                    |
| $N_0$        | Memory length   |

|                 |  |
|-----------------|--|
| $N_{\max}$      | Maximum iteration number   |
| $P$             | Covariance matrix  |
| $P_0$           | Initial covariance matrix of FUDRLS                                    |
| $P_d$           | Power demand in W  |
| $P_{\max}$      | Maximum power possibly supplied by a battery in W                      |
| $P_p$           | Possible power supplied by a battery in W                              |
| $P_{pso}$       | Fitness function of PSO  |
| $q_{\max}$      | Total number of banks in a battery system                              |
| $q_{MBMS}$      | Number of banks determined by MBMS                                     |
| $q_{MMS}$       | Number of banks determined by MMS                                      |
| $q$             | Number of banks in the module to be used                               |
| $q_e$           | Eigenvector of a constrained Rayleigh quotient                         |
| $q_e^*$         | Unbiased TLS solution  |
| $q_0 \sim q_5$  | Coefficients of the empirical equations of OCV in hybrid battery model |
| $Q_i$           | Small-signal JFET  |
| $Q_{ij}$        | Small-signal BJTs  |
| $q_t$           | Selected total number of series banks                                  |
| $r_1$ and $r_2$ | Uniformly distributed random numbers between 0 and 1                   |
| $R$             | Redundancy of a battery system   |
| $R_{ct}$        | Charge transfer resistor in Ohm  |
| $R_{DS}$        | Conduct resistance of power MOSFET in Ohm                              |
| $R_{in}$        | Internal resistance of a battery model in Ohm                          |
| $R_s$           | Series resistance in Ohm   |

|                 |  |
|-----------------|--|
| $R_{sd}$        | Short-term diffusion resistance in Ohm                     |
| $R_u$           | Stochastic quantities                                      |
| $\tilde{R}_u$   | Autocorrelation matrix of a noisy input $\tilde{u}$        |
| $\bar{R}_x$     | Autocorrelation matrix of a noisy input $\bar{x}$          |
| $S$             | Sliding surface  |
| $S_i$           | P-channel power MOSEFT                                     |
| $S_{ij}$        | N-channel power MOSEFT                                     |
| $S_D$           | Self-discharge rate  |
| $sat$           | Saturation function  |
| $sign$          | Sign function  |
| $SOC_{avg}$     | Average SOC of battery cells                               |
| $SOC_b$         | SOC of a bank  |
| $SOC_{b\_max}$  | Maximum bank SOC in a module                               |
| $SOC_{b\_min}$  | Minimum bank SOC in a module                               |
| $SOC_E$         | Equilibrium SOC (i.e., Coulomb counting SOC)               |
| $SOC_i$         | SOC of the $i$ th cell in a bank                           |
| $SOC_{initial}$ | Initial SOC  |
| $SOC_T$         | Enhanced Coulomb counting SOC (i.e., actual real-time SOC) |
| $SOC_m$         | SOC of a module  |
| $SOC_{new}$     | Compensated SOC  |
| $SOC_{run}$     | Runtime SOC  |
| $SOC_V$         | Estimated SOC from the open-circuit voltage                |
| $t$             | Continuous time in s                                       |

|              |   |
|--------------|---|
| $T$          | Ambient temperature in Kelvin (K)                     |
| $t_0$        | Discharge beginning time in s                         |
| $T_c$        | Duration of the control cycle in s                    |
| $t_d$        | Discharge ending time in s                            |
| $T_l$        | Large time-scale sampling period in s                 |
| $t_r$        | Rest ending time in s                                 |
| $T_{ref\_L}$ | Reference temperature at low temperature in K         |
| $T_{ref}$    | Reference temperature in K                            |
| $T_s$        | Sampling period of data in s                          |
| $T_{smo}$    | Sampling period of the ADSMO in s                     |
| $u$          | Input of RTLS   |
| $U$          | Input vector of RTLS                                  |
| $U_M$        | Observation matrix of LS for capacity estimation      |
| $U_{new}$    | New upper-triangular matrix                           |
| $U_{old}$    | Old upper-triangular matrix                           |
| $\tilde{u}$  | Noisy input   |
| $v$          | Valve parameter of KiBaM                              |
| $V_{avg}$    | Average voltage of all banks in a battery system in V |
| $V_B$        | Output voltage of DC/DC converter in V                |
| $V_{B\_REF}$ | Reference output voltage of DC/DC converter in V      |
| $V_{cell}$   | Terminal voltage of a battery cell in V               |
| $V_{ct}$     | Charge transfer voltage response in V                 |
| $V_d$        | Demand voltage of a battery system in V               |

|                        |   |
|------------------------|---|
| $V_{DC}$               | Input voltage of a DC/DC converter in V                       |
| $V_{DC\_REF}$          | Reference input voltage of a DC/DC converter in V             |
| $V_{DS}$               | Voltage of drain-to-source of power MOSFET in V               |
| $V_{DSS}$              | Maximum voltage of drain-to-source of power MOSFET in V       |
| $V_{gs}$               | Voltage of gate-to-source of power MOSFET in V                |
| $V_h$                  | Hysteresis voltage in V                                       |
| $V_{hmax}$             | Maximum hysteresis voltage in V                               |
| $V_i$                  | Velocity vector of PSO  |
| $V_{impedance}$        | Impedance voltage of a battery cell in V                      |
| $V_{limit}$            | Threshold terminal voltage of a battery in V                  |
| $V_{limit\_discharge}$ | Minimum discharge voltage of a battery cell in V              |
| $V_{limit\_charge}$    | Maximum charge voltage of a battery cell in V                 |
| $V_{min}$              | Minimum terminal voltage of a battery in V                    |
| $V_{oc}$               | Voltage-controlled voltage source (or trajectory of OCV) in V |
| $V_{oc,eq}$            | Equilibrium (or average) OCV in V                             |
| $V_{oc,c}$             | Charge equilibrium OCV in V                                   |
| $V_{oc,d}$             | Discharge equilibrium OCV in V                                |
| $V_{oc\_max}$          | Maximum possible OCV in V                                     |
| $V_{oc\_min}$          | Minimum possible OCV in V                                     |
| $V_s$                  | Instantaneous voltage drop/rising response in V               |
| $V_{sd}$               | Short-term diffusion voltage response in V                    |
| $V_{SD}$               | Voltage of source-to-drain of power MOSFET in V               |
| $V_{sg}$               | Voltage of source-to-gate of power MOSFET in V                |

|                     |  |
|---------------------|--|
| $V_{terminal}$      | Terminal voltage of a battery cell or system in V            |
| $V_t$               | Transient voltage of a battery cell in V                     |
| $V_{th}$            | Threshold voltage of power MOSFET in V                       |
| $\hat{V}_{cell}$    | Estimated voltage of a battery cell in V                     |
| $w$                 | Value of redundancy function                                 |
| $W$                 | Variable weighting factor                                    |
| $w_{in}$            | Inertial weight  |
| $X$                 | Optimal solution   |
| $X_i$               | Position vector  |
| $X_{i,pbest}$       | Individual best position                                     |
| $X_{gbest}$         | Global best position   |
| $\hat{x}_{k+1 k}$   | Predicted state estimates at time $k$                        |
| $\hat{x}_{k+1 k+1}$ | Corrected (or posteriori) state estimates at time $k+1$      |
| $\hat{x}_{k k}$     | State estimate at time $k$                                   |
| $\bar{x}$           | Augment data of RTLS   |
| $y_1$               | Charge in an available charge well in As                     |
| $y_2$               | Charge in a bound charge well in As                          |
| $\hat{y}_{k+1 k}$   | Predicted measurement in V                                   |
| $z$                 | Current integration during a capacity estimation index in As |
| $Z$                 | Variable switching function                                  |
| $Z_M$               | Measurement matrix for capacity estimation                   |
| $Z_0$               | Width of the boundary layer                                  |

|                      |  |
|----------------------|--|
| $\tilde{z}$          | Noisy output                                   |
| $\alpha$ and $\beta$ | Discharge and charge constants of PSO          |
| $\alpha_u$           | Updating parameter of RTLS                     |
| $\beta_w$            | Output noise-to-input noise ratio              |
| $\gamma$             | $\exp(-T_s/(R_{ct}C_d))$                       |
| $\gamma_s$           | SVSF convergence rate                          |
| $\delta$             | Height difference between two wells in KiBaM   |
| $\delta_0$           | Initial covariance coefficient                 |
| $\delta_1$           | Weighting factor of VF                         |
| $\Delta SOC_b$       | $SOC_{b\_max} - SOC_{b\_min}$                  |
| $\Delta T$           | $T - T_{ref}$                                  |
| $\Delta u$           | SOC estimation error                           |
| $\Delta z$           | Integrated current measurement error in As     |
| $\varepsilon$        | Priori voltage estimation error of FUDRLS in V |
| $\varepsilon_v$      | Voltage estimation error of ADSMO in V         |
| $\zeta$              | Variable percentage used in $T_c$              |
| $\eta$               | Coulomb efficiency                             |
| $\Theta$             | Estimated parameter vector                     |
| $\lambda$            | Forgetting factor of VF                        |
| $\lambda_{max}$      | Maximum forgetting factor of VF                |
| $\lambda_{min}$      | Minimum forgetting factor of VF                |
| $\mu$                | Forgetting factor of stochastic quantity       |

|              |  |
|--------------|--|
| $\nu$        | Self-discharge multiplier for hysteresis expression            |
| $\zeta$      | Arbitrary input signal for approximate linear parameterization |
| $\rho$       | Hysteresis parameter representing the convergence rate         |
| $\sigma_0^2$ | Mean value of the variance of the prediction error             |
| $\sigma_u^2$ | Variance of $u$  |
| $\sigma_z^2$ | Variance of $z$  |
| $\tau_L$     | Long-term time constant in s                                   |
| $\tau_S$     | Short-term time constant in s                                  |
| $\phi$       | Rest constant of PSO   |
| $\Phi$       | Regression matrix of FUDLRS                                    |
| $\Phi_a$     | Augmented matrix   |
| $\Psi$       | Smoothing boundary layer widths                                |
| $\omega$     | Small damping parameter  |
| $\circ$      | Schur product  |

## LIST OF FIGURES

|   |    |
|---|----|
| Figure 2.1: Framework of a typical BMS. (Courtesy of [6].) .....  | 6  |
| Figure 2.2: A reconfigurable multicell battery topology. (Courtesy of [21].).....   | 8  |
| Figure 2.3: An electrical circuit battery model. (Courtesy of [42].).....   | 14 |
| Figure 2.4: The kinetic battery model. (Courtesy of [42].).....   | 14 |
| Figure 2.5: Conceptual relationship of the battery states. (Courtesy of [6].) .....   | 16 |
| Figure 2.6: Diagram of dual EKF. (Courtesy of [67].).....   | 21 |
| Figure 2.7: The relationship between SOF, SOC, and SOH of a battery. (Courtesy of<br>[86].) .....   | 24 |
| Figure 3.1: The hybrid battery model. ....  | 27 |
| Figure 3.2: The time-domain responses of the terminal voltage, OCV, and equilibrium   | 31 |
| Figure 3.3: The KiBaM: (a) discharge mode and (b) charge mode. ....   | 34 |
| Figure 3.4: The enhanced hybrid battery model. ....   | 35 |
| Figure 3.5: The experimental setup. ....  | 38 |
| Figure 3.6: The measured or estimated values and corresponding fitted curves of (a)<br>$C_{available}$ as the function of $L(I_D)$ at three different ambient temperature<br>conditions, (b) $C_{max}$ , (c) $k'$ , and (d) $c$ as functions of temperature. .... | 41 |
| Figure 3.7: Measured and fitted curves obtained at the ambient temperatures of<br>$0^\circ\text{C}$ , $23^\circ\text{C}$ , and $40^\circ\text{C}$ : (a) $V_{oc,eq}$ vs. $SOC_E$ and (b) $K_{VOC}$ vs. $SOC_E$ .....   | 44 |
| Figure 3.8: The curve of a typical impedance voltage response in the condition of 0.6C<br>pulsed current discharge and $0^\circ\text{C}$ ambient temperature for the extraction of<br>the RC parameters of the enhanced hybrid battery model. ....                | 45 |
| Figure 3.9: The measurement and corresponding fitted curves: (a) $R_{s,d}(SOC_E, I)$ , (b)  |    |

|   |    |
|---|----|
| $R_{s,d}(SOC_E, T)$ , (c) $R_{ct,d}(SOC_E, T)$ , (d) $C_{d,d}(SOC_E, T)$ , (e) $R_{sd,d}(SOC_E, T)$ , and<br>(f) $C_{sd,d}(SOC_E, T)$ . .....   | 49 |
| Figure 3.10: The enhanced hybrid battery model implemented in MATLAB/Simulink.  | 52 |
| Figure 3.11: Comparison of simulation results of the enhanced hybrid battery model and<br>experimental results for the test battery cell with pulsed discharge and<br>charge currents: (a) the pulsed current profiles, (b) voltage respond at 0 °C,<br>(c) the estimated SOCs at 0 °C, (d) the voltage respond at 23 °C, and (e) the<br>estimated SOCs at 23 °C, (f) the voltage respond at 40 °C, and (g) the<br>estimated SOCs at 40 °C..... | 56 |
| Figure 3.12: Comparison of simulation results of the proposed enhanced hybrid battery<br>model and experimental results for the test battery cell with (a) a randomly<br>varied current profile and terminal voltage responses at (b) 0 °C, (c) 23 °C,<br>and (d) 40 °C.....  | 58 |
| Figure 3.13: The electrical circuit with hysteresis battery model.....  | 60 |
| Figure 3.14: OCV curves. ....   | 61 |
| Figure 4.1: The self-X, multicell battery module design. ....   | 64 |
| Figure 4.2: The cell switching circuit topology. ....   | 66 |
| Figure 4.3: Switch implementation for Cell $C_{ij}$ using an n-channel power MOSFET and<br>for Bank $i$ using a p-channel power MOSFET with a gate drive circuit using<br>(a) small-signal BJTs and (b) optocouplers. ....  | 68 |
| Figure 4.4: Transient waveforms of the switching implementation for Cell $C_{ij}$ with a 1C<br>(0.86 A) load current: (a) $S_{ij}$ turns on and $S_i$ turns off; (b) $S_{ij}$ turns off and $S_i$<br>turns on.....  | 70 |

|   |    |
|---|----|
| Figure 4.5: Schematic diagram of the module management system. ....   | 71 |
| Figure 4.6: The functional block flow chart of one control cycle of the control and protection module. ....   | 74 |
| Figure 4.7: A self-X multicell battery system for EVs and PHEVs. ....   | 77 |
| Figure 4.8: The modified functional block flow chart of one control cycle of the control and protection module of each MMS.....   | 79 |
| Figure 4.9: The value of $f(\cdot)$ with respect to $\Delta SOC_b$ . ....   | 80 |
| Figure 4.10: The value of $w$ with respect to $\Delta SOC_m$ . ....   | 82 |
| Figure 4.11: The proposed series-connected, self-reconfigurable, multicell battery module with a bidirectional DC/DC converter. ....  | 83 |
| Figure 4.12: The proposed series-connected, self-reconfigurable, multicell battery topology. ....   | 84 |
| Figure 4.13: The proposed bidirectional DC/DC converter with the unified CCAV controller for charging and discharging control of the multicell battery. ....                                | 85 |
| Figure 4.14: Control duty cycle $D$ versus average inductor current $I_L$ . ....  | 86 |
| Figure 4.15: The scheduling algorithm for the implementation of CCAV control in the charge mode of the battery.....   | 87 |
| Figure 4.16: Total energy in Wh that can be supplied by (a) the fixed-configuration and (b) the proposed self-X, $6 \times 3$ -cell battery module for different SOCs of Banks 1 and 6..... | 89 |
| Figure 4.17: The experimental system setup of the self-X battery module. ....   | 92 |
| Figure 4.18: Comparison of the terminal voltage responses of the self-X battery module obtained from the simulation and the experiment for Scenario 2. ....                                 | 92 |

|  |     |
|--|-----|
| Figure 4.19: The SOCs of the cell banks in discharge mode: three banks were used simultaneously. ....  | 94  |
| Figure 4.20: Comparison of the terminal voltage responses of the self-X battery module when different durations for the control cycle were used. ....  | 94  |
| Figure 4.21: The SOCs of the cell banks in charge mode: three banks were used simultaneously. ....   | 95  |
| Figure 4.22: The operation of a five-module battery system in the charge mode: (a) the SOCs of the six banks in Module 3; (b) the SOCs of the five modules; and (c) the terminal voltage and charge current of the battery. .... | 98  |
| Figure 4.23: The current flow control between 1 A charge and -1 A discharge: (a) the inductor and battery currents; (b) the HV-side and LV-side (battery terminal) voltages. ....  | 100 |
| Figure 4.24: Cell balancing control in the charge mode: (a) the SOC of each cell; (b) the terminal voltage of Cell 1, 2, and 6; (c) the terminal voltage and charge current of the battery. ....                                 | 102 |
| Figure 4.25: Normalized power losses of the cell switching circuit as functions of normalized discharge current for a single 3.7 V, 0.86 Ah polymer lithium-ion cell. ....   | 104 |
| Figure 4.26: Comparison of the efficiency of the cell switching circuit as a function of normalized discharge current for 0.86 Ah, 5 Ah, 10 Ah, and 20 Ah polymer lithium-ion cells. ....  | 105 |
| Figure 5.1: The proposed PSO-based SOC and electrical parameter estimation method for a series-connected $m$ -cell battery pack. ....  | 107 |

|   |     |
|---|-----|
| Figure 5.2: The proposed closed-loop weighting SOC estimation algorithm. ....   | 114 |
| Figure 5.3: The experimental setup for electrical parameter and SOC estimation.....   | 115 |
| Figure 5.4: Comparison of true and estimated RC parameters of the hybrid battery model<br>for the four cells: (a) $R_s$ , (b) $R_{ct}$ , (c) $C_d$ , (d) $R_{sd}$ , (e) $C_{sd}$ , and (f) the dynamic<br>current cycle applied to the battery pack. ....                 | 118 |
| Figure 5.5: Comparison of the estimated and measured SOCs for the four cells when<br>using a wrong initial SOC for each cell in the proposed method. ....   | 119 |
| Figure 6.1: The SOC and SOH estimation method for a series-connected $m$ -cell battery<br>pack.....   | 121 |
| Figure 6.2: A block diagram of the ADSMO-based SOC estimator. ....  | 125 |
| Figure 6.3: The proposed closed-loop weighting SOC estimation algorithm with<br>ADSMO.....  | 126 |
| Figure 6.4: The experimental setup for simplified hybrid battery model-based SOC and<br>SOH estimation.....   | 128 |
| Figure 6.5: Comparison of true and estimated parameters of a battery cell: (a) $V_{cell}$ , (b)<br>$V_{oc}$ , (c) $C_{max}$ , and (f) the dynamic current cycle used for the test. ....   | 131 |
| Figure 6.6: Comparison of the estimated and measured SOCs for the four cells.....   | 132 |
| Figure 7.1: The model-based condition monitoring strategy for embedded BMS. ....  | 134 |
| Figure 7.2: The SVSF estimation concept. (Courtesy of [112].).....  | 143 |
| Figure 7.3: Comparison of linear regression methods: (a) LS and (b) TLS. ....   | 146 |
| Figure 7.4: Comparison of true and estimated impedance, SOC, and maximum capacity<br>of the battery cell from the proposed condition monitoring algorithms and<br>DEKF: (a) input current profile; (b) $R_s$ ; (c) $R_{ct}$ ; (d) $C_d$ ; (e) $SOC$ ; and (f) $C_{max}$ . |     |

..... 154

Figure 7.5: Comparison of estimated impedance, SOC, and maximum capacity from the proposed condition monitoring algorithms and DEKF on the experimental data: (a) the pulse current cycle ( $i_B = 10C$ ) applied to the battery; (b)  $R_s$ ; (c)  $R_{ct}$ ; (d)  $C_d$ ; (e)  $SOC$ ; and (f)  $C_{max}$  ..... 160

## LIST OF TABLES

|   |     |
|---|-----|
| Table 3.1: The coefficients of the empirical equations of the runtime SOC prediction module parameters and OCV for the test cylindrical lithium-ion cells. .... | 42  |
| Table 3.2: The coefficients of the RC parameter expressions for the test cylindrical lithium-ion cell in the discharge mode.....                                | 50  |
| Table 3.3: The coefficients of the RC parameter expressions for the test cylindrical lithium-ion cell in charge mode. ....                                      | 50  |
| Table 4.1: Comparison of simulation and experimentation results for the six-bank battery .....  | 91  |
| Table 5.1: Set of Parameter for PSO implementation PSO .....  | 112 |
| Table 5.2: Boundary condition of $V_{oc}$ .....   | 112 |
| Table 7.1: FUDRLS algorithm.....  | 140 |
| Table 7.2: Electrical circuit with hystereisis battery model parameters.....  | 150 |
| Table 7.3: Comparison of RMSEs for the parameter identification algorithms.....   | 155 |
| Table 7.4: Comparison of RMSEs and computational times for the SOC and the capacity estimation algorithms.....  | 155 |
| Table 7.5: Parameters of the proposed condition monitoring algorithms.....  | 156 |
| Table 7.6: Comparison of RMSEs and computational times for the SOC and the capacity estimation algorithms on the experimental data.....                         | 160 |

## CHAPTER 1: INTRODUCTION

### 1.1 Motivation for the Work

Rechargeable electrochemical batteries have been more and more pervasively used as the energy storage and power source for various electrical systems and devices [1]-[5], such as communication systems, electronic devices, renewable power systems, electric vehicles, etc. However, due to the existence of cell state variation, limited thermal stability, and the aging process, safety, reliability, and performance degradation are still of concern in using rechargeable batteries. Exceeding the limitations of temperature, voltage, and/or current will lead to rapid attenuation of battery performance and even a safety problem [6]. Moreover, cell state variations are commonly present [7]. The imbalanced cell states may cause overcharge and overdischarge of some battery cells. These unstable conditions will result in a degradation of the battery life and low reliability of the battery system. The problem of cell imbalance is especially severe when the battery has a long string of cells [8]. Furthermore, in a large battery system, the risk of catastrophic faults increases because a large number of cells are used [9].

An effective battery management system (BMS) consisting of hardware components and software algorithms is the key to guaranteeing the safety, reliability, and optimal performance of the batteries [10]. However, several design deficiencies in current battery systems have impeded them from being used for large-scale energy storage. These deficiencies include: 1) adopting a fixed configuration for cell connections, resulting in low reliability and low fault-tolerance capability from abnormal operating conditions, such as high temperature, overcharge, overdischarge, overcurrent, and failure of one or more

cells [11]; 2) lacking an effective method to utilize cell state variations, resulting in nonoptimal energy conversion efficiency; and 3) lacking a capability for flexible dynamic power management, resulting in nonoptimal system performance.

A commonly used method for solving the problem of faulty or abnormal cells in a fixed-configuration battery is the use of a safety circuit. The safety circuit protects the cells from high temperature, overcharge, overdischarge, and overcurrent by monitoring the temperature, voltage, and current of each cell [12]. However, lacking an effective reconfigurable topology, the safety circuit cuts off the whole battery system when any single cell is operated in these abnormal conditions. Moreover, cell state variations are commonly present in multicell batteries. In that case, the fixed-configuration design can only utilize a part of the total battery capacity. To overcome this deficiency, cell balancing circuits [13]-[17] have been used together with protection circuits. However, this solution highly increases the cost and volume of the battery system. Recently, several reconfigurable multicell battery topologies [18]-[22] have been introduced to control individual battery cells. However, these topologies are too complex and unrealistic for battery systems with large numbers of cells. Therefore, a new low-cost BMS hardware design enabling reconfigurable cell connections, cell balancing, protection, and independent control for individual battery cells is desired.

In addition, the development of condition monitoring and control algorithms has become a main research topic in battery management and has attracted interest from industry, academia, and the various governments. A key function of the condition monitoring software in a BMS is to estimate the states, such as state of charge (SOC), state of health (SOH), instantaneous available power (i.e., state of power (SOP)), and critical

parameters, such as internal impedance, capacity, etc., of the battery cells during operation. The estimated parameters and states offer fault diagnosis and prognosis capability and enable intelligent control of the battery system [23]. Unfortunately, since the values of those parameters and states cannot be directly measured by using sensors, they are commonly estimated using the measurable states of the battery cells, such as voltage, current, and surface temperature. Poor estimation or control of a battery cell's SOC may lead to improper charge and discharge of the battery cells and may degrade the efficiency and reliability of the batteries [24]. Moreover, the battery SOH is required to help determine whether a battery would fail and the remaining useful life of the battery [24]. Hence, the development of condition monitoring algorithms that accurately identify battery states and parameters using measured system quantities plays an important role in achieving an effective BMS.

## **1.2 Goal and Objectives of the Research**

The goal of the research discussed herein was to design and validate a novel BMS for condition monitoring and power management of rechargeable multicell batteries. Compared to the state-of-the-art BMSs, the BMS presented here will extend the lifetime, enhance the reliability, and optimize the performance of battery systems. Specifically, the goal was achieved through the execution of the following three objectives.

- **Develop high-fidelity battery models for BMS execution and online condition monitoring of battery cells:** The battery models developed are capable of capturing the dynamic circuit characteristics, nonlinear capacity and

open-circuit voltage effects, hysteresis effect, and temperature effect of battery cells.

- **Develop a cell switching circuit topology and hardware design to achieve self-X (self-reconfiguration, self-healing, self-balance, and self-optimization) of multicell batteries:** The proposed cell switching circuit is able to protect individual cells from abnormal conditions, balance cell state variations, and improve energy conversion efficiency of each individual cell in a multicell battery. The hardware of the cell switching circuit was implemented with relatively low cost and complexity. Moreover, a bidirectional DC/DC converter was designed to control the charge and discharge of the multicell battery and to coordinate with the cell switching circuit to balance the cell state variation for a battery system. Finally, a system-level design was developed to show the scalability of the proposed self-X battery design for real-world applications in electric vehicles (EVs) and plug-in hybrid electric vehicles (PHEVs).
- **Develop model-based online condition monitoring algorithms for battery cells:** These included the online parameter identification algorithms, maximum capacity estimation algorithm, SOC estimation algorithms, and SOH estimation algorithms. The condition monitoring algorithms were balanced between accuracy and complexity in order to be suitable for the real-time, embedded BMS.

### 1.3 Outline of Dissertation

The outline of the dissertation is as follows:

Chapter 2 provides a literature review of the hardware and software of a BMS as well as the online condition monitoring algorithms for batteries.

Chapter 3 provides high-fidelity battery models for BMS execution and online condition monitoring of battery cells.

Chapter 4 develops a self-X multicell battery module and system design, which is validated by simulation and experimental studies for multicell lithium-ion batteries.

Chapter 5 proposes a particle swarm optimization (PSO)-based impedance and SOC estimation scheme using a discrete-time hybrid battery model developed in Chapter 3. Simulation and experimental results are provided to validate the proposed estimation scheme for single-cell and multicell lithium-ion batteries.

Chapter 6 proposes a simplified hybrid battery model-based condition monitoring algorithm. Simulation and experimental results are provided to validate the proposed algorithm for single-cell and multicell lithium-ion batteries.

Chapter 7 provides an electrical circuit with hysteresis model-based condition monitoring algorithm. Simulation and experimental results are provided to validate the proposed algorithm for a Mitsubishi lithium-ion battery cells.

Chapter 8 describes the concluding remarks and contributions of this dissertation research as well as recommendations for future research.

## CHAPTER 2: LITERATURE REVIEW

### 2.1 BMS

There is still no exact definition of BMS. This research adopted the definition that a BMS is a system consisting of hardware, such as sensors, a controller, electrical circuits, and communication wires, as well as software algorithms embedded in controller [25] to perform the functions of condition monitoring, fault diagnosis and prognosis, cell balancing, charge and discharge control, and protection for batteries and reporting the data, etc. The framework of a typical BMS is shown in Figure 2.1 [6].

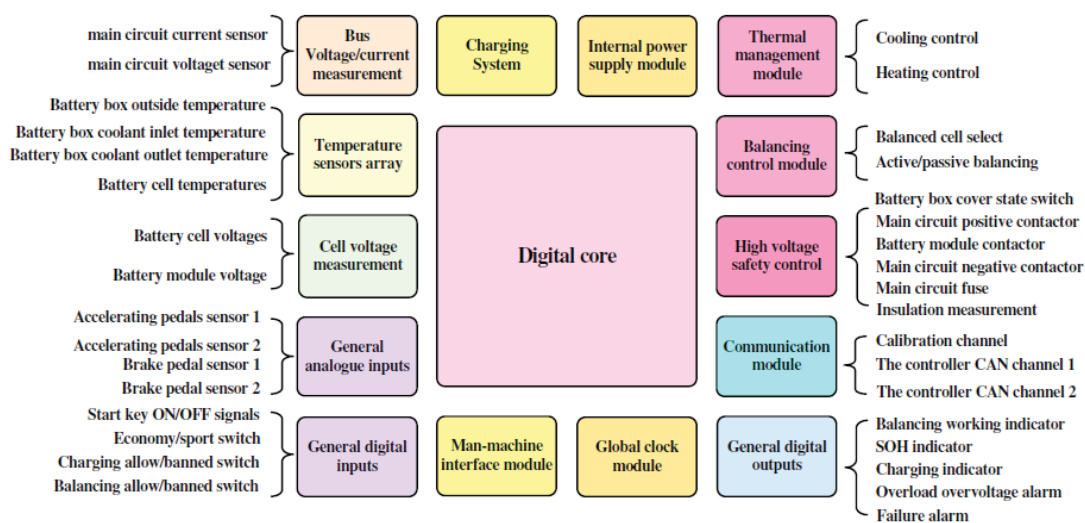


Figure 2.1: Framework of a typical BMS. (Courtesy of [6].)

## 2.2 Hardware of a BMS

The BMS hardware can be categorized into two parts [6]: input hardware and output hardware. The input hardware provides data to the BMS software. The input hardware is mainly composed of current and voltage sensors to measure the main-circuit current and voltage and the voltages of individual cells, temperature sensors to measure the cell temperature and the ambient temperature outside the battery module, and dedicated analog wire and digital wire for communication, etc. [25].

The output hardware of a BMS typically consists of the following: 1) safety circuits [12], such as the main battery pack relay, battery module relays, and/or a fuse embedded in each battery cell [26]; 2) thermal management circuits, such as a cooler and an electric heater for cooling and heating control of the battery; 3) general digital outputs, such as mode (charge, discharge, and failure alarm) indicators; 4) output communication/network circuits; and 5) balancing circuits for battery equalization. The output hardware is controlled by the BMS software.

In recent years, cell balancing techniques have been widely studied [13]-[17]. The balancing circuits equalize the voltages or SOCs between cells as consistently as possible. However, most existing balancing circuits use dissipative resistors, resulting in energy loss and generating considerable heat [13]. To reduce energy loss, active balancing circuits were proposed by using transformers and switches [14], switched capacitors [15], and DC/DC converters [16]. The products of cell balancing integrated circuits (ICs) [17] use electronic converters to transfer charge from cell to cell during operation. However, this solution increases the cost and volume of the battery system, is unable to handle faulty cells, and only works for the batteries with multiple cells connected in series.

Recently, several reconfigurable multicell battery topologies were proposed for portable electronic devices [18]-[21] and for a large-scale battery system [22]. Figure 2.2 shows the reconfigurable multicell battery topology in [21]. In a reconfigurable multicell battery, the optimal cell configuration is dynamically selected to minimize the system power consumption and maximize the usable battery capacity and operation time [20]. Moreover, the reconfigurable design can provide multiple voltage levels, which may improve the efficiency, scalability, and fault tolerance of the battery and reduce the complexity of the DC/DC converter circuit for charging and discharging the battery [18], [21]. However, these topologies are too complex and unrealistic for battery systems with large numbers of cells. The relay switches used in [19]-[22] are expensive and bulky and have low tolerance to high voltage spikes; and, therefore, they are difficult to implement in real-world applications.

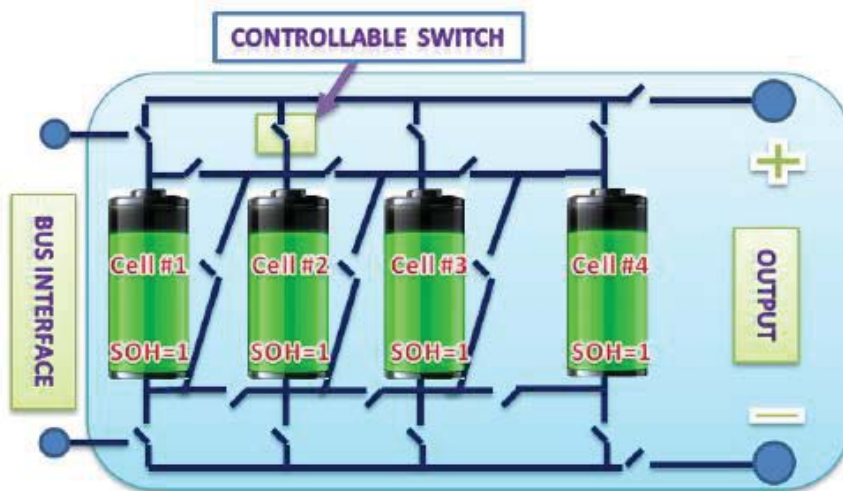


Figure 2.2: A reconfigurable multicell battery topology. (Courtesy of [21].)

In the reconfigurable battery, the switches are the key components that allow the cell array to be dynamically configured. More switches mean more versatility but lower reliability and higher cost. In addition to the aforementioned components, the BMS hardware may also have an internal power supply module, a global clock module, a charging system, and a man-machine interface module. It should also ensure that the BMS hardware meets electromagnetic compatibility requirements [6].

### **2.3 Software of a BMS**

The functions of the BMS software usually include the following: 1) online parameter detection from sensors and condition monitoring, such as monitoring the parameters and states related to the operating and health conditions of the battery; 2) fault diagnosis and prognosis; 3) safety and operation control; 4) cell balancing; 5) communication between the internal battery modules and the external devices; 6) external device control, such as charge control; and 7) networking and information storage.

Battery parameter detection includes voltage, current, and temperature detection to prevent overcharging; overdischarging; overtemperature; smoke detection; insulation detection; collision detection; impedance detection, etc. Online condition monitoring involves tracking the changes in the parameters and states related to the operating and health conditions of the battery, such as SOC, SOH, and SOP or state of function (SOF). The SOC is defined as the ratio of the available capacity with respect to the maximum capacity of a battery. The SOH is an indicator of battery aging and wear, which can be estimated by the measured or estimated impedance or conductance or estimated maximum capacity of the battery cell [27]. The SOF is used to describe, while the battery is in

operation, how its performance meets the real demand [6]. The SOF can be estimated according to the SOC, SOH, and operating environment of the battery [6], [28].

The faults in a battery system include sensor fault, communication fault, cell fault, loose connection, insulation fault, etc. The battery cell faults include mild fault and incipient fault. Thermal runaway [29] is an incipient fault usually caused by overheating and is accelerated by increased temperature. The fault prognosis mainly predicts how much time remains in the useful life of the battery [30]. The fault diagnosis and prognosis is performed by using the data obtained from battery parameter detection and condition monitoring [31].

Battery safety control includes the thermal system control and the high voltage and current safety control. When a fault is diagnosed, the safety control unit is informed through the BMS communication and is required to protect the battery system from the fault. When a certain threshold value of the battery temperature, or voltage, or current is exceeded, the BMS cuts off the battery power supply to prevent damage to the battery. According to the temperature distribution within the battery pack and the requirements of charge or discharge, the safety control unit decides whether to start heating or cooling as well as the heating or cooling power. Moreover, the operation control unit controls the cell balancing circuit according to the voltage or SOC of each cell.

The BMS can communicate and give commands to external devices, such as the charger and converter [25]. For example, the BMS controls the charger that charges the battery based on the battery states and the power level of the charger [32].

Since it is not convenient to disassemble a BMS, a network function is required [6] for online calibration and monitoring, automatic code generation, and online program

download/update. A controller area network (CAN) is commonly used [25]. Moreover, the BMS usually has an information storage unit to store the key data, such as SOC, SOH, accumulated charge and discharge Ah values, fault code, and uniformity.

The BMS of a battery system in an EV/PHEV may only have some of the aforementioned hardware and software units. Usually, there is at least one voltage sensor and one temperature sensor for each battery cell. For a battery system with only several cells, the BMS may only have one controller whose function may even be integrated into the main controller of the battery system. For a battery system with multiple modules and hundreds of cells, the BMS may consist of one master controller and several slave controllers; each slave controller only manages one battery module.

For each battery module, there can be some module circuit contactor and balancing circuit. A slave controller is typically employed to manage the battery module, such as measuring the voltage and current, controlling the contactor, equalizing the cells, and communicating with the master controller. The master controller performs the functions of battery state estimation, fault diagnosis, thermal management, etc., according to the data reported by the slave controllers.

## **2.4 Battery Modeling**

The performance of a BMS relies on a high-fidelity battery model to monitor conditions of the battery, such as the run-time SOC, SOH, and SOP, as well as to optimally control the charging/discharging operation of the battery to prolong the battery life and usage and reduce the risk of overcharge and overdischarge [33]. To achieve these objectives, the battery model should accurately capture various nonlinear capacity effects,

such as the rate capacity and recovery effects, and dynamic current-voltage (I-V) characteristics of the battery. The nonlinear capacity effects and dynamic I-V characteristics strongly depend on run-time factors, such as temperature and history of current, such as current rate (i.e., C-rate) and the direction of the current [27]. In addition, a balance between the accuracy and complexity of the battery model should be considered for real-time execution.

The widely used battery models to characterize the run-time behaviors of electrochemical batteries, in general, can be classified into two categories: electrochemical models and electrical circuit models. The electrochemical models use complex nonlinear partial differential equations (PDEs) to describe electrochemical physics of the batteries, such as the concentration of ions in the electrodes and electrolyte [34]. The electrochemical models are the most accurate. However, establishing these models requires detailed knowledge of the battery chemical processes and the need to identify a great number of parameters, which makes the models difficult to configure. Furthermore, it is difficult to use these models for real-time application due to the high complexity and intensive computation requirement. Therefore, the electrochemical models may be more feasible for offline battery cell design and analysis of the fundamental processes which occur during cell operation. The recently developed electrochemical models employ many approximations and linearization methods to reduce computational complexity. For example, the single-particle models neglect the concentration gradients in the electrolyte [35]. Therefore, the accuracy of the single-particle model is only acceptable at low current rates. A polynomial approximation [36] and fade approximation [37] were used to model the concentration profile in the solid phase of a battery cell to eliminate the need for the

PDEs. Recently, reduced order models based on Laplace transfer function analysis were presented in [38]. In [39], temperature-dependent parameters, including the diffusion coefficient, ionic conductivity, transference number of lithium ions, etc., were considered to more completely characterize the thermal behavior of the polymer lithium-ion batteries. However, effort is still needed to further reduce the computational cost of these simplified electrochemical models for real-time BMS applications.

The electrical circuit models use equivalent electrical circuits to capture I-V characteristics of batteries and have lower computational costs than electrochemical models. The selection of the structures and circuit components of an electrical circuit model depends on the experimental methods as well as the desired accuracy [40]. An electrical circuit model can be constructed as a frequency domain model, e.g., Randle's circuit model [41], using an electrochemical impedance spectroscopy or a time domain model [42], by measuring the pulsed discharge/charge behavior. Figure 2.3 shows an example of a time domain model [42]. If more resistor-capacitor (RC) components are used, the model has better accuracy in characterizing the I-V dynamics but higher complexity [43]. A comparison of various electrical circuit models is presented in [44]. The fidelity of these electrical circuit models can be improved by making the model parameters depend on several factors, such as SOC [42], C-rate [45], and temperature [46], of the battery.

However, the traditional electrical circuit models do not integrate battery nonlinear capacity behaviors, leading to an inaccurate prediction of run-time I-V characteristics and SOC [27]. An enhanced circuit-based model [47] was introduced by replacing its left-hand side RC, shown in Figure 2.3, with Rakhmatov's diffusion model [48] to characterize the nonlinear capacity effect. Recently, a hybrid battery model [27], shown in Figure 2.4, was

developed by the author to replace Rakhmatov's diffusion model with a kinetic battery model (KiBaM) [49], which has lower computational cost and is simple to implement; and, therefore, is more feasible for real-time BMS. However, the existing electrical circuit battery models with nonlinear capacity effects only considered the discharge mode at a certain ambient temperature, e.g., the room temperature.

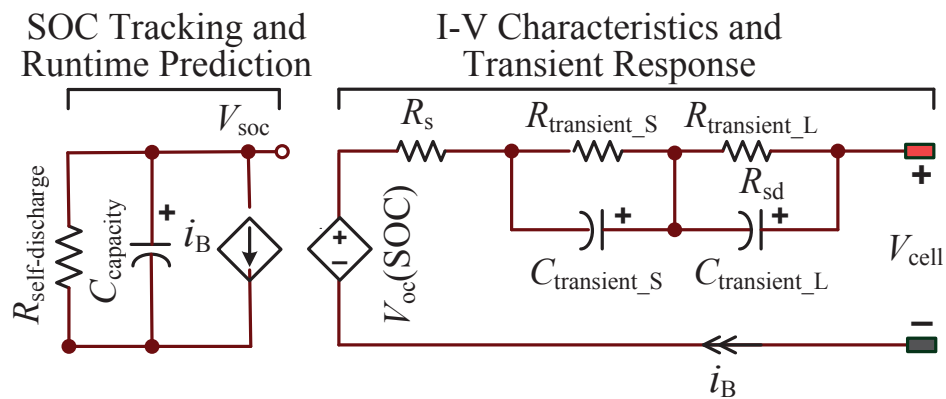


Figure 2.3: An electrical circuit battery model. (Courtesy of [42].)

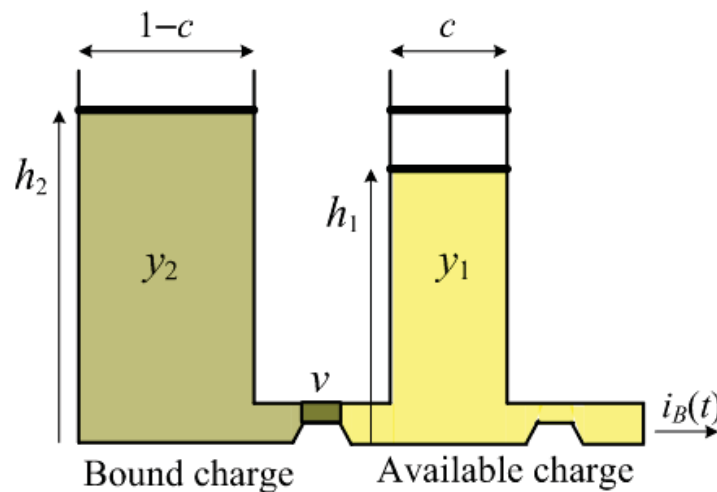


Figure 2.4: The kinetic battery model. (Courtesy of [49].)

## 2.5 Condition Monitoring Algorithms

The condition monitoring algorithms provide information, such as crucial parameters and states related to the operating and health conditions of the battery [23]. A key function of the BMS software is to monitor the SOC, SOH, SOP, and the parameters, such as internal impedance and capacity, etc., of each cell during operation [33]. However, since these parameters and states are not directly measurable, state estimation and parameter identification techniques are commonly used to extract their values [23]. The parameters and states enable the fault diagnostic and prognostic capability of the battery system [50]. This capability allows proper maintenance to be scheduled, which helps reduce unscheduled downtime of the battery system as well as the cost of repairing the damaged system [23]. The state and parameter estimation methods should be selected appropriately based on the accuracy, robustness or sensitivity to noise, and computational burden or complexity.

The conceptual relationship of the battery states, including SOC, SOH, and SOF, is illustrated in Figure 2.5 [6]. The SOH is determined by service life prediction and fault diagnosis output [6]. The SOF is determined by taking into consideration the influence of the aging factor (i.e., SOH), SOC, operating temperature, fault level, and the charge/discharge history, if needed.

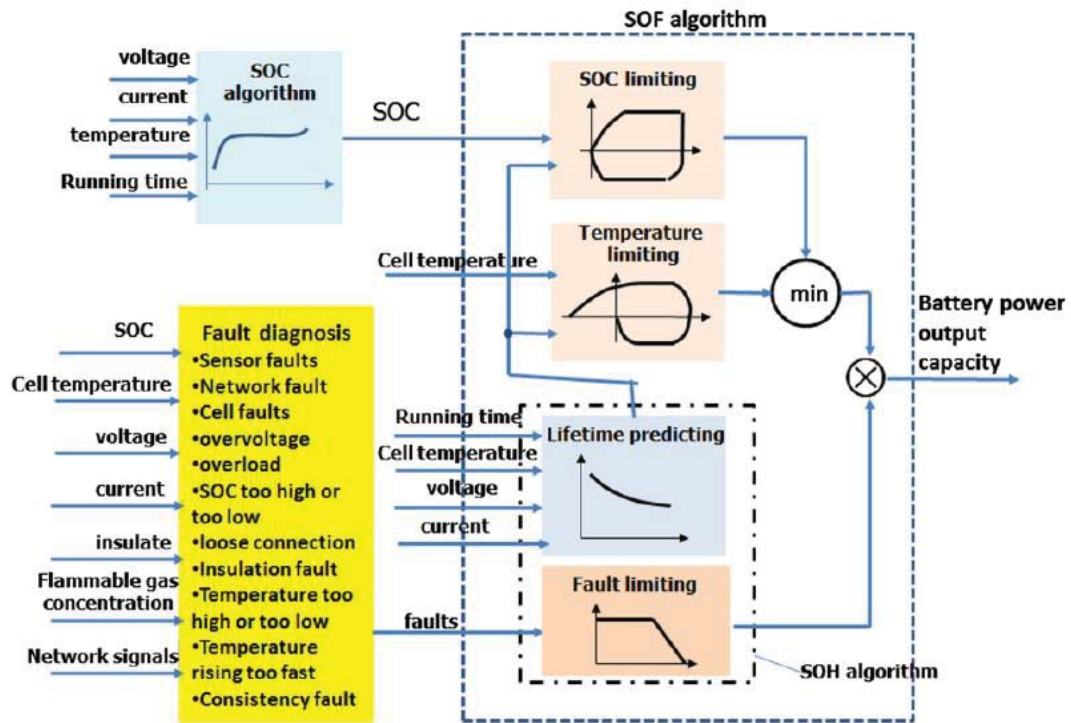


Figure 2.5: Conceptual relationship of the battery states. (Courtesy of [6].)

### 2.5.1 Model Parameter Identification

The model parameter identification algorithms estimate the parameters of the mathematical models of a physical system from the data observed [51]. The model parameter identification algorithms can be grouped into frequency-domain methods and time-domain methods. The time-domain methods are widely used for battery parameter identification. They utilize discrete time-domain models or state-space models to estimate the parameters. In general, this can be achieved by using offline batch methods, such as the least square (LS) or recursive least square (RLS) methods or online Kalman filter-based methods [28].

For example, a discrete-time transfer function can be obtained based on the discrete time-domain model of a battery, as follows.

$$\frac{y(z)}{u(z)} = \frac{b_0 + b_1 z^{-1} + b_2 z^{-2} + \dots + b_n z^{-n}}{1 + a_1 z^{-1} + a_2 z^{-2} + \dots + a_n z^{-n}} \quad (2-1)$$

Then, the corresponding difference equation of the input/output relationship will be formulated into the regression form (2-2) as follows to estimate the parameters of the discrete-time transfer function:

$$y(k) = b_0 u(k) + b_1 u(k-1) + \dots + b_n u(k-n) - a_1 y(k-1) - \dots - a_n y(k-n) = \Phi^T \Theta \quad (2-2)$$

where the regression vector is  $\Phi^T(k) = [u(k), \dots, u(k-n), -y(k-1), \dots, -y(k-n)]$ , and the vector of the parameters to be estimated is  $\Theta = [b_0, \dots, b_n, a_1, \dots, a_n]^T$ .

The linear LS regression-based methods are by far the most widely used to estimate the parameters of a battery model due to their low computational cost and relatively high accuracy. In order to perform online estimations of the time-varying parameters, the RLS [52], [53] and moving window least square (MWLS) methods [41], [54], [55] have been introduced with an exponential forgetting (EF). Recently, a Bierman's upper-triangular and diagonal factorization-based RLS (UDRLS) estimation method with an EF [56] was proposed to solve the digital computer implementation problem of the RLS. The Bierman method with an EF preserves a positive covariance, thus the numerical stability is improved. However, it has drawbacks, such as windup when a data vector is not persistently exciting [57] as well as nonoptimal tracking ability and noise influence due to the use of a fixed forgetting factor value [57].

## 2.5.2 State of Charge Estimation

The SOC is defined as the ratio of the available capacity with respect to the maximum capacity of a battery [27]. For example, if a battery is fully charged, its SOC is 1 (or 100%). On the other hand, a 0 (or 0%) SOC means that the battery is fully discharged. A variety of battery SOC estimation methods have been developed, which, in general, can be classified into four categories: directive measurement, computational intelligence based, model based, and mixed methods.

The directive measurement methods include voltage translation and Coulomb counting [58]. They are simple and easy to implement. For example, the SOC can be calculated by simply measuring the open-circuit voltage (OCV) in the voltage translation method and by integrating the measured current ( $i_B$ ) over time with the information on the initial SOC ( $SOC_{initial}$ ) and maximum capacity ( $C_{max}$ ) in the Coulomb counting method expressed by the following equation.

$$SOC(t) = \frac{C_{usable}(t)}{C_{max}} = SOC_{initial} - \frac{\int i_B(t)}{C_{max}} \quad (2-3)$$

However, both methods have limitations. For example, the former requires the battery to rest for a long period and to be cut off from the external circuit to measure the OCV, which may be impossible during operation. The latter suffers from unrecoverable problems that might be caused by factors such as an inaccurate initial SOC value or maximum capacity value, cumulative integration errors, and noise corruption. Moreover, the Coulomb counting-based methods cannot keep track of nonlinear battery capacity variation effects, such as the rate capacity effect and recovery effect [27].

The computational intelligence-based methods describe the nonlinear relationship between the SOC and the factors influencing the SOC, such as battery voltage, current, and temperature [59]-[61]. Artificial neural network (ANN) based methods [59], fuzzy logic method [60], and support vector machines [61] have been used to estimate the SOC of a battery. Although the ANN methods do not have to take into consideration the details of the batteries and are suitable for the SOC estimation of all types of batteries, the learning process required by these methods has a quite high computational burden and is difficult to implement in real-time SOC tracking. The fuzzy logic method simulates the fuzzy thinking of human beings by using fuzzy logic based on a great number of test curves, experience, and reliable fuzzy logic theories to eventually realize the SOC prediction [62]. This method requires a strong understanding of the batteries behaviors and entails a relatively high computational cost [6].

Recent research on SOC estimation has been focused on model-based methods. The model-based SOC estimation methods basically utilize the state-space electrochemical battery models or electrical circuit battery models to design an observer for online SOC estimation. Electrical circuit models and extended Kalman filter (EKF) types of approaches have been extensively proposed for online SOC estimation. These methods provide accurate SOC estimation in general [63], [64]. However, they require an accurate battery model, whose parameters, e.g., resistances and capacitances, typically vary with the SOC, temperature, current, aging, etc., of the battery cell. Therefore, additional online parameter estimation is usually needed to reduce the estimation error. Joint methods have been proposed by combining the EKF-based SOC estimation and parameter estimation [65]. Some lithium-ion batteries have a relatively large nonlinearity of the OCV (i.e., the

hysteresis effect [66]). Therefore, the battery model should also include the hysteresis effect. To take into account the time-varying model parameters and hysteresis effect, a dual EKF [67], shown in Figure 2.6, and a dual sigma-point Kalman filter (SPKF) [68], which outperforms the EKF, were proposed to estimate the parameters and states on the same timescale. Nevertheless, errors can be large when the process and measurement noise are uncorrelated zero-mean white Gaussian and their covariance values are not properly defined. Moreover, the joint/dual EKF and dual SPKF SOC estimation methods have a high computational complexity.

Other observer design methods have been used to design the electrical circuit battery model-based SOC estimators with regression-based parameter estimation, including a linear observer [54] and an SMO [69]. A primary advantage of these observers is that they are computationally simple and allow robust convergence of the estimation. However, they have moderate performance in terms of accuracy. Moreover, the accuracy of the SMO-based method degrades due to the chattering problem when model uncertainties are significant [70].

The mixed SOC estimation methods combine the advantages of the aforementioned three methods. For example, in [71], the SOC of lithium-ion batteries is estimated by using ANNs and EKF.

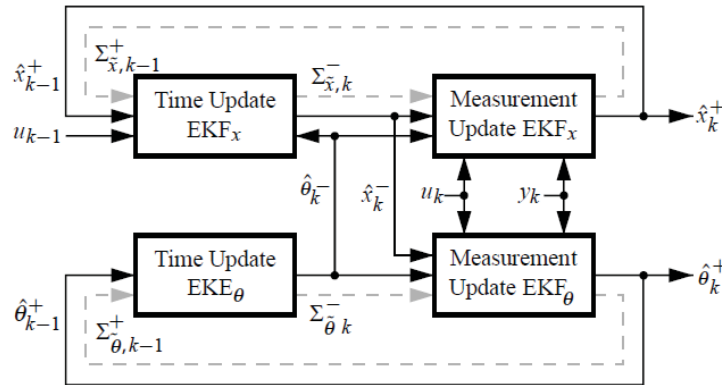


Figure 2.6: Diagram of dual EKF. (Courtesy of [67].)

### 2.5.3 State of Health Estimation

The SOH is an indicator of battery aging and wear, resulting in capacity and power degradation. In general, capacity [72] and impedance components (e.g., internal resistance [73], diffusion resistance [63], and diffusion capacitance [74]) or total impedance [75] are the commonly used battery parameters to quantify capacity fade and power fade, respectively. A commonly used standard for SOH is that a battery should be replaced once the maximum capacity is reduced to 80% of the original (or new). This criterion, while simple, is somewhat arbitrary. The 80% capacity is only valid for a given current profile, usually a constant current discharge; with other discharge profiles, the capacity may be different. Another SOH indication method is to compare the relative impedance between the original (or new) and present battery.

The SOH estimation methods can be classified into two categories: directive measurement methods (i.e., nonmodel-based methods) and model-based methods. In the directive measurement method, the value of battery capacity is extracted from a full discharge test with a small current [72]. This method, however, requires a long time to

implement and is not suitable for online application. The impedance methods do not determine the available capacity but measure the impedance of the battery. In these methods, signal injection and impedance measurement or estimation [76] devices are required, which results in additional costs and the devices may not be implemented in real time. In many applications, such as EVs and PHEVs, due to the unpredictability of the user and battery behaviors, accurate estimation of the SOH requires adaptive methods together with one of the aforementioned techniques.

The same or similar model-based adaptive techniques used for SOC estimation can be applied to SOH estimation, and an accurate SOC estimation will facilitate the estimation of the SOH [77]. For example, the dual EKF [63], [67] and SMO [78] were also applied to the estimation of the SOH of a battery. A multiscale framework with a dual EKF [79] was used on the same model [67] for SOH estimation. The method adapted the slow time-varying capacity parameter, estimated by an EKF with a large timescale, while keeping the estimation of the fast time-varying states, such as SOC and terminal voltage, by another EKF with a small timescale [67]. This scheme achieved higher accuracy and efficiency than the traditional dual EKF. Recently, a recursive approximate weight total LS method [80] was used to estimate the battery capacity based on the Coulomb counting equation. This method required lower computation than the model-based adaptive methods and was more accurate than the LS-based method [80].

#### **2.5.4 State of Power and State of Function Estimation**

The constraints on the capability of a battery consist of not only its remaining charge reflected in the SOC but also its power delivery/storage capability [81]. For example,

the power capability of a battery constantly changes throughout its discharge cycle. The change in the power capability comes from both the drop in the internal OCV and the rise in the internal impedance [82]. Since battery manufacturers usually offer the upper and lower limits of the operating voltage for a battery, the BMS needs to ensure that these limits are satisfied during battery operation. Therefore, many researchers have focused on power capability estimation as well [81]-[85]. Two definitions have been proposed for battery power capability [83]: SOP and SOF. The SOP is found in [83], [84], which use an electrical circuit battery model to predict the maximum power that a battery can deliver within the specified voltage limits, as follows:

$$SOP(t) = \frac{V_{limit\_discharge} \times (V_{oc}(t) - V_{limit\_discharge})}{\sum R_{in}} \text{ [W]} \quad (2-4)$$

where  $V_{limit\_discharge}$  and  $V_{oc}$  are the minimum discharge voltage of the battery allowed by the manufacturer and OCV, respectively;  $R_{in}$  is the internal resistance of the battery model. Equation (2-4) can be adopted for the charging operation by changing  $V_{limit\_discharge}$  to  $V_{limit\_charge}$ . Therefore, the SOP can be estimated by using estimated  $V_{oc}$  and internal resistance or impedance.

The SOF describes how the battery meets the power demand. The SOF predicts whether the battery can provide the necessary power to complete a task. Therefore, the SOF could be defined as a yes/no logical function [28]. An SOF equaling 1 means the battery can meet the demand, while an SOF equaling 0 means it cannot.

$$SOF = \begin{cases} 1 & \text{if } V_{min} \geq V_{limit} \\ 0 & \text{if } V_{min} < V_{limit} \end{cases} \quad (2-5)$$

The simple criterion of SOF usually consists of checking the minimum terminal voltage,  $V_{min}$ , which should be larger than the threshold terminal voltage,  $V_{limit}$ , for acceptable battery performance. However, defining the SOF as follows is preferred [6]:

$$SOF = \frac{P_p - P_d}{P_{max} - P_d} \quad (2-6)$$

where  $P_p$  denotes the possible power supplied by the battery;  $P_d$  is the demand of the power; and  $P_{max}$  is the maximum power which can possibly be supplied by the battery. For example, if the SOF equals 0, the battery barely meets the power demand.

The SOF can be comprehensively determined by the SOC, SOH, temperature, and the fault state of the battery. The relations between the SOF, SOC, and SOH are shown in Figure 2.7 [86]. The SOF can be defined as the ratio of the remaining available energy in the battery and the maximum possible energy that could be stored in the battery [86].

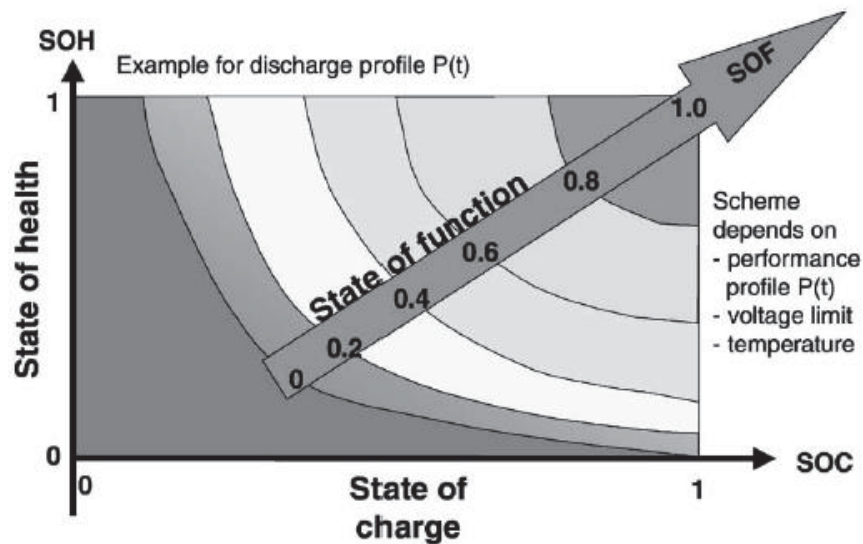


Figure 2.7: The relationship between SOF, SOC, and SOH of a battery. (Courtesy of [86].)

## CHAPTER 3: BATTERY MODELING

A high-fidelity battery model capable of accurately predicting real-time battery performance for various operating conditions is crucial to the design and operation of battery-powered systems. Such a battery model generally needs to meet the following requirements: 1) low computational complexity; 2) ability to estimate cell electrical parameters at various operating conditions, including various charge/discharge current rates and ambient temperature conditions; and 2) ability to accurately capture the conditions of battery cells, such as runtime state of charge (SOC) and state of health (SOH) of the battery. This chapter is organized as follows. First, a hybrid battery model is briefly introduced as well as its discrete-time version and a simplified version of the hybrid battery model is introduced. An enhanced hybrid battery model is then proposed to accurately predict runtime behaviors of batteries under various temperatures and charge/discharge currents. The enhanced hybrid battery model is validated by simulation and experimental studies for a newly developed high-voltage, cylindrical, lithium-ion battery cell in various current and temperature conditions. Finally, an electrical circuit battery model incorporating the hysteresis effect is developed.

### 3.1 Hybrid Battery Model

The hybrid battery model [27] was developed by the author to integrate a battery's nonlinear capacity effects into the electrical circuit model, as shown in Figure 3.1. The module on the left of the hybrid battery model performs the function of an enhanced Coulomb counting algorithm-based SOC tracking for the battery cell. The enhanced Coulomb counting algorithm offers the actual real-time SOC (i.e.,  $SOC_T$ ), shown in (3-1).

A voltage-controlled voltage source,  $V_{oc}(SOC_T)$ , is used to bridge the SOC to the cell's open-circuit voltage (OCV). The RC circuit on the right simulates the I-V characteristics and transient response of the battery cell, where the series resistance,  $R_s$ , is used to characterize the charge/discharge energy losses of the cell due to the electrode, electrolyte, separator, and contact resistances. Other resistances and capacitances are used to characterize the transient voltage responses of the battery, including the charge transfer voltage response  $V_{ct}$  and the short-term diffusion voltage response  $V_{sd}$ . The former is due to the double-layer capacitance  $C_d$  and charge transfer resistance  $R_{ct}$  while the latter is due to the short-term diffusion capacitance  $C_{sd}$  and resistance  $R_{sd}$ .  $V_{cell}$  represents the terminal voltage of the battery cell. The hybrid battery model is expressed by the following equations (3-1)-(3-7) [27]:

$$SOC_T(t) = \frac{C_{available}(t)}{C_{max}} = SOC_T(0) - \frac{[\int i_B(t)dt + C_{unavailable}(t)]}{C_{max}} \quad (3-1)$$

$$C_{unavailable}(t) = \begin{cases} C_{unavailable}(t_0)e^{-k'(t-t_0)} + (1-c)\frac{i_B}{c} \frac{1-e^{-k'(t-t_0)}}{k'}, & t_0 < t < t_d \\ C_{unavailable}(t_d)e^{-k'(t-t_d)}, & t_d < t < t_r \end{cases} \quad (3-2)$$

$$V_{oc}[SOC_T(t)] = q_0 e^{-q_1 SOC_T(t)} + q_2 + q_3 SOC_T(t) - q_4 SOC_T^2(t) + q_5 SOC_T^3(t) \quad (3-3)$$

$$V_{cell}(t) = V_{oc}[SOC_T(t)] - i_B(t) \cdot R_s - V_t(t) \quad (3-4)$$

$$V_t(t) = V_{ct}(t) + V_{sd}(t) \quad (3-5)$$

$$V_{ct}(t) = \begin{cases} R_{ct} \cdot i_B(t) [1 - e^{-(t-t_0)\tau_s}], & t_0 < t < t_d \\ V_{ct}(t_d) \cdot e^{-(t-t_d)\tau_s}, & t_d < t < t_r \end{cases} \quad (3-6)$$

$$V_{sd}(t) = \begin{cases} R_{sd} \cdot i_B(t) [1 - e^{-(t-t_0)\tau_L}], & t_0 < t < t_d \\ V_{sd}(t_d) \cdot e^{-(t-t_d)\tau_L}, & t_d < t < t_r \end{cases} \quad (3-7)$$

where  $SOC_T(0)$  is the initial SOC at the beginning of the battery operation (i.e.,  $t = 0$ );  $k'$  ( $= v/[c(1-c)]$ ) is a constant diffusion rate;  $v$  and  $c$  are valve and capacity ratio of the KiBaM, respectively;  $i_B$  is the cell current, which is positive if the battery cell is operated in the discharge mode and negative if operated in the charge mode;  $t_0$ ,  $t_d$ , and  $t_r$  are the beginning time, discharge ending time, and (rest) ending time, respectively, of a period during which  $i_B$  is constant;  $C_{max}$ ,  $C_{available}$ , and  $C_{unavailable}$  are the maximum, available, and unavailable capacities of the cell, respectively;  $q_0, \dots, q_5$  are coefficients;  $\tau_S = R_{ct} \cdot C_d$ ;  $\tau_L = R_{sd} \cdot C_{sd}$ . The  $SOC_T$  of the battery cell reduces when it delivers charge to load, expressed by the enhanced Coulomb counting term in (3-1). The nonlinear SOC variation due to the nonlinear capacity effects of the battery is represented by  $C_{unavailable}$ .

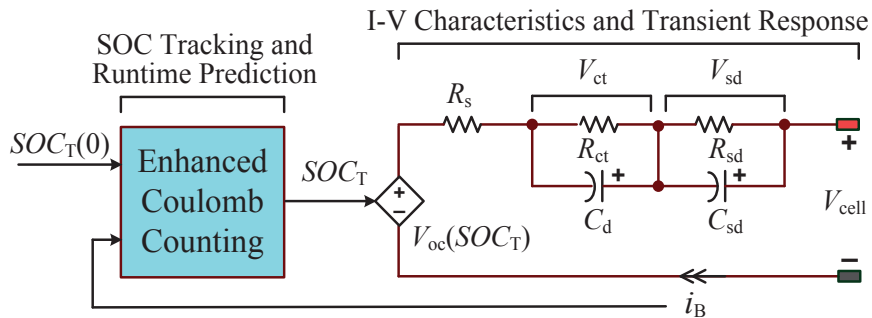


Figure 3.1: The hybrid battery model.

As in (3-4), the terminal voltage,  $V_{cell}$ , is estimated by  $V_{oc}$ , the voltage across  $R_s$  (i.e.,  $i_B \cdot R_s$ ), and the transient voltage term,  $V_t$ , which represents the transient response of the RC network.

To facilitate real-system applications, a discrete-time version of the hybrid battery model [87] is expressed as follows:

$$SOC_T(k) = \frac{C_{available}(k)}{C_{max}} = SOC_T(k-1) - \frac{1}{C_{max}} [i_B(k-1) \cdot T_s + \Delta C_{unavailable}(k-1)] \quad (3-8)$$

$$C_{unavailable}(k) = C_{unavailable}(k-1) \cdot e^{-kT_s} + (1-c) \frac{(1-e^{-kT_s})}{c \cdot k'} \times i_B(k) \quad (3-9)$$

$$V_{cell}(k) = V_{oc}(k) - R_s \cdot i_B(k) - V_{ct}(k) - V_{sd}(k) \quad (3-10)$$

$$\begin{bmatrix} V_{ct}(k) \\ V_{sd}(k) \end{bmatrix} = \begin{bmatrix} e^{-\frac{T_s}{\tau_s}} & 0 \\ 0 & e^{-\frac{T_s}{\tau_L}} \end{bmatrix} \cdot \begin{bmatrix} V_{ct}(k-1) \\ V_{sd}(k-1) \end{bmatrix} + \begin{bmatrix} R_{ct}(1-e^{-\frac{T_s}{\tau_s}}) \\ R_{sd}(1-e^{-\frac{T_s}{\tau_L}}) \end{bmatrix} \cdot i_B(k) \quad (3-11)$$

where  $T_s$  is the sampling period;  $i_B(k)$  is the instantaneous current of the battery cell at the time index  $k$ ; and  $\Delta C_{unavailable}$  is the variation of the unavailable capacity of the battery cell during  $T_s$ . In this dissertation, the discrete version of the hybrid battery model is referred to as the hybrid battery model.

In addition, a simplified hybrid battery model [55] was developed to provide a lower computational cost hybrid battery model. Assuming that  $V_{oc}(SOC_T)$  is  $b_1 \cdot SOC_T + b_0$  and  $V_{sd}$  is neglected, the simplified hybrid battery model can be expressed as follows:

$$\begin{bmatrix} SOC_T(k+1) \\ V_{ct}(k+1) \end{bmatrix} = \begin{bmatrix} 1 & 0 \\ 0 & e^{-\left(\frac{T_s}{\tau_s}\right)} \end{bmatrix} \cdot \begin{bmatrix} SOC_T(k) \\ V_{ct}(k) \end{bmatrix} + \begin{bmatrix} \frac{-T_s}{C_{max}} \\ R_{ct}(1-e^{-\left(\frac{T_s}{\tau_s}\right)}) \end{bmatrix} \cdot i_B(k) - \begin{bmatrix} \frac{\Delta C_{unavailable}(k)}{C_{max}} \\ 0 \end{bmatrix} \quad (3-12)$$

$$V_{cell}(k) = [b_1 \quad -1] \cdot \begin{bmatrix} SOC_T(k) \\ V_{ct}(k) \end{bmatrix} - R_s i_B(k) + b_0 \quad (3-13)$$

where  $b_0$  and  $b_1$  are coefficients. The parameterization of  $V_{oc}(SOC_T)$  as  $b_1 \cdot SOC_T + b_0$  is more accurate than the methods that assume a constant  $V_{oc}$  [40], [53], [56] to derive regression forms

of the difference equations of the electrical circuit battery model which will decrease the parameter estimation accuracy, especially when  $V_{oc}$  is subject to a high nonlinearity.

## **3.2. Enhanced Hybrid Battery Model**

An enhanced hybrid battery model [88] was developed, which is capable of capturing accurate runtime SOC and I-V dynamics of batteries under various charge and discharge currents and ambient temperatures. The enhanced hybrid battery model includes a new runtime SOC estimation module, reflects the nonlinear OCV effect; and uses temperature- and current-dependent parameters. The enhanced hybrid battery model was validated by simulation and experimental studies for a cylindrical lithium-ion battery.

### **3.2.1 Related Works**

#### **3.2.1.1 Nonlinear Capacity and Nonlinear OCV effect**

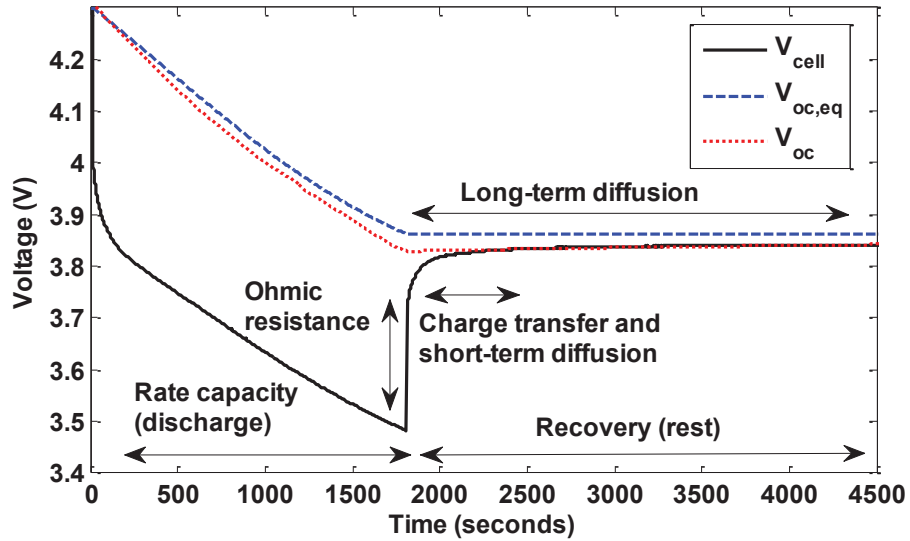
A rechargeable electrochemical battery cell consists of an anode and a cathode placed in an electrolyte medium. The electric current through a cell is generated by the electrochemical reactions occurring at the electrode-electrolyte interface. The battery capacity depends nonlinearly on its current profile due to two effects: the rate capacity effect and the recovery effect. The rate capacity effect is defined as: less charge can be drawn from a battery at a higher discharge current because of the high concentration gradient of active reaction sites, thus resulting in a lower SOC compared to the battery under a lower current rate [34]. However, the unavailable charge due to a large discharge current is still left behind in the battery if the thermal dissipation and self-discharge are neglected [27]. The unavailable

charge will be available after a period with no or a low current due to the reduced gradient of the concentration. This is the recovery effect.

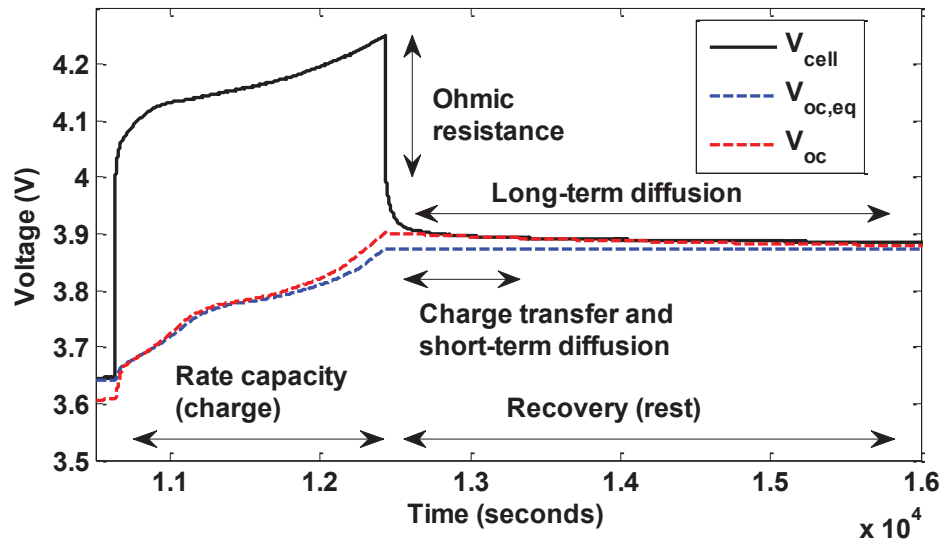
The nonlinear capacity effect is originally defined and observed in the discharge process. It is assumed that the rate capacity effect in the charge mode is that less charge can be stored into a battery at a higher charge current rate due to a higher concentration gradient, thus resulting in lower charge acceptance compared to the battery charged under a lower current rate. The charge acceptance is the ability of the battery to accept charge [89]. For example, there is a limitation on lithium-ions going into the layers of the anode due to the low ion conductivity and slow diffusion process in a lithium-ion battery cell. However, the charge acceptance is recovered if the battery relaxes. This can be explained as the recovery effect in the charge mode. If the charge current through the battery is too high in the high SOC region, e.g.,  $\text{SOC} > 80\%$ , it will cause surplus ions to be deposited on the anode in the form of lithium metal. This phenomenon is called lithium plating [90] and will result in a loss of charge and heat dissipation. A part of the charge lost in the lithium plating process is irreversible. The lithium plating will become more significant at a lower temperature [90], causing a lower charge acceptance.

The nonlinear capacity effects cause a nonlinear OCV response of the battery as well, which is called the nonlinear OCV effect. The time-domain responses of the terminal voltage ( $V_{cell}$ ), OCV ( $V_{oc}$ ), and equilibrium OCV ( $V_{oc,eq}$ ) of a lithium-ion battery cell using a pulsed current profile in the discharge and charge processes are shown in Figure 3.2, where the equilibrium OCV is the steady-state terminal voltage of the battery cell when no current flows for a long time. The trajectory of the OCV depends on the history of the battery usage. These voltage responses clearly show the nonlinear OCV effect as a consequence of the

nonlinear capacity effects of the battery cell, namely, the  $V_{oc}$  is smaller/larger than the  $V_{oc,eq}$  due to the rate capacity effect in the discharge/charge process. It then rises up/falls down to slowly converge with the  $V_{oc,eq}$  due to the recovery effect.



(a)



(b)

Figure 3.2: The time-domain responses of the terminal voltage, OCV, and equilibrium OCV showing the nonlinear capacity effects and nonlinear OCV effect of a lithium-ion battery cell with a pulsed current in the (a) discharge process and (b) charge process

### 3.2.2 Simple Expression of KiBaM

This dissertation utilizes two forms of the SOC: a transient SOC ( $SOC_T$ ) and an equilibrium SOC ( $SOC_E$ ). The former is the state of available capacity which takes into account the nonlinear capacity effects; and the latter is the state of usable capacity calculated by using the Coulomb counting method while neglecting the nonlinear capacity effects. The usable capacity is the charge stored in the battery; while the available capacity is the charge in the battery that can be actually used [27]. Both the SOC<sub>T</sub> offer useful information. The  $SOC_T$  is the actual real-time SOC and provides a runtime prediction for the battery (e.g., the remaining end of discharge time and end of charge time). The  $SOC_E$  will be used to estimate the maximum capacity of the battery [91].

The KiBaM is a model well suited for capturing the nonlinear capacity effects of batteries. A detailed description of the KiBaM can be found in [27] and [49]. In the KiBaM, it assumes that a battery has two charge wells, and the charge is distributed with a capacity ratio  $c$  ( $0 < c < 1$ ) between the two charge wells, as shown in Figure 3.3(a) and (b). In the discharge mode, the available charge well delivers charge directly to the load; while the bound charge well supplies charge only to the available charge well through a valve  $v$ . The rate of the charge flowing from the bound charge well to the available charge well depends on  $v$  and the difference in heights of the two wells,  $h_1$  and  $h_2$ , where  $h_1$  is related to the  $SOC_T$  of the battery. The battery is fully discharged when  $h_1$  becomes zero. The change of the charges in the two wells is expressed as [49]:

$$\begin{cases} \frac{dy_1(t)}{dt} = -i_B(t) + v[h_2(t) - h_1(t)] \\ \frac{dy_2(t)}{dt} = -v[h_2(t) - h_1(t)] \end{cases} \quad (3-14)$$

where  $y_1$  and  $y_2$  are the total charges in the available charge well and the bound charge well, respectively. The height difference,  $\delta = h_2 - h_1$ , between the two wells plays an important role in obtaining the nonlinear capacity variation in the discharge mode for  $SOC_T$  prediction using the enhanced Coulomb counting method in (3-1) and (3-2). On the other hand,  $SOC_E$  can be calculated using the Coulomb counting method by omitting the term of  $C_{unavailable}$  in (3-1).

A simpler formula of the KiBaM regarding the SOC<sub>s</sub> was derived. First,  $dy_1(t)/dt$  in (3-14) can be expressed as:

$$\frac{dy_1(t)}{dt} = k'[1-c]y_1 + k' \cdot c \cdot y_2 - i_B(t) \quad (3-15)$$

where  $y_1 = c \cdot h_1$ ,  $y_2 = (1-c) \cdot h_2$ , and  $k' = v/[c(1-c)]$ . By using  $SOC_E = (y_1 + y_2)/C_{max}$ , (3-15) can be reformulated as follows:

$$\frac{dy_1(t)}{dt} = -k'y_1(t) + k' \cdot c \cdot C_{max} SOC_E - i_B(t) \quad (3-16)$$

Since  $y_1 = c \cdot C_{max} \cdot SOC_T$ ,  $dSOC_T(t)/dt$  can be obtained from (3-16) as:

$$\frac{dSOC_T(t)}{dt} = k'SOC_E - k'SOC_T - \frac{i_B(t)}{c \cdot C_{max}} \quad (3-17)$$

By adding a differential equation of Coulomb counting equation for  $SOC_E$ , the simple expression of the KiBaM regarding the two forms of the SOC can be determined by the following:

$$\begin{bmatrix} \frac{dSOC_E(t)}{dt} \\ \frac{dSOC_T(t)}{dt} \end{bmatrix} = \begin{bmatrix} 0 & 0 \\ k' & -k' \end{bmatrix} \cdot \begin{bmatrix} SOC_E(k) \\ SOC_T(k) \end{bmatrix} + \begin{bmatrix} -1 \\ C_{max} \\ -1 \\ c \cdot C_{max} \end{bmatrix} \cdot i_B(t) \quad (3-18)$$

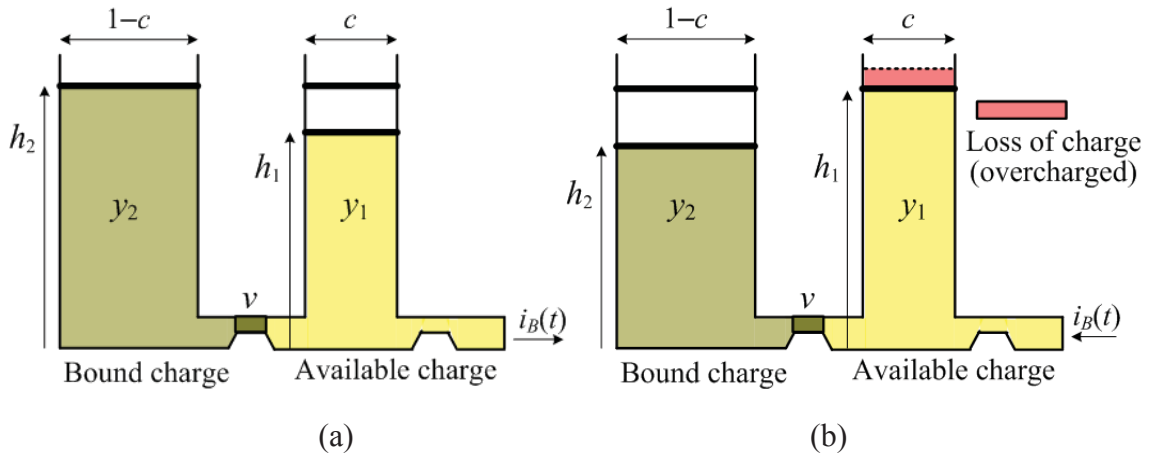


Figure 3.3: The KiBaM: (a) discharge mode and (b) charge mode.

### 3.2.3 The Enhanced Hybrid Battery Model

The enhanced hybrid model consists of two parts: a runtime SOC prediction module and an electrical circuit model, as illustrated in Figure 3.4. The runtime SOC prediction module implements (3-18) for  $SOC_T$  and  $SOC_E$  prediction while taking into account the nonlinear capacity variation of the battery; while the electrical circuit model is designed to capture the I-V characteristics of the battery. The parameters of the battery model are functions of the current directions, SOC, C-rate, and ambient temperatures of the battery and are updated online during the battery operation. Therefore, the enhanced hybrid battery model is capable of capturing the comprehensive runtime performance of a battery in any operating conditions. To facilitate real-system applications, a discrete-time version of the enhanced battery model was developed.

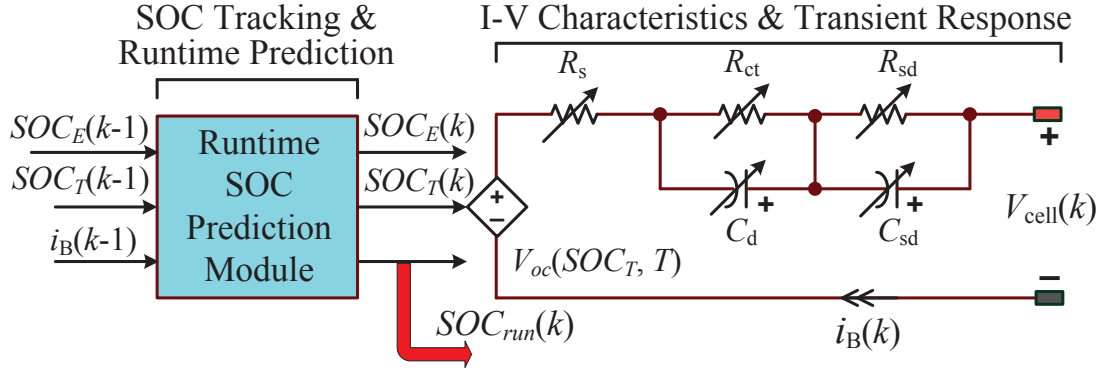


Figure 3.4: The enhanced hybrid battery model.

### 3.2.3.1 Runtime SOC Prediction Module

Using the first-order forward Euler method, the discrete-time form of (3-18) is derived as follows:

$$\begin{bmatrix} SOC_E(k+1) \\ SOC_T(k+1) \end{bmatrix} = \begin{bmatrix} 1 & 0 \\ k'T_S & (1-k'T_S) \end{bmatrix} \cdot \begin{bmatrix} SOC_E(k) \\ SOC_T(k) \end{bmatrix} + \begin{bmatrix} -T_S \\ C_{\max} \\ -T_S \\ c \cdot C_{\max} \end{bmatrix} \cdot i_B(k) \quad (3-19)$$

In [27], the  $SOC_T$  was used to represent the actual real-time SOC in the discharge mode. However, it will be inappropriate to use  $SOC_T$  in the charge mode because the  $SOC_T$  (or  $C_{available}$ ) will be larger than the  $SOC_E$  (or  $C_{usable}$ ), while by the definition, the  $SOC_T$  should always be smaller than or equal to the  $SOC_E$ . Therefore, using the  $SOC_T$  in the charge mode will inaccurately indicate that the charge stored in the battery is more than that is actually stored. To solve this problem, a new term called runtime SOC,  $SOC_{run}$ , is used. The  $SOC_{run}$  is the same as the  $SOC_T$  when the  $SOC_T$  is smaller than the  $SOC_E$  in the discharge mode; while the  $SOC_{run}$  will be the same as the  $SOC_E$  when the  $SOC_T$  is larger than  $SOC_E$ , which usually happens in the charge mode. In addition, the loss of charge due to the limit of the

charge acceptance in the charge mode should be considered when the available charge well is overcharged (i.e.,  $SOC_T > 1$ ), as shown in Figure 3.3(b). This issue was not considered in the original KiBaM in [49]. In other words, only part of the charge will be stored. Therefore, the  $SOC_{run}$  is expressed as follows:

$$\begin{cases} SOC_{run} = \min[SOC_T, SOC_E], & SOC_T \leq 1 \\ SOC_{run} = SOC_E - (SOC_T - 1), & SOC_T > 1 \end{cases} \quad (3-20)$$

In this research, the influence of ambient temperature on the KiBaM was investigated more explicitly than it was in [27] and [49]. According to experiments, the empirical equations of the KiBaM's parameters are formulated as functions of the ambient temperature  $T$  in Kelvin (K):

$$\begin{cases} C_{max}(T) = a_0 e^{-a_1 \left( \frac{1}{T-a_2} - \frac{1}{T_{ref\_L}-a_2} \right)} \\ k'(T) = a_3 e^{a_4(T-T_{ref\_L})} + a_5 \\ c(T) = a_6 e^{-\frac{(T-a_7)^2}{a_8}} \end{cases} \quad (3-21)$$

where  $T_{ref\_L}$  is 273.15 K (i.e., 0 °C).

### 3.2.3.2 Electrical Circuit Battery Model

The electrical circuit battery model describes the I-V characteristics and transient response of the battery cell, where a temperature-dependent voltage-controlled voltage source,  $V_{oc}(SOC_T, T)$ , is used to bridge the  $SOC_T$  to the cell's nonlinear OCV and characterizes the long-term diffusion effect. All of the sources contributing to the voltage response of the electric circuit battery model are shown in Figure 3.2. The electrical circuit battery model is expressed as follows:

$$V_{oc}(SOC_T, T) = V_{oc}(SOC_T, T_{ref}) \cdot K_{VOC}(SOC_T, T) \quad (3-22)$$

$$V_{cell}(k) = V_{oc}(SOC_T, T) - R_s \cdot i_B(k) - V_{ct}(k) - V_{sd}(k) \quad (3-23)$$

$$\begin{bmatrix} V_{ct}(k) \\ V_{sd}(k) \end{bmatrix} = \begin{bmatrix} e^{\frac{-T_s}{R_{ct} \cdot C_d}} & 0 \\ 0 & e^{\frac{-T_s}{R_{sd} \cdot C_{sd}}} \end{bmatrix} \cdot \begin{bmatrix} V_{ct}(k-1) \\ V_{sd}(k-1) \end{bmatrix} + \begin{bmatrix} R_{ct}(1 - e^{\frac{-T_s}{R_{ct} \cdot C_d}}) \\ R_{sd}(1 - e^{\frac{-T_s}{R_{sd} \cdot C_{sd}}}) \end{bmatrix} \cdot i_B(k) \quad (3-24)$$

where  $K_{VOC}$  is a correction coefficient of the temperature effect. The impedance parameters (i.e.,  $R_s$  and other RC network parameters) are functions of the  $SOC_E$ , C-rate, direction of the current, and ambient temperature. The expressions of the parameters will be discussed in Section 3.2.4 of this chapter.

### 3.2.4 Model Parameter Extraction

Numerous experiments have been conducted using Samsung's ICR18650-28A cylindrical lithium-ion battery cells to extract the model parameters. The ICR18650-28A is a newly developed 2.8-Ah high-voltage battery cell with a nominal voltage of 3.75 V. In the experiments, data on the voltages and currents of the test cells were collected by a CADEX C8000 battery tester with a SUN ELECTRONIC SYSTEMS' EC12 temperature chamber (shown in Figure 3.5). The temperature chamber was connected to a nitrogen tank to inflow liquid nitrogen for the test at low ambient temperature condition in the temperature chamber. All of the parameters of the battery model are represented by empirical equations, such as (3-21). The coefficients of the empirical equations are influenced by many factors, such as the C-rate, direction of the cell current, and ambient temperature. In this dissertation, the coefficients of the empirical equations are identified using curve fitting through constant discharge current and pulsed discharge/charge current tests at three different ambient temperature conditions: low temperature (i.e., 0 °C or 273.15 K, which is the lowest

operating temperature of the battery), room temperature (23 °C or 296.15 K), and high temperature (40 °C or 313.15 K). Before the tests, the battery cells were fully charged using the constant current constant voltage (CCCV) charge method, where the charge cutoff voltage in the constant current mode is 4.3 V; and the charge cutoff current in the constant voltage mode is 0.01C (i.e.,  $i_B = 0.028$  A). During each test, the fully charged battery cell was placed in the temperature chamber for four hours in order for the cell to reach thermal equilibrium (i.e., the internal temperature was the same as the ambient temperature) before the cell was tested.

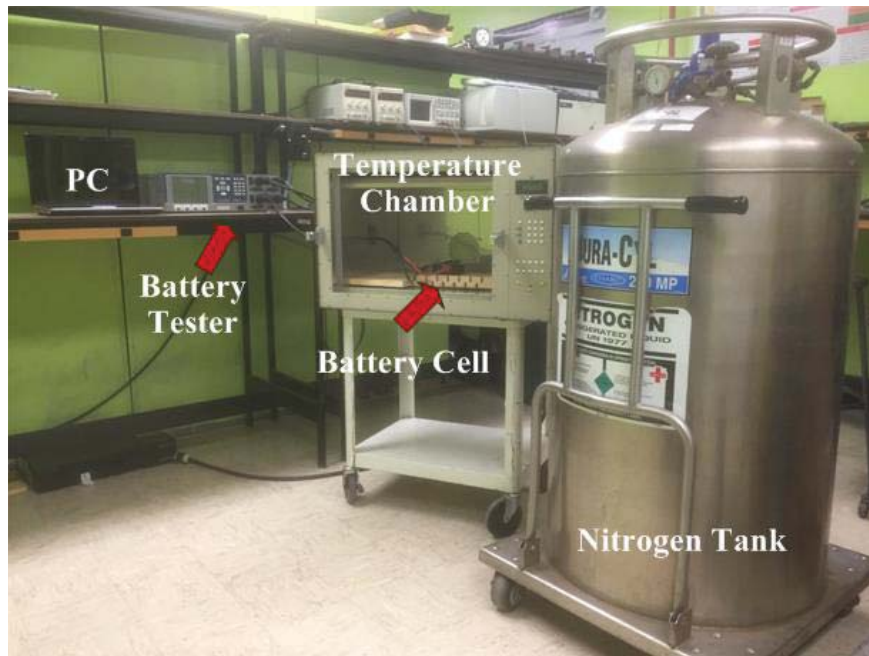


Figure 3.5: The experimental setup.

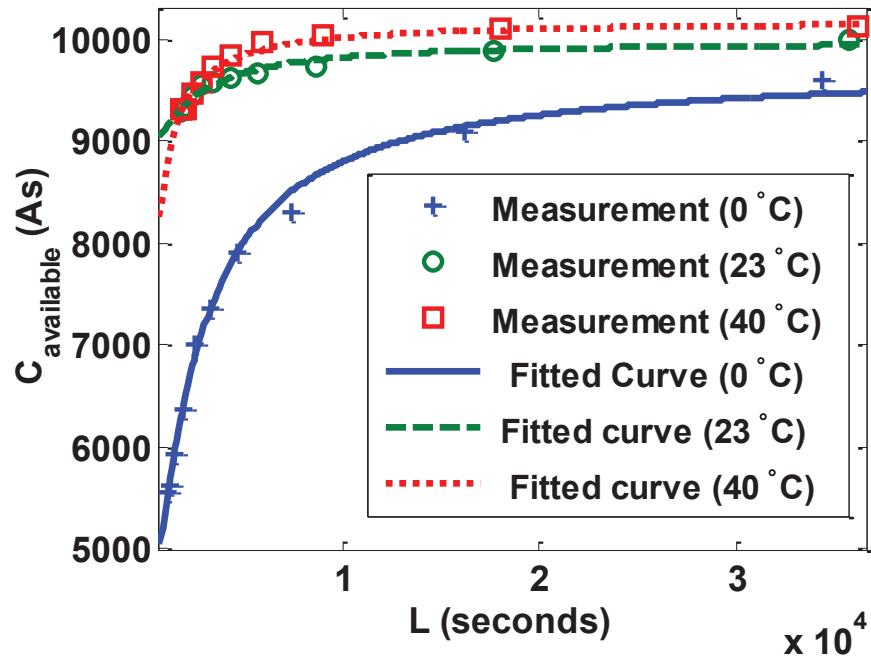
#### 3.2.4.1 Runtime SOC Prediction Module Parameters

The parameters of the runtime SOC prediction module were identified using constant discharge current tests. Specifically, the maximum capacity,  $C_{\max}$ , was extracted by

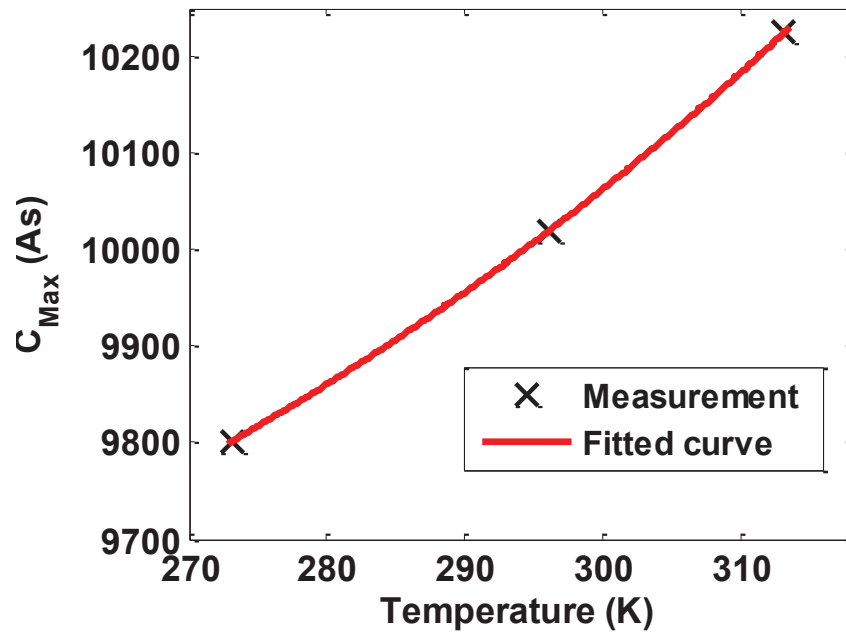
discharging the cell with a small constant current, e.g., 0.05C, until it was fully discharged, where the cell voltage reached the discharge cutoff voltage of 3 V. Then, the parameters  $c$  and  $k'$  were obtained by curve fitting using the following equation [92]:

$$C_{available}(I_D) = \frac{C_{max} k' c L(I_D)}{(1 - e^{-k'L(I_D)} + c \cdot (k'L(I_D) - 1 + e^{-k'L(I_D)}))} \quad (3-25)$$

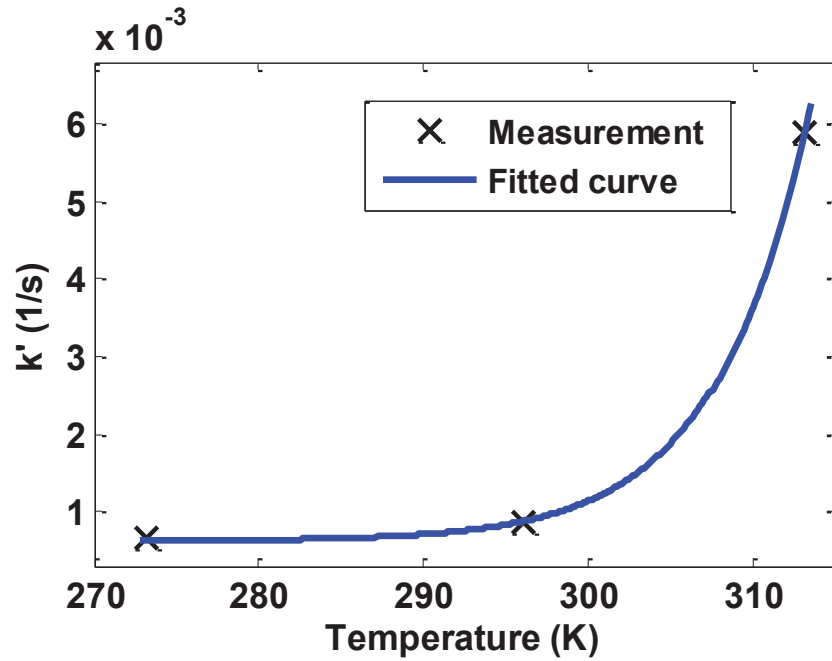
where  $I_D$  is a vector of the constant discharge current rate (i.e., C-rate) from 0.1C to 1.8C with an increment of 0.2C;  $C_{available}(I_D)$  and  $L(I_D)$  are the vectors of available capacity and the end of discharge times corresponding to the vector  $I_D$ , respectively. Figure 3.6(a) illustrates the measured values of  $C_{available}$  and the corresponding fitted  $C_{available}$  curves (3-25) at three different ambient temperature conditions. The extracted values of  $C_{max}$ ,  $c$ , and  $k'$  for the three different ambient temperature conditions and the fitted curves of these parameters as functions of the ambient temperature are plotted in Figure 3.6(b)-(d), respectively. The values of the coefficients  $a_0$ – $a_8$  in (3-21) obtained from the curve fitting are listed in Table 3.1. The values of  $k'$  and  $C_{max}$  increased with ambient temperature since most chemical processes in the cell speed up at higher temperatures. However, the temperature effect on parameter  $c$  was not consistent with the other two parameters. Parameter  $c$  had the highest value at room temperature.



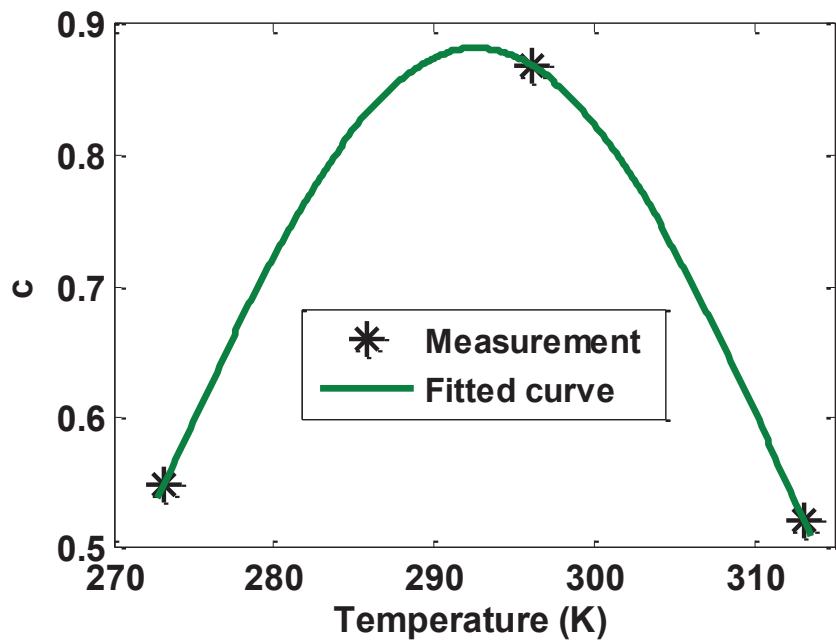
(a)



(b)



(c)



(d)

Figure 3.6: The measured or estimated values and corresponding fitted curves of (a)  $C_{available}$  as the function of  $L(I_D)$  at three different ambient temperature conditions, (b)  $C_{max}$ , (c)  $k'$ , and (d)  $c$  as functions of temperature.

Table 3.1: The coefficients of the empirical equations of the runtime SOC prediction module parameters and OCV for the test cylindrical lithium-ion cells.

|          |        |          |          |          |         |          |          |
|----------|--------|----------|----------|----------|---------|----------|----------|
| $a_0$    | 9801   | $a_1$    | 36.49    | $a_2$    | 479.9   | $a_3$    | 4.463e-6 |
| $a_4$    | 0.1768 | $a_5$    | 6.226e-4 | $a_6$    | 0.8819  | $a_7$    | 292.6    |
| $a_8$    | 28.27  | $a_9$    | -0.1364  | $a_{10}$ | 61.94   | $a_{11}$ | 3.616    |
| $a_{12}$ | 1.095  | $a_{13}$ | -2.949   | $a_{14}$ | 4.295   | $a_{15}$ | -1.765   |
| $a_{16}$ | 150.8  | $a_{17}$ | 33.17    | $a_{18}$ | 8.67e-5 | $a_{19}$ | 1.025    |

### 3.2.4.2 Electrical Circuit Model Parameters

All of the electrical circuit parameters (i.e.,  $V_{oc}$  and RC) of the battery model were extracted using a pulsed current discharge and charge test cycle under the three ambient temperature conditions; the pulsed current discharge test was conducted first followed by the pulsed current charge test once the cell voltage reached the discharge cutoff voltage. Each current pulse lasted for a period during which the  $SOC_E$  of the battery cell decreased or increased by 5% in the discharge or charge mode, respectively. Before performing the test, the value of  $C_{max}$  was extracted for accurate  $SOC_E$  calculation to account for the change in  $C_{max}$  caused by the ambient temperature variation.

The discharge and charge equilibrium OCV values are the terminal voltage measured at the end of the rest period of each current pulse during the pulsed current discharge and charge test, respectively, where the rest period should be long enough (e.g., 3 hours at 40 °C, 6 hours at 23 °C, and 9 hours at 0 °C). The pulsed current discharge and charge test cycle was conducted with with a current rate of 0.6C (i.e., 1.68 A) to extract the equilibrium OCVs. Figure 3.7(a) shows the  $V_{oc,eq}$ , which is the same as the average equilibrium OCV of discharge and charge equilibrium OCVs, versus  $SOC_E$  for the test lithium-ion battery cell under the ambient temperatures of 0 °C, 23 °C, and 40 °C. The values of  $V_{oc,eq}$  strongly

depended on SOC and temperature when the SOC was less than 10%. In addition, the difference between the discharge equilibrium OCV and the charge equilibrium OCV was less than 5 mV. Therefore, the hysteresis effect [56] can be ignored.

The empirical equation of the  $V_{oc,eq}$  at room temperature ( $T_{ref}$ ), which is called the reference  $V_{oc,eq}$ , can be obtained using the following equation:

$$V_{oc,eq}(SOC_E, T_{ref}) = a_9 e^{-a_{10} SOC_E} + a_{11} + a_{12} SOC_E + a_{13} SOC_E^2 + a_{14} SOC_E^3 + a_{15} SOC_E^4 \quad (3-26)$$

where  $T_{ref} = 296.15$  K and  $a_9, \dots, a_{15}$  are coefficients. Then, the correction coefficient for the temperature effect,  $K_{VOC}$ , shown in Figure 3.7(b) can be obtained from the  $V_{oc,eq}$  values measured at the low and high ambient temperatures and the measured reference  $V_{oc,eq}$  values as follows:

$$K_{VOC}(SOC_E, T) = \frac{V_{oc,eq}(SOC_E, T)}{V_{oc,eq}(SOC_E, T_{ref})} \quad (3-27)$$

The empirical equation of  $K_{VOC}$  is formulated as:

$$K_{VOC}(SOC_E, T) = a_{16} \left( \frac{1}{T} - \frac{1}{T_{ref}} \right) \cdot e^{-a_{17} SOC_E} - a_{18} T + a_{19} \quad (3-28)$$

The coefficients  $a_9$ – $a_{18}$  in (3-26) and (3-28) are obtained from curve fitting and are listed in Table 3.1. The equation of  $V_{oc}(SOC_E, T)$  in (3-27) is similar to (3-22); the major difference is that (3-22) replaces  $SOC_E$  in (3-27) with  $SOC_T$  to characterize the nonlinear OCV effect while (3-27) does not.

All of the RC parameters of the proposed battery model were extracted from the impedance voltage response (i.e.,  $V_{impedance} = |V_{cell} - V_{oc}(SOC_T, T)|$ ) obtained from the pulsed discharge and charge current test cycle described in the first paragraph of this section. Figure 3.8 depicts a typical curve of  $V_{impedance}$  response and a fitting window buffer which stores the

data for the rest period during the test for extraction of the RC parameters of the model. A 10-minute window buffer was used based on the assumption that the charge transfer and short-term diffusion corresponding to RC parameters could be observed for a 10-minute rest period.

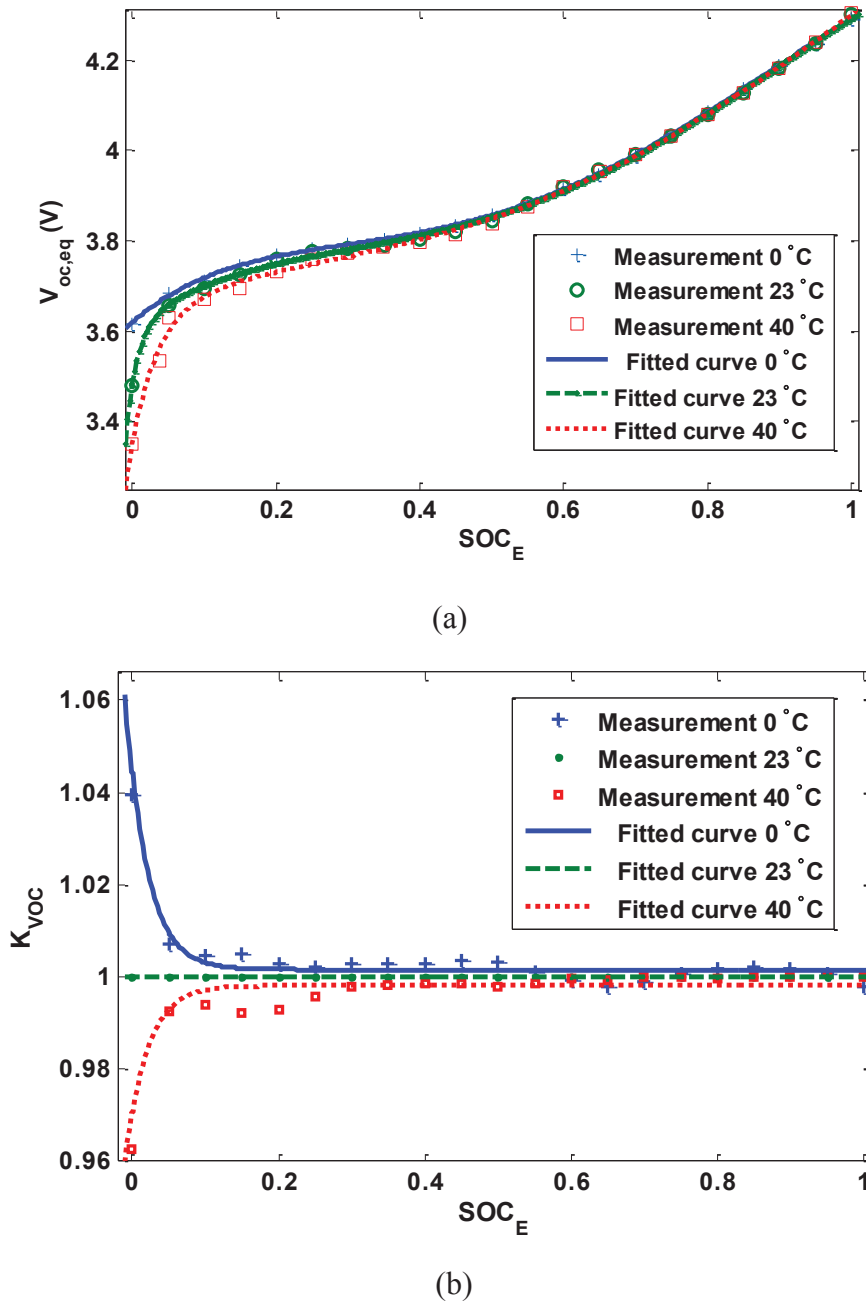


Figure 3.7: Measured and fitted curves obtained at the ambient temperatures of 0 °C, 23 °C, and 40 °C: (a)  $V_{oc,eq}$  vs.  $SOC_E$  and (b)  $K_{VOC}$  vs.  $SOC_E$

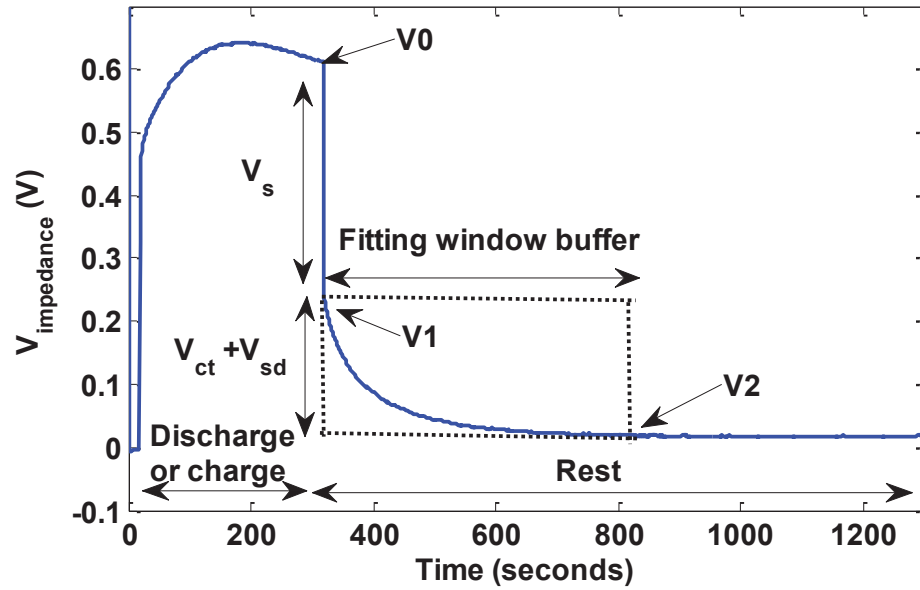


Figure 3.8: The curve of a typical impedance voltage response in the condition of 0.6C pulsed current discharge and 0 °C ambient temperature for the extraction of the RC parameters of the enhanced hybrid battery model.

The instantaneous voltage drop/rise when the discharge/charge was completed was related to  $R_s$  according to (3-23), which can be expressed by the following equation:

$$R_s = \frac{V_s}{|i_B|} = \frac{V0 - V1}{|i_B|} \quad (3-29)$$

The following equation was used to estimate the other RC network parameters:

$$V_{ct}(k) + V_{sd}(k) = a \cdot e^{-b \cdot k} + c \cdot e^{-d \cdot k} + e \quad (3-30)$$

where  $k = 1, \dots, 600$  and  $e$  is  $V2$ . The coefficients  $a$ ,  $b$ ,  $c$ , and  $d$  were determined by using nonlinear least-square curve fitting. The RC network parameters were then calculated as:

$$R_{ct} = a/|i_B|, \quad C_d = 1/(R_{ct} \cdot b), \quad R_{sd} = c/|i_B|, \quad C_{sd} = 1/(R_{sd} \cdot d) \quad (3-31)$$

Since the RC parameters depend on the C-rate  $I$ , the  $SOC_E$ , the temperature  $T$ , and the direction of the current (i.e., discharge mode and charge mode) of the battery cell, numerous experiments were conducted to extract all RC parameters using the pulsed current

discharge and charge test cycle by changing  $I$  and  $T$ . Then, the empirical expressions of the RC parameters were derived. First, the empirical equations of the RC parameters as functions of  $SOC_E$  and  $I$  for the discharge mode were derived at three different  $I$  of 0.2C, 0.6C, and 1C at room temperature in the following form.

$$\begin{cases} R_{s,d}(SOC_E, I) = (a_{d0} - a_{d1}I)e^{-a_{d2}SOC_E} + a_{d3} + a_{d4}I + a_{d5}SOC_E + a_{d6}SOC_E^2 + a_{d7}SOC_E^3 \\ R_{ct,d}(SOC_E, I) = (b_{d0} - b_{d1}I)e^{-b_{d2}SOC_E} + b_{d3} + b_{d4}I + b_{d5}SOC_E \\ R_{sd,d}(SOC_E, I) = (c_{d0} - c_{d1}I)e^{-c_{d2}SOC_E} + c_{d3} + c_{d4}I + c_{d5}SOC_E \\ C_{d,d}(SOC_E, I) = d_{d0}SOC_E + d_{d1}SOC_E^2 + d_{d2}SOC_E^3 + d_{d3} \\ C_{sd,d}(SOC_E, I) = e_{d0}e^{-e_{d1}SOC_E} + e_{d2} + e_{d3}I + e_{d4}I^2 \end{cases} \quad (3-32)$$

where the subscript  $d$  of each RC parameter indicates the discharge mode. Then, the temperature dependency was added to the expression of each RC parameter, which changed (3-32) to:

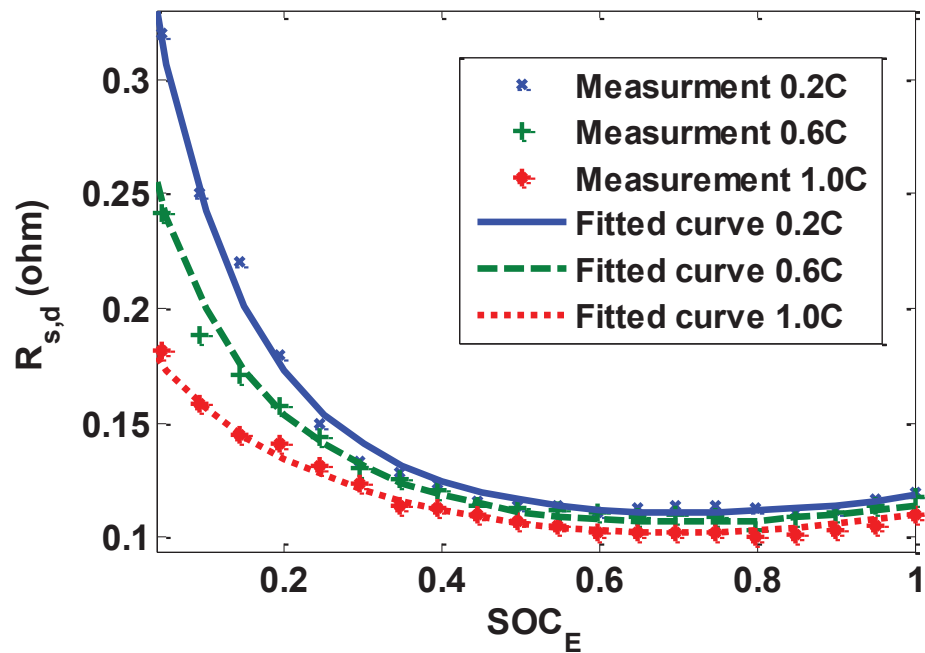
$$\begin{cases} R_{s,d}(SOC_E, I, T) = R_{s,d}(SOC_E, I) \cdot (e^{-f_{d0}\Delta T} + f_{d1}SOC_E^{f_{d2}\Delta T}) + K_{LV} \\ R_{ct,d}(SOC_E, I, T) = R_{ct,d}(SOC_E, I) \cdot e^{f_{d3}\left(\frac{1}{T} - \frac{1}{T_{ref}}\right)} \\ R_{sd,d}(SOC_E, I, T) = R_{sd,d}(SOC_E, I) \cdot e^{f_{d4}\left(\frac{1}{T} - \frac{1}{T_{ref}}\right)} \\ C_{d,d}(SOC_E, I, T) = C_{d,d}(SOC_E, I) \cdot e^{f_{d5}\left(\frac{1}{T} - \frac{1}{T_{ref}}\right)} \\ C_{sd,d}(SOC_E, I, T) = C_{sd,d}(SOC_E, I) \cdot e^{f_{d6}\left(\frac{1}{T} - \frac{1}{T_{ref}}\right)} \end{cases} \quad (3-33)$$

where  $\Delta T = T - T_{ref}$ , and

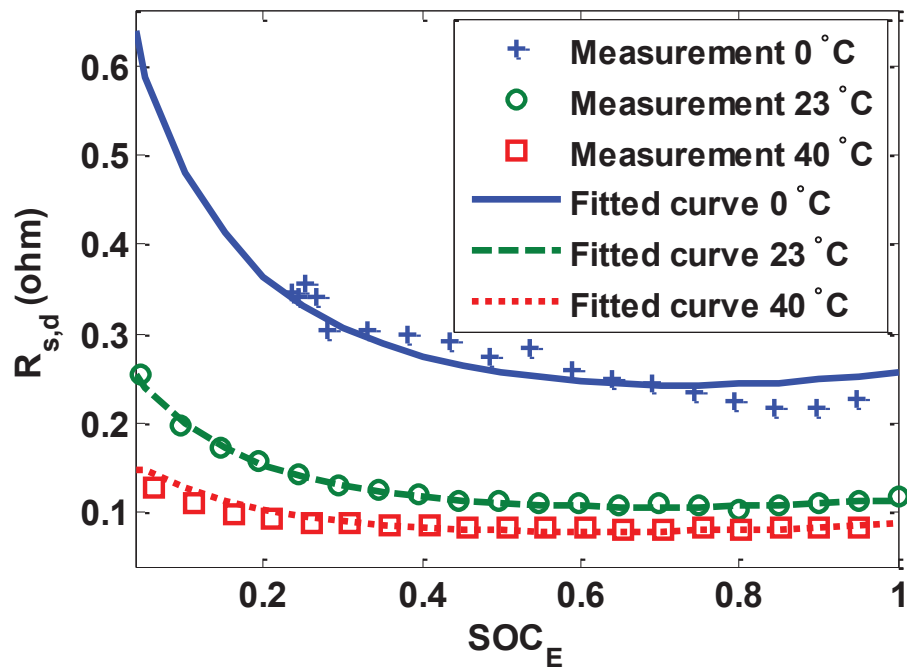
$$K_{LV}(SOC_T, I, T) = f_{d7}e^{-f_{d8}(T - T_{ref} - L)}(e^{-f_{d9}SOC} - I_c^{f_{d10}}) \quad (3-34)$$

Due to the increase in the fitting error at low temperatures, an additional correction factor  $K_{LV}$  was added to the expression of  $R_{s,d}$ . The extracted values and the corresponding fitted

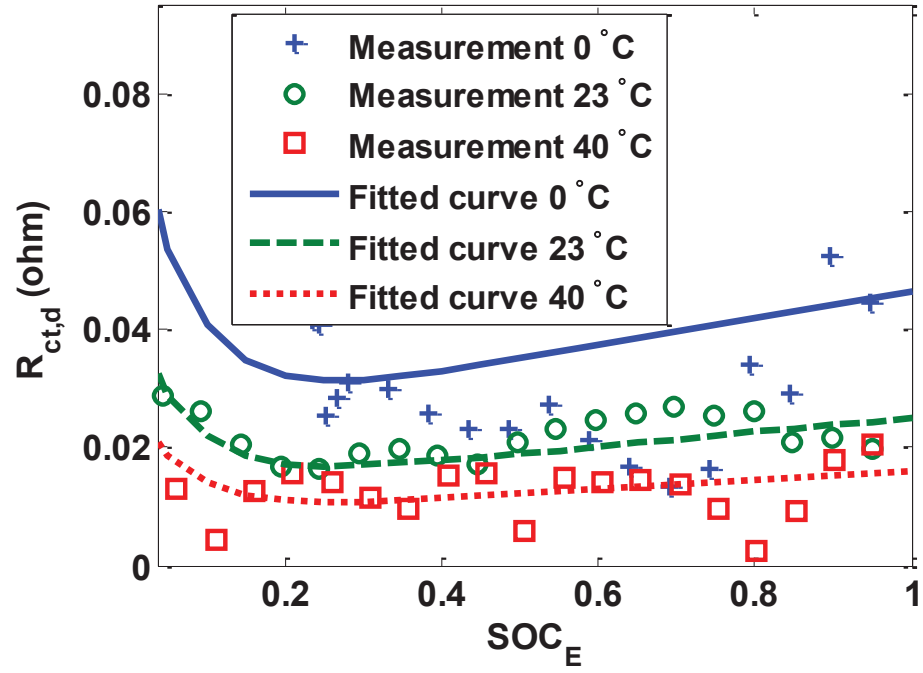
curves of the RC parameters are illustrated in Figure 3.9. All of the coefficients of the RC parameter expressions (3-32)-(3-34) are listed in Table 3.2.



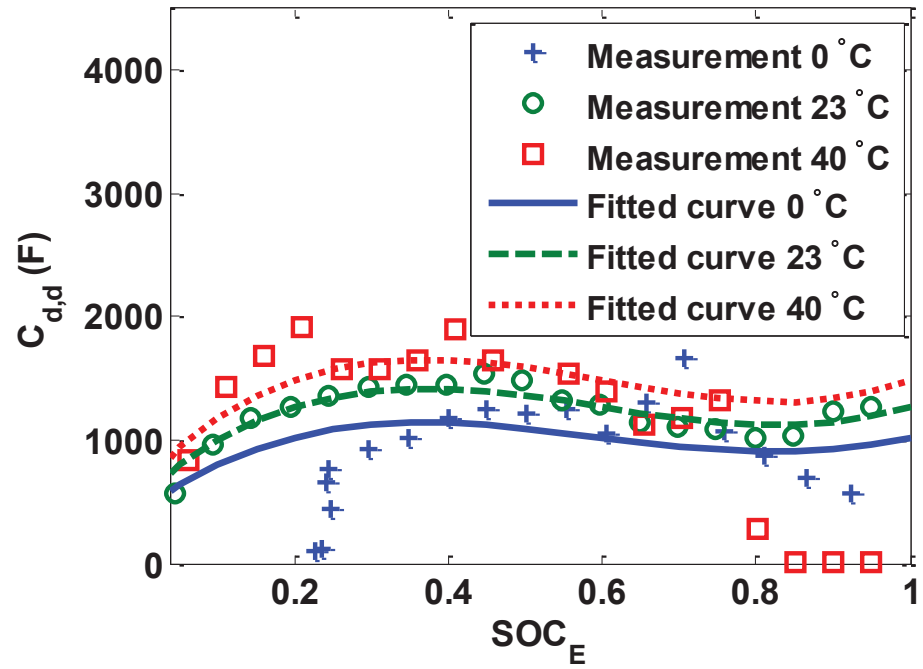
(a)



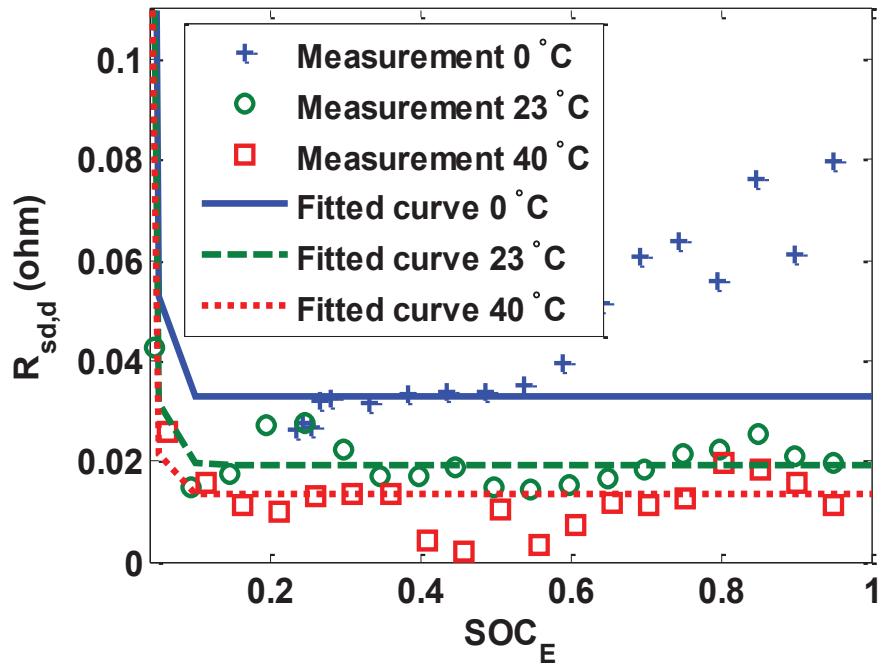
(b)



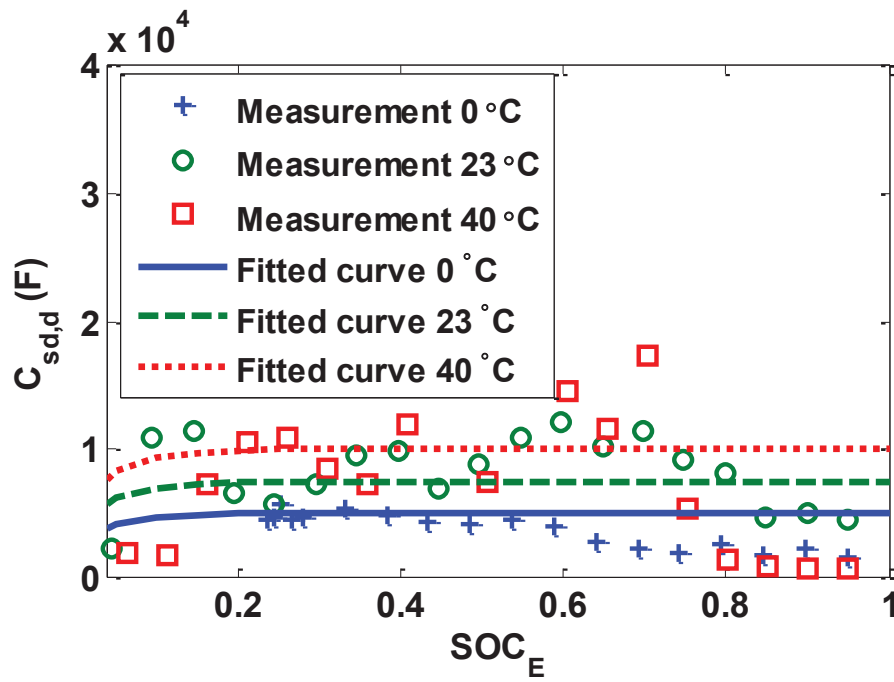
(c)



(d)



(e)



(f)

Figure 3.9: The measurement and corresponding fitted curves: (a)  $R_{s,d}(SOC_E, I)$ , (b)  $R_{s,d}(SOC_E, T)$ , (c)  $R_{ct,d}(SOC_E, T)$ , (d)  $C_{d,d}(SOC_E, T)$ , (e)  $R_{sd,d}(SOC_E, T)$ , and (f)  $C_{sd,d}(SOC_E, T)$ .

Table 3.2: The coefficients of the RC parameter expressions for the test cylindrical lithium-ion cell in the discharge mode.

|          |         |          |         |          |         |           |          |
|----------|---------|----------|---------|----------|---------|-----------|----------|
| $a_{d0}$ | 0.2904  | $a_{d1}$ | 0.2521  | $a_{d2}$ | 9.485   | $a_{d3}$  | 0.1674   |
| $a_{d4}$ | -0.0100 | $a_{d5}$ | -0.1726 | $a_{d6}$ | 0.1553  | $a_{d7}$  | -0.02982 |
| $b_{d0}$ | 0.0664  | $b_{d1}$ | 0.0558  | $b_{d2}$ | 13.44   | $b_{d3}$  | 0.01358  |
| $b_{d4}$ | 5.48E4  | $b_{d5}$ | 0.0134  | $c_{d0}$ | 0.3255  | $c_{d1}$  | 0.3842   |
| $c_{d2}$ | 45.07   | $c_{d3}$ | 0.0387  | $c_{d4}$ | -0.0248 | $c_{d5}$  | -2.85e-3 |
| $d_{d0}$ | 5528    | $d_{d1}$ | -10850  | $d_{d2}$ | 6044    | $d_{d3}$  | 550.5    |
| $e_{d0}$ | -3112   | $e_{d1}$ | 17.1    | $e_{d2}$ | 8058    | $e_{d3}$  | -9560    |
| $e_{d4}$ | 14300   | $f_{d0}$ | 0.0419  | $f_{d1}$ | 0.0163  | $f_{d2}$  | 0.25     |
| $f_{d3}$ | 1554    | $f_{d4}$ | 1513    | $f_{d5}$ | -771    | $f_{d6}$  | -1421    |
| $f_{d7}$ | 39.85   | $f_{d8}$ | 0.2993  | $f_{d9}$ | 1.91e-3 | $f_{d10}$ | 0.0022   |

The empirical equations of the RC parameters of the enhanced hybrid model of the cylindrical lithium-ion battery cells for charge mode are listed in (3-35) and the values of their coefficients are given in Table 3.3:

$$\left\{ \begin{array}{l}
 R_{s,c}(SOC_E, I, T) = (a_{c0}SOC_E + a_{c1}SOC_E^2 + a_{c2}SOC_E^3 + a_{c3}) \cdot (a_{c4}I^{-a_{c5}} + a_{c6}) \\
 \quad \cdot (e^{-a_{c7}\Delta T} + a_{c8}SOC_E^{a_{c9}}\Delta T) \\
 R_{ct,c}(SOC_E, I, T) = (b_{c0}e^{-b_{c1}SOC_E} + b_{c2}) \cdot (e^{-b_{c3}\Delta T} + b_{c4}SOC_E^{b_{c5}}\Delta T) \\
 R_{sd,c}(SOC_E, I, T) = (c_{c0}e^{-c_{c1}SOC_E} + c_{c2}) \cdot (c_{c3}I^{-c_{c4}} + c_{c5}) \cdot e^{c_{c6}\left(\frac{1}{T} - \frac{1}{T_{ref}}\right)} \\
 C_{d,c}(SOC_E, I, T) = d_{c0}e^{-d_{c1}SOC_E} + d_{c2} \\
 C_{sd,c}(SOC_E, I, T) = (e_{c0}e^{-e_{c1}SOC_E} + e_{c2}) \cdot e^{e_{c3}\left(\frac{1}{T} - \frac{1}{T_{ref}}\right)}
 \end{array} \right. \quad (3-35)$$

Table 3.3: The coefficients of the RC parameter expressions for the test cylindrical lithium-ion cell in charge mode.

|          |         |          |          |          |         |          |         |
|----------|---------|----------|----------|----------|---------|----------|---------|
| $a_{c0}$ | -0.1233 | $a_{c1}$ | 0.191    | $a_{c2}$ | -0.1295 | $a_{c3}$ | 0.1556  |
| $a_{c4}$ | 0.4472  | $a_{c5}$ | 0.1515   | $a_{c6}$ | 0.3407  | $a_{c7}$ | 0.03541 |
| $a_{c8}$ | -0.0577 | $a_{c9}$ | -0.0412  | $b_{c0}$ | 2.68e-5 | $b_{c1}$ | -5.007  |
| $b_{c2}$ | 0.0230  | $b_{c3}$ | -1.16e-3 | $b_{c4}$ | -0.0312 | $b_{c5}$ | 0.6319  |
| $c_{c0}$ | 1.14e-5 | $c_{c1}$ | -8.112   | $c_{c2}$ | 0.0122  | $c_{c3}$ | 0.5869  |
| $c_{c4}$ | 0.7105  | $c_{c5}$ | 0.4211   | $c_{c6}$ | 3098    | $d_{c0}$ | -4788   |
| $d_{c1}$ | 0.0202  | $d_{c2}$ | 5965     | $e_{c0}$ | -246.9  | $e_{c1}$ | 3       |
| $e_{c2}$ | 9856    | $e_{c3}$ | 1338     |          |         |          |         |

### 3.2.5 Model Validation

The enhanced hybrid battery model was constructed using MATLAB/Simulink. The parameters of the single-cell battery model were obtained by using the model extraction method in Section 3.2.4. Figure 3.10 shows the implementation of the enhanced hybrid battery model in MATLAB/Simulink. The Runtime SOC prediction module calculates the values of  $SOC_T$ ,  $SOC_E$ , and  $SOC_{run}$  of the battery cell by taking into account its nonlinear capacity variation during the operation. The  $I$  detector module tracks the change of the battery cell current  $i_B$  and converts it to  $I$ . All modules are implemented using the standard modules from the Simulink toolbox.

Simulation results obtained from the proposed enhanced hybrid battery model for a single ICR18650-28A cell in the low (0° C), room (23° C), and high (40° C) temperature conditions using pulsed and random discharge and charge current profiles were compared to the experimental data to validate the battery model. Figures 3.11(b), (d), and (f) compare the terminal voltage responses obtained from simulations with experimental results for the pulsed discharge and charge current profiles given in Fig. 3.11(a).

The model captures the dynamic voltage responses of the battery cell accurately in all pulsed discharge/charge current and temperature conditions. The maximum root mean square error (RMSE) of the cell terminal voltage predicted by the model over each test process was only 31 mV or 2.4% of the nominal terminal voltage variation range of 1.3 V (= 4.3 – 3 V), which occurred in the 0 °C condition, as shown in Fig 3.11(b). The maximum error of the cell terminal voltage predicted by the battery model was about 92 mV or 7.1% of the nominal terminal voltage variation range, which occurred at 40 °C, as shown in Figure 3.11(f). Furthermore, by capturing the variations of the nonlinear capacity effects, the battery

model is able to accurately capture the remaining end of discharge time until  $SOC_{run} = 0$  and the end of charge time until  $SOC_{run} = 1$  in the single cell in different pulsed current and temperature conditions, as shown in Figure 3.11(c), (e), and (g).

The battery model is further validated by applying a randomly varied discharge and charge current profile, as shown in Figure 3.12(a). Figure 3.12(b)-(d) compares the corresponding terminal voltage responses of the cell obtained from the simulation and experiment. The voltage responses predicted by the model were excellent at the high and room temperatures and were quite good at the low temperature. The worst case occurred at 0 °C, where the RMSE of the voltage predicted by the model was about 59 mV or 4.5% of the nominal terminal voltage variation range; while they were about 14 mV (or 1.2%) and 15 mV (or 1.3%) at 23 °C and 40 °C, respectively. These results show that the model can accurately capture the nonlinear capacity variations and dynamic electric circuit characteristics of lithium-ion batteries under various current profiles and ambient temperatures.

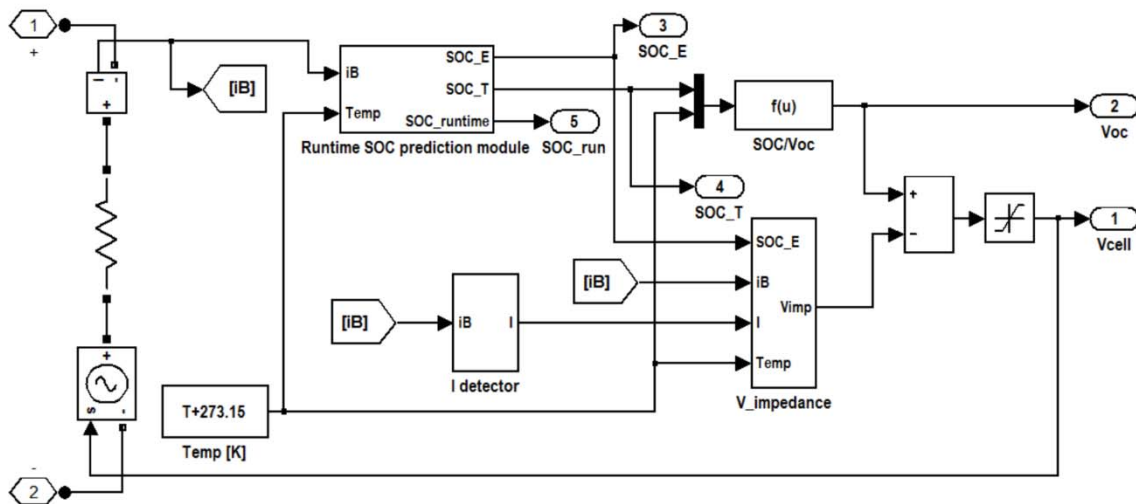
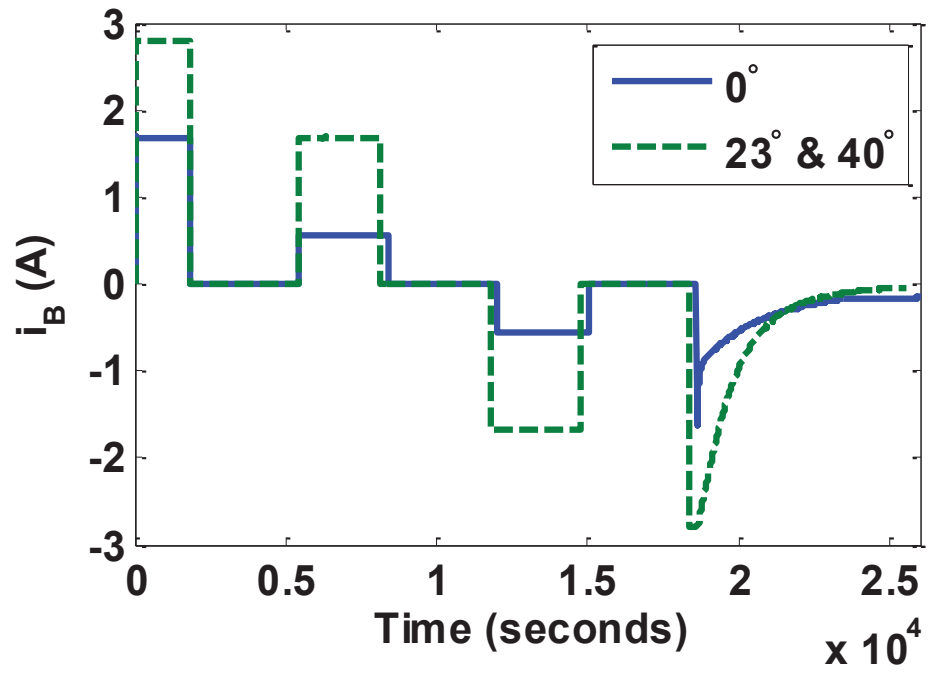
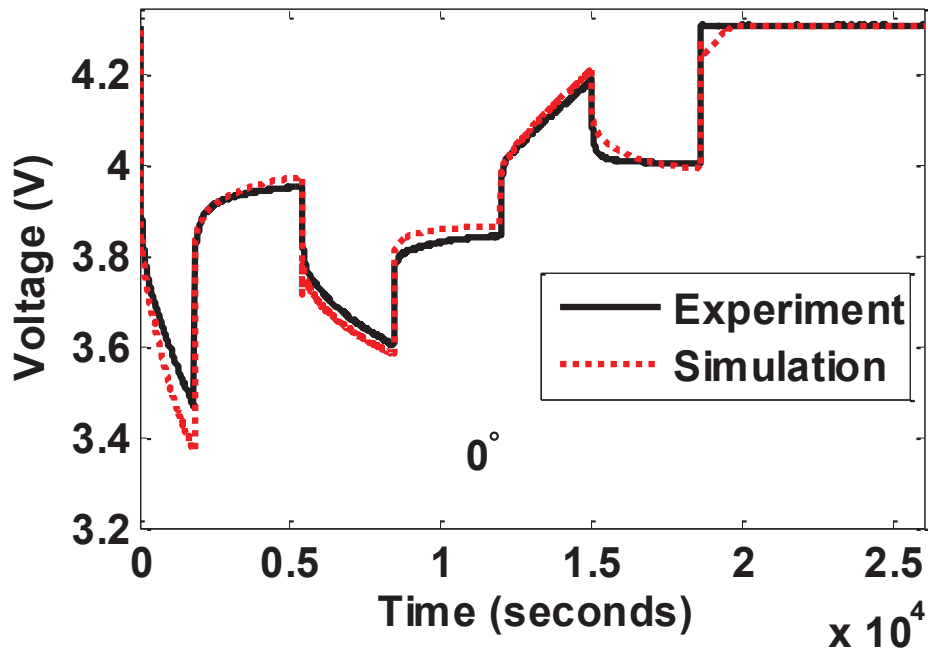


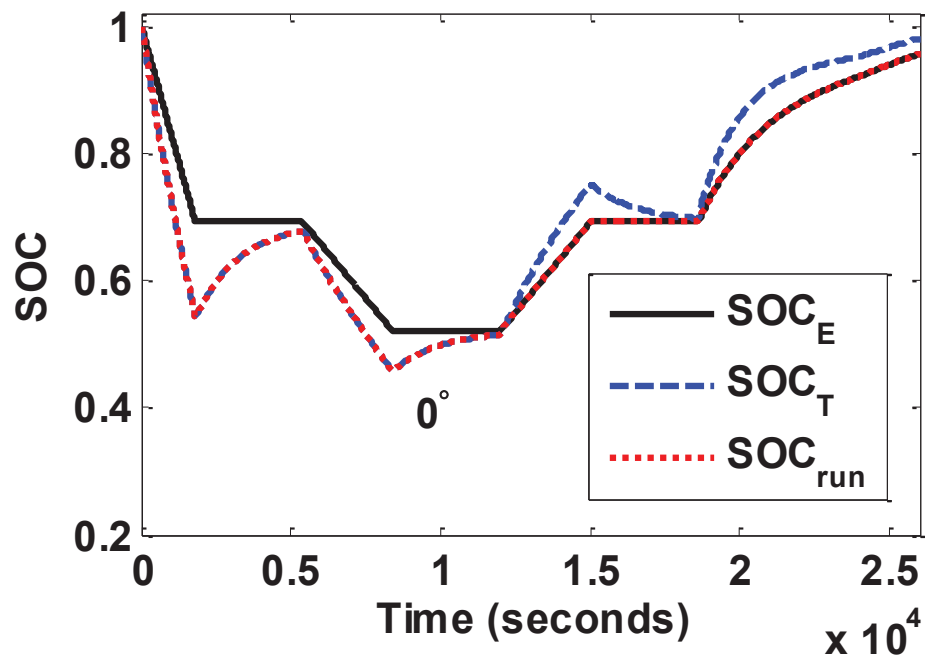
Figure 3.10: The enhanced hybrid battery model implemented in MATLAB/Simulink.



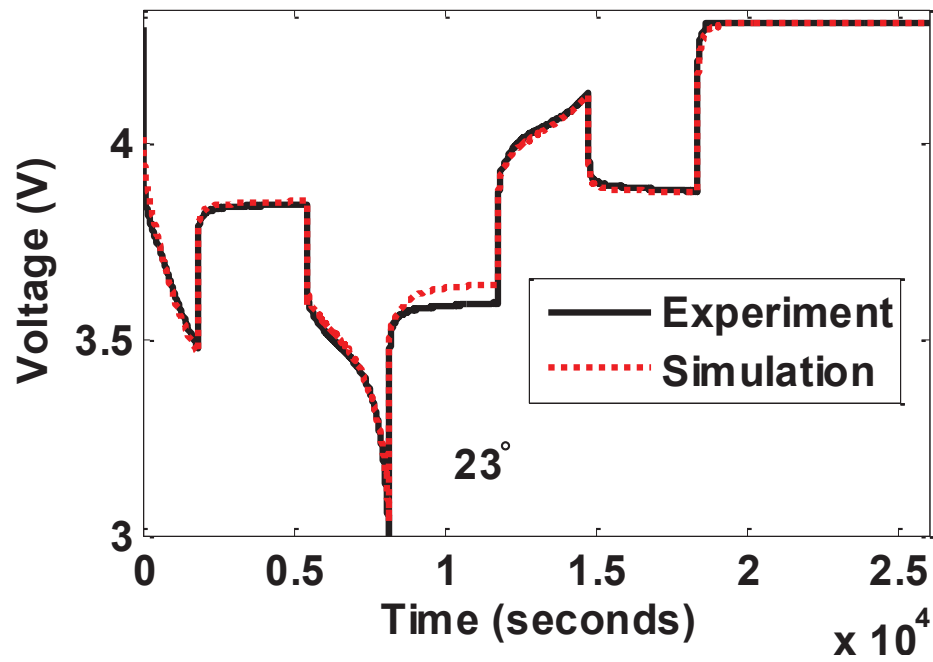
(a)



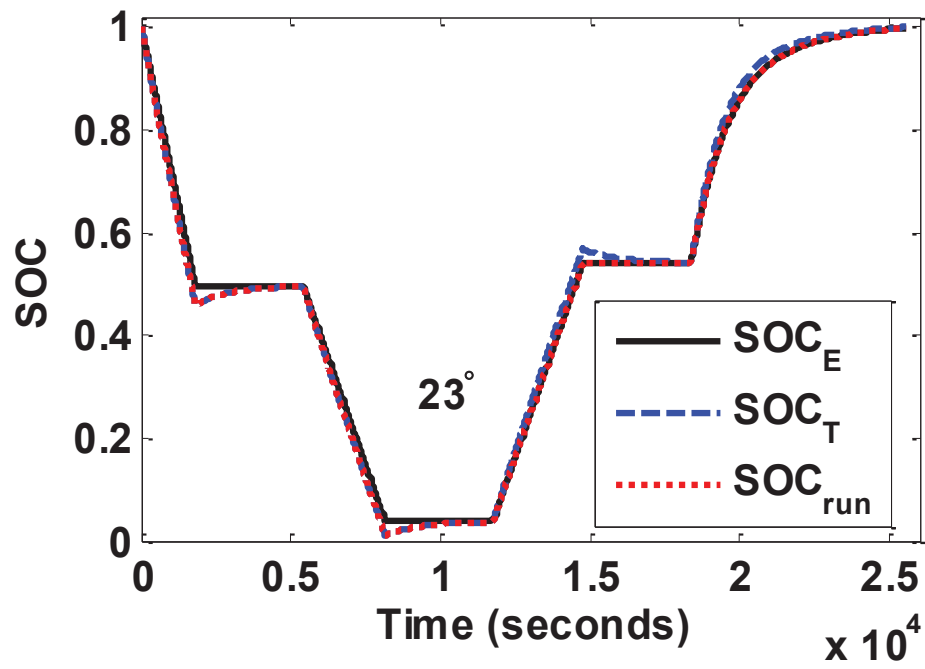
(b)



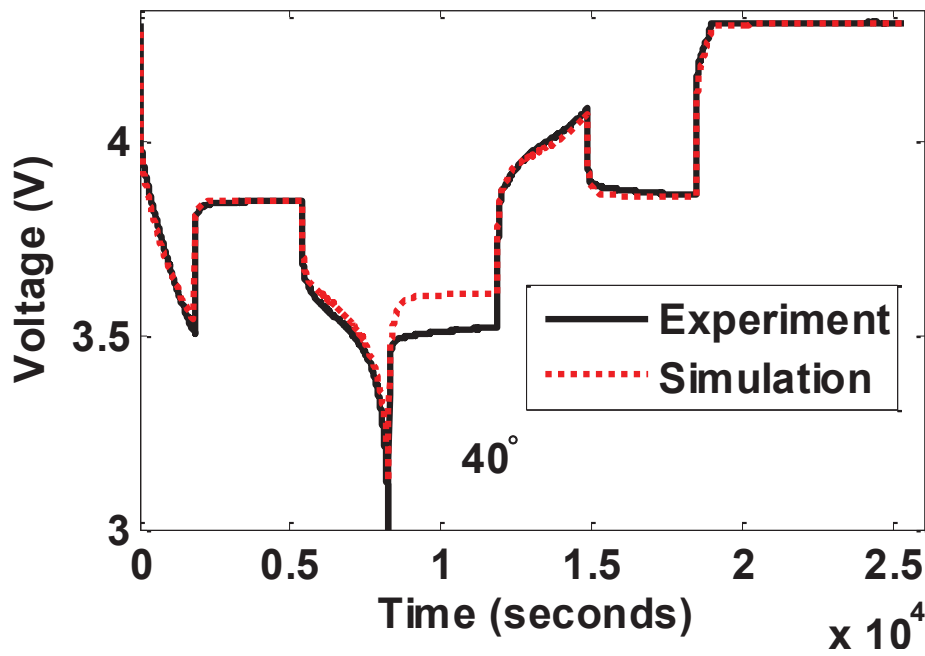
(c)



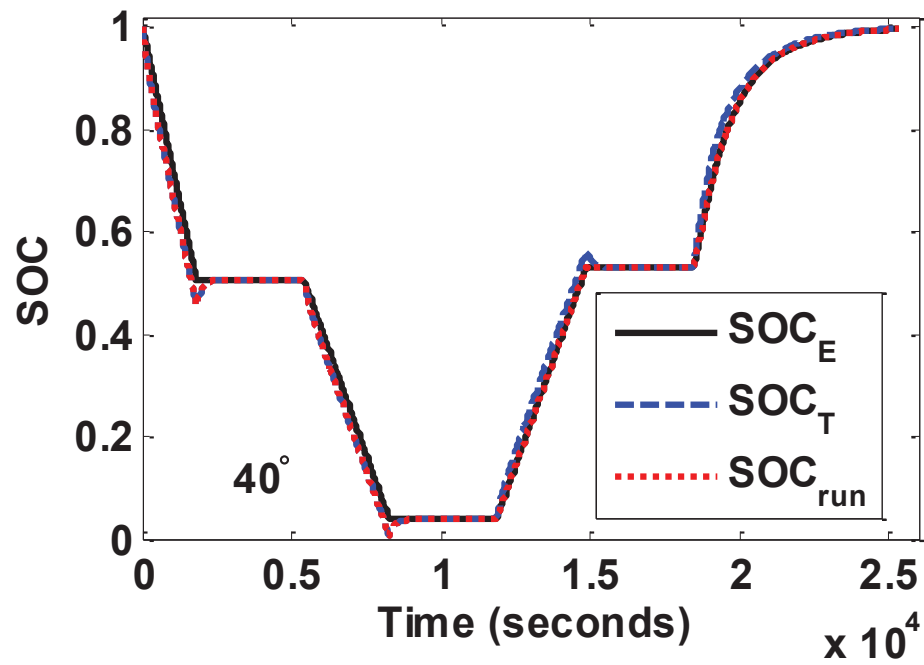
(d)



(e)

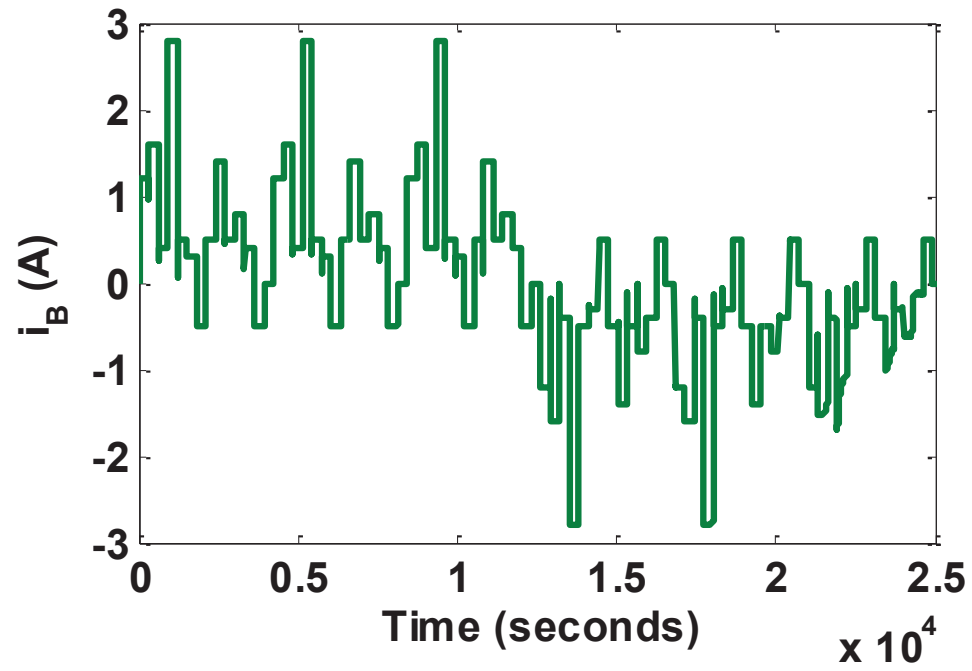


(f)

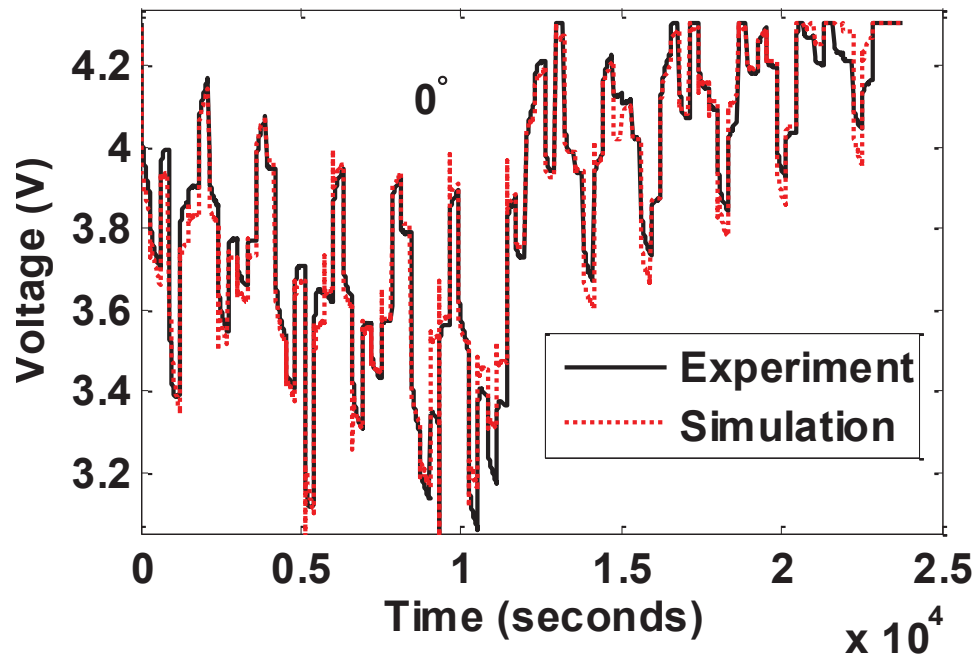


(g)

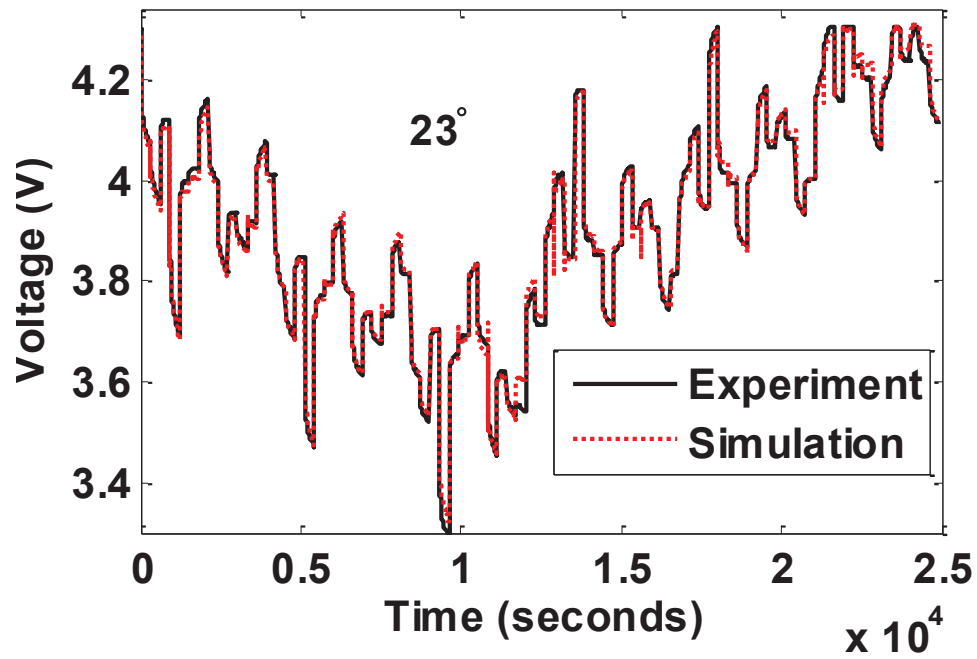
Figure 3.11: Comparison of simulation results of the enhanced hybrid battery model and experimental results for the test battery cell with pulsed discharge and charge currents: (a) the pulsed current profiles, (b) voltage respond at 0 °C, (c) the estimated SOC<sub>s</sub> at 0 °C, (d) the voltage respond at 23 °C, and (e) the estimated SOC<sub>s</sub> at 23 °C, (f) the voltage respond at 40 °C, and (g) the estimated SOC<sub>s</sub> at 40 °C.



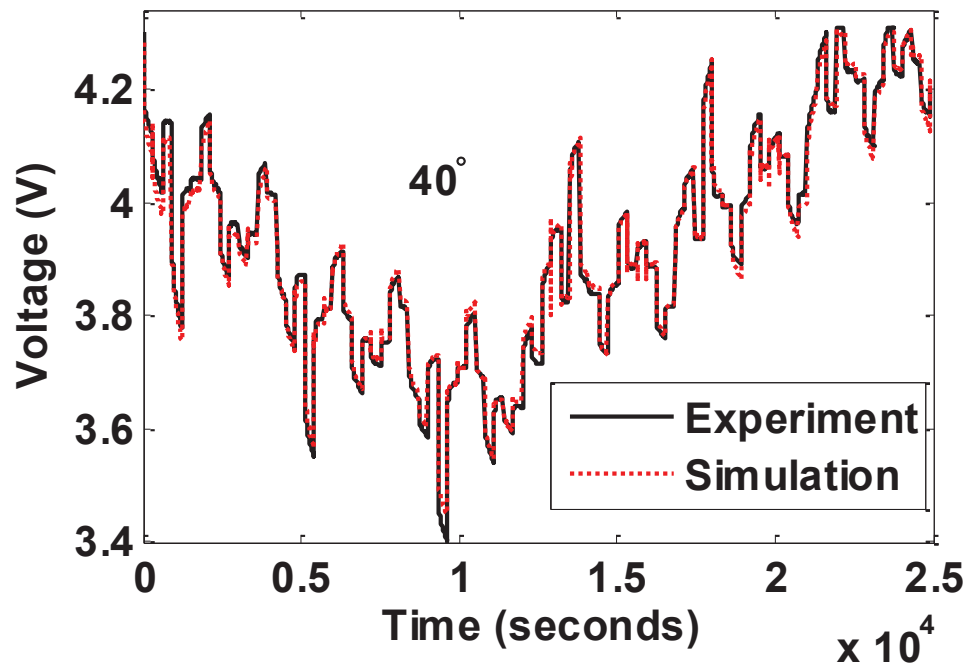
(a)



(b)



(c)



(d)

Figure 3.12: Comparison of simulation results of the proposed enhanced hybrid battery model and experimental results for the test battery cell with (a) a randomly varied current profile and terminal voltage responses at (b) 0 °C, (c) 23 °C, and (d) 40 °C.

### 3.3 Electrical Circuit with Hysteresis Battery Model

The hysteresis effect [66] is a fundamental phenomenon of batteries which shows an difference between the equilibriums of the battery in the charging and discharging modes. The equilibrium difference depends on the history of battery usage. The hysteresis effect widely exists in lithium-ion batteries, especially the popular LiFePo4-type cells. The accuracy of SOC estimation will deteriorate if the battery model does not incorporate the hysteresis effect. It was also demonstrated that the first-order RC circuit model with hysteresis provided a good balance between model accuracy and complexity [44]. Therefore, the electrical circuit with hysteresis battery model considered here was based on a first-order RC circuit model with a hysteresis model as proposed in [93], as shown in Figure 3.13.

In Figure 3.13,  $V_{oc}$  includes two parts. The first part, denoted by  $V_{oc,eq}(SOC_E)$ , represents the equilibrium OCV, which was used to bridge the SOC to the cell OCV. The second part  $V_h$  was the hysteresis voltage to capture the nonlinearity of OCV. The RC circuit models the I-V characteristics and the transient response of the battery cell. A discrete-time state-space version of the electrical circuit with hysteresis battery model was developed and is expressed as follows:

$$x(k+1) = \begin{bmatrix} 1 & 0 & 0 \\ 0 & \gamma & 0 \\ 0 & 0 & H \end{bmatrix} x(k) + \begin{bmatrix} \frac{-\eta T_s}{C_{\max}} & 0 \\ R_{ct}(1-\gamma) & 0 \\ 0 & (H-1)\text{sign}(i_B) \end{bmatrix} \begin{bmatrix} i_B(k) \\ V_{h\max} \end{bmatrix} \quad (3-36)$$

$$y(k) = V_{cell}(k) = V_{oc}(SOC_E(k)) - V_{ct}(k) - R_s i_B(k) + V_h(k) \quad (3-37)$$

$$V_{oc}(SOC_E) = q_0 \exp(-q_1 SOC_E) + q_2 + q_3 SOC_E - q_4 SOC_E^2 + q_5 SOC_E^3 \quad (3-38)$$

where  $x(k+1) = [SOC_E(k+1), V_{ct}(k+1), V_h(k+1)]^T$  is the state,  $y(k)$  is the measured output,  $k$  is the time index,  $\eta$  is the Coulomb efficiency (assuming  $\eta = 1$ );  $V_{hmax}$  is the maximum hysteresis voltage, and  $\gamma = \exp(-T_s/(R_{ct}C_d))$ ;  $\rho$  is the hysteresis parameter representing the convergence rate,  $sign(\cdot)$  is the sign function and  $H(i_B) = \exp(-\rho|i_B|T_s)$ ;  $a_i$  ( $i = 0, \dots, 5$ ) are the coefficients used to parameterize the OCV curve. Figure 3.14 shows the four OCV curves as functions of SOC extracted for a lithium-ion battery, where  $V_{oc,c}$  and  $V_{oc,d}$  represent major upper and lower hysteresis loops, respectively;  $V_{oc,eq}(SOC_E)$  is the average value of the charge and discharge OCV curves;  $V_{oc}$  represents the trajectory of the instantaneous OCV whose boundary is the major upper and lower hysteresis loops. By subtracting  $V_h(k)$  from  $V_{oc}$ , the  $V_{oc,eq}(SOC_E)$ , which has a one-to-one mapping to SOC is extracted [94].

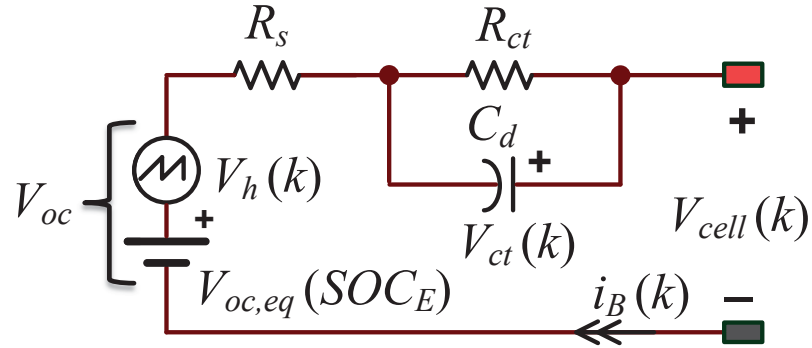


Figure 3.13: The electrical circuit with hysteresis battery model.

Work [94] proposed the following first-order differential equation to model the dynamics of the  $V_h$ :

$$\frac{\partial V_h}{\partial t} = -\rho(\eta i_B - \nu S_D)[V_{hmax} + sign(i_B)V_h] \quad (3-39)$$

where  $\nu$  is a self-discharge multiplier for hysteresis expression, and  $S_D$  is a self-discharge rate. This hysteresis model (3-39) describes the dependency of the hysteresis voltage  $V_h$  on the current rate, current direction, self-discharge, and hysteresis boundaries. For example, after

a long-term charge current or short but very large charge current is applied, the hysteresis voltage converges to  $V_{hmax}$  [94]. In other words,  $V_{oc}$  converges to the upper major loop. In the opposite case,  $V_{oc}$  converges to the lower major loop.  $V_{hmax}$  can be calculated by the difference between the  $V_{oc,c}$  and the  $V_{oc,eq}$ . The state,  $V_h(k)$ , in (3-36) is the discrete-time version of that in (3-39) using exact calculation [95]. The self-discharge effect was ignored in order to reduce the complexity of the battery model.

The parameter  $\rho$  was chosen to minimize the errors between the simulation and experimental results of  $V_{oc}$  versus SOC curves. The parameters  $\rho$  and  $V_{hmax}$  may depend on the SOC and the battery temperature [66], [94]. The coefficient  $a_i$  ( $i = 0, \dots, 5$ ) can be extracted by pulsed current tests [27] or constant charge and discharge current tests using a small current to minimally excite the transient response of the battery cell [96]. In this research, the temperature dependency was ignored by testing the battery under the ambient temperature of 23 °C.

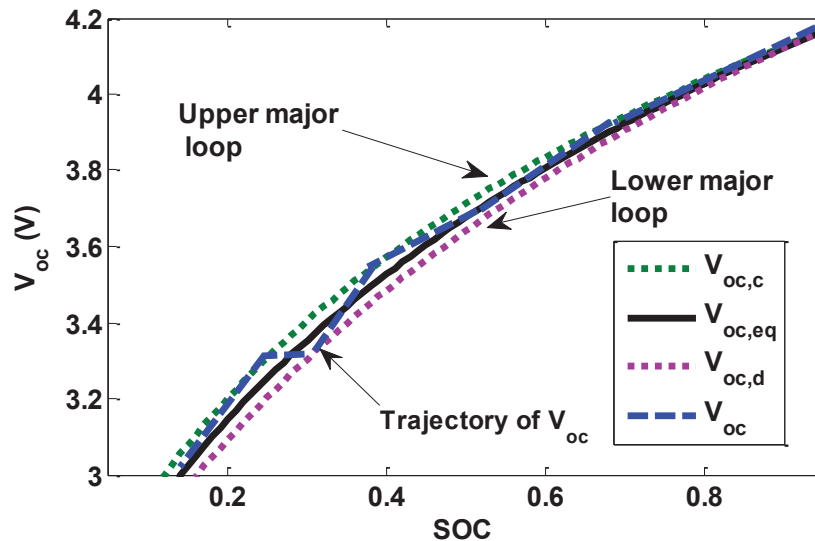


Figure 3.14: OCV curves.

### **3.4 Chapter Summary**

This chapter presented two hybrid battery models which were capable of capturing the dynamic circuit characteristics, nonlinear capacity and nonlinear OCV effects, and temperature effect of battery cells. The enhanced hybrid battery model is capable of predicting runtime behaviors of batteries under various temperatures and charge/discharge currents. These were validated by simulation and experimental studies for a newly developed high-voltage, cylindrical, lithium-ion battery cell. In addition to the hybrid battery models, an electrical circuit model incorporating the hysteresis effect was developed for some batteries having hysteresis characteristics. The proposed work provides high-fidelity real-time battery models for the battery and BMS designers to study various battery characteristics and optimally design BMSs for various applications.

## CHAPTER 4: SELF-X MULTICELL BATTERY DESIGN

This chapter proposes a self-X multicell battery design for configuration and power management of rechargeable multicell batteries [97]. The proposed design includes a power electronic switching circuit to connect multiple battery cells or modules in series and/or parallel to form a reconfigurable battery pack, where a module consists of multiple cells connected in series and/or in parallel. The power electronics-enabled, self-X multicell battery automatically configures itself according to the dynamic load/storage demand and the condition of each cell. For a large-size battery system, such as those in EVs and PHEVs, the self-X design can be used for the multiple modules in the battery system as well for the multiple cells in each battery module to achieve the required terminal voltage and power [98]. For various applications, a bidirectional DC/DC converter can be used as the interface between the self-X battery system and the load/source to control charge and discharge of the battery [99]. This chapter is organized as follows. The self-X designs for a battery module consisting of multiple cells and a battery system consisting of multiple modules are described. Then, a bidirectional DC/DC converter for charge, discharge, and cell balancing control of the self-X multicell battery system is designed for EV/PHEV applications. The self-X multicell battery system design is validated by simulations and experimental studies.

### 4.1 Self-X Multicell Battery Module Design

The self-X design for a multicell battery module [97] is shown in Figure 4.1. It consists of three parts: 1) a cell pack, 2) a cell switching circuit, and 3) a module management system (MMS). The external system can be a master battery management system (MBMS) if the

battery system is comprised of multiple modules or a bidirectional DC/DC converter as an interface between the battery and the source and load to control the charge and discharge of the battery.

The nominal voltages and currents of most single battery cells are limited to several volts and tens of amperes, e.g., 3.7 V and 0.86 A for the polymer lithium-ion cells used in this research, which is much lower than the voltages and currents required in many applications. In the design, the cell pack consists of  $m \times n$  cells, which are dynamically configured by the cell switching circuit during operation to meet the voltage and current requirements.

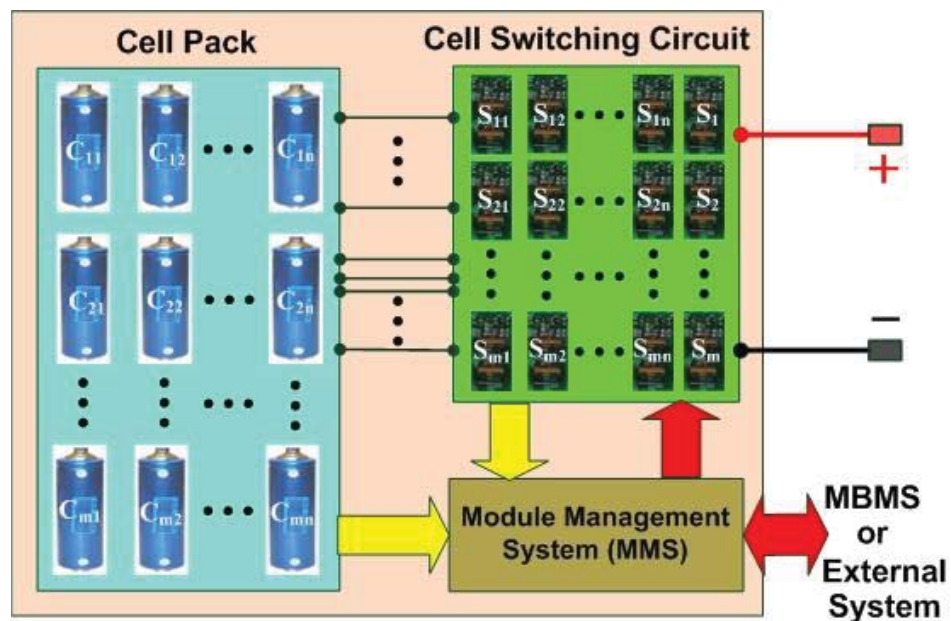


Figure 4.1: The self-X, multicell battery module design.

### 4.1.1 Cell Switching Circuit

Figure 4.2 shows the cell switching circuit topology for an  $m \times n$  cell battery pack, where  $n$  cells are connected in parallel to form a cell bank to provide higher currents; and  $m$  banks are connected in series to step up the voltage at the terminals of the battery. Only  $m \times (n+1)$  controllable switches are needed to form the cell switching circuit. Each cell only uses one switch, e.g., the switch  $S_{ij}$  for Cell  $C_{ij}$  ( $i = 1, \dots, m$  and  $j = 1, \dots, n$ ), which turns on/off alternatively to connect/cut off the cell from the battery, respectively. Moreover, if switch  $S_{ij}$  is on, it is able to conduct the current of Cell  $C_{ij}$  in two directions to charge/discharge the cell. Additional  $m$  switches  $S_1, \dots, S_m$  are used where  $S_i$  ( $i = 1, \dots, m$ ) is off if any of the  $n$  switches ( $S_{i1}, \dots, S_{in}$ ) in bank  $i$  are on. However, if all of the  $n$  switches in bank  $i$  ( $i = 1, \dots, m$ ) are off, then  $S_i$  should be turned on. Turning on  $S_i$  ensures that the cells in lower rows ( $S_{(i+1)1}, \dots, S_{(i+1)n}, \dots, S_{m1}, \dots, S_{mn}$ ) can be connected to supply (discharge) or store (charge) energy through the terminals of the battery. The proposed cell switching circuit ensures that each cell in the battery pack can be controlled independently in three modes, i.e., off, on/charge, and on/discharge.

Low-cost, high-efficiency power metal-oxide-semiconductor field-effect transistors (MOSFETs) are used for implementation of the switches in the cell switching circuit. The power MOSFETs conduct bidirectional currents and have a negligible conduction loss because of their negligible “on” resistance. In this application, switching losses are not a concern because it typically takes a long time, e.g., 10 minutes or longer, for a switch to change its state.

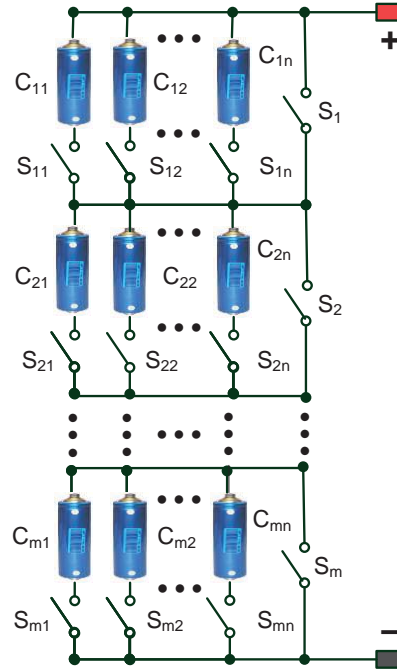
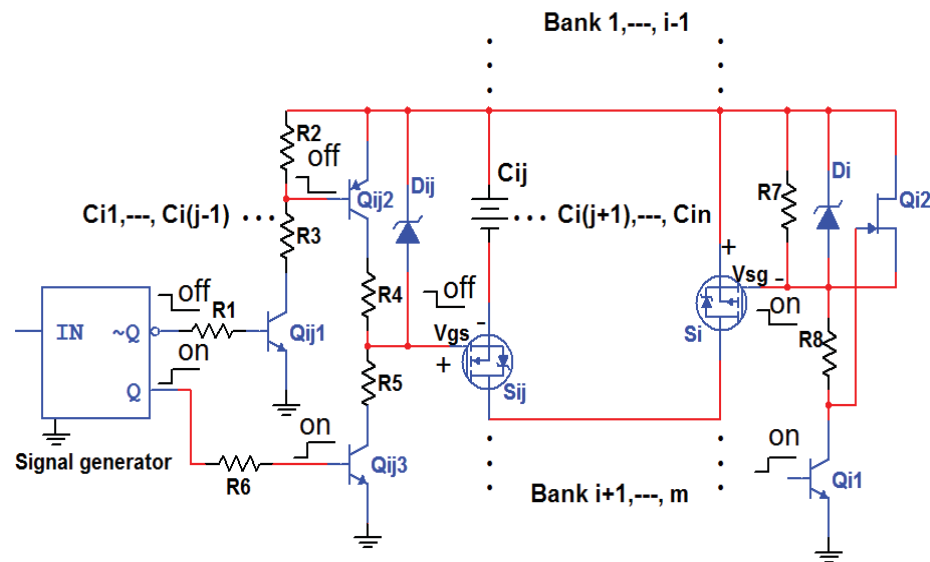


Figure 4.2: The cell switching circuit topology.

Figure 4.3 illustrates switch implementations for Cell  $C_{ij}$  ( $i = 1, \dots, m$  and  $j = 1, \dots, n$ ) using an n-channel power MOSFET ( $S_{ij}$ ) and for Bank  $i$  using a p-channel power MOSFET ( $S_i$ ) using two different gate drive circuits. It is crucial to connect the power MOSFETs in the correct direction due to the internal body diodes in the MOSFETs. As shown in Figure 4.3, the anode of the body diode of the MOSFET  $S_{ij}$  should be connected to the negative terminal of Cell  $C_{ij}$ . This connection blocks the unwanted discharges of Cell  $C_{ij}$ . On the other hand, the cathode of the body diode of MOSFET  $S_i$  should be connected to the positive terminal of the cell, which prohibits unwanted charges from flowing through the body diode to Banks  $i+1, \dots, n$  when Cell  $C_{ij}$  is connected, i.e.,  $S_{ij}$  is on. The gate drive circuit in Figure 4.3(a) is implemented by using four low-cost, small-signal bipolar junction transistors (BJTs) ( $Q_{ij1}, Q_{ij2}, Q_{ij3}$ , and  $Q_{i1}$ ) and a junction gate field-effect transistor (JFET) ( $Q_{i2}$ ). The small-signal BJTs can be replaced by small-signal MOSFETs. The gate drive

circuit only uses the voltage of Cell  $C_{ij}$  to turn on the power MOSFET  $S_{ij}$ ; no additional voltage source is required. When  $Q_{ij1}$  turns on, it drives  $Q_{ij2}$  on, which turns on  $S_{ij}$  by using the voltage of Cell  $C_{ij}$ . Turning off  $S_{ij}$  is accomplished by turning off  $Q_{ij1}$  while turning on  $Q_{ij3}$ , which discharges the parasitic capacitor between the gate and source terminals of  $S_{ij}$ . When  $Q_{i1}$  turns on, it provides a gate signal to turn on the power MOSFET  $S_i$ . Turning off  $S_i$  is accomplished by turning off  $Q_{i1}$  while turning on  $Q_{i2}$ . The value of  $R7$  should be large enough to ensure that the energy consumption of the gate drive circuit is negligible, which results in a slow turn-off of  $S_i$ . To speed up the turnoff of  $S_i$ ,  $Q_{i2}$  is implemented by using a JFET. In this switching implementation, an n-channel MOSFET with a low threshold  $V_{gs}$ , e.g., 1.5~2 V, should be used for  $S_{ij}$  because the voltage of Cell  $C_{ij}$  is in the range of 4.2 V to 3V. Two Zener diodes,  $D_{ij}$  and  $D_i$ , are used to limit the voltage between the source and the gate terminals of  $S_{ij}$  and  $S_i$ , respectively.



(a)

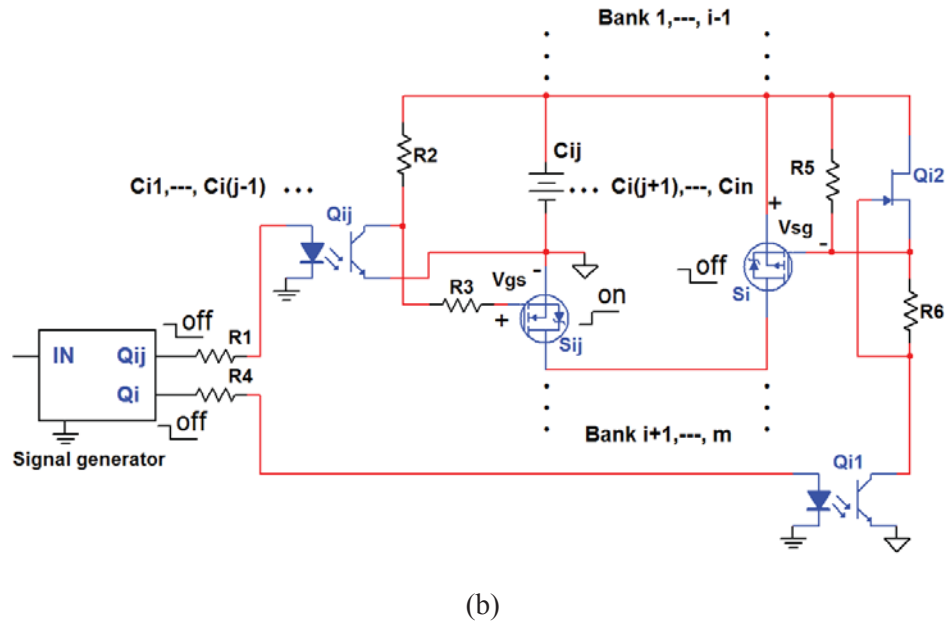


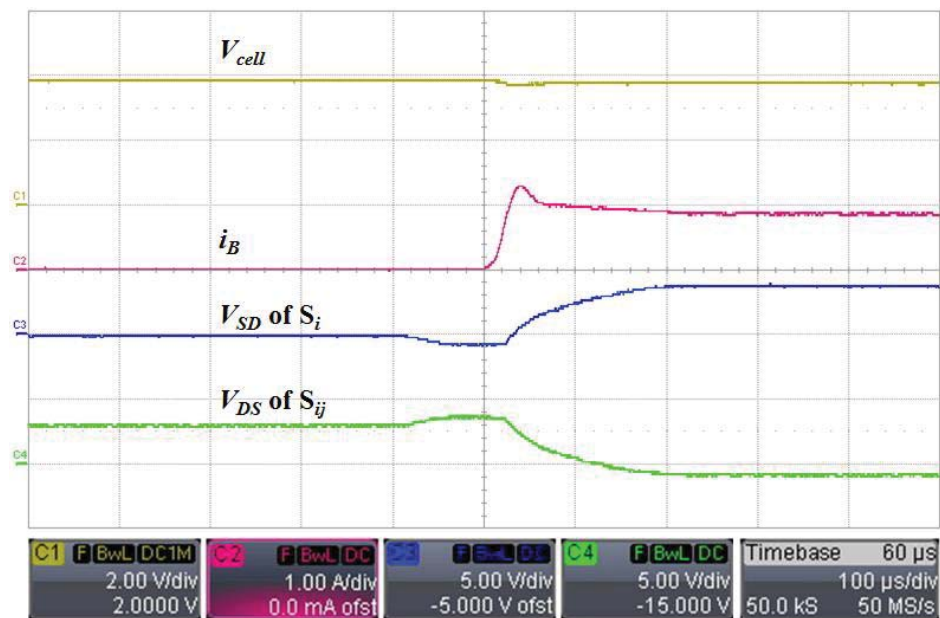
Figure 4.3: Switch implementation for Cell  $C_{ij}$  using an n-channel power MOSFET and for Bank  $i$  using a p-channel power MOSFET with a gate drive circuit using (a) small-signal BJTs and (b) optocouplers.

Figure 4.3(b) shows an alternative gate drive circuit, which uses two optocouplers to replace the four small-signal BJTs in Figure 4.3(a). The negative terminal of the battery cell is used as the virtual ground for the gate drive circuit. The gate signal generated by the signal generator is applied to the gate terminals of the power MOSFETs through the corresponding optocouplers to drive the power MOSFETs. Since the grounds of the gate drive circuit and signal generator are separated from that of the cell switching circuit, the switching implementation in Figure 4.3(b) can be used for multicell batteries at any voltage levels. In Figure 4.3(b) when  $Q_{ij}$  turns on, it drives  $S_{ij}$  off. Turning on  $S_{ij}$  is accomplished by turning off  $Q_{ij}$ . When  $Q_{i1}$  turns on, it provides a gate signal to turn on  $S_i$ . Turning off  $S_i$  is accomplished by turning off  $Q_{i1}$  while turning on  $Q_{i2}$ .

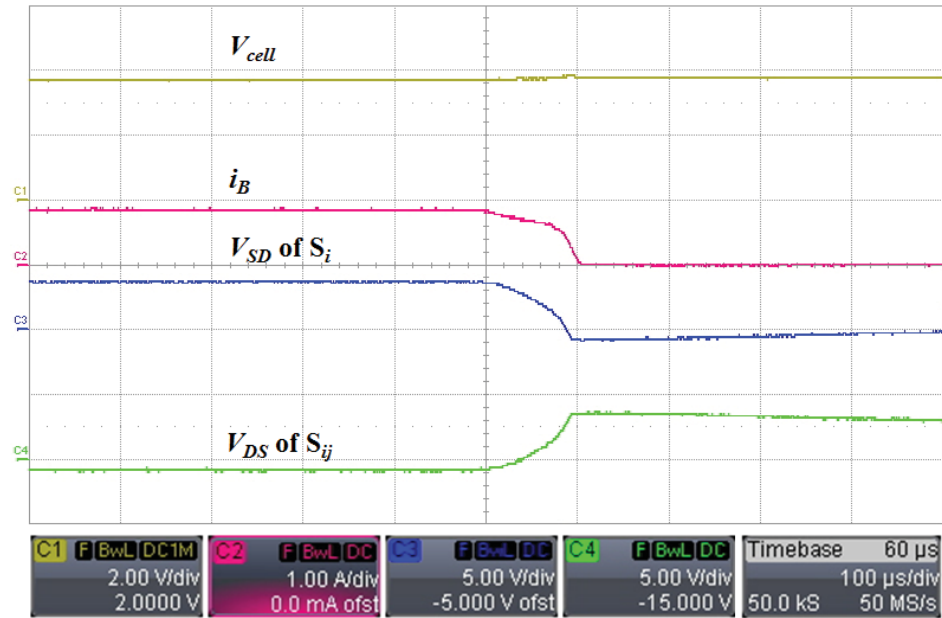
The small-signal components in the gate drive circuits are appropriately chosen to ensure that the energy consumption of the gate drive circuits is negligible compared to the

energy flow in the cell and that there is no short circuit between  $S_{ij}$  and  $S_i$  during transient switching periods. Figure 4.4 illustrates the transient waveforms of Cell  $C_{ij}$  and its switching circuit (Figure 4.3(a)) when the cell is operated with a 1C (0.86 A) load current. During the transient switching periods, there is no short circuit between  $S_{ij}$  and  $S_i$ , and the transition from one operating mode to another is smooth, as demonstrated in the waveforms of the cell terminal voltage ( $V_{cell}$ ) and current ( $i_B$ ) and the voltages between the source and drain terminals of  $S_{ij}$  and  $S_i$ . This ensures safe operation of Cell  $C_{ij}$ .

Although the design in Figure 4.3 illustrates cell-level switching, the design can also be used for module-level switching, where each module consists of multiple cells connected in parallel and/or series. The individual cells in the cell pack (Figures 4.1 and 4.2) become modules. Consequently, the cell pack and cell switching circuit become a cell module pack and a module switching circuit, respectively.



(a)



(b)

Figure 4.4: Transient waveforms of the switching implementation for Cell  $C_{ij}$  with a 1C (0.86 A) load current: (a)  $S_{ij}$  turns on and  $S_i$  turns off; (b)  $S_{ij}$  turns off and  $S_i$  turns on.

#### 4.1.2 Module Management System (MMS)

The MMS, as shown in Figure 4.5, performs the functions of sensing, model-based condition monitoring, control and protection, gate signal generation, and interfacing with the MBMS or external systems. The sensing circuit monitors the voltage, current, and temperature for each cell. The model-based condition monitoring performs the functions of SOC and SOH tracking. The control and protection module uses the information sensed to protect the battery cells from overcharge/overdischarge, overcurrent, and overtemperature. If any of these abnormal conditions occurs in a cell or the cell fails, it will be cut off immediately. The remaining cells will still be used to supply/store power and, therefore, the whole battery system self-heals from abnormal conditions or cell failures. The SOC and SOH of each cell are tracked by the model-based condition monitoring algorithms presented in Chapters 6 and 7.

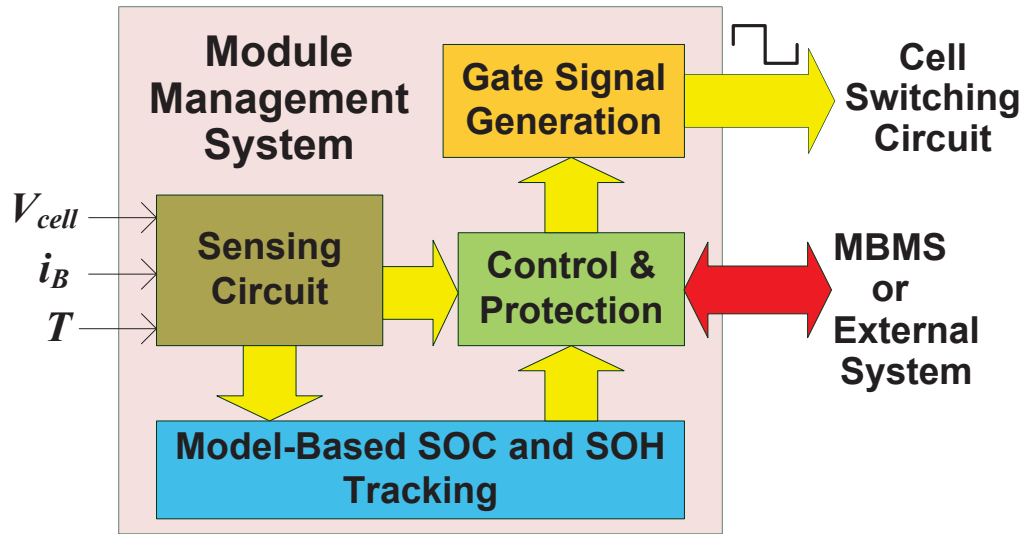


Figure 4.5: Schematic diagram of the module management system.

The control and protection module determines the best cell configuration based on the dynamic load/storage demand and the condition of each cell to achieve the optimal energy conversion efficiency of the battery system and self-balancing from cell state variations.

The functional block flow chart of the control and protection module is illustrated in Figure 4.6. Many applications require the battery systems to supply power to load at a constant voltage level and absorb power from a constant voltage source. Therefore, a bidirectional DC-DC converter (i.e., the external system in Figure 4.1) is commonly used as the interface between the battery and the load/source to control charge and discharge of the battery. In this case, the battery system can be operated with variable voltages by using  $k_B$  ( $k_B = 1, \dots, m$ ) out of  $m$  banks simultaneously. This means that some banks can be disconnected from the battery module for self-healing, self-optimization, and self-balancing during operation. Given the power demand ( $P_d$ ) from the load or the power supplied by the source as well as the required voltage by the load or source, the control

module determines the optimal values of the voltage ( $V_d$ ) and current ( $I_d$ ) of the battery, where  $P_d = V_d I_d$ , using the tradeoff between two conditions:

- 1) Since the efficiency of the DC/DC converter depends on its power and duty cycle (voltage gain), the terminal voltage of the battery should be set at a value such that the DC/DC converter is operated with a voltage gain leading to maximum efficiency of the converter.
- 2) The current should be as small as possible to utilize the rate capacity effect to maximize the energy conversion efficiency of the battery. In practice, a lookup table can be created offline to store the optimal voltage and current of the battery at each load/source power and voltage condition for the entire system operating range. The lookup table can then be used online to determine the optimal battery voltage and current according to the real-time system operating condition.

Based on the desired voltage, the number of series banks to be used,  $k_B$  ( $0 < k_B \leq m$ ), is determined by dividing the desired voltage by the average voltage of the banks. The control and protection module then checks the condition and SOC of each cell. If a cell fails, is in an abnormal condition, or its SOC is lower than a low limit (in discharge mode) or higher than a high limit (in charge mode), the cell will be disconnected from the battery module to prevent catastrophic failure of all of the cells. The remaining cells are still used to supply/store power; and, therefore, the whole battery module self-heals from abnormal conditions or cell failures. The SOCs of the usable banks are then sorted in a descending order, where the SOC of a bank ( $SOC_b$ ) is calculated by

$$SOC_b = \frac{1}{n} \sum_{i=1}^n SOC_i \quad (4-1)$$

where  $SOC_i$  is the SOC of the  $i$ th cell in the bank. If a cell is disconnected, then its SOC is zero. If the control module determines that  $k_B$  out of  $m$  banks should be used, the  $k_B$  banks with the lowest (highest) SOC's will be used in the charge (discharge) mode, provided that the selected banks can conduct the desired current, i.e., the following condition must be satisfied for each selected bank.

$$I_d \leq I_{br} = n_a I_{cr} \quad (4-2)$$

where  $n_a$  is the number of usable cells in the bank; and  $I_{br}$  and  $I_{cr}$  are the current of the bank and each cell, respectively. By using these criteria, the control module determines which banks in the battery module are connected to supply power to the load or absorb power from the source. All of the usable parallel cells in each selected bank are used simultaneously to charge/discharge with continuous currents. This whole process is called a control cycle, as illustrated in Figure 4.6. The control cycle restarts with a certain predefined time interval  $T_c$  or when the load/source condition is changed. The proposed control scheme always tends to balance the SOC's of the battery cells in both charge and discharge modes.

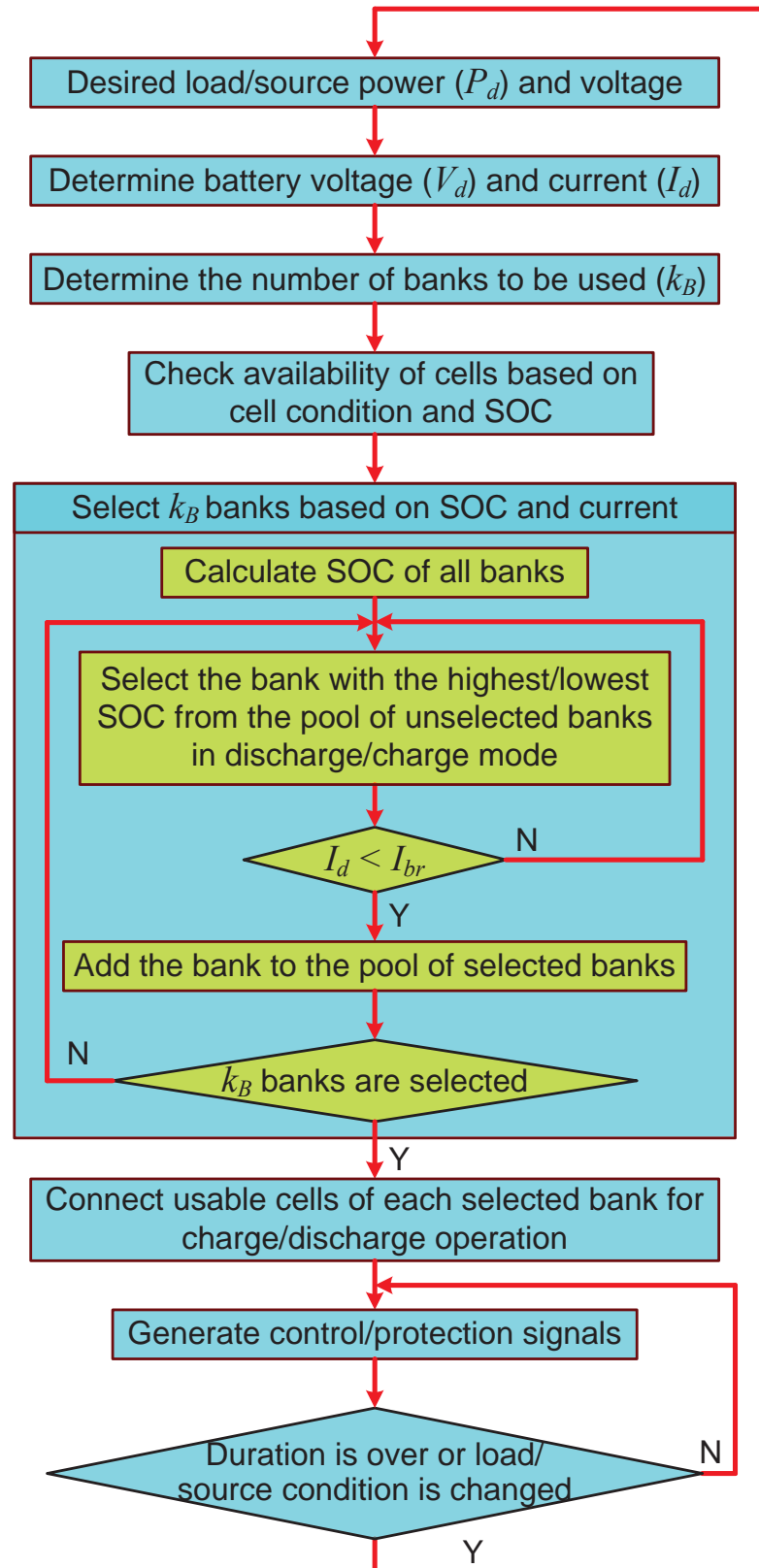


Figure 4.6: The functional block flow chart of one control cycle of the control and protection module.

In the proposed MMS, since all of the healthy cells in a selected bank will always be connected in parallel and used simultaneously to supply/store power, the cell voltages will be equal. However, in a worst case scenario where the cells in a bank have unequal voltages, cell balancing will be performed for the bank by discharging the cells sequentially starting with the one with the highest SOC (if in a discharge operation) or by charging the cells sequentially starting with the one with the lowest SOC (if in a charge operation) until the voltages of all cells become equal. Based on the output of the control and protection module, the gate signal generation module generates appropriate signals to control the power MOSFETs through their gate drive circuits.

The duration  $T_c$  of the control cycle will affect the performance of the proposed battery module. Generally, the operating time of the battery increases as  $T_c$  decreases. However, using a very small  $T_c$  will result in frequent switching of the power MOSFETs and will, therefore, increase the switching loss of the cell switching circuit. In practice, the value of  $T_c$  should be selected such that the SOC of all  $m$  banks will be balanced before any single bank is fully charged in a charge operation or fully discharged in a discharge operation. In this work, the value of  $T_c$  is determined by:

$$T_c = \frac{3,600}{I} \times \zeta \quad (4-3)$$

where  $T_c$  is in seconds;  $I$  is the normalized battery current in C-rate; and  $\zeta$  is a percentage. If the SOC of all banks are higher than a low threshold, e.g., 10%, in a discharge operation or lower than a high threshold, e.g., 90%, in a charge operation, a large  $\zeta$  (e.g.,  $\zeta = 5\%$ ) will be used. On the other hand, if the SOC of a bank becomes lower than the low threshold in a discharge operation or higher than the high threshold in a charge operation, a small  $\zeta$  (e.g.,  $\zeta = 1\%$  or  $0.5\%$ ) will be used.

An important issue in the design of the self-X multicell battery module is the grounding of the power MOSFET gate drive circuits, cell sensing circuits, and control and protection circuits. If the cell switching circuit is implemented by using the circuit in Figure 4.3(a), the power MOSFET gate drive circuits, cell sensing circuits, and control and protection circuits use the same ground. However, if the cell switching circuit is implemented by using the circuit in Figure 4.3(b), the power MOSFET gate drive circuits and cell sensing and monitoring circuits use the same virtual grounds, which are the negative terminals of the corresponding battery cells. The ground of the control and protection circuits will be separated from the ground of the gate drive circuits and cell sensing circuits. In this case, optically coupled signal isolators will be used between the sensing and monitoring circuits and control and protection circuits for transferring the sensed information.

## **4.2 Self-X Multicell Battery System Design for EVs and PHEVs**

The performance of EVs and PHEVs strongly relies on their battery storage systems, which usually consist of multiple modules connected in series and parallel. However, cell state variations are commonly present, which reduces the energy conversion efficiency of the battery system. Furthermore, in a large battery system, the risk of catastrophic cell faults increases because a large numbers of cells are used. These problems can be solved by the self-X multicell battery system, consisting of self-X multicell modules connected in series [98]. Figure 4.7 illustrates the self-X multicell battery system connected to an electric motor load in an EV. An EV or PHEV usually requires the battery system to supply power to the load at a constant voltage level and to absorb power from a constant voltage source, e.g., a

charger or regenerative brake. Therefore, a bidirectional DC/DC converter is commonly used as the interface between the battery system and the load/source to control charge and discharge of the battery. In this case, the battery system can be operated with variable voltages. The motor bridge inverter generally requires a DC voltage at several hundred volts, e.g., 450 V. In order to achieve the best efficiency of the DC/DC converter, a terminal voltage of 150 to 300 V is needed for the battery [100]. Therefore, the battery system consists of several battery modules connected in series to achieve the required terminal voltage. For example, the Chevrolet Volt's lithium-ion battery system consists of three modules [101]. An MBMS is used to coordinate the operations of the multiple battery modules and the DC/DC converter.

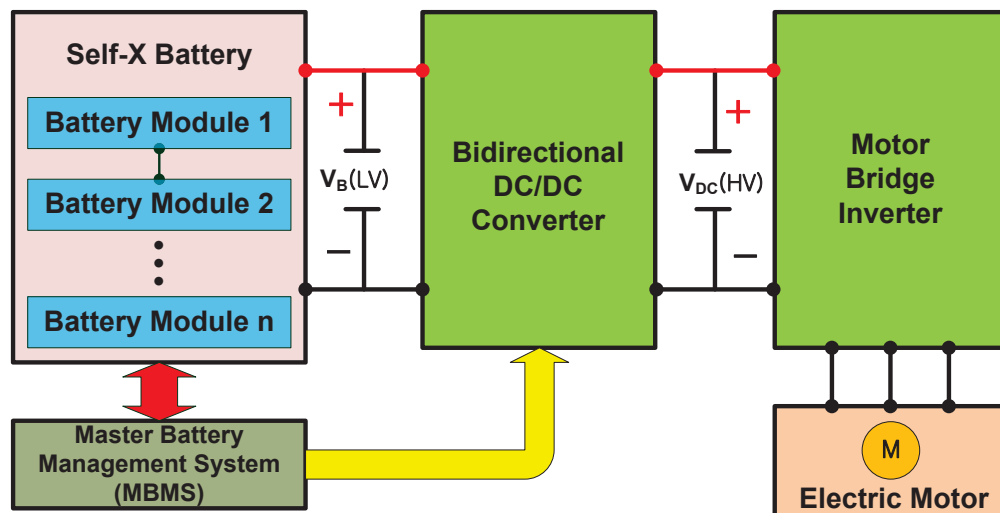


Figure 4.7: A self-X multicell battery system for EVs and PHEVs.

## 4.2.1 Control and Protection for Each Module of Self-X Multicell

### Battery System

In the battery system, the control and protection module of each MMS in Section 4.1.2 is coordinated by an MBMS. Figure 4.8 illustrates the modified functional block flow chart of one control cycle of the control and protection module. The control scheme always tends to protect the battery cells and balance the SOC<sub>s</sub> of the battery cells and modules. The MBMS determines the number of banks,  $q_{MBMS}$ , of each battery module to be used simultaneously to balance the SOC<sub>s</sub> of the modules of the battery system. This is called global balancing. The SOC of a module ( $SOC_m$ ) is defined as

$$SOC_m = \frac{1}{m} \sum_{j=1}^m SOC_{b,j} \quad (4-4)$$

where  $SOC_{b,j}$  is the SOC of the  $j$ th bank in the module. If a cell is disconnected, then its SOC is zero. Moreover, the control and protection block in the MMS of each battery module also determines the number of series banks,  $q_{MMS}$ , to be used simultaneously to balance the SOC<sub>s</sub> of the banks in the module. This is called local balancing.

$$q_{MMS} = m - f(\Delta SOC_b) \quad (4-5)$$

where  $\Delta SOC_b = SOC_{b,max} - SOC_{b,min}$ ;  $SOC_{b,max}$  and  $SOC_{b,min}$  are the maximum and minimum SOC<sub>s</sub> of the banks in the module, respectively. The value of  $f(\cdot)$  with respect to  $\Delta SOC_b$  used in this work is shown in Figure 4.9. Finally, the number of banks in the module to be used,  $q$  ( $0 < q \leq m$ ), can be determined to be the smaller of  $q_{MBMS}$  and  $q_{MMS}$ . Once  $q$  is determined, the SOC<sub>s</sub> of all usable banks are sorted in a descending order; and the  $q$  banks with the highest SOC<sub>s</sub> will be used in the discharge mode; or the  $q$  banks with the

lowest SOC<sub>s</sub> will be used in the charge mode until the SOC<sub>s</sub> of all of the banks in the module become balanced.

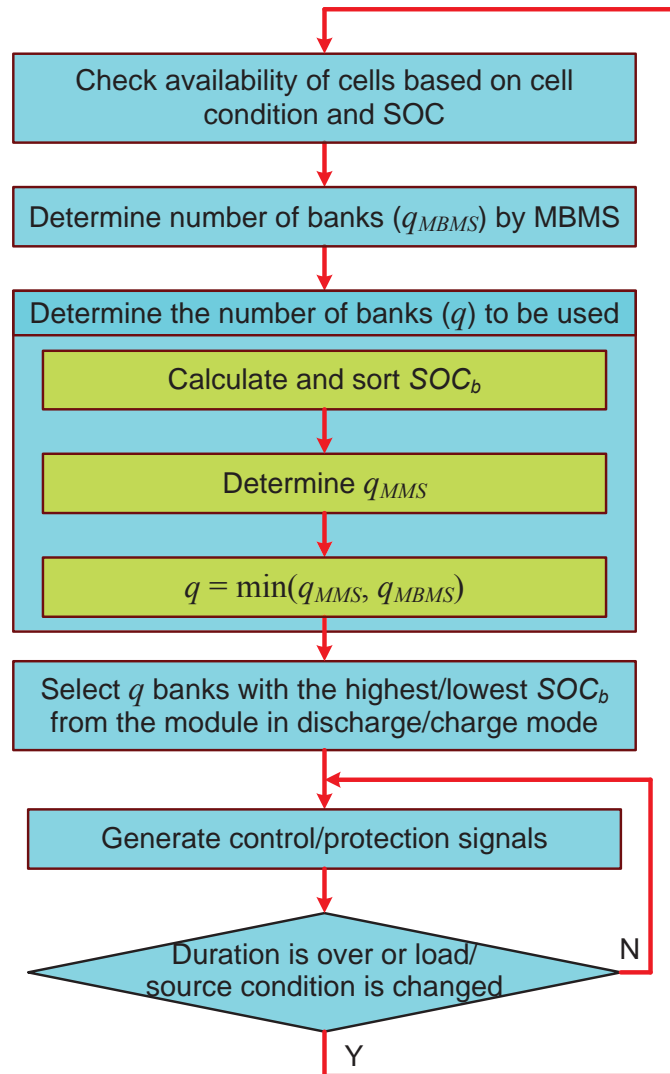


Figure 4.8: The modified functional block flow chart of one control cycle of the control and protection module of each MMS.

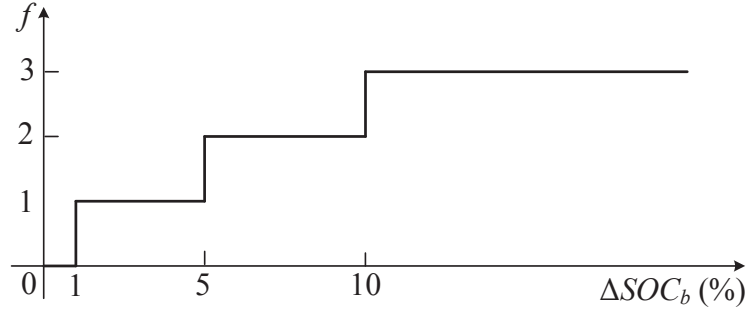


Figure 4.9: The value of  $f(\cdot)$  with respect to  $\Delta SOC_b$ .

## 4.2.2 Master Battery Management System

The MBMS coordinates the battery modules to globally balance their SOC<sub>s</sub> and control the bidirectional DC/DC converter to safely charge/discharge the battery system with optimal efficiency. Given battery states and the power demand ( $P_d$ ) from the load, or the power supplied by the source, the MBMS determines the optimal values of the voltage ( $V_d$ ) and current ( $I_d$ ) of the battery, where  $P_d = V_d \cdot I_d$ , using the tradeoff of the two conditions introduced in Section 4.1.2. According to these two criteria, the total number of series banks ( $q_t$ ) to be used in the battery system can be determined by:

$$q_t(V_{avg}, w, P_d) = q_{max} - R(V_{avg}, w, P_d) \quad (4-6)$$

$$R = \text{floor} \left\{ q_{max} \min \left[ w \times \left( \frac{V_{avg} - V_{limit\_discharge}}{V_{avg}} \right), \left( 1 - \frac{P_d}{P_{max}} \right) \right] \right\} \quad (4-7)$$

where  $V_{avg}$  is the average voltage of all of the banks in the battery system;  $V_{limit\_discharge}$  is the discharge cutoff voltages of a cell;  $q_{max}$  is the total number of banks in the battery system;  $P_{max}$  is the maximum power of the battery;  $R$  is the redundancy of the battery;  $\min(a, b)$  denotes the minimum value of  $a$  and  $b$ ;  $\text{floor}(\cdot)$  stands for rounding a number down to the nearest integer; and  $w$  is determined by

$$w = g(\Delta SOC_m) \quad (4-8)$$

where  $\Delta SOC_m = SOC_{m\_max} - SOC_{m\_min}$ ;  $SOC_{m\_max}$  and  $SOC_{m\_min}$  are the maximum and minimum SOC of the modules in the battery system, respectively. The value of  $w$  with respect to  $\Delta SOC_m$  as used in this work is shown in Figure 4.10. Once  $q_t$  is calculated, the MBMS determines the number of banks,  $q_{MBMS}$ , for each module to be used simultaneously based on the SOC of each module and the operating mode of the battery. The sum of all  $q_{MBMS}$  is  $q_t$ .

In the discharge mode, the BMS continuously protects and balances the battery cells as well as control the battery system to supply the required voltage and power to the motor bridge inverter via the DC/DC converter. On the other hand, due to protection and balancing control, the terminal voltage of the battery system is variable, which is controlled by regulating the duty cycle of the DC/DC converter in the charge mode. The charge reference voltage ( $V_{B\_REF}$ ) is determined by the number of banks connected in the battery, the charge cutoff voltage of a cell ( $V_{limit\_charge}$ ), and the voltage drop caused by conduction losses of the switches.

In the charge mode, the multicell battery is first charged with a constant current until the terminal voltage reaches  $V_{B\_REF}$ . Thereafter, the voltage of each cell is kept constant; the charge current is reduced as the SOC of each cell approaches the maximum value, e.g., 95% for EVs and 90% for PHEVs. This is called CCCV control, under which the battery can be charged fully and safely. The design of the DC/DC converter used with the self-X multicell battery will be discussed in the next section.

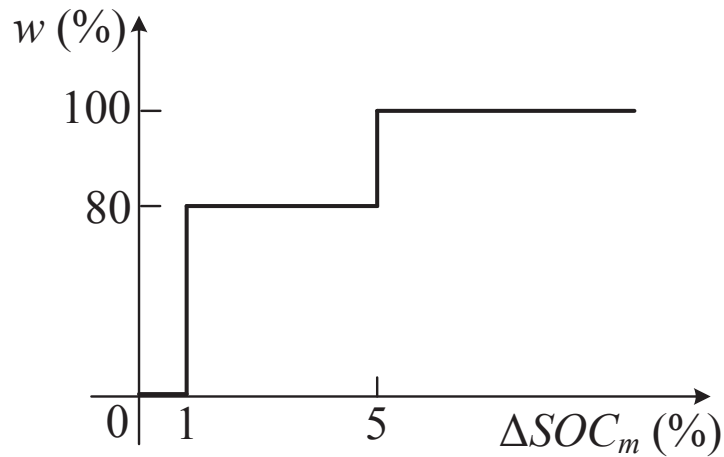


Figure 4.10: The value of  $w$  with respect to  $\Delta SOC_m$ .

### 4.3 A Bidirectional DC/DC Converter for Multicell Batteries

This section discusses a bidirectional DC/DC converter with a unified constant current adaptive voltage (CCAV) control scheme and a balancing control scheme for a series-connected, self-reconfigurable, multicell battery module, as shown in Figure 4.11 [99]. Moreover, the proposed DC/DC converter can be used for the self-X multicell battery system, as shown in Figure 4.7. The CCAV control scheme allows the battery to be charged or discharged with a constant current or with an adaptive reference voltage, which is determined by the required voltage levels for charge and discharge, cell states, and voltage drop resulting from conduction losses of the multicell batteries. The CCAV scheme enables fast and full charge of individual cells without any damage. Moreover, balancing and self-healing can be achieved during charge and discharge operations, which enhance the reliability and performance of the multicell batteries. Compared to existing active balancing circuits [13]-[17], the number of balancing components, such as inductors, capacitors, and switches, in

the self-X battery design is significantly reduced. This reduces the overall cost, complexity, and control effort of the battery system.

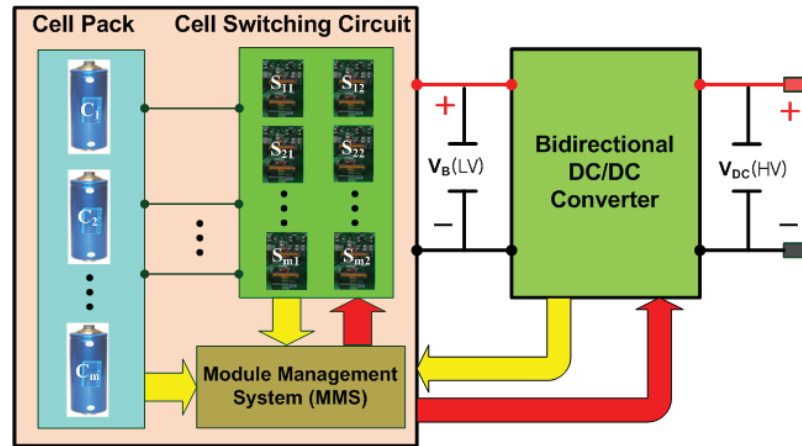


Figure 4.11: The proposed series-connected, self-reconfigurable, multicell battery module with a bidirectional DC/DC converter.

### 4.3.1 Series-Connected, Self-Reconfigurable Multicell Battery Pack

A series-connected, self-reconfigurable, multicell battery topology was proposed in [102] and is shown in Figure 4.12. This topology is a simple version of the proposed self-X multicell battery module, shown in Figure 4.2, created by removing parallel connected cells. It consists of a cell pack and a switching circuit, where each individual cell is controlled independently by using only two power electronic switches.

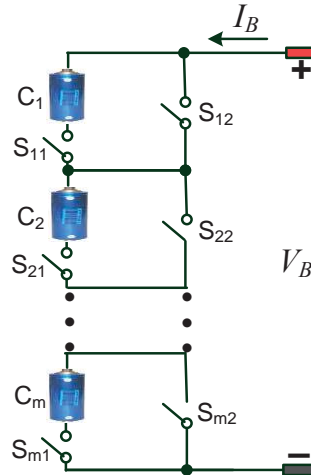


Figure 4.12: The proposed series-connected, self-reconfigurable, multicell battery topology.

### 4.3.2 The Bidirectional DC/DC Converter with the Unified CCAV

#### Control Scheme

Figure 4.13 illustrates the proposed bidirectional DC/DC converter with the unified CCAV control scheme for charging and discharging control of the multicell battery. The CCAV controller outputs gate control signals  $G_1$  and  $G_2$  to turn on/off two switches,  $S_1$  and  $S_2$ , alternatively. In the charge mode, the DC/DC converter acts as a buck converter (charger) to charge the multicell battery at the low-voltage (LV) side from a source at the high-voltage (HV) side. In the discharge mode, the DC/DC converter acts as a boost converter. The unified CCAV control scheme is used for bidirectional current flow control in the continuous conduction mode (CCM). The two switches of the DC/DC converter are complementarily controlled by a common duty ratio generated by the unified CCAV controller [32]. In the charge mode,  $V_{B\_REF}$  is used as the reference voltage of the unified CCAV controller; while  $V_{DC\_REF}$  is used in the discharge mode. The direction of the current flow  $I_L$  depends only on

the relationship between the control duty cycle  $D$  and the zero current duty cycle  $D_o$ , which is equal to  $V_B/V_{DC}$ , as shown in Figure 4.14. The average inductor current  $I_L$  is the same as the battery current  $I_B$ . When charging the battery, the average inductor current  $I_L$  is greater than zero. This means that duty cycle  $D$  should be adjusted to be greater than  $D_o$ . When discharging the battery, on the other hand, the average inductor current  $I_L$  is less than zero. Consequently, the duty cycle  $D$  should be adjusted to be less than  $D_o$ .

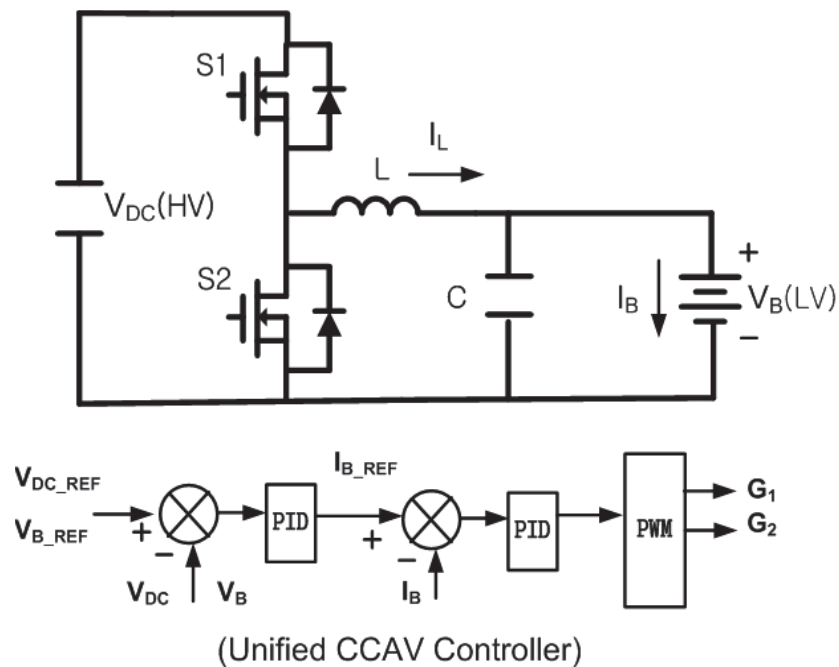


Figure 4.13: The proposed bidirectional DC/DC converter with the unified CCAV controller for charging and discharging control of the multicell battery.

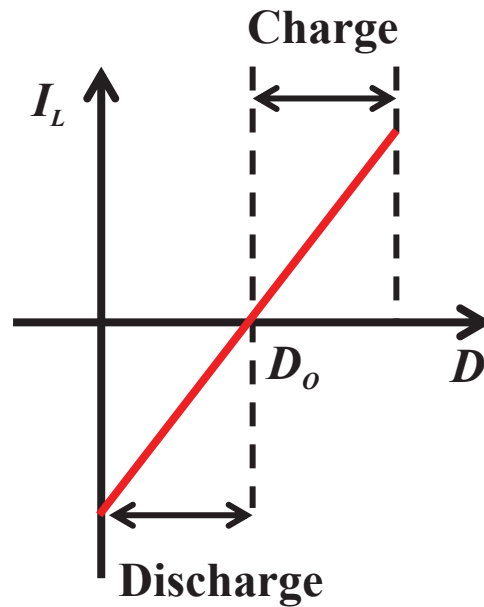


Figure 4.14: Control duty cycle  $D$  versus average inductor current  $I_L$ .

An output capacitor is connected at the LV side to further smooth the output current and allow the output voltage to be adjusted prior to charging the battery. In the charge mode, the multicell battery is first charged with a constant current (C.C.) until the terminal voltage reaches an adaptive reference value ( $V_{B\_REF}$ ), which is determined by the number of cells connected in the battery, charge cutoff voltage, and voltage drop caused by conduction losses of the switches used in the DC/DC converter. Thereafter, the voltage of each cell is kept constant (constant voltage C.V.); the charge current is reduced to a very small value, e.g.,  $1/40C$ , as the SOC of each cell approaches 100%. Hence, the series-connected multicell battery can be charged fully and safely.

Figure 4.15 illustrates the flow chart of the scheduling algorithm for the implementation of the CCAV controller when the battery is operated in normal charge mode. The scheduling algorithm when the battery is operated in discharge mode can be illustrated

by a flow chart in a similar way. In Figure 4.15,  $I_{ABS}$  is the minimum charge/discharge current of the battery;  $SOC_{avg}$  is the average SOC of the battery cells; and  $\alpha$  is a small positive number. If a battery cell is in an abnormal condition or its SOC is lower than a low limit in the discharge mode or higher than a high limit in the charge mode, the cell will be disconnected from the battery system. The scheduling algorithm balances the SOC of the remaining healthy cells. The scheduling algorithm always tends to balance the SOC of the battery cells. Therefore, it can fully charge and utilize the available capacity of individual cells of the multicell battery during operation.

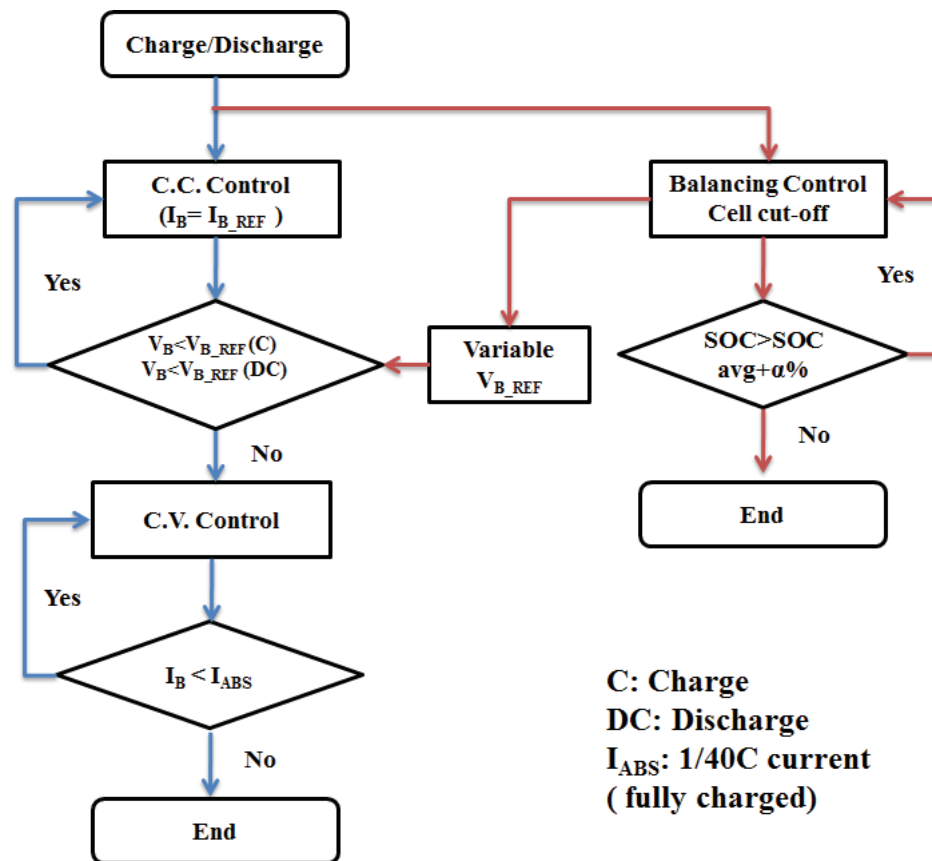


Figure 4.15: The scheduling algorithm for the implementation of CCAV control in the charge mode of the battery.

## 4.4 Validation

The proposed self-X multicell battery design was validated by simulations and experimental results.

### 4.4.1 Module-Level Self-Healing

A  $6 \times 3$ -cell battery module was built using the self-X design developed and was simulated in MATLAB/Simulink. Each cell was a 3.7 V, 860 mAh polymer lithium-ion cell, which is represented by the hybrid battery model in Section 3.1. Assuming all of the cells in the same bank have the same SOC and the initial SOC of Banks 2-5 are all at 100%, Figure 4.16(a) and (b) compare the total energy in Wh that can be supplied by the fixed configuration and the proposed self-X multicell battery module for different SOC of Banks 1 and 6. These results clearly show that the self-X design significantly improves the energy usage of the multicell battery. For example, when the SOC of Bank 1 or 6 or both becomes zero, the whole battery with the fixed configuration has to be cut off and cannot supply any energy to the load although the usable capacity of the battery is still significant. On the other hand, the proposed self-X battery module can supply energy from other banks even if the SOC of one or both of Banks 1 and 6 becomes zero. For example, in the worst case scenario, when the SOC of Banks 1 and 6 are both zero, the self-X battery module can still supply a total energy of 36.88 Wh from Banks 2-5, which is 66.7% of the maximum energy capacity of the battery. This shows the self-healing feature of the proposed design.

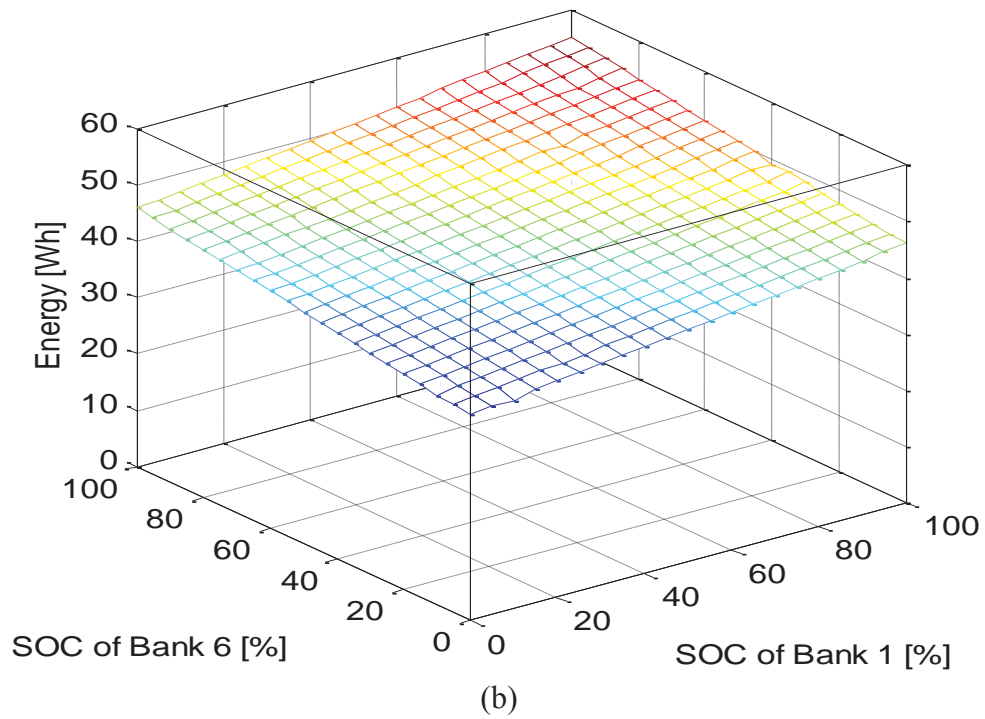
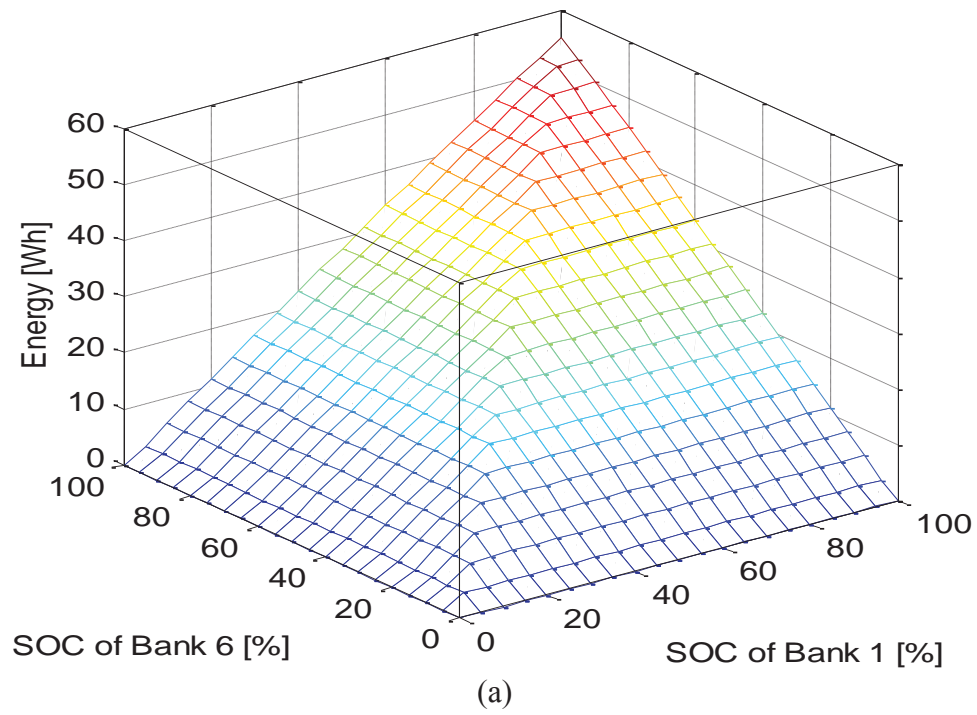


Figure 4.16: Total energy in Wh that can be supplied by (a) the fixed-configuration and (b) the proposed self-X,  $6 \times 3$ -cell battery module for different SOC of Banks 1 and 6.

Next, the self-X multicell battery module used in simulation studies was constructed in hardware to further validate the proposed design. Figure 4.17 shows the experimental system setup. High-efficiency power MOSFETs were used to form the cell switching circuit on a printed circuit board (PCB). The gate drive circuit in Figure 4.3(a) was used to drive the power MOSFETs in the cell switching circuit. The sensing, control, and protection functions were also implemented on the PCB. The cells were charged by a variable DC source and discharged through a programmable DC electronic load. Table 4.1 compares the simulation and experimental results of the self-X battery module design and simulation results of the fixed-configuration design for three scenarios. Scenarios 1 and 2 were used to validate the self-healing feature of the proposed design. Self-optimizing for improving the energy conversion efficiency was validated by Scenario 3. In all scenarios, the discharge current of the battery was 2.58 A, i.e., 1C. For all scenarios, the experimental results agreed with the simulation results.

In Scenarios 1 and 2, the 18 cells were discharged simultaneously using the C.C. mode. Since the initial SOCs of the cell banks were different, the cell banks were fully discharged sequentially. In the fixed-configuration design, once a cell bank was fully discharged, the whole battery had to be cut off and could not supply any energy to the load, although the usable capacity of the battery was still significant. In the self-X design, once a cell bank is fully discharged, it is disconnected from the battery pack by the cell switching circuit but the remaining cell banks still provide energy to the load. Compared to the fixed-configuration design, the proposed self-X battery module design can supply 16 Wh and 24.73 Wh more energy, which represented 28.9% and 44.7% of the maximum capacity of the battery in Scenarios 1 and 2, respectively. Figure 4.18 compares the terminal voltage

response of the self-X battery module obtained from the simulation and the experiment for Scenario 2. It shows that not only the steady state but also the dynamic responses of the battery obtained from simulations agree with those from experiments. Therefore, the comparison in Figure 4.16 is effective to validate the superiority of the proposed self-X battery module design over the traditional fixed-configuration design.

In Scenario 3, the six banks of the self-X battery module were divided into two groups, three banks per group. The two groups of cell banks were discharged alternately, i.e., pulsed current (P.C.), with a time interval of 300 s until all of the cells were fully discharged. Compared to the fixed-configuration battery that used C.C. discharge, more energy ( $\sim 1$  Wh) was supplied by the self-X battery module when the P.C. discharge was used. The P.C. discharge method utilized the recovery effect to improve the energy conversion efficiency of the battery, which, however, cannot be achieved by the traditional fixed-configuration battery design.

Table 4.1: Comparison of simulation and experimentation results for the  $6 \times 3$ -cell battery module.

| Scenario | Discharge Method                                  | Initial Conditions of Cell Banks Expressed by SOC [%] |     |     |     |     |     | Energy [Wh]   |             |   |
|----------|---|---|-----|-----|-----|-----|-----|---------------|-------------|---|
|          |   | Bank  |     |     |     |     |     | Self-X Design |             | Fixed-Configuration Design (Simulation) |
|          |   | 1   | 2   | 3   | 4   | 5   | 6   | Simulation    | Experiment  |   |
| 1        | C.C. = 2.58 A                                     | 80  | 100 | 100 | 100 | 100 | 60  | 49.5          | 49.0        | 33.5                                    |
| 2        | C.C. = 2.58A                                      | 75  | 100 | 100 | 100 | 100 | 40  | 47.1          | 46.87       | 22.37                                   |
| 3        | C.C. = 2.58 A;<br>P.C.=2.58 A (300s on, 300s off) | 100   | 100 | 100 | 100 | 100 | 100 | 56.32 (P.C.)  | 56.0 (P.C.) | 55.3 (C.C.)                             |

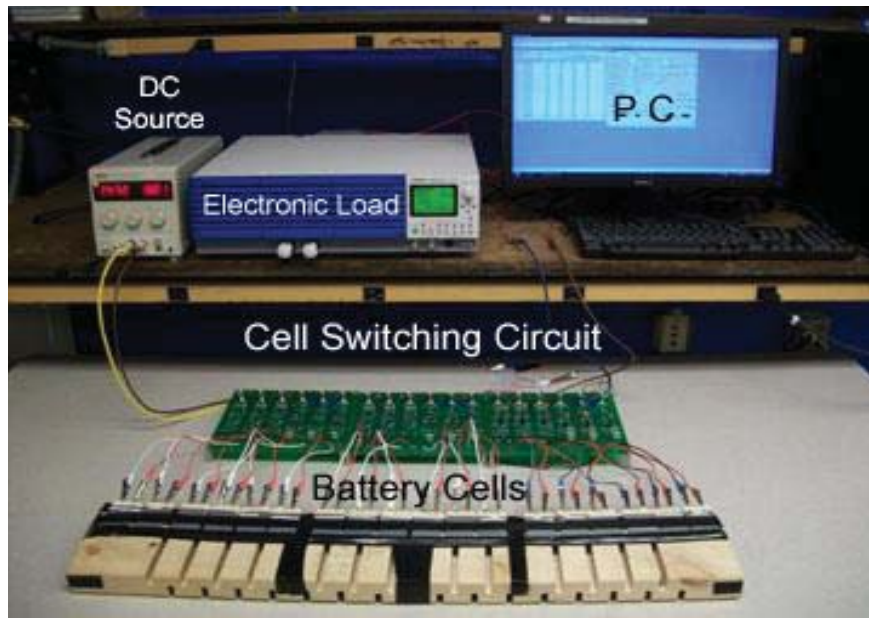


Figure 4.17: The experimental system setup of the self-X battery module.

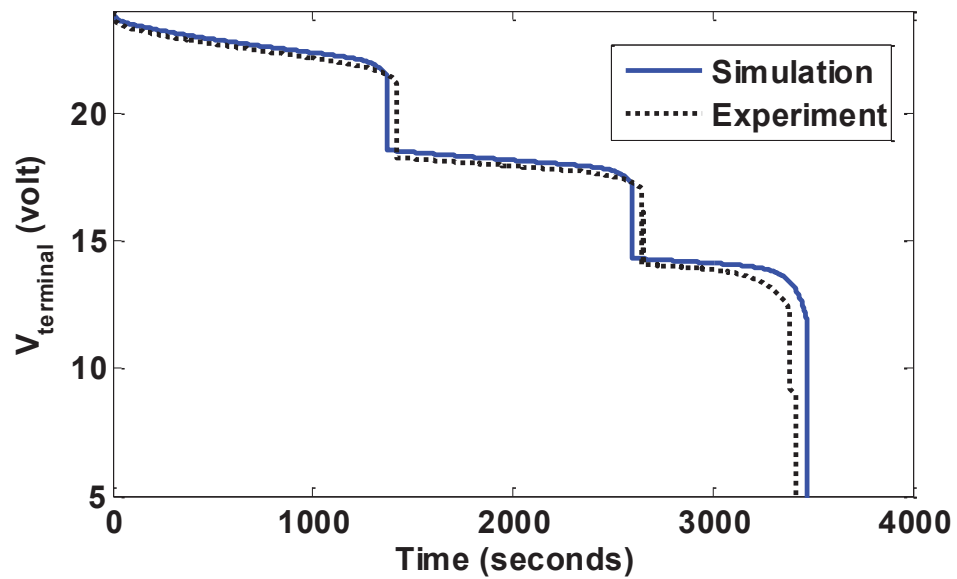


Figure 4.18: Comparison of the terminal voltage responses of the self-X battery module obtained from the simulation and the experiment for Scenario 2.

#### 4.4.2 Module-Level Self-Balancing

The self-X battery model built in MATLAB/Simulink was operated in the discharge mode. The MMS determined that three banks should be used with a discharge current of 2.58 A. It was assumed that all of the 18 cells were healthy; and the initial SOC of the six banks were 100% (Bank 1), 95% (Bank 2), 90% (Bank 3), 85% (Bank 4), 80% (Bank 5), and 75% (Bank 6). Three out of the six banks were discharged simultaneously. An interval of one control cycle was chosen to be  $T_c = 75$  seconds. The battery module was continuously discharged until no bank had usable capacity. Figure 4.19 shows the SOC of the six banks during the whole discharge operation. It clearly shows that the MMS balanced SOC of the cell banks during the battery discharge process. The SOC of the six banks were balanced at about 1000 seconds. This cannot be achieved by using the fixed-configuration design. Figure 4.20 compares the terminal voltage responses of the self-X battery when using different durations for the control cycle. The operating time of the battery increased as the duration of the control cycle decreased. The reason is that the banks became more balanced when a shorter control cycle was used.

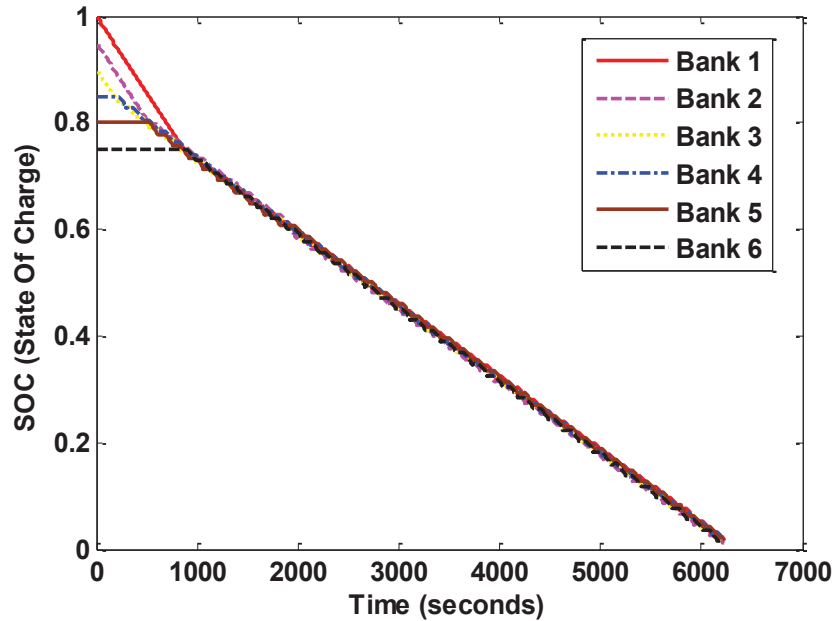


Figure 4.19: The SOC of the cell banks in discharge mode: three banks were used simultaneously.

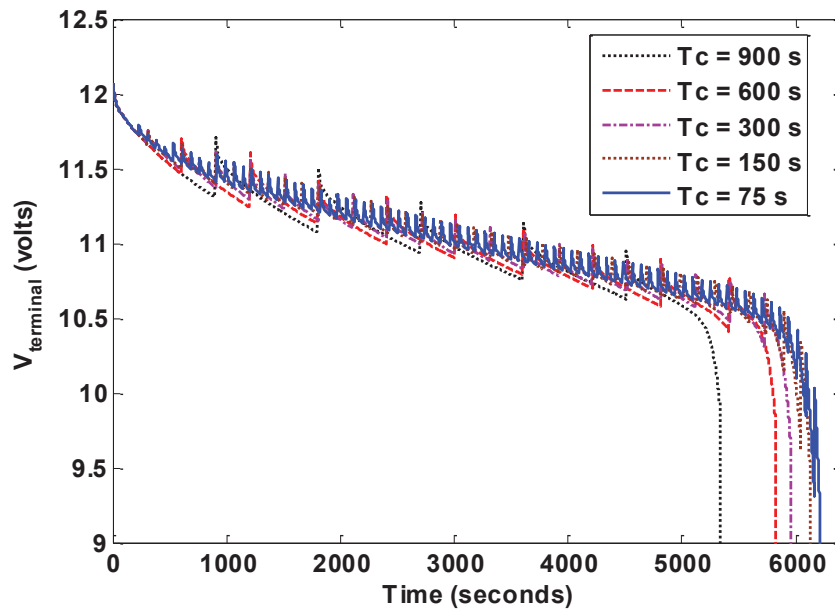


Figure 4.20: Comparison of the terminal voltage responses of the self-X battery module when different durations for the control cycle were used.

A similar test was performed for the self-X battery module operated in the charge mode. The initial SOC of the six banks were 20% (Bank 1), 25% (Bank 2), 30% (Bank 3),

35% (Bank 4), 40% (Bank 5), and 45% (Bank 6). Three out of the six banks were charged simultaneously. The battery was continuously charged with a current of 2.58 A until all of the six banks were fully charged. Figure 4.21 shows the SOC of the six banks during the whole process. The results clearly show that the MMS balanced the SOC of the cell banks during the battery charge process. Again, the SOC of the six banks was balanced at about 1000 seconds.

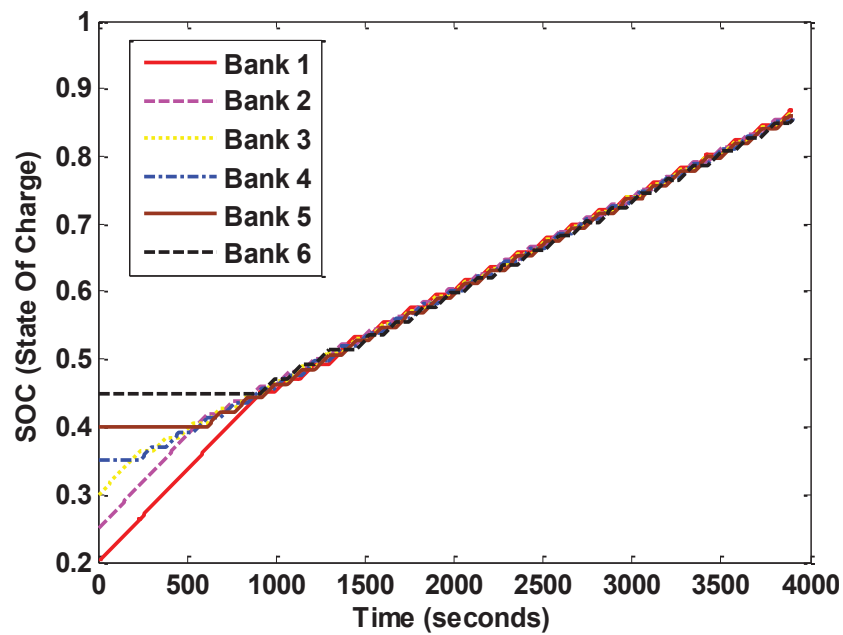
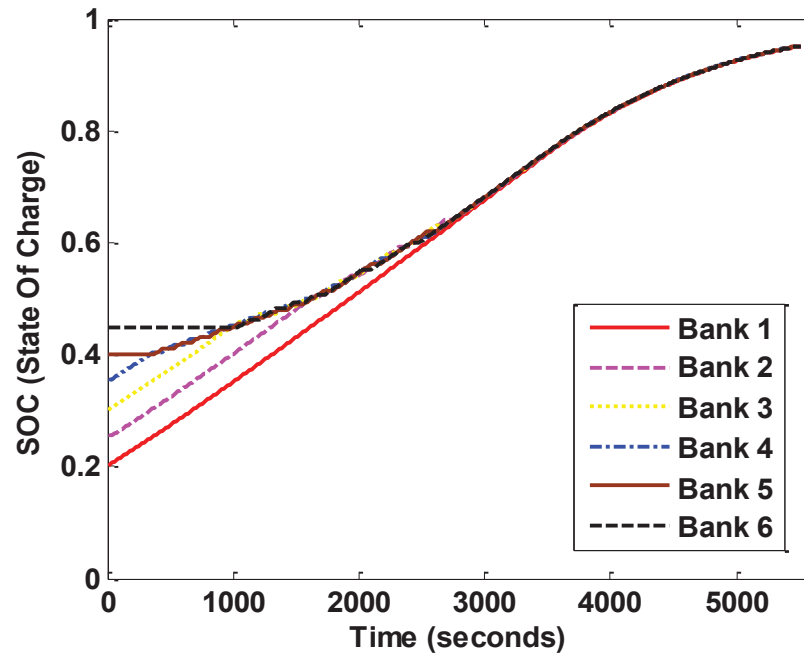


Figure 4.21: The SOC of the cell banks in charge mode: three banks were used simultaneously.

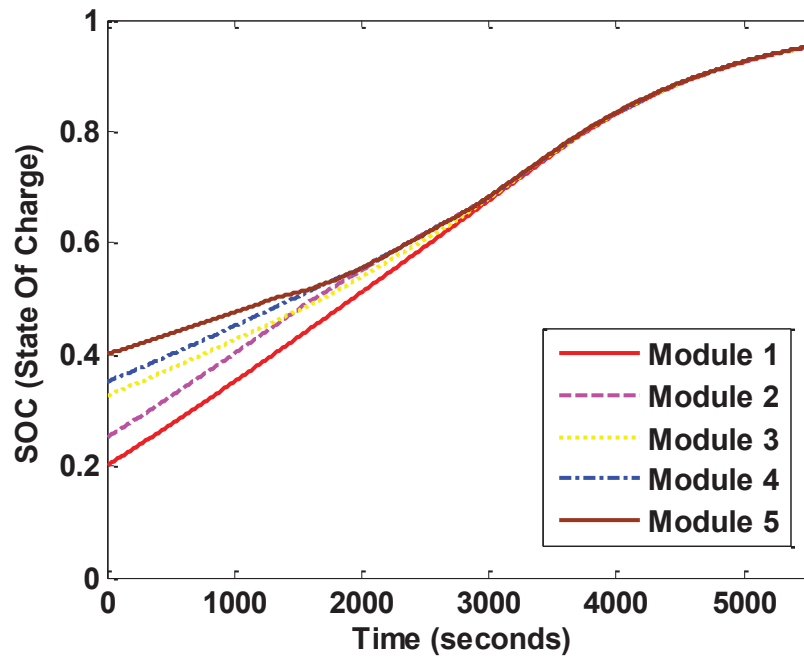
#### 4.4.3 System-Level Simulation with a DC/DC Converter

Five battery modules were connected in series to form a self-X battery system with a bidirectional DC/DC converter where each module had  $6 \times 3$  cells. The system was built and simulated in MATLAB/Simulink. The whole battery system was charged at 4.68 A, the initial SOC of the five modules were assumed to be 20% (Module 1), 25% (Module 2), 32.5%

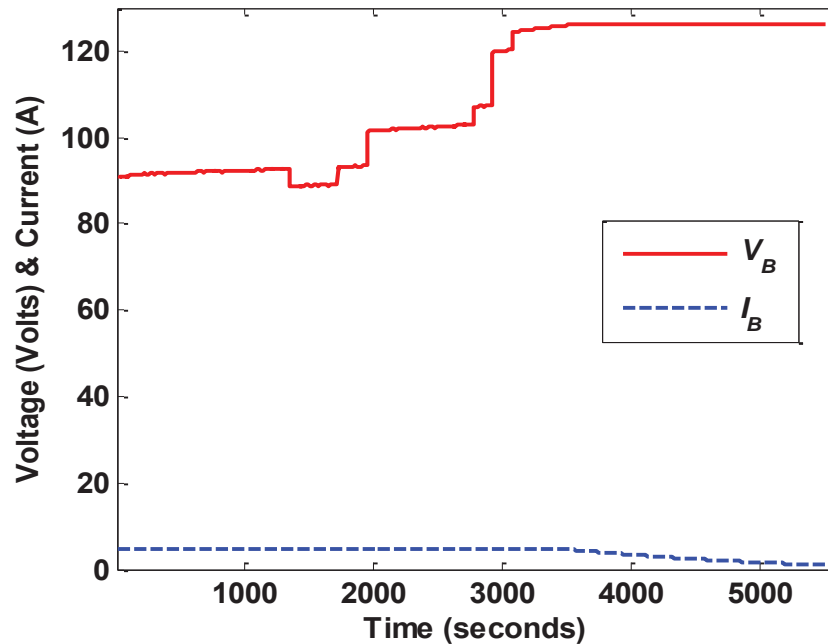
(Module 3), 35% (Module 4), and 40% (Module 5); the initial SOCs of the six banks in Module 3 were 20% (Bank 1), 25% (Bank 2), 30% (Bank 3), 35% (Bank 4), 40% (Bank 5), and 45% (Bank 6). All of the five modules were used simultaneously; while the MBMS and the MMS of each module determined the number of banks used in each module in this charge operation. Figures 4.21(a) and (b) show the SOCs of the six banks in Module 3 and the SOCs of the five modules, respectively, by using the CCCV control. The SOCs of the six banks in Module 3 became balanced at around 2,800 seconds. The SOCs of the five modules became balanced at around 3,100 seconds, as shown in Figure 4.21(b). The cells were fully charged, e.g., 95% for EVs, by using the CCCV control. Figure 4.21(c) shows the terminal voltage and current of the battery system. Under the CCCV charge control, the battery was first charged with a constant current; and the terminal voltage of the battery was increased until it reached the cutoff value of 126 V. However, by that time, the cells had not been fully charged. Therefore, from that moment onward, the battery was charged with an adaptively reduced current at a constant voltage until the SOC of each cell reached 95%. These results clearly demonstrate that the multicell battery design is capable of safe and effective charging, discharging, and balancing operations.



(a)



(b)



(c)

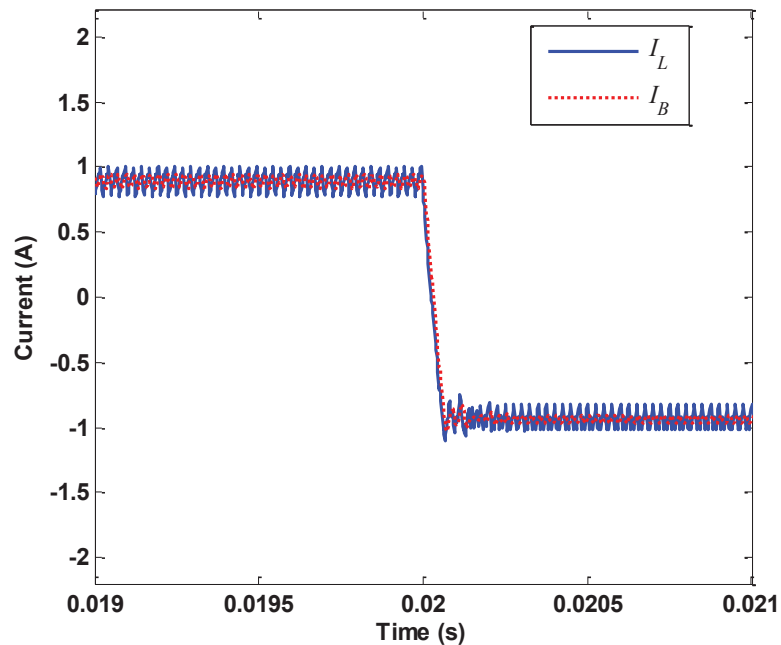
Figure 4.22: The operation of a five-module battery system in the charge mode: (a) the SOCs of the six banks in Module 3; (b) the SOCs of the five modules; and (c) the terminal voltage and charge current of the battery.

#### 4.4.4 Bidirectional DC/DC Converter Simulation

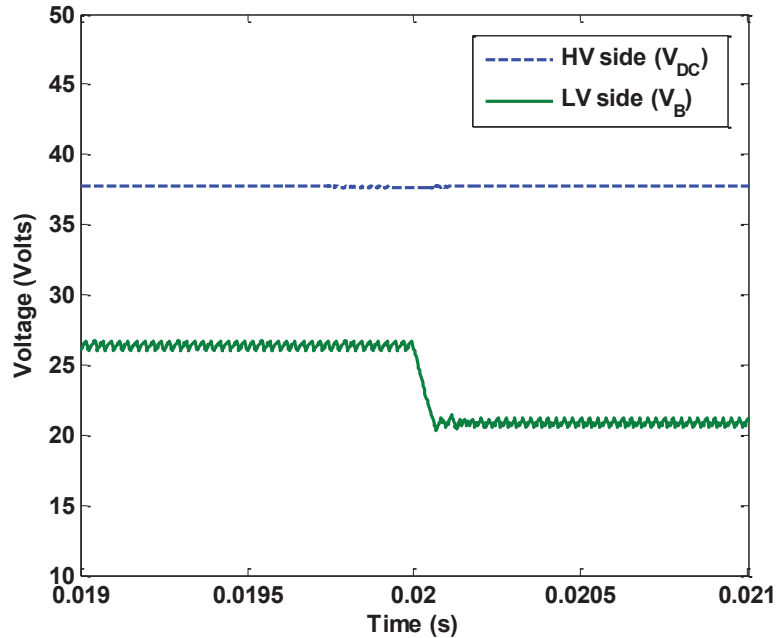
A six-cell, series-connected, self-reconfigurable battery pack with the bidirectional DC/DC converter, discussed in Section 4.3, was built and simulated in MATLAB/Simulink. Each cell was a 3.7 V, 2.6 Ah lithium-ion cell. First, the unified CCAV controller in the bidirectional DC/DC converter was simulated to validate the bidirectional current flow control. The HV side of the DC/DC converter was connected to a 40 V large-capacity battery. The charging current was set to be 1 A, and the discharging current was set to be  $-1$  A. As shown in Figure 4.23(a), the battery current ( $I_B$ ) was stabilized at 1 A when the reference current ( $I_{B\_REF}$ ) of the controller was set at 1 A. The average inductor current ( $I_L$ ) was around 1 A as well. At 20 ms,  $I_{B\_REF}$  was step changed from 1 A to  $-1$  A. Consequently,  $I_B$  changed

from 1 A to  $-1$  A quickly. During the transition, the controller accurately regulated both charge and discharge currents smoothly. The battery terminal voltage also changed smoothly when the operating mode changed, as shown in Figure 4.23(b).

Next, the cell balancing control was tested in charge and discharge modes. In the charge mode, it was assumed that the initial SOCs of Cells 3-5 were all at 35% while the initial SOCs of Cells 1, 2, and 6 were 25%, 30%, and 40%, respectively. The value of  $k_B$  was predetermined to be 5 out of 6 healthy cells. In each control cycle, five cells with the lowest SOCs were selected by using the cell switching circuit and charged at 1.56 A. Figure 4.24(a) shows the SOC of each cell by using the CCAV control. The SOCs of the six cells became balanced at around 3,200 seconds. The cells were fully charged by using the CCAV control. Figure 4.24(b) showed the terminal voltages of Cells 1, 2, and 6, which all reached the charge cutoff voltage of 4.2 V at the end of the charge mode operation.



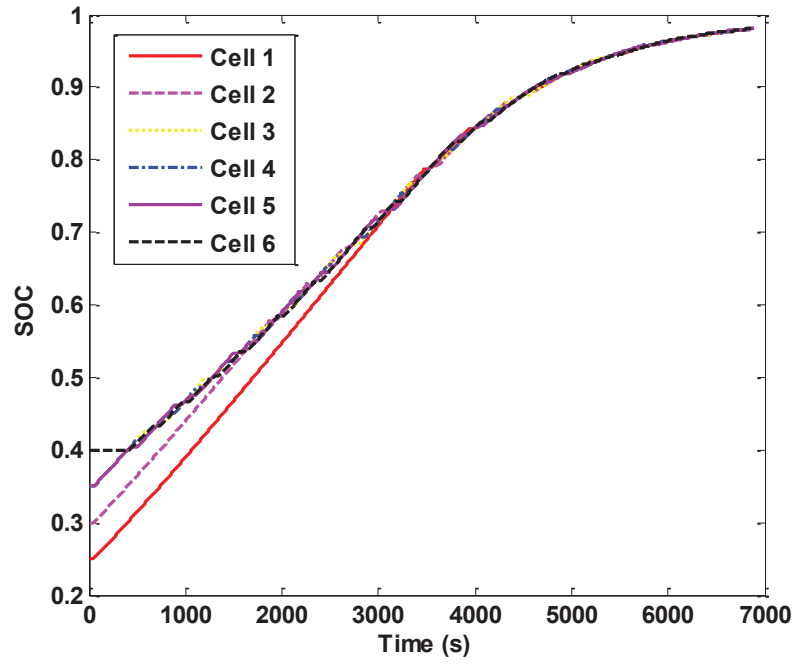
(a)



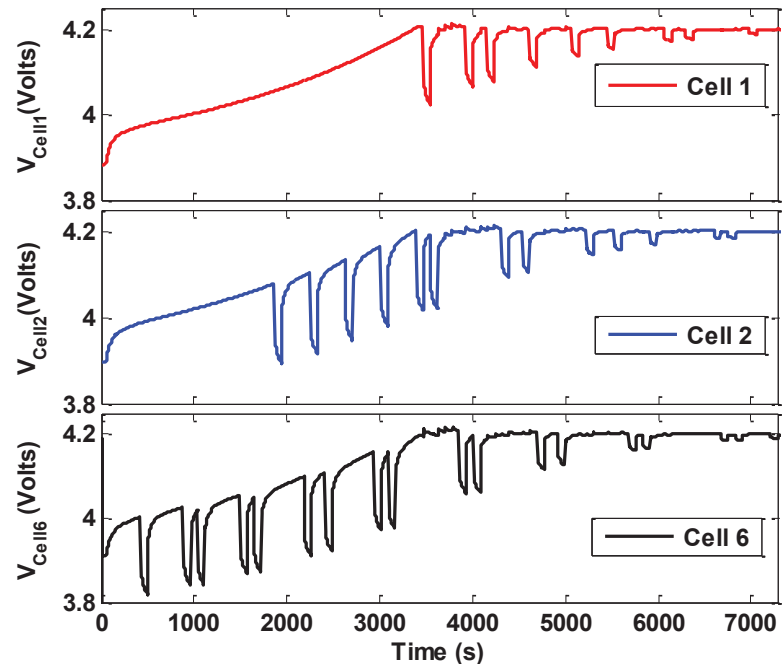
(b)

Figure 4.23: The current flow control between 1 A charge and -1 A discharge: (a) the inductor and battery currents; (b) the HV-side and LV-side (battery terminal) voltages.

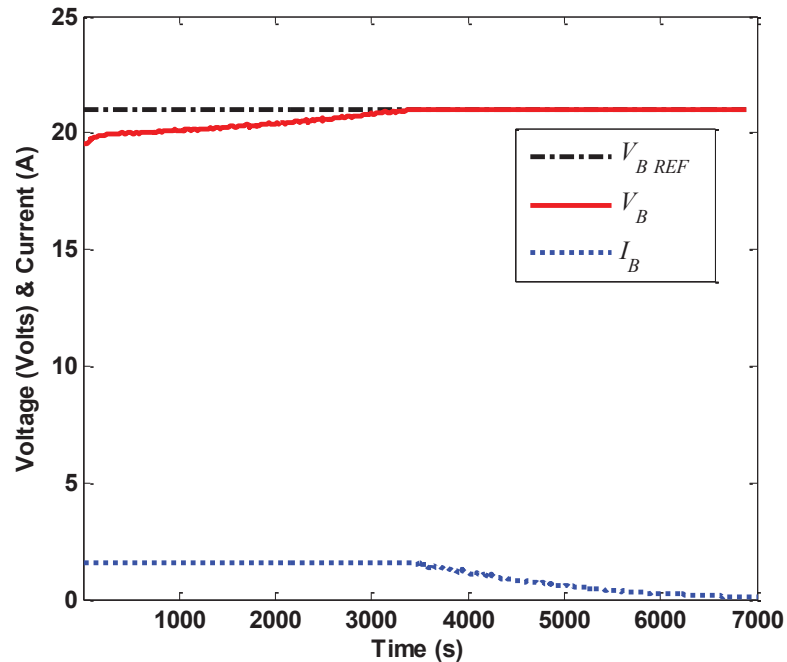
Figure 4.24(c) shows the terminal voltage and current of the battery pack. Under the CCAV charge control, the battery was first charged with a constant current; and the terminal voltage of the battery increased until it reached the cutoff value of 21 V, since five cells were always connected in series and charged simultaneously. However, by that time, the cells had not been fully charged. Therefore, from that moment onward, the battery was charged with an adaptively reduced current and a constant voltage until the SOC of each cell reached 100%. These results clearly demonstrate that the proposed series-connected, self-reconfigurable multicell battery with a bidirectional DC/DC converter is capable of safe and effective charging, discharging, and balancing operations.



(a)



(b)



(c)

Figure 4.24: Cell balancing control in the charge mode: (a) the SOC of each cell; (b) the terminal voltage of Cell 1, 2, and 6; (c) the terminal voltage and charge current of the battery.

#### 4.4.5 Efficiency Analysis for Cell Switching Circuit

Compared to the traditional fixed-configuration design, the self-X design caused additional power losses to the battery system due to the cell switching circuit. An efficiency analysis was performed for the cell switching circuit to further validate the proposed design. The total power loss of the cell switching circuit included the losses in the MOSFET switching circuit and the gate drive circuits. The power losses in the MOSFET switching circuit included the conduction and switching losses of the power MOSFETs. The switching losses were neglected because it typically takes a long time for a MOSFET to change its state, as mentioned in Chapter 4.1. The conduction losses depend on the current flowing through the battery cell and power MOSFET. The power losses of the gate drive

circuit (see Figure 4.3(a)) depend on the small-signal components in the circuit and the current of the battery cell. The small-signal components were appropriately chosen to ensure that the energy consumption of the gate drive circuit was negligible compared to the energy flow in the cell. The parameters of the small-signal components are listed in the Appendix.

Figure 4.25 shows the experimental results of the normalized power losses of the MOSFET switching circuit and the gate drive circuit as well as the normalized total power loss of the cell switching circuit as functions of the discharge current for a single 3.7 V, 0.86 Ah polymer lithium-ion cell of the  $6 \times 3$ -cell self-X battery module. The current was normalized to the capacity of the cell, i.e., the C-rate. The power losses were normalized to the power output of the cell. The results show that the normalized power loss of the MOSFET switching circuit increased linearly with the cell current. On the other hand, the normalized power loss in the gate drive circuit decreased with the discharge current. At low currents, the power loss of the gate drive circuit was dominant and the normalized total power loss reduced as the cell current was increased. When the current was higher than 0.5C, the power loss in the MOSFET switching circuit became dominant; and the normalized total power loss was increased gradually.

Large-scale battery systems, such as those used for vehicle and power grid energy storage, usually employ large capacity cells. Figure 4.26 compares the round-trip efficiency as a function of the normalized discharge current for 0.86, 5, 10, and 20 Ah polymer lithium-ion cells. The efficiency of the cell switching circuit decreased with an increase in cell capacity. However, even for 20 Ah cells, the round-trip efficiency of the cell switching circuit was still higher than 99% over the entire operating current range of the cell. The

efficiency can be further improved by several approaches: 1) using power MOSFETs with a lower on resistance; 2) using multiple power MOSFETs connected in parallel to form a switch of the cell switching circuit in Figure 4.2 to share the corresponding cell current; and 3) applying the switching circuit to battery modules instead of cells, where each module consists of multiple cells connected in series.

Therefore, it is not a problem for the cell switching circuit to achieve a round trip efficiency of over 99% for the battery systems with large-capacity cells, which is common in power and energy system applications. These results indicate that the self-X battery design does not reduce the efficiency of the battery systems for power and energy system applications.

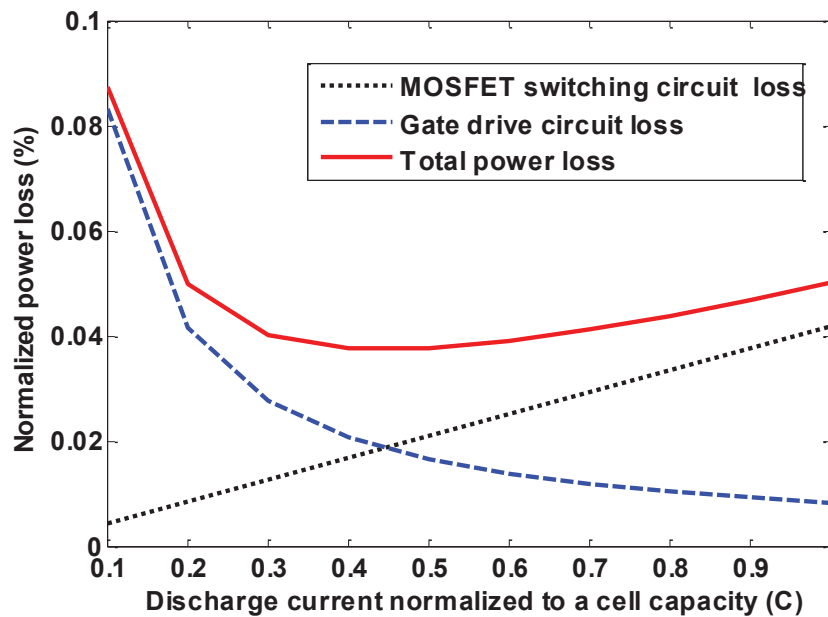


Figure 4.25: Normalized power losses of the cell switching circuit as functions of normalized discharge current for a single 3.7 V, 0.86 Ah polymer lithium-ion cell.

In addition to the losses in the cell switching circuit, other losses of the battery system included the losses in the sensing and monitoring circuit as well as the control and protection circuit. These losses were almost constant and did not depend on the capacity of the battery cells or the operating conditions of the battery system. For battery systems using large-capacity cells, these losses were negligible compared to the power of the battery systems. Moreover, these losses were also present in traditional fixed-configuration battery systems. Therefore, they are not discussed in this dissertation.

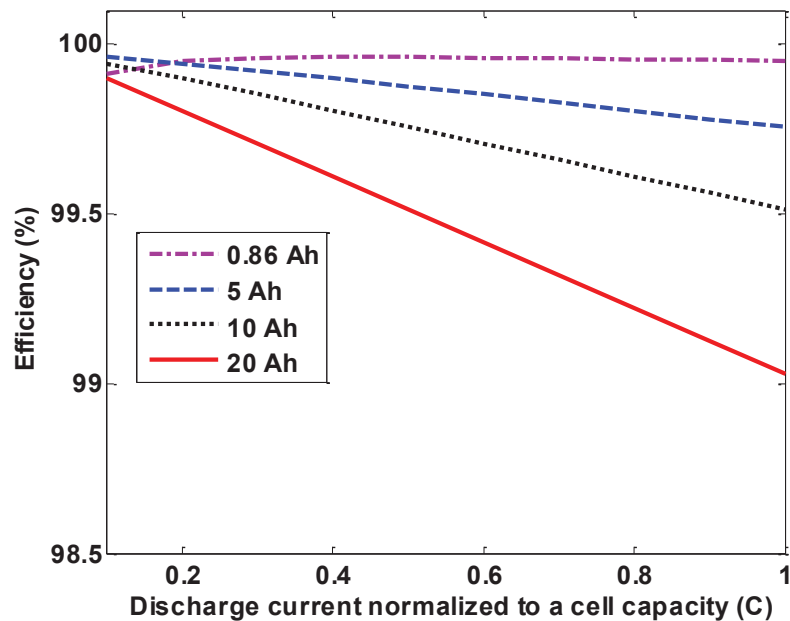


Figure 4.26: Comparison of the round-trip efficiency of the cell switching circuit as a function of normalized discharge current for 0.86 Ah, 5 Ah, 10 Ah, and 20 Ah polymer lithium-ion cells.

## 4.5 Chapter Summary

This chapter presented a novel power-electronics-enabled, self-X, multicell battery design for managing multicell battery modules and battery systems consisting of multiple multicell battery modules. The self-X multicell battery can automatically configure itself according to the dynamic load/storage demand and the condition of each cell, self-heal from failures and abnormal operating conditions of single or multiple cells, self-balance from cell state variations, and self-optimize to achieve the improved energy conversion efficiency. These features are achieved by: 1) a highly efficient cell switching circuit; 2) high-performance condition monitoring and control system; and 3) a bidirectional DC/DC converter with a unified CCAV control scheme.

Simulation and experimental results showed a remarkably improved energy usage, reliability, and energy conversion efficiency of multicell batteries using the proposed self-X design. The self-X design is universal and can be applied to any type and size of battery cells. By using the self-X design, additional monitoring, control, protection, and optimization functions can be readily added to each cell and the overall battery system, leading to a smart battery.

## CHAPTER 5: PARTICLE SWARM OPTIMIZATION-BASED ELECTRICAL PARAMETER AND SOC ESTIMATION

This chapter describes a cell-level SOC and electrical parameter estimation method for multicell lithium-ion batteries [87], [103]. An enhanced Coulomb-counting algorithm was applied to estimate the SOC for each cell. An SOC compensator was designed to sequentially correct the error of the estimated SOC for each cell by using the estimated cell open-circuit voltage  $V_{oc}$ . The values of  $V_{oc}$  and electrical parameters of the cells were estimated sequentially in real-time by using a particle swarm optimization (PSO)-based online parameter identification algorithm. Therefore, the method is capable of capturing nonlinear capacity effects of a battery and ensuring the robustness of the SOC estimation to unknown initial SOC, error accumulation, and the error due to neglect of the self-discharge effect. The method was validated by using simulation and experimental results for a four-cell polymer lithium-ion battery pack.

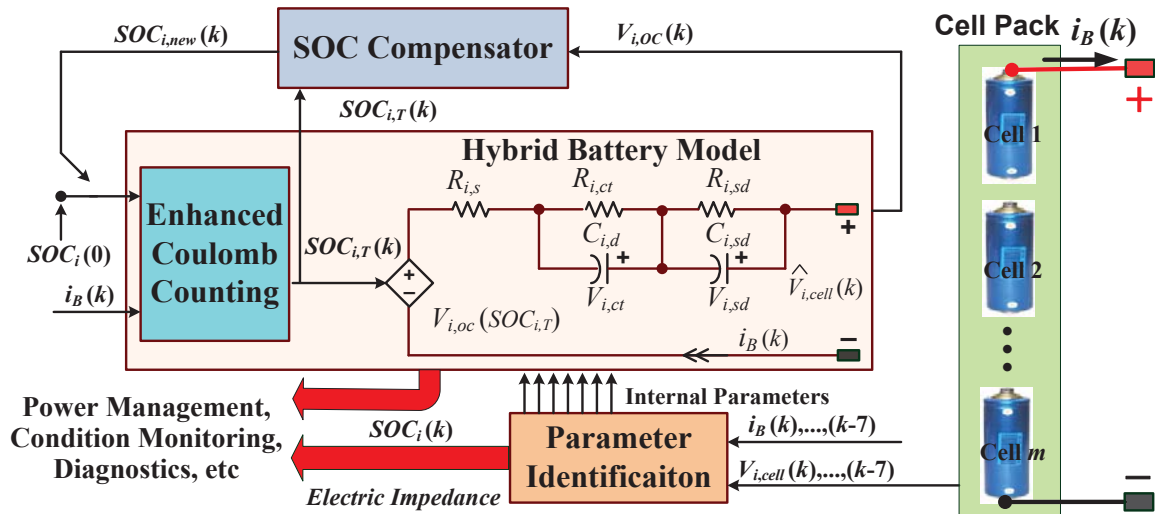


Figure 5.1: The proposed PSO-based SOC and electrical parameter estimation method for a series-connected  $m$ -cell battery pack.

The SOC and electrical parameter estimation method for multicell batteries consisted of three parts as shown in Figure 5.1: a hybrid battery model, a PSO-based parameter identification algorithm, and an SOC compensator correcting the error of the enhanced Coulomb-counting-based SOC estimation. The method estimated the SOC and electrical parameters sequentially for each cell of a series-connected  $m$ -cell pack.

### 5.1 Hybrid Battery Model for Model-Based Condition Monitoring

The enhanced Coulomb-counting algorithm was designed to estimate the SOC of a battery cell in (3-8) and (3.9). The enhanced Coulomb-counting algorithm for Cell  $i$ , (where  $i = 1, \dots, m$ ) is shown below:

$$SOC_{i,T}(k) = \frac{C_{i,available}(k)}{C_{i,max}} = SOC_{i,T}(k-1) - \frac{1}{C_{i,max}} [i_B(k-1) \cdot T_s + \Delta C_{i,unavailable}(k-1)] \quad (5-1)$$

$$C_{i,unavailable}(k) = C_{i,unavailable}(k-1) \cdot e^{-kT_s} + (1-c) \frac{(1-e^{-kT_s})}{c \cdot k'} \times i_B(k) \quad (5-2)$$

The electrical circuit battery model (i.e., the electrical circuit in the hybrid battery model in Figure 5.1) of Cell  $i$  can be expressed in a regression form as follows:

$$\begin{bmatrix} V_{i,ct}(k) \\ V_{i,sd}(k) \end{bmatrix} = \begin{bmatrix} x_1 & 0 \\ 0 & x_3 \end{bmatrix} \cdot \begin{bmatrix} V_{i,ct}(k-1) \\ V_{i,sd}(k-1) \end{bmatrix} + \begin{bmatrix} x_2 \\ x_4 \end{bmatrix} \cdot i_B(k-1) \quad (5-3)$$

where

$$x_1 = e^{\frac{-T_s}{\tau_{i,S}}}, \quad x_2 = R_{i,ct} \cdot (1 - e^{\frac{-T_s}{\tau_{i,S}}}), \quad x_3 = e^{\frac{-T_s}{\tau_{i,L}}}, \quad x_4 = R_{i,sd} \cdot (1 - e^{\frac{-T_s}{\tau_{i,L}}}) \quad (5-4)$$

$$V_{i,cell}(k) = V_{i,oc}(k) - R_{i,s} \cdot i_B(k) - V_{i,ct}(k) - V_{i,sd}(k) \quad (5-5)$$

where  $\tau_{i,S} = R_{i,ct} \cdot C_{i,d}$  and  $\tau_{i,L} = R_{i,sd} \cdot C_{i,sd}$ . Assuming that  $V_{i,oc}$  is a constant, the z-transfer function of (5-5) is given in (5-6) and the corresponding difference equation is given in (5-

7). The battery electrical parameters can be derived from (5-4), (5-7) and (5-8) if  $V_{i,cell}$  and  $i_B$  are known.

$$\frac{V_{i,oc} - V_{i,cell}(z)}{i_B(z)} = \frac{b_0 - b_1 z^{-1} + b_2 z^{-2}}{1 - a_1 z^{-1} + a_2 z^{-2}} \quad (5-6)$$

$$\begin{aligned} V_{i,cell}(k) = & a_1 \cdot V_{i,cell}(k-1) - a_2 \cdot V_{i,cell}(k-2) - b_0 \cdot i_B(k) \\ & + b_1 \cdot i_B(k-1) - b_2 \cdot i_B(k-2) + [1 - a_1 + a_2] \cdot V_{i,oc} \end{aligned} \quad (5-7)$$

where,

$$\begin{aligned} a_1 = (x_1 + x_3), \quad a_2 = x_1 x_3, \quad b_1 = R_{i,s}(x_1 + x_3) - (x_2 + x_4) \\ b_0 = R_{i,s}, \quad \text{and} \quad b_2 = R_{i,s} x_1 x_3 - (x_1 x_4 + x_2 x_3) \end{aligned} \quad (5-8)$$

## 5.2 Electrical Parameter Identification by PSO

The PSO method was employed to identify the electrical parameters of the hybrid battery model. The PSO method can find the global optimal solution with a high computational efficiency and a low implementation cost. The battery's electrical parameters include the OCV,  $V_{oc}$ , and RC parameters,  $R_s$ ,  $R_{ct}$ ,  $C_d$ ,  $R_{sd}$ , and  $C_{sd}$ , which are unknown variables of (5-7). At least six independent equations are needed to solve for the six unknown parameters. The six equations can be obtained from (5-7) by using measured battery cell terminal voltage and current at eight sequential operating points, as follows:

$$\begin{aligned} F_j(X) = & V_{i,cell}(k-j) - (x_1 + x_3)V_{i,cell}(k-1-j) + x_1 \cdot x_3 \cdot V_{i,cell}(k-2-j) \\ & + i_B(k-j) \cdot R_{i,s} - [R_{i,s}(x_1 + x_3) - (x_2 + x_4)] \cdot i_B(k-1-j) \\ & + [R_{i,s}(x_1 \cdot x_3) - (x_1 \cdot x_4 + x_2 \cdot x_3)] \cdot i_B(k-2-j) - [1 - (x_1 + x_3) + x_1 \cdot x_3] \cdot V_{i,oc} \end{aligned} \quad (5-9)$$

where  $j = 0, \dots, n, n \geq 5$ ; and  $X = [x_1, x_2, x_3, x_4, R_s, V_{oc}]$  is a vector of the unknown parameters.

The PSO algorithm is designed to search for the optimal  $X$  to minimize the value of the following fitness function.

$$P_{ps0}(X) = \sum_{j=0}^n |F_j(X)| \quad (5-10)$$

Theoretically, the optimal  $X$  should make the fitness function value zero. In practice, once the value of  $P_{ps0}(X)$  is below a predefined small threshold, e.g.,  $10^{-6}$ , the corresponding  $X$  can be treated as the optimal solution. From the optimal solution of  $X$ , the electrical parameters can be calculated from (5-8).

The PSO algorithm searches for the optimal solution using a population of moving particles. Each particle has a position represented by a position vector ( $X_i$ ) and a moving velocity represented by a velocity vector ( $V_i$ ) in the problem space. The position of each particle represents a potential solution. Each particle keeps track of its coordinates in the problem space, which are associated with the individual best position ( $X_{i,pbest}$ ) achieved by the particle so far. Furthermore, the best position among all the particles obtained so far in the population is tracked by all particles as the global best position ( $X_{gbest}$ ). The PSO algorithm is implemented in the following iterative steps for electrical parameter estimation of a battery:

- (i) Define the problem space with its boundaries extracted from off-line battery tests under various operating conditions.
- (ii) Initialize a population of particles with random positions and velocities in the problem space.
- (iii) Evaluate the fitness function.
- (iv) Compare each particle's current position  $X_i$  with its  $X_{i,pbest}$  based on the fitness evaluation. If  $X_i$  is better than  $X_{i,pbest}$ , then replace  $X_{i,pbest}$  with  $X_i$ .

- (v) If  $X_{i,pbest}$  is updated, then compare the particle's  $X_{i,pbest}$  with  $X_{gbest}$  based on the evaluation of the fitness function. If  $X_{i,pbest}$  is better than  $X_{gbest}$ , then replace  $X_{gbest}$  with  $X_{i,pbest}$ .
- (vi) Compute each particle's new velocity ( $V_i$ ) and position at iteration  $k$  as follows:

$$V_i(k+1) = w_{in}V_i(k) + c_1r_1(X_{i,pbest}(k) - X_i(k)) + c_2r_2(X_{gbest}(k) - X_i(k)), \quad i = 1, 2, \dots, N \quad (5-11)$$

$$X_i(k+1) = X_i(k) + V_i(k+1), \quad i = 1, 2, \dots, N \quad (5-12)$$

- (vii) Repeat Steps (iii)-(vi) until the stopping criterion is satisfied, e.g., an error threshold is reached or the maximum number of iterations is accomplished. The final value of  $X_{gbest}$  is the optimal solution to the problem.

In (5-11),  $c_1$  and  $c_2$  are the cognition learning rate and social learning rate of particles, respectively;  $w_{in}$  is the inertial weight which decreases as the number of iterations increases;  $r_1$  and  $r_2$  are uniformly distributed random numbers between 0 and 1; and  $N$  is the number of particles in the swarm. The set of parameters for the PSO implementation used in this dissertation are listed in Table 5.1.

Due to slow changes in the electrical parameters, the final solution  $X$  in each execution of the PSO algorithm, instead of random numbers, will be used as the initial positions for the population of particles in the next execution of the PSO algorithm. This will reduce the number of iterations needed to identify the optimal solution. Moreover, it is important to choose appropriate boundary conditions for position  $X$  and velocity  $V$  in the PSO algorithm. The electrical parameters of the battery cells extracted from off-line battery

tests under various operating conditions will be used to set the boundary conditions for  $X$  and  $V$ . The adaptive boundary condition, shown in Table 5.2, is proposed for  $V_{oc}$  to improve the accuracy of the parameter estimation, where  $V_{oc\_max}$  and  $V_{oc\_min}$  are the maximum and minimum possible  $V_{oc}$ , respectively;  $\phi$ ,  $\alpha$ , and  $\beta$  are the rest, discharge, and charge constants, respectively;  $\Delta V_{cell}$  is the variation of  $V_{cell}$  during the rest time; and  $i_{rated}$  is the rated current (i.e., 1C). The inverse hyperbolic sine function is used to express the transient voltage in terms of the current rate during charge and discharge [104].

Table 5.1: Set of Parameter for PSO implementation.

|                    |       |            |       |                  |       |
|--------------------|-------|------------|-------|------------------|-------|
| Swarm Size ( $N$ ) | 20    | $c_1$      | 2     | $w_{in}$ (start) | 0.7   |
| Iteration          | 1000  | $c_2$      | 2     | $w_{in}$ (end)   | 0.1   |
| $\alpha_1$         | 0.198 | $\alpha_2$ | 0.118 | $\beta_1$        | 0.188 |
| $\beta_2$          | 0.104 | $\phi$     | 0.001 |                  |       |

Table 5.2: Boundary condition of  $V_{oc}$ .

|                             |                  |  |
|-----------------------------|------------------|--|
| $i_B(k) > 0$<br>(Discharge) | $V_{oc\_max}(k)$ | $V_{cell}(k) + \alpha_1 \cdot \sinh^{-1}(i_{cell}(k)/i_{rated})$ |
|                             | $V_{oc\_min}(k)$ | $V_{cell}(k) + \alpha_2 \cdot \sinh^{-1}(i_{cell}(k)/i_{rated})$ |
| $i_B(k) < 0$<br>(Charge)    | $V_{oc\_max}(k)$ | $V_{cell}(k) + \beta_1 \cdot \sinh^{-1}(i_{cell}(k)/i_{rated})$  |
|                             | $V_{oc\_min}(k)$ | $V_{cell}(k) + \beta_2 \cdot \sinh^{-1}(i_{cell}(k)/i_{rated})$  |
| $i_B(k) = 0$<br>(Rest)      | $V_{oc\_max}(k)$ | $V_{oc\_max}(k-1)$   |
|                             | $V_{oc\_min}(k)$ | $V_{oc\_min}(k-1)$   |
|                             | $V_{oc\_max}(k)$ | $V_{cell}(k), \quad \text{if } \Delta V_{cell}(k) < \phi$        |
|                             | $V_{oc\_min}(k)$ |  |

### 5.3 SOC Estimation and Compensation

The enhanced Coulomb-counting method, based on (5-1) and (5-2), is an open-loop SOC estimation method. It may be subject to problems which include an inaccurate initial

SOC and accumulating estimation errors, leading to a wrong SOC estimation. To solve these problems, this dissertation proposes a closed-loop weighting SOC estimation method, which uses an SOC compensator to correct the error of the SOC, i.e.,  $SOC_{i,T}$ , obtained from the enhanced Coulomb-counting algorithm for each cell in the pack sequentially, as shown in Figure 5.2. The corresponding equations are given by the following:

$$SOC_{i,new}(k) = W \cdot SOC_{i,T}(k) + (1 - W) \cdot SOC_{i,V}(k) \quad (5-13)$$

$$SOC_i(k-1) = SOC_{i,new}(k-1) \quad (5-14)$$

where  $W$  is a variable weighting factor ( $0 < W < 1$ ); and  $SOC_{i,V}$  is the SOC estimated from the OCV,  $V_{i,oc}$ , of Cell  $i$ , which in turn is estimated from the PSO-based parameter identification algorithm for the electrical circuit model of the battery cell and the measured cell current and terminal voltage. The SOC compensator uses the estimated  $V_{i,oc}$  and the  $SOC_{i,T}$  as the inputs. The  $V_{i,oc}$  is converted to the  $SOC_{i,V}$  by using a SOC- $V_{oc}$  lookup table because the OCV is highly related to the SOC. In practice, the SOC- $V_{oc}$  relationship can be obtained from laboratory experiments. The  $SOC_{i,V}$  and  $SOC_{i,T}$  are multiplied by their weighting factors and then added together to generate a compensated SOC, i.e.,  $SOC_{i,new}$ . The  $SOC_{i,new}$  is then used as the initial SOC, i.e.,  $SOC_i$ , of the enhanced Coulomb-counting algorithm to estimate the SOC in the next time step.

The SOC compensator is executed periodically at a certain interval during operation or during a long relaxation period of the battery cell. The performance of the SOC compensator highly depends on the accuracy of the internal electrical parameters of the battery and the weighting factor  $W$ . The default value of  $W$  is one only when the enhanced Coulomb counting algorithm is used for SOC estimation. The value of  $W$  is changed when the SOC compensator is used. In this dissertation,  $W$  is set to be 0.5 once the SOC

compensator is activated. Moreover, when the battery is operated for a long time in relaxation mode, the  $SOC_{i,V}$  will be close to the real SOC. In this case, the weighting factor  $W$  will be set to zero. When  $W$  is zero and the battery is operated in the charge/discharge mode again, the execution of the SOC compensator will be over; and  $W$  will be reset to one.

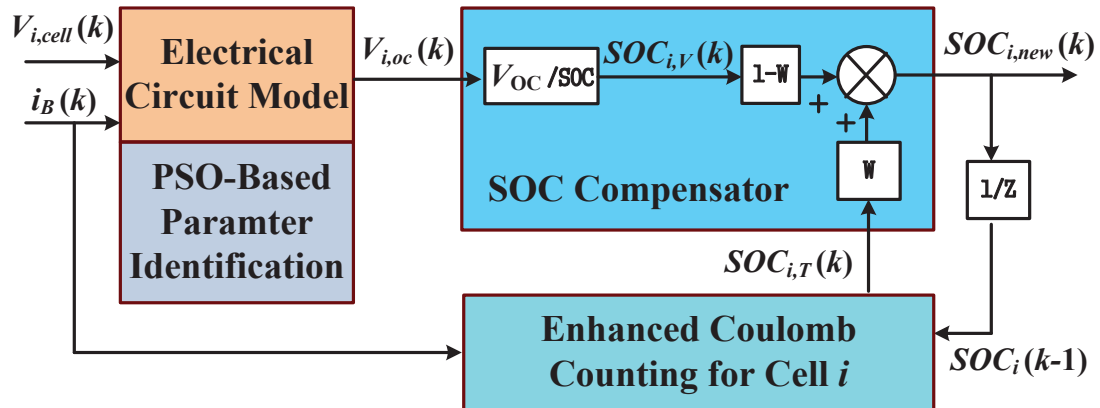


Figure 5.2: The proposed closed-loop weighting SOC estimation algorithm.

## 5.4 Validation

The proposed electrical parameter and SOC estimation method was validated by simulation and experimental data for a four-cell polymer lithium-ion pack. The nominal capacity, nominal voltage, and cutoff voltage of a single cell were 860 mAh, 3.7 V, and 3 V, respectively (see Appendix). The experimental data for the cell voltage and current were collected from a CADEX battery tester C8000 (shown in Figure 5.3) under ambient temperature. The method shown in Figure 5.1 was implemented in MATLAB/Simulink on a laptop computer (see Figure 5.3). The measured cell voltage and current from the battery tester were used for real-time SOC and electrical parameter estimation for each individual battery cell. The parameters of the electrical circuit battery model were first extracted offline

for each battery cell by using the method described in [27]. These parameters were then used as the true values for comparison with those obtained from the method in real time.

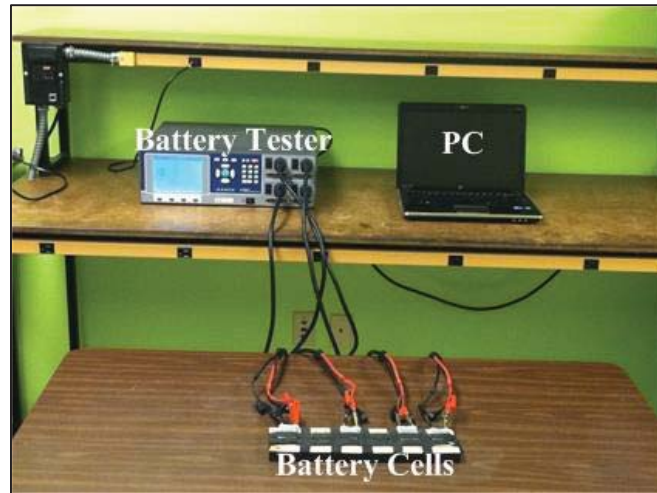
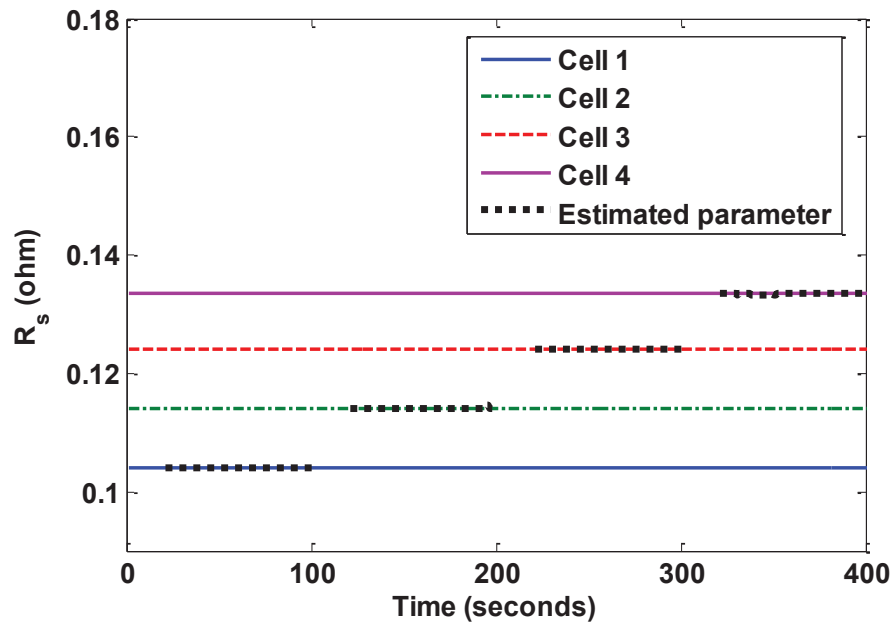


Figure 5.3: The experimental setup for electrical parameter and SOC estimation.

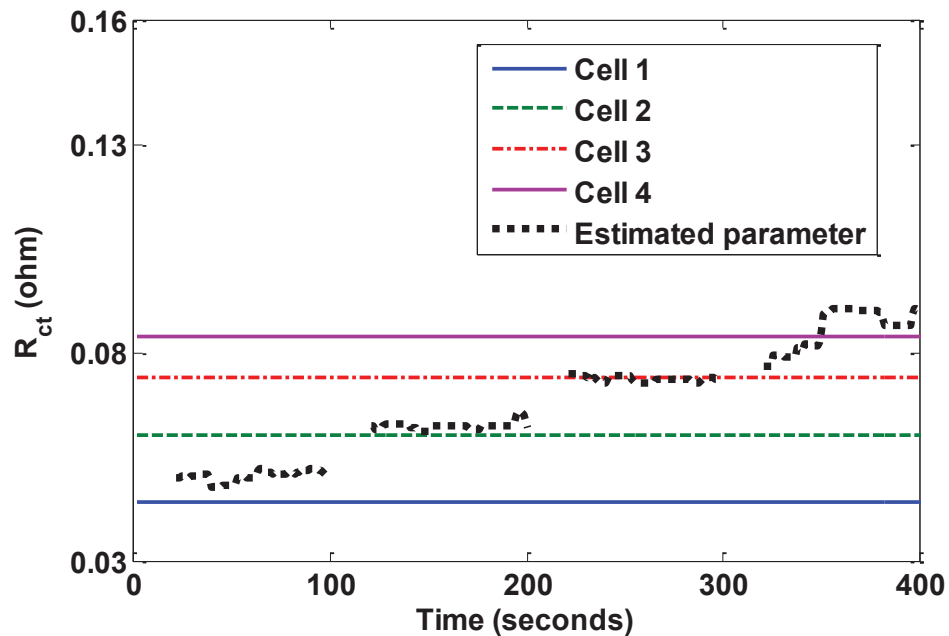
Figure 5.4(a)-(e) compares the RC parameters of the hybrid battery model for each cell estimated by using the proposed online parameter identification algorithm with their true values. The impedances for the four battery cells were estimated online for a dynamic current cycle shown in Figure 5.4(f). The parameter identification algorithm was executed 100 seconds sequentially for each cell. The results show that the parameter identification algorithm estimates the cell parameters quickly and accurately.

Next, the SOC estimation algorithm was investigated with a wrong initial SOC of 50% for all of the four cells in the battery pack. The real initial SOC of Cells 1, 2, 3, and 4 are 90, 80, 70, and 60%, respectively. The multicell battery pack was operated with a dynamic current cycle, as shown in Figure 5.4(f). The SOC compensator was executed 100 seconds sequentially for each cell to correct its SOC. Figure 5.5 compares the SOC estimated by the proposed method with those measured by the battery tester. The estimated

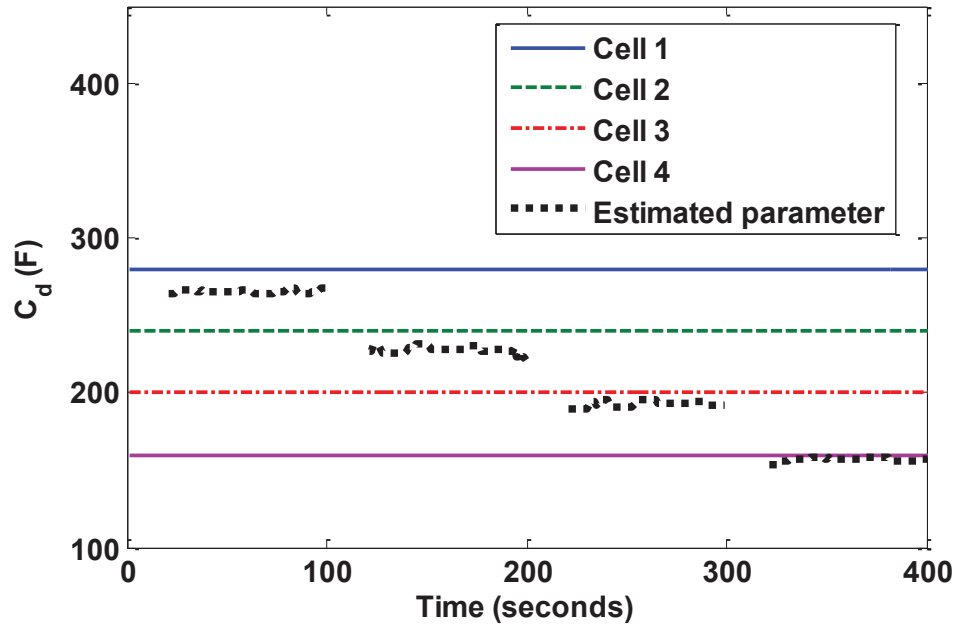
SOC of each cell matched the measured value well even though the initial SOC was set wrong using the method. This result clearly shows that the algorithm is robust to the error of initial SOC, which however is important to the accuracy of the traditional Coulomb counting method.



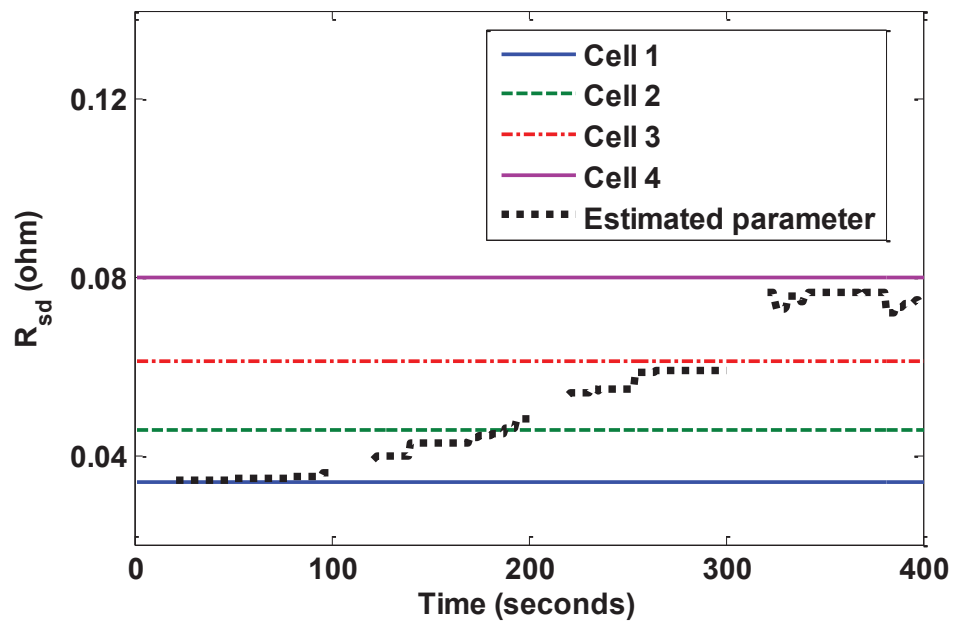
(a)



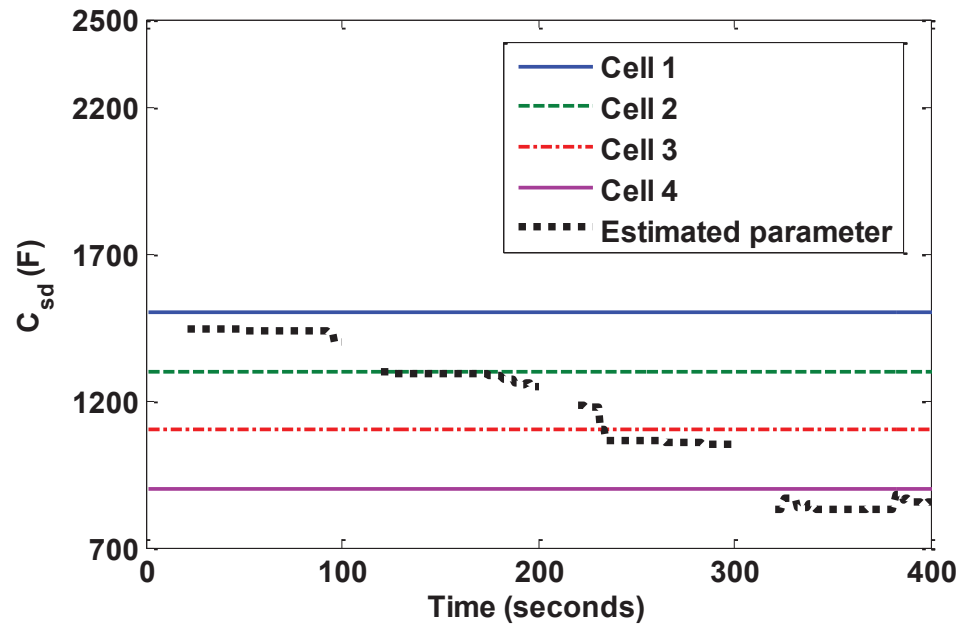
(b)



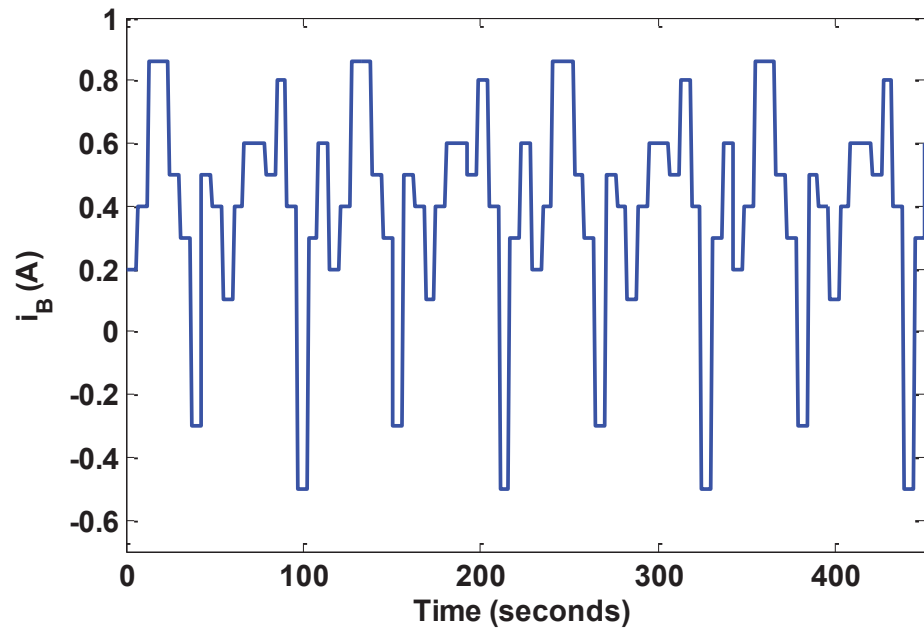
(c)



(d)



(e)



(f)

Figure 5.4: Comparison of true and estimated RC parameters of the hybrid battery model for the four cells: (a)  $R_s$ , (b)  $R_{ct}$ , (c)  $C_d$ , (d)  $R_{sd}$ , (e)  $C_{sd}$ , and (f) the dynamic current cycle applied to the battery pack.

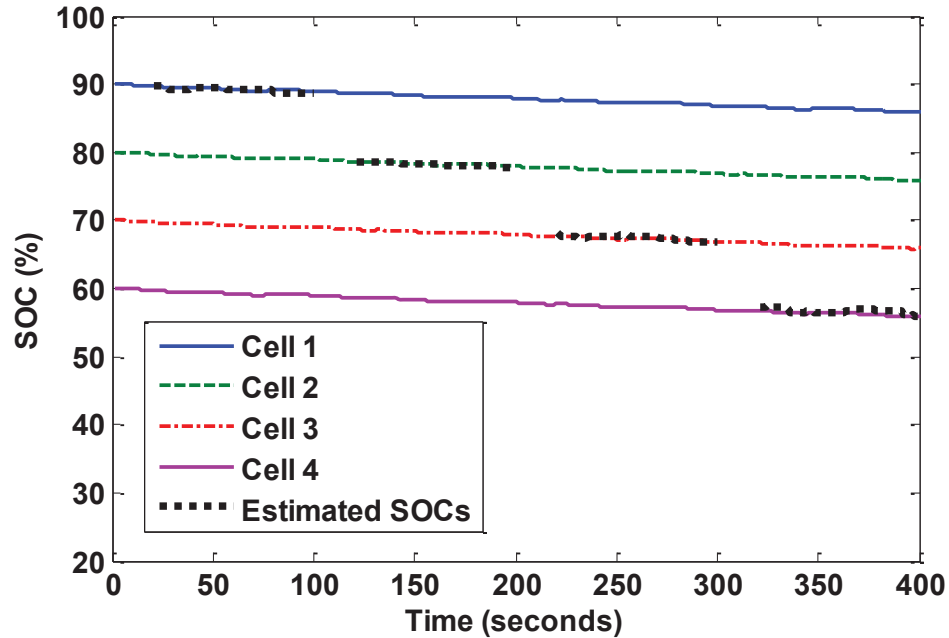


Figure 5.5: Comparison of the estimated and measured SOC for the four cells when using a wrong initial SOC for each cell in the proposed method.

## 5.5 Chapter Summary

This chapter has proposed a novel hybrid model-based online SOC and electrical parameter estimation method for multicell lithium-ion batteries. The proposed method was implemented in MATLAB/Simulink and validated by simulation and experimental results for a four-cell polymer lithium-ion battery pack. The proposed method can be used for real-time power management, condition monitoring, and diagnostics of batteries used in EVs and PHEVs.

## **CHAPTER 6: SIMPLIFIED HYBRID BATTERY MODEL-BASED, REAL-TIME IMPEDANCE, SOC, AND SOH ESTIMATION**

This chapter introduces a real-time impedance, SOC, and SOH estimation for multicell batteries based on a simplified hybrid battery model [55]. The simplified hybrid battery model consists of an enhanced Coulomb-counting algorithm and an electrical circuit battery model [27]. The former is used to estimate the SOC of each battery cell, while the latter is used as a system model for designing an adaptive discrete-time sliding mode observer (ADSMO), which is executed in real time to sequentially estimate the terminal and open-circuit voltages of the cells in a battery pack. The OCV obtained from the ADSMO is used to estimate the SOC of the battery cell. The estimated SOC is then used by the SOC compensator to correct the errors of the Coulomb-counting-based SOC estimation sequentially for the cells in the battery pack based on a closed-loop weighting SOC estimation algorithm. The parameters of the electrical circuit battery model of each cell required to implement the ADSMO are identified by a moving window least square (MWLS)-based online parameter identification algorithm [105]. Therefore, the hybrid battery method is capable of capturing nonlinear capacity effects of each battery cell and ensuring the robustness of the SOC estimation to unknown initial SOC, wrong maximum capacity, and error accumulation. In addition, the SOH is determined by comparing the rated capacity and the estimated maximum capacity of a cell. Furthermore, the estimated electrical parameters, such as series resistance [68], diffusion resistance [63], and diffusion capacitance [74], can be used as additional indicators for SOH estimation. The hybrid

battery method was validated by using simulation and experimental results for a four-cell cylindrical lithium-ion battery pack.

The SOC and SOH estimation method consists of four parts, as shown in Figure 6.1, for a series-connected  $m$ -cell battery pack: 1) a simplified hybrid battery model presented in Section 3.1, including an enhanced Coulomb-counting algorithm and an electrical circuit battery model; 2) an MWLS-based parameter identification algorithm; 3) an SOC compensator consisting of an ADSMO-based SOC estimator and a closed-loop weighting SOC compensation algorithm for correcting the error of the enhanced Coulomb-counting-based SOC estimation; and 4) an SOH estimator. The simplified hybrid battery model, parameter identification algorithm, SOC compensator, and SOH estimator are executed sequentially for each cell of the series-connected  $m$ -cell battery pack.

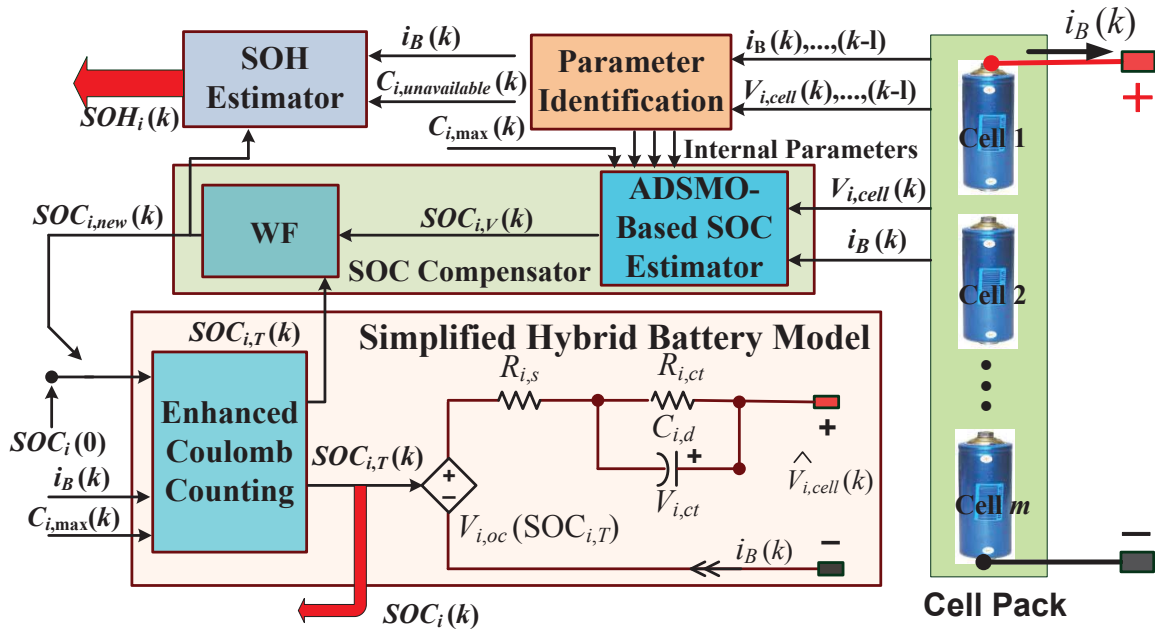


Figure 6.1: The SOC and SOH estimation method for a series-connected  $m$ -cell battery pack.

## 6.1 Parameter Identification by MWLS Method

The MWLS method is employed to identify the RC parameters  $R_{i,s}$ ,  $R_{i,ct}$ , and  $C_{i,d}$  of the electrical circuit model of each battery cell  $i$  ( $i = 1, \dots, m$ ). Assuming that  $T_s$  is short, e.g.,  $T_s \leq 1$  second, such that  $\Delta C_{i,unavailable}$  is negligible, the z-transfer function between the estimated terminal voltage  $\hat{V}_{i,cell}$  and current  $i_B$  of the electrical circuit battery model in Figure 6.1 is given in (6-1) and the corresponding difference equation is given in (6-2).

$$\frac{\hat{V}_{i,cell}(z) - b_{i,0}}{i_B(z)} = C_i(zI_{2 \times 2} - A_i)^{-1} B_i - D_i = \frac{x_{i,3} + x_{i,4}z^{-1} + x_{i,5}z^{-2}}{1 + x_{i,1}z^{-1} + x_{i,2}z^{-2}} \quad (6-1)$$

$$\begin{aligned} \hat{V}_{i,cell}(k) = & -x_{i,1} \cdot V_{i,cell}(k-1) - x_{i,2} \cdot V_{i,cell}(k-2) + x_{i,3} \cdot i_B(k) \\ & + x_{i,4} \cdot i_B(k-1) + x_{i,5} \cdot i_B(k-2) + b_{i,0}(1 + x_{i,1} + x_{i,2}) \end{aligned} \quad (6-2)$$

where

$$A_i = \begin{bmatrix} 1 & 0 \\ 0 & e^{\frac{-T_s}{\tau_{i,s}}} \end{bmatrix}, \quad B_i = \begin{bmatrix} \frac{-T_s}{C_{\max}} \\ R_{ct}(1 - e^{\frac{-T_s}{\tau_{i,s}}}) \end{bmatrix}, \quad C_i = [b_{i,1} - 1], \quad D_i = -R_{i,s} \quad (6-3)$$

$$\left\{ \begin{aligned} x_{i,1} &= -e^{\frac{-T_s}{\tau_{i,s}}} - 1, \\ x_{i,2} &= e^{\frac{-T_s}{\tau_{i,s}}}, \\ x_{i,3} &= -R_{i,s}, \\ x_{i,4} &= \frac{-b_{i,1}T_s}{C_{i,\max}} + R_{i,ct}(e^{\frac{-T_s}{\tau_{i,s}}} - 1) + R_{i,s}(e^{\frac{-T_s}{\tau_{i,s}}} + 1), \\ x_{i,5} &= R_{i,ct}(1 - e^{\frac{-T_s}{\tau_{i,s}}}) + e^{\frac{-T_s}{\tau_{i,s}}} \left( \frac{b_{i,1}T_s}{C_{i,\max}} - R_{i,s} \right) \end{aligned} \right. \quad (6-4)$$

where  $\tau_{i,S} = R_{i,ct} \cdot C_{i,d}$ ; Because  $(1+x_{i,1}+x_{i,2})$  is zero, (6-1) can be reformulated into the regression form of the input/output relationship.

$$\begin{aligned} \hat{V}_{i,cell}(k) = & -x_{i,1} \cdot V_{i,cell}(k-1) - x_{i,2} \cdot V_{i,cell}(k-2) + x_{i,3} \cdot i_B(k) \\ & + x_{i,4} \cdot i_B(k-1) + x_{i,5} \cdot i_B(k-2) = \Phi_i^T(k) \cdot \Theta_i \end{aligned} \quad (6-5)$$

where the regressor is  $\Phi_i^T(k) = [-V_{i,cell}(k-1), -V_{i,cell}(k-2), i_B(k), i_B(k-1), i_B(k-2)]$  and the vector of the parameters to be estimated is  $\Theta_i = [x_{i,1}, x_{i,2}, x_{i,3}, x_{i,4}, x_{i,5}]^T$ . Then, the MWLS algorithm is designed to estimate the vector  $\Theta_i$ . The MWLS is an advanced least squares estimation algorithm with a forgetting factor [105]. It uses the block data captured by a sliding window to keep track of the nonlinear time-variant parameters. The RC parameters of the electrical circuit battery model can then be calculated from (6-4) after  $\Theta_i$  is identified. This leads to an adaptive battery model.

The length of the sliding window can be variable depending on the estimation error of the terminal voltage by using (6-5) [105]. Due to the nonlinear time-variant parameters of battery cells, a long sliding window includes more information on the nonlinearity but may degrade the accuracy of the parameter estimation, resulting in a large estimation error of the terminal voltage. Furthermore, the excitation level of the input signal is also an important factor in choosing the length of the sliding window [54]. For example, if long discharge current pulses are applied to the battery, the sliding window should have at least one of the pulse edges. On the other hand, the length of the window can be set to be short, e.g., the allowed minimum value, if the input signal is fully excited within a short window. The abnormal values of the estimated RC parameters due to low perturbation or quality of the input signal are discarded.

## 6.2 Real-Time SOC Estimation by ADSMO

The ADSMO is proposed to estimate  $V_{i,oc}$  of Cell  $i$  ( $i = 1, \dots, m$ ). Figure 6.2 shows a block diagram of the ADSMO. Using the first-order forward Euler method, the actual terminal voltage  $V_{i,cell}$  can be written as follows [78]:

$$V_{i,cell}(k+1) = \left(1 - \frac{T_{smo}}{\tau_{i,S}}\right) V_{i,cell}(k) + \frac{T_{smo}}{\tau_{i,S}} V_{i,OC}(k) - \left(\frac{T_{smo}}{C_{i,max}} + \frac{T_{smo}}{C_{i,ct}} + \frac{T_{smo} R_{i,s}}{\tau_{i,S}}\right) i_B(k) \quad (6-6)$$

The ADSMO is designed as:

$$\hat{V}_{i,cell}(k+1) = \left(1 - \frac{T_{smo}}{\tau_{i,S}}\right) \hat{V}_{i,cell}(k) + \frac{T_{smo}}{\tau_{i,S}} lZ - \left(\frac{T_{smo}}{C_{i,max}} + \frac{T_{smo}}{C_{i,ct}} + \frac{T_{smo} R_{i,s}}{\tau_{i,S}}\right) i_B(k) \quad (6-7)$$

where  $l$  is the SMO gain of the switching control vector  $Z$ , and  $T_{smo}$  is the sampling period of the ADSMO. In (6-7), the internal parameters  $R_{i,s}$ ,  $R_{i,ct}$ , and  $C_{i,t}$  are used, which are obtained from the parameter identification process. By defining the voltage estimation error  $\varepsilon_v(k) = V_{i,cell}(k) - \hat{V}_{i,cell}(k)$ , (6-8) can be obtained by subtracting (6-7) from (6-6):

$$\varepsilon_v(k+1) = \left(1 - \frac{T_{smo}}{\tau_{i,S}}\right) \varepsilon_v(k) + \frac{T_{smo}}{\tau_{i,S}} V_{i,oc}(k) - \frac{T_{smo}}{\tau_{i,S}} lZ \quad (6-8)$$

The sliding surface is designed as  $S(k) = \varepsilon_v(k) = 0$ . The dynamic of the ADSMO can be written as:

$$\frac{S(k+1) - S(k)}{T_s} = -\frac{1}{\tau_{i,S}} S(k) + \frac{1}{\tau_{i,S}} V_{i,oc}[k] - \frac{1}{\tau_{i,S}} lZ \quad (6-9)$$

A variable switching function for the ADSMO is defined as follows.

$$Z = \begin{cases} Z_0 & \varepsilon_v(k) \geq Z_0 \\ \varepsilon_v(k) & -Z_0 > \varepsilon_v(k) > Z_0 \\ -Z_0 & \varepsilon_v(k) \leq -Z_0 \end{cases} \quad (6-10)$$

where  $Z_0$  is the width of the boundary layer. Due to the switching function,  $S$  is bounded.

According to (6-9), the Lyapunov stability condition, i.e.,  $\dot{S} \cdot S < 0$ , is satisfied if  $l > V_{i,oc\_max}/Z_0$ , where  $V_{i,oc\_max}$  is the maximum OCV of Cell  $i$ . Finally, the state trajectory approaches the sliding surface defined by  $\dot{S} = S = 0$ . When the tracking error is zero, the output of the designed switching function,  $lZ$ , is equal to  $V_{i,oc}$ . If there is an abrupt change in the cell current (such as pulsed charge or discharge current), the ADSMO is not able to quickly catch up with the change in the terminal voltage when  $T_{smo}$  is large, e.g.,  $T_s = 1$  second. As a result, the output of the switching function oscillates until  $\varepsilon$  becomes small. The moving average (or low-pass filter) and selector module in Figure 6.2 smooth  $lZ$  and discard the highly oscillated values, respectively.

The estimated OCV  $\hat{V}_{i,oc}$  is then used to calculate the SOC ( $SOC_{i,v}$ ) of Cell  $i$  according to the a SOC- $V_{oc}$  lookup table obtained under the ambient temperature. Assuming that the hysteresis effect is negligible in the lithium-ion battery cells, the relationship between SOC and  $V_{oc}$  depends on temperature and aging; but their influence may be negligible if the SOC is expressed using the relative capacity [106].

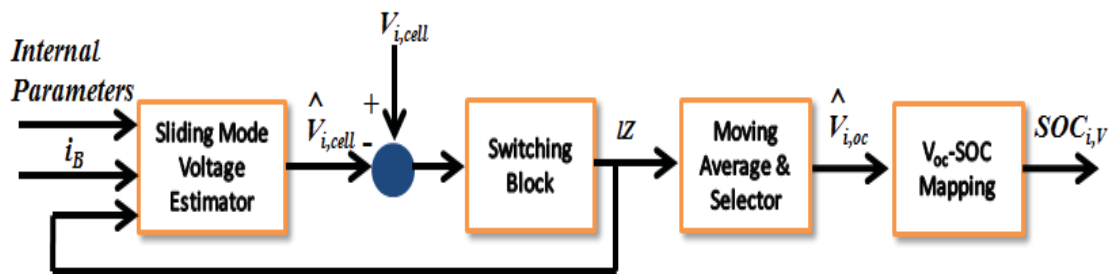


Figure 6.2: A block diagram of the ADSMO-based SOC estimator.

### 6.3 Real-Time SOC Estimation and Compensation

The closed-loop weighting SOC compensator in (5-13) and (5-14) ([87], [103]) is used with the ADSMO-based SOC estimator to correct the error of the SOC, i.e.,  $SOC_{i,T}$ , obtained sequentially for the cells from the enhanced Coulomb counting algorithm in (5-1) and (5-2), as shown in Figure 6.3.  $SOC_{i,V}$  is the SOC estimated from the ADSMO-based SOC estimator shown in Figure 6.2. The SOC compensator uses  $SOC_{i,V}$  to correct the  $SOC_{i,T}$ . In this dissertation,  $C_{i,max}$  of Cell  $i$  in the enhanced Coulomb counting algorithm is updated by the capacity estimation in the SOH estimator, which is discussed in (6-11) in the next section. The  $SOC_{i,V}$  and  $SOC_{i,T}$  are multiplied by their weighting factors and then added together to generate a compensated SOC (i.e.,  $SOC_{new}$ ), as discussed in Chapter 5.3. The  $SOC_{new}$  is then used as the initial SOC ( $SOC_i$ ) of the enhanced Coulomb counting algorithm to estimate the SOC in the next time step.

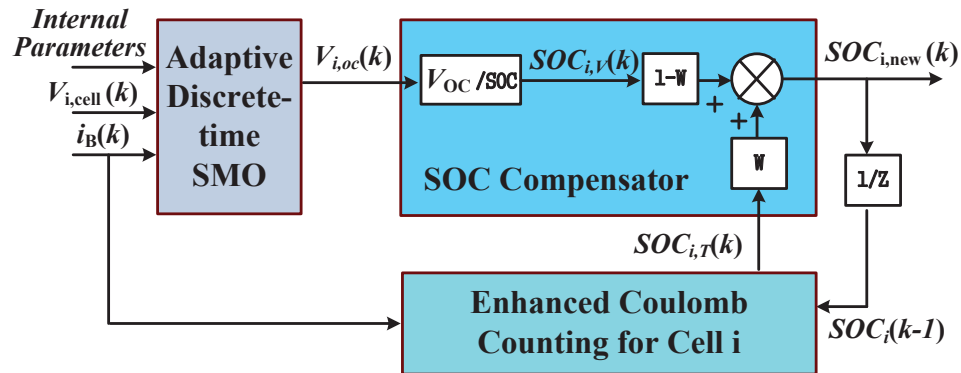


Figure 6.3: The proposed closed-loop weighting SOC estimation algorithm with ADSMO.

## 6.5 SOH Estimation by Two-Point Method

Due to cell state variations, the maximum capacities of the battery cells in a pack are unequal to the nominal capacity that the manufacturer offers. Such variations depend on manufacturing environment and temperature conditions. Moreover, the maximum capacity of a cell reduces due to aging. Therefore, the value of  $C_{i,\max}$  is a good indicator of the SOH of a battery cell Cell  $i$  and can be updated from (6-11) using the compensated  $SOC_i$  as follows:

$$C_{i,\max}(k) = \frac{T_S \sum_{k=k_1}^{k_2} i_B(k) + C_{i,unavailable}(k)}{SOC_i(k_1) - SOC_i(k_2)} \quad (6-11)$$

where  $k_1$  and  $k_2$  are the beginning and end times of the SOH estimation period, respectively.

The SOH represents a battery cell's capacity and power capability for delivering the specified performance compared to a new battery. The SOH can be indicated by a single measurement of the conductance or impedance of a cell, which is easy to determine but imprecise. Other battery parameters, such as maximum capacity, internal resistance, self-discharge rate, charge acceptance, and discharge capability are used to estimate the SOH. In this dissertation, the SOH is estimated as the ratio of the maximum capacity of a battery cell, i.e.,  $C_{i,\max}$ , to that of the cell when it is new (i.e.,  $C_{i,\max\_new}$ ). Such an SOH represents the capacity degradation of the cell.

$$SOH_i(k) = \frac{C_{i,\max}(k)}{C_{i,\max\_new}} \quad (6-12)$$

In addition, the impedance estimated by using the MWLS method can be utilized for SOH estimation from the perspective of power degradation.

## 6.6 Validation

The SOC and SOH estimation method was validated by simulation and experimental data for a four-cell cylindrical lithium-ion battery pack (see Appendix). The experimental data of the cell voltage and current were collected from a CADEX battery tester C8000 (shown in Figure 6.4) under ambient temperature. The method shown in Figure 6.1 was implemented in MATLAB/Simulink.

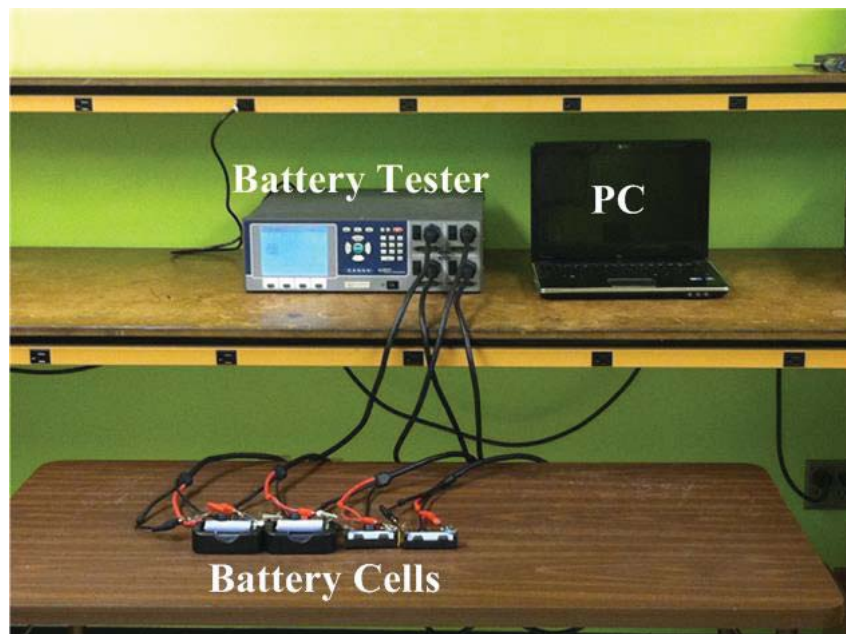
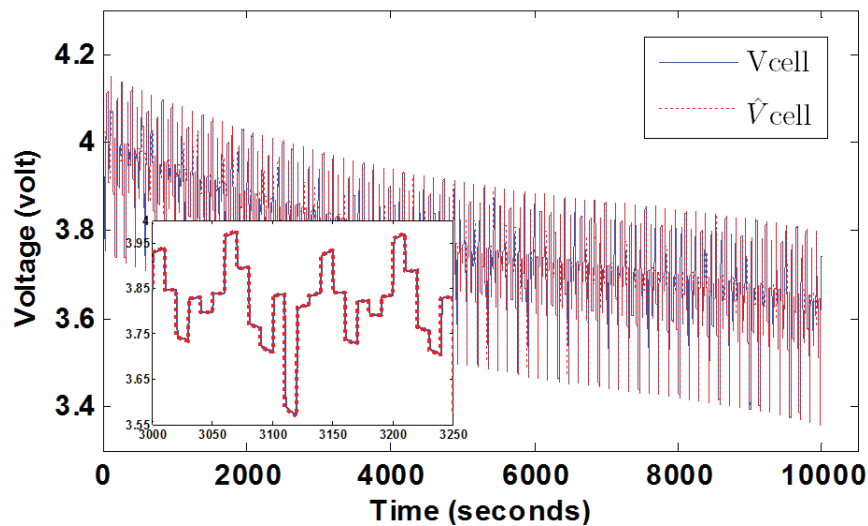


Figure 6.4: The experimental setup for simplified hybrid battery model-based SOC and SOH estimation.

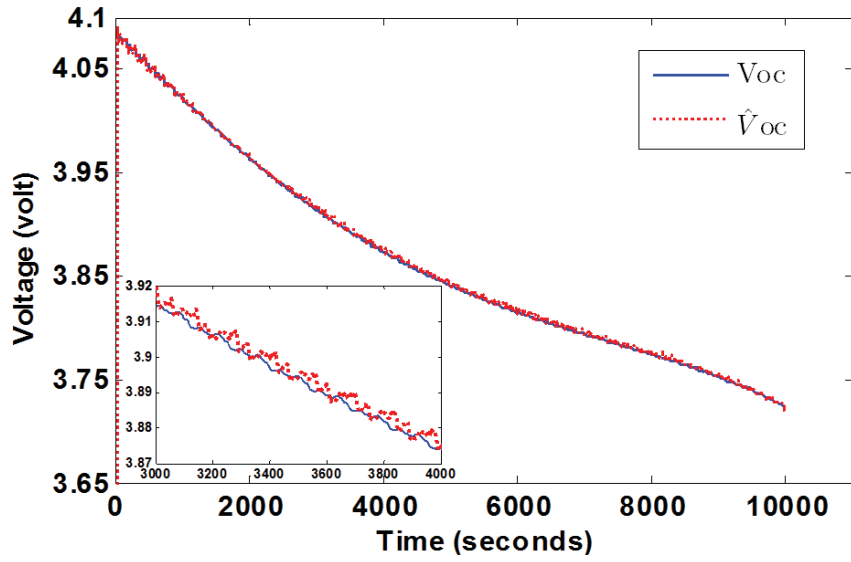
The cell voltage and current measured by the battery tester were used by the estimation method for real-time SOC and SOH estimation of each battery cell. The values of  $V_{oc}(SOC)$  and  $C_{max}$  were extracted offline for each battery cell [27] first. They were then used as the true values and compared with the values obtained from the estimation method in real

time. In order to set initial SOCs for the test battery cells, they were fully charged and rested for one hour first. Then the cells were discharged, using a small current, to the desired initial SOC values. Finally, the cells rested (or they may have needed further charge or discharge using very small currents) until their OCVs were equal to the true values corresponding to the initial SOCs.

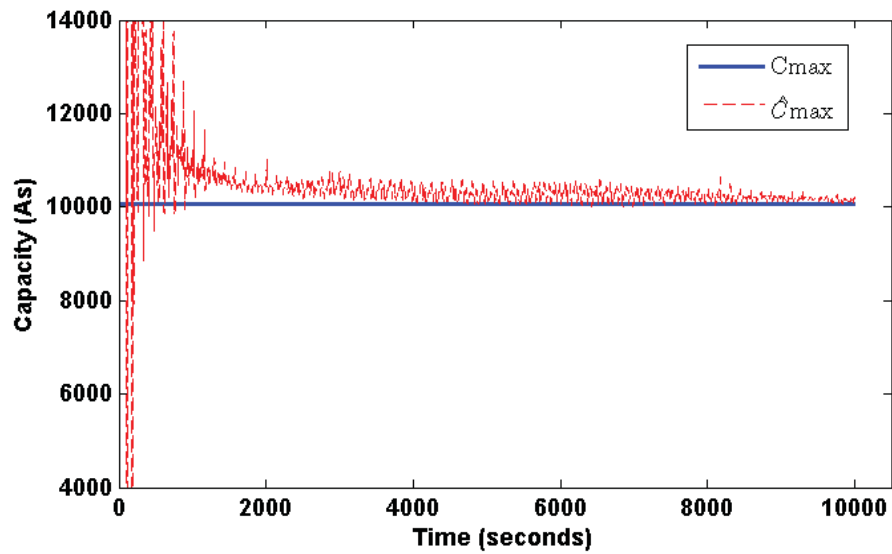
First, the identification of  $V_{oc}$  and  $C_{max}$  was investigated. Figure 6.5(a)-(c) compares the true and estimated  $V_{cell}$ ,  $V_{oc}$ , and  $C_{max}$  for a dynamic current cycle, shown in Figure 6.5(d). The parameter identification algorithm was executed by using the data sampled with a 1 Hz rate and a 20-second moving window. Then, the ADSMO was executed with a sampling rate of 100 Hz to estimate the  $V_{oc}$ . The results show that the values of  $V_{cell}$ ,  $V_{oc}$ , and  $C_{max}$  were estimated accurately in real time. The SOH of the cell could be estimated using the estimated  $C_{max}$ . However, it takes a relatively long time to get  $C_{max}$  close to its true value.



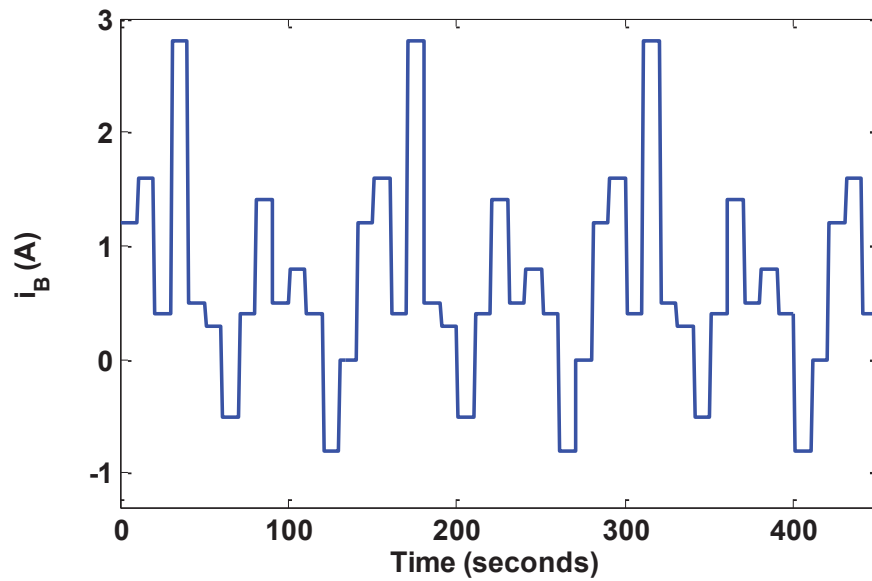
(a)



(b)



(c)



(d)

Figure 6.5: Comparison of true and estimated parameters of a battery cell: (a)  $V_{cell}$ , (b)  $V_{oc}$ , (c)  $C_{max}$ , and (f) the dynamic current cycle used for the test.

Next, the SOC estimation algorithm for multicell batteries was investigated using the measured data of the four-cell battery pack. All cells were initially set with a wrong initial SOC of 50%; while the real initial SOC of Cells 1, 2, 3, and 4 were 100%, 90%, 80%, and 70%, respectively. The battery pack was operated with a dynamic current cycle, as shown in Figure 6.5(d). The SOC compensator was executed sequentially with an interval of 100 seconds for each cell to compensate its SOC. Figure 6.6 compares the SOC estimated by the proposed method with those measured by the battery tester. The estimated SOC of each cell matched the value measured, although the initial SOC was set wrong in the proposed method. This result clearly shows that the proposed algorithm is robust to the error of the initial SOC, which, however, will reduce the accuracy of the traditional Coulomb-counting methods.

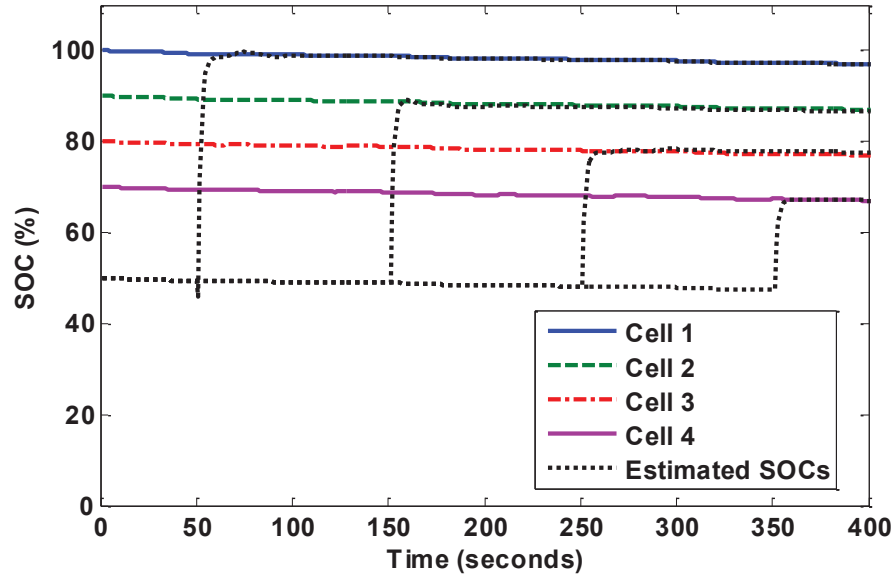


Figure 6.6: Comparison of the estimated and measured SOC for the four cells.

## 6.7 Chapter Summary

A novel simplified hybrid model-based, real-time impedance, SOC and SOH estimation method was developed for multicell lithium-ion batteries. The method was implemented in MATLAB/Simulink and validated by simulation and experimental results for a four-cell cylindrical lithium-ion battery pack. The method can be used for real-time power management, condition monitoring, and diagnostics of batteries in various applications, such as EVs and PHEVs.

## **CHAPTER 7: AN ELECTRICAL CIRCUIT WITH HYSTERESIS BATTERY MODEL-BASED REAL-TIME IMPEDANCE, SOC, AND SOH ESTIMATION**

This chapter describes an electrical circuit with hysteresis model-based condition monitoring strategy for lithium-ion batteries [107]. The strategy systematically integrates: 1) a fast upper-triangular and diagonal recursive least square (FUDRLS) online parameter identification algorithm [93], which estimates the parameters of the electrical circuit battery model, 2) a smooth variable structure filter (SVSF) for the SOC estimation of the battery, and 3) a recursive total least square (RTLS) algorithm for maximum capacity estimation of the battery [91], which indicates the SOH of the battery and improves the SOC estimation algorithm. Advantages of the proposed strategy include high accuracy, low computational cost, and simple implementation, and, therefore, it is suitable for deployment and use in real-time embedded battery management systems. Simulations and experiments validated the effectiveness of the proposed condition monitoring strategy.

### **7.1 The Electrical Circuit with Hysteresis Battery Model-Based- Condition Monitoring Strategy**

The condition monitoring strategy, shown in Figure 7.1, consists of three parts:

1. A FUDRLS-based impedance estimator
2. An SVSF-based SOC estimator
3. An RTLS-based SOH, i.e., maximum capacity, estimator

The strategy operates at different time scales, where the FUDRLS and SVSF run with a smaller time scale to estimate the fast time-varying electrical parameters and the SOC; and the RTLS runs slower to track the slow time-varying maximum capacity parameter. In this way, the low computational resources are used economically with guaranteed estimation performance.

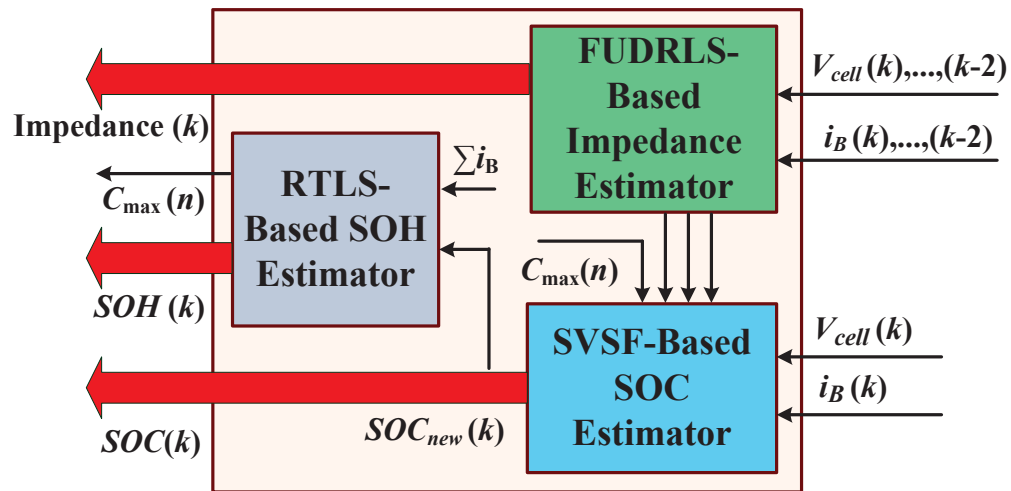


Figure 7.1: The model-based condition monitoring strategy for embedded BMS.

## 7.2. Impedance Estimation by FUDRLS

Since the internal impedance of a battery cell changes with SOC, temperature, and charge/discharge current rate, etc., an online impedance estimation algorithm is required to provide an accurate electrical circuit battery model. The FUDRLS algorithm was used to identify three impedance parameters:  $R_s$ ,  $R_{ct}$ , and  $C_d$ , of the electrical circuit battery model shown in Figure 3.13. Developing a regression form for the electrical circuit battery model is similar to that described in Section 6.1. To estimate the impedance parameters, the hysteresis voltage dynamics are ignored; and  $V_{oc} = b_1 \cdot SOC + b_0$  is assumed. Then, the

simplified electrical circuit with hysteresis battery model (3-36) is reduced to the following second-order state space form:

$$\begin{aligned} \begin{bmatrix} SOC(k+1) \\ V_{ct}(k+1) \end{bmatrix} &= A \begin{bmatrix} SOC(k) \\ V_{ct}(k) \end{bmatrix} + Bi_B(k), \\ V_{cell}(k) &= C \begin{bmatrix} SOC(k) \\ V_{ct}(k) \end{bmatrix} - R_s \cdot i_B(k) + b_0 \end{aligned} \quad (7-1)$$

where

$$A = \begin{bmatrix} 1 & 0 \\ 0 & \gamma \end{bmatrix}, \quad B = \begin{bmatrix} \frac{-\eta T_s}{C_{\max}} \\ R_{ct}(1-\gamma) \end{bmatrix}, \quad C = [b_1 \quad -1], \quad D = -R_s$$

Taking the z-transformation of (7-1) gives [95]:

$$\frac{\bar{V}_{cell}(z)}{i_B(z)} = C(zI_{2 \times 2} - A)^{-1}B + D = \frac{x_3 + x_4 z^{-1} + x_5 z^{-2}}{1 + x_1 z^{-1} + x_2 z^{-2}} \quad (7-2)$$

where  $\bar{V}_{cell}(z) = V_{cell} - b_0$ ,  $I_{2 \times 2}$  is a 2 by 2 identity matrix, and

$$\begin{cases} x_1 = -e^{\frac{-T_s}{R_{ct}C_d}} - 1, \\ x_2 = e^{\frac{-T_s}{R_{ct}C_d}}, \\ x_3 = -R_s, \\ x_4 = \frac{-b_1 T_s}{C_{\max}} + R_{ct} \left( e^{\frac{-T_s}{R_{ct}C_d}} - 1 \right) + R_s \left( e^{\frac{-T_s}{R_{ct}C_d}} + 1 \right) \\ x_5 = R_{ct} \left( 1 - e^{\frac{-T_s}{R_{ct}C_d}} \right) + e^{\frac{-T_s}{R_{ct}C_d}} \left( \frac{b_1 T_s}{C_{\max}} - R_s \right) \end{cases}$$

The difference equation corresponding to (7-2) is given by:

$$\begin{aligned} V_{cell}(k) &= -x_1 \cdot V_{cell}(k-1) - x_2 \cdot V_{cell}(k-2) + x_3 \cdot i_B(k) + x_4 \cdot i_B(k-1) \\ &\quad + x_5 \cdot i_B(k-2) + b_0(1 + x_1 + x_2) \end{aligned} \quad (7-3)$$

Since  $1 + x_1 + x_2 = 0$ , (7-3) can be reformulated into the following regression form.

$$[V_{cell}(k) - V_{cell}(k-1)] = \Phi^T(k)\Theta, \quad (7-4)$$

where  $\Theta = [x_2, x_3, x_4, x_5]^T$  and  $\Phi^T(k) = [V_{cell}(k-1) - V_{cell}(k-2), i_B(k), i_B(k-1), i_B(k-2)]$ .

**Remark 1:** The z-transformation technique is applied to derive (7-4) because matrices  $A$ ,  $B$ ,  $C$ , and  $D$  are time invariant. Alternatively, one can perform a derivation in the time domain, i.e., directly work on the difference equation (7-3) and establish (7-4).

The derivation of (7-4) is performed on the basis of the second-order battery model (7-1) and the parameterization of  $V_{oc}$  as  $b_1 \cdot SOC + b_0$  for impedance estimation. Specifically, a linear parameterization of  $V_{oc}$  is critical to the derivation; and the second-order battery model (7-1) is merely to simplify the presentation. Linear parameterization of  $V_{oc}$  is valid in the neighborhood of  $SOC$  while the hysteresis voltage  $V_{hmax}$  reaches steady state but is invalid during the transient of  $V_h$ . This limitation can be addressed by imposing a less restrictive assumption: linear parameterizations of the  $V_{oc}$ -SOC curve, which is always valid locally. This allows to perform parameter identification for impedance and  $V_{hmax}$  based on (3-36) and the following dynamics.

$$y(k) = V_{cell}(k) = b_0 + b_1 SOC - V_{st}(k) - R_s i_B(k) + V_h(k) \quad (7-5)$$

Note that notations  $b_0$  and  $b_1$  are used here.

Since the state matrix  $A$  of the model (3-36) are current dependent or time varying, the model (3-36) does not allow  $z$ -transformation. It is not straightforward to rewrite (3-36) into a linear regression form. However, an approximate linear regression form of the model (3-36) can be derived; and thus parameter identification can be readily carried out. Notice that the main difficulty in establishing the linear regression form arises from the time-varying  $V_h$ -dynamics, which fortunately are independent of the  $V_{ct}$  and  $SOC$ -dynamics. This decoupling feature allows to obtain an approximate linear regression form.

In order to obtain an approximate linear parameterization of  $y$ , consider the following system based on (3-36):

$$\xi(k+1) = H\xi(k) + (H-1)\text{sign}(i_B), \quad \xi(0) = \xi_0.$$

Considering  $V_h(k) = \xi(k)V_{h\max}$  for  $\xi_0 = V_h(0)/V_{h\max}$ , the following linear parameterizations of  $y(k)$  is obtained:

$$y(k) = b_0 + b_1\text{SOC} - V_{ct}(k) - R_s i_B(k) + \xi(k)V_{h\max} \quad (7-6)$$

where  $V_{h\max}$  is unknown. A time-varying open-loop filter is introduced to estimate  $\xi$

$$\hat{\xi}(k+1) = H\hat{\xi}(k) + (H-1)\text{sign}(i_B), \quad \hat{\xi}(0) = \xi_0.$$

Since  $H < 1$ , the aforementioned time-varying open-loop filter produces an exponentially convergent estimate of  $\xi(k)$ , i.e.,  $\hat{\xi}(k)$  converges to  $\xi(k)$  as  $k \rightarrow \infty$  for any bounded  $\xi_0$ .

Combining (7-6) and the fact that  $\hat{\xi}(k) \rightarrow \xi(k)$  as  $k \rightarrow \infty$ , the approximate linear parameterizations of  $y(k)$  are as follows:

$$y(k) = b_0 + b_1\text{SOC} - V_{ct}(k) - R_s i_B(k) + \hat{\xi}(k)V_{h\max}, \quad (7-7)$$

from which, together with the dynamics of  $\text{SOC}$ ,  $V_{ct}$ , the approximate linear regression of (3-36) can be established. Compared to (7-1), the approximate linear regression has an extra parameter  $V_{h\max}$  in  $\Theta$  and an extra signal  $\hat{\xi}(k)$  in  $\Phi(k)$ .

Given (7-4), the parameter vector  $\Theta$  can be estimated by a multitude of algorithms, for instance the conventional Bierman's upper-triangular and diagonal recursive least square (UDRLS) method [56], Gentleman's UDRLS [108], etc. The UDRLS is a factorization algorithm to solve digital computer implementation problem of RLS, which preserves the positive covariance  $P$  by updating the U-upper triangular and D-diagonal

matrices, thus the numerical stability has been improved. The Gentleman's UDRLS is attractive to embedded applications due to its parallel implementation and resultant fast computational speed. The RLS-based methods can be improved by using the forgetting factor [53]. The estimation algorithm with a small forgetting factor may track time-varying parameters fairly well at the expense of increased susceptibility to noise; while the forgetting factor is large, the tracking ability will be poor but robust to noises. In general, the RLS technique utilizes exponential forgetting (EF) whose forgetting rate is constant [53], [56]. The main drawback of the EF method is called windup, and it comes when a data vector is not persistently exciting [109] and is not optimal for tracking and noise influence due to the constant forgetting rate [109].

The FUDRLS algorithm combines the Gentleman's UDRLS with a variable forgetting factor to estimate  $\Theta$ . Methods with variable forgetting (VF) adaptively change the forgetting rate. The main VF mechanism is: the algorithm takes a smaller forgetting factor at the presence of large prediction errors and a larger forgetting factor otherwise. In this dissertation, the forgetting factor  $\lambda$  is adjusted as follows:

$$\lambda(k+1) = \left[ 1 - \frac{E(k)}{\sigma_0^2 N_0} \right], \quad \lambda_{\min} \leq \lambda \leq \lambda_{\max} \quad (7-8)$$

$$E(k) = \delta_1 E(k) + (1 - \delta_1) \cdot e(k)^2$$

where  $\delta_1$  is a weighting factor ( $0.9 < \delta_1 < 1$ );  $E$  is a time-average expression of  $e(k)^2$  and  $E(0)$  is set to be  $\sigma_0^2$ ; the parameter  $\sigma_0^2$  is the mean value of the variance of the prediction error obtained from the method implemented in the FUDRLS with a constant forgetting factor, e.g.,  $\lambda = 0.98$ , assuming that the expected noise variance is much smaller than  $\sigma_0^2$ ;  $N_0$  represents the memory length (e.g.,  $N_0 = 50$  corresponding to a mean forgetting factor of

0.98); and  $\lambda_{\max}$  (e.g., 0.999) and  $\lambda_{\min}$  (e.g., 0.95) denote the maximum forgetting and minimum forgetting factors, respectively. An intuitive interpretation of (7-8) is that the forgetting factor  $\lambda$  is adjusted according to the square of the time-averaged estimation of the autocorrelation of posterior error  $e(k)$ .

In the FUDRLS, the regression matrix  $\Phi^T(k)$  is combined with  $v_1(k) = V_{cell}(k) - V_{cell}(k-1)$  to produce an augmented matrix:  $\Phi^T(k) = [\Phi^T(k) \ v_1(k)]$ . The detailed FUDRLS algorithm is given in Table 7.1, where  $\delta_0$  denotes an initial covariance value, e.g.,  $10^5$ . For real-time implementation, the computation of  $f_F$  and the triangularization can be pipelined.

In a practical BMS application, the parameter identification algorithm is implemented in a system-on-a-chip [110]. Due to the advent of very-large-scale integration (VLSI) technology, the features of parallel processing and pipelining implementation will be attractive to improve the computation speed and reduce the size of ICs [111]. Therefore, FUDRLS will be beneficial to the development of real BMS ICs in this sense.

Table 7.1: FUDRLS algorithm.

|   |   |
|---|---|
| <p>1: algorithm initialization. Set <math>k = 0</math>, <math>K_{FUDRLS} = [0, 0, 0, 0, 0]^T</math>, and <math>P_0 = \delta_0 I_{5 \times 5} = U_{old} D_{old} U_{old}^T</math> where</p> |   |
| $U_0 = \begin{bmatrix} 1 & 0 & 0 & 0 & \theta_1 \\ 0 & 1 & 0 & 0 & \theta_2 \\ 0 & 0 & 1 & 0 & \theta_3 \\ 0 & 0 & 0 & 1 & \theta_4 \\ 0 & 0 & 0 & 0 & -1 \end{bmatrix}$                  | $, \quad D_0 = \delta_0 \begin{bmatrix} 1 & 0 & 0 & 0 & 0 \\ 0 & 1 & 0 & 0 & 0 \\ 0 & 0 & 1 & 0 & 0 \\ 0 & 0 & 0 & 1 & 0 \\ 0 & 0 & 0 & 0 & 0 \end{bmatrix} \quad \text{or} \quad D_0 = \delta_0 [1, 1, 1, 1, 0]$ |
| <p>2: <b>repeat</b></p>   |   |
| <p>3:   <math>k \leftarrow k+1</math></p>   |   |
| <p>4:   read new data <math>V_{cell}(k)</math> and <math>i_B(k)</math></p>  |   |
| <p>5:   compute <math>f_F = U_0^T \Phi_a(k)</math> and <math>\varepsilon = -f_F(5)</math></p>   |   |
| <p>6:   initialize <math>r(0) = \lambda</math></p>  |   |
| <p>7:   <b>for</b> <math>h=1</math> to 5 <b>do</b></p>  |   |
| <p>8:       compute the parameters Gentleman's transformation</p>   |   |
| $r(h) = r(h-1) + D_{old}(h) f_F(h)^2$   |   |
| $D_{new}(h) = D_{old}(h) r(h-1) / (\lambda r(h))$   |   |
| $\text{alpha}(h) = -f_F(h)$   |   |
| $\text{beta}(h) = D_{old}(h) f_F(h) / r(h)$   |   |
| $K_{FUDRLS}(h) = \text{beta}(h)$  |   |
| <p>9:   <b>end for</b></p>  |   |
| <p>10:   <b>for</b> <math>j = 2</math> to 5 <b>do</b></p>   |   |
| <p>11:       compute the Gentleman's transformation</p>   |   |
| <p>12:       <b>for</b> <math>i = 1</math> to <math>j-1</math> <b>do</b></p>  |   |
| <p>13:           compute the Gentleman's transformation</p>   |   |
| $U_{new}(i,j) = U_{old}(i,j) + \text{alpha}(j) K_{FUDRLS}(i)$   |   |
| $K_{FUDRLS}(i) = K_{FUDRLS}(i) + \text{beta}(j) U_{new}(i,j)$   |   |
| <p>14:       <b>end for</b></p>   |   |
| <p>15:   <b>end for</b></p>   |   |
| <p>16:   update parameter estimate <math>\Theta</math> and <math>U_{old}, D_{old}</math></p>  |   |
| $\Theta = [U_{new}(1,5), U_{new}(2,5), U_{new}(3,5), U_{new}(4,5)]^T$   |   |
| $U_{old} = U_{new}, D_{old} = D_{new}$  |   |
| <p>17:   map <math>\Theta</math> to <math>R_s, R_{ct}</math>, and <math>C_d</math></p>  |   |
| <p>18:   check whether estimated parameters are within the predefined range of values</p>   |   |

### 7.3 SOC Estimation by SVSF

The SVSF estimates the battery SOC by using a state space model (3-36). The internal parameters  $R_s$ ,  $R_{ct}$ , and  $C_d$  in (3-36) are updated by the FUDRLS online parameter identification algorithm.

The SVSF, originally proposed in [112], is a predictor-corrector method for state and parameter estimation and is based on variable structure theory and a sliding mode concept. A switching gain is implemented to keep the state estimate within a bounded domain, which is an invariant set containing the true states. The SVSF is relatively stable and robust for modeling uncertainties and noises, given that uncertainties are upper-bound. The basic concept of the SVSF-based state estimation is shown in Figure 7.2, where the solid line is a trajectory of a system state. The estimated state trajectory is forced towards the system state trajectory until it enters the neighborhood of the actual state trajectory, referred to as the existence of subspace. The existence of subspace is an invariant set because once the estimated state enters, it remains within the region. The SVSF was applied to estimate battery parameters and SOC in [113], albeit the result was validated by simulation only.

In this dissertation, SVSF is designed on the basis of the state space model (3-36) to perform the state estimation for a battery cell. The dynamics of the proposed SVSF are given by

$$\begin{aligned}\hat{x}_{k+1|k} &= f(\hat{x}_{k|k}, i_B(k)), \\ \hat{y}_{k+1|k} &= C_{SVSF} \hat{x}_{k+1|k}\end{aligned}\tag{7-9}$$

where  $\hat{x}_{k+1|k}$  is the predicted state estimate,  $\hat{x}_{k|k}$  is the state estimate at time  $k$ ,  $f$  is a vector field,  $\hat{y}_{k+1|k}$  is the predicted measurement, and  $C_{SVSF}$  is the linearized measurement matrix given by

$$C_{SVSF} = \frac{\partial h(x, i_B)}{\partial x} = \text{diag} \left[ \frac{\partial V_{OC}(SOC)}{\partial SOC}, -1, 1 \right].$$

where  $h$  is smooth function of  $x$  and  $i_B$ . Defining the innovation as  $e_{z,k+1|k} = y_{k+1} - C_{SVSF} \hat{x}_{k+1|k}$ , the SVSF gain is calculated as follows:

$$K_{SVSF,k+1} = C_{SVSF}^{-1} (| e_{z,k+1|k} | + \gamma_s | e_{z,k|k} |) \circ \text{sat}(e_{z,k+1|k}, \Psi) \quad (7-10)$$

where  $e_{z,k|k}$  is a posteriori measurement error of previous step;  $\text{sat}(\cdot)$  is a saturation function;  $\Psi$  is the smoothing boundary layer widths;  $\gamma_s$  ( $0 < \gamma_s < 1$ ) is the SVSF convergence rate; and  $\circ$  is the Schur product. To ensure numerical stability, the components of  $C_{SVSF}$  should be positive values. This can be accomplished by using a simple *if* statement with a very small threshold, i.e.,  $10^{-10}$ , or calculating the pseudoinverse  $C_{SVSF}^{-I}$  with a small damping parameter  $\omega$ , i.e.,  $10^{-8}$ , such as the following:

$$C_{SVSF}^{-1} = C_{SVSF}^T (C_{SVSF} C_{SVSF}^T + \omega I_3)^{-1} \quad (7-11)$$

The corrected (or posteriori) state estimates are computed as follows:

$$\begin{aligned} \hat{x}_{k+1|k+1} &= \hat{x}_{k+1|k} + K_{SVSF,k+1} e_{z,k+1|k} \\ e_{y,k+1|k+1} &= y_{k+1} - C_{SVSF} \hat{x}_{k+1|k+1} \end{aligned} \quad (7-12)$$

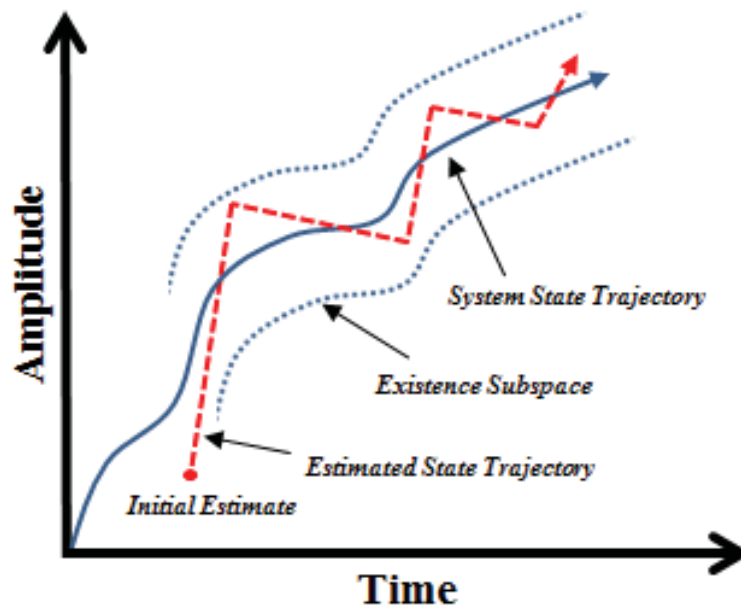


Figure 7.2: The SVSF estimation concept. (Courtesy of [112].)

In order to speed up the convergence rate of the SVSF, the iterated SVSF (ISVSF) can be applied [114]. It consists of two procedures: prediction and update. The formulae for the ISVSF in the prediction procedure are the same as the original SVSF. If  $e_{y,k+1|k+1}$  is larger than a prespecified error tolerance level, it will go to the update procedure, which is implemented iteratively as follows:

$$\begin{cases} C_{SVSF} = \text{diag} \left[ \frac{\partial V_{oc}(SOC^{(i)})}{\partial SOC^{(i)}} \right], & -1, \quad 1] \\ K_{SVSF,k+1}^{(i)} = C_{SVSF}^{-1(i)} (|e_{z,k+1|k}^{(i-1)}| + \gamma_s |e_{z,k|k}|) \circ \text{sat}(e_{z,k+1|k}^{(i-1)}, \Psi) \\ \hat{x}_{k+1|k}^{(i)} = \hat{x}_{k+1|k}^{(i-1)} + K_{SVSF,k+1}^{(i)} \\ e_{y,k+1|k}^{(i)} = y_{k+1} - C_{SVSF}^{(i)} \hat{x}_{k+1|k}^{(i)} \end{cases} \quad (7-13)$$

The iteration process stops when the estimation error becomes less than the prespecified tolerance level or the value of  $i$  reaches the predefined maximum iteration number  $N_{\max}$ . In the latter case, the estimated state  $\hat{x}_{k+1|k}^{(i)}$  corresponding to the minimum

error is set to be  $\hat{x}_{k+1|k+1}$ . Once the estimated state  $\hat{x}_{k+1|k+1}$  converges, the iteration process will stop. It should be pointed out that the values of the system parameter  $\gamma_s$  and  $\Psi$  will affect the performance of the SVSF, as well as those of a prespecified tolerance level and  $N_{\max}$  for ISVSF.

## 7.4 SOH Estimation by RTLS

The SOH represents a battery cell's capacity and power capability for delivering the specified performance compared with a new battery. Different quantities have been used to indicate the SOH, e.g., impedance. As mentioned in Section 6.5, this dissertation considers the following quantity as a measure of the SOH.

$$SOH(n) = \frac{C_{\max}(n)}{C_{\max\_new}} \quad (7-14)$$

where  $n$  is the update index of the maximum capacity estimation algorithm, and  $C_{\max\_new}$  is the maximum capacity of a new battery cell. Such an SOH represents the capacity degradation of the cell. Also, it is clear that an accurate  $C_{\max}$  is a prerequisite for Coulomb counting-based SOC estimation algorithms to provide a good estimation of the SOC.

In [55] and [115], the maximum capacity is simply calculated as follows:

$$C_{\max} = \frac{T_s \sum_{k=k_1}^{k_2} \frac{\eta i_B(k)}{3600}}{SOC(k_2) - SOC(k_1)} \quad (7-15)$$

where  $k_1$  and  $k_2$  are the beginning and end time instants. Rearrangement of (7-15) gives the following linear regression form:

$$z = C_{\max} u \quad (7-16)$$

where  $u = SOC(k_2) - SOC(k_1)$  and

$$z = T_s \sum_{k=k_1}^{k_2} \frac{\eta_{i_B}(k)}{3600}.$$

Under certain conditions on  $z$  and  $u$ , an unbiased estimation of  $C_{\max}$  can be achieved by solving an LS problem. The solution has been widely used and is written as follows:

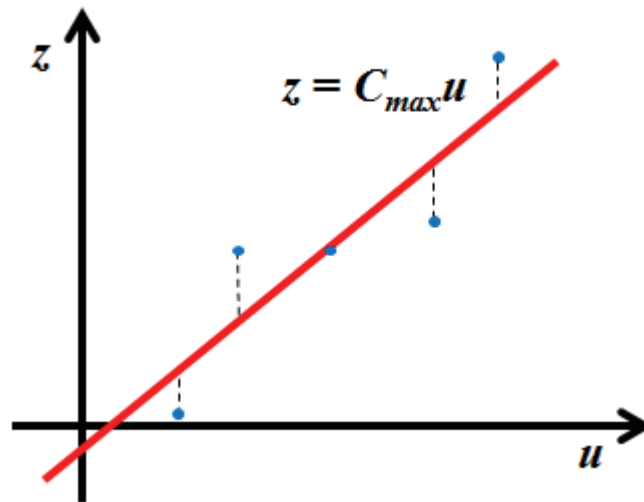
$$C_{\max} = (U_M^T U_M)^{-1} U_M^T Z_M \quad (7-17)$$

where  $U_M = [u(1), \dots, u(n)]^T$  and  $Z_M = [z(1), \dots, z(n)]^T$ . Figure 7.3(a) illustrates the concept of the LS method, where the dots represent the data points, the solid line represents the fitting line, and the dashed lines represent the vertical distances from the data points to the fitting line. The output of the standard LS method is accurate only if the estimated values of the SOC, i.e.,  $u$ , are correct. This is because the LS method minimizes the sum of the squared vertical distances between the data points and the fitting line. If the estimated SOC values are incorrect, the LS method leads to a biased maximum capacity estimation [80].

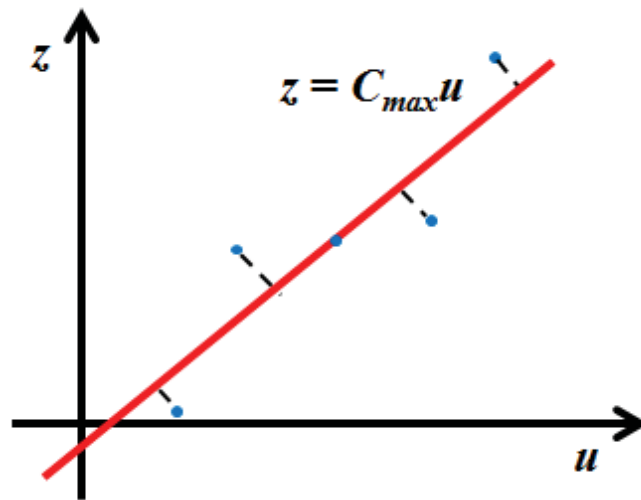
The total least square (TLS) algorithm was proposed to alleviate the limitation of the LS method when the elements of both the observation matrix  $U_M$  and the measurement matrix  $Z_M$  are inaccurate. Unlike the LS, the TLS performs the orthogonal regression which minimizes the sum of the squared orthogonal distances from the data points to the fitting line [117]. The idea of the TLS algorithm is illustrated in Figure 7.3(b), where the dashed lines represent the orthogonal distances from the data points to the fitting line. Therefore, TLS alleviates the limitation of the LS by performing orthogonal regression [117].

The TLS algorithm is generally solved by using singular value decomposition (SVD) methods [117] which incur high computational complexity and thus are not suitable for the embedded system [118]. A fast RTLS algorithm is applied for maximum capacity estimation [91]. The algorithm is based on the constrained Rayleigh quotient, which can run in real-time

and enjoys fast convergence [119]. Compared to the TLS, the proposed RTLS algorithm entails much lower computational load; and the estimation accuracy is comparable to the TLS algorithm.



(a)



(b)

Figure 7.3: Comparison of linear regression methods: (a) LS and (b) TLS.

To facilitate the presentation of the proposed algorithm, it is first assumed that (7-16) is represented with the noisy output and input given by

$$\underbrace{z(n) - \Delta z}_{\tilde{z}(n)} = C_{\max} \underbrace{(u(n) - \Delta u)}_{\tilde{u}(n)},$$

where  $u(n)$  and  $z(n)$  in (7-16) are the true input and output, respectively;  $\Delta z$  is output measurement error which is assumed to be a zero-mean Gaussian process with a known variance of  $\sigma_z^2$ ; and  $\Delta u$  is the SOC estimation error which is assumed to be a zero-mean Gaussian process with a known variance of  $\sigma_u^2$ . The autocorrelation matrix of the noisy input is defined as:

$$\tilde{R}_u(n) = E[\tilde{u}(n)\tilde{u}^T(n)] = R_u(n) + \sigma_u^2 \quad (7-18)$$

where  $R_u(n) = E[u(n)u^T(n)]$ . The augmented data is defined as  $\bar{x}(n) = [\tilde{u}(n), \tilde{z}(n)]^T$ . The autocorrelation matrix of  $\bar{x}(n)$  can be expressed as:

$$\bar{R}_x = E[\bar{x}(n)\bar{x}^T(n)] = \begin{bmatrix} R_u(n) & b_s(n) \\ b_s^T(n) & c_s(n) \end{bmatrix},$$

where  $b_s = E[\tilde{u}(n)\tilde{z}^T(n)]$  and  $c_s = E[\tilde{z}(n)\tilde{z}^T(n)]$ . When  $n$  is sufficiently large, the stochastic quantities  $R_u(n)$ ,  $b_s(n)$ , and  $c_s(n)$  can be expressed as follows [119]:

$$\begin{aligned} R_u(n) &= \mu R_u(n-1) + \tilde{u}(n)\tilde{u}^T(n), \\ b_s(n) &= \mu b_s(n-1) + \tilde{u}(n)\tilde{y}^T(n), \\ c_s(n) &= \mu c_s(n-1) + \tilde{y}(n)\tilde{y}^T(n), \end{aligned}$$

where  $\mu$  is the forgetting factor.

The maximum capacity estimation on the basis of (7-18) is performed by minimizing the following constrained Rayleigh quotient:

$$J(C_{\max}) = \frac{q_e^T \bar{R}_x q_e}{q_e^T \bar{D} q_e} = \frac{R_u C_{\max}^2 - 2b_s C_{\max} + c_s}{C_{\max}^2 + \beta_w} \quad (7-19)$$

where the eigenvector  $q_e = [C_{\max}, -1]^T$ , and  $\bar{D} = \text{diag}(1, \beta_w)$  is a diagonal weighting matrix with  $\beta_w = \sigma_y^2 / \sigma_u^2$ . If the eigenvector  $q_e^*$  which minimizes  $J(C_{\max})$  and corresponds to the smallest eigenvalue of  $\bar{R}_x$ , then  $q_e^*$  is the unbiased TLS solution [120].

To avoid solving the constrained Rayleigh quotient minimization problem at each step, the  $C_{\max}$  is assumed to be updated as follows:

$$C_{\max}(n) = C_{\max}(n-1) + \alpha_u(n) \tilde{u}(n), \quad (7-20)$$

where  $\alpha_u(n)$  is chosen to minimize (7-19) in the direction of  $\tilde{u}(n)$ , i.e.,

$$\frac{\partial J(C_{\max}(n-1) + \alpha_u(n) \tilde{u}(n))}{\partial \alpha_u(n)} = \frac{d_1 \alpha_u^2(n) + d_2 \alpha_u(n) + d_3}{d(\alpha_u(n))} = 0 \quad (7-21)$$

where

$$\begin{aligned} d_1 &= 2\tilde{u}^3(n) b_s(n), \\ d_2 &= 2\tilde{u}^2(n) (2b_s(n) C_{\max}(n-1) + \beta_w R_u(n) - c_s(n)), \\ d_3 &= 2\tilde{u}(n) [b_s(n) C_{\max}^2(n-1) - (\beta_w R_u(n) + c_s(n)) C_{\max}(n-1) + \beta_w b_s(n)] \end{aligned}$$

Then,  $\alpha_u(n)$  can be obtained by solving the following quadratic equation formed by the numerator term of (7-21):

$$d_1 \alpha_u^2(n) + d_2 \alpha_u(n) + d_3 = 0 \quad (7-22)$$

The quadratic equation (7-22) has two roots, from which the solution of  $\alpha_u(n)$  can be obtained as follows:

$$\alpha_u(n) = \frac{-d_2 + \sqrt{d_2^2 - 4d_1 d_3}}{2d_1} \quad (7-23)$$

The proposed RTLS method requires three running time-averaged estimations,  $d_1$ ,  $d_2$ , and  $d_3$ , to update  $\alpha_u(n)$ . On the other hand, the TLS method in [80] has six running time-averaged estimations and finds the optimal solution from four roots using the Ferrari method. Therefore, the proposed RTLS method has lower computational complexity and cost than the TLS method in [80].

## 7.5 Validation

Simulation and experimental studies were carried out to validate the condition monitoring algorithms for a lithium-ion battery cell subject to various pulsed current operations. Comparisons with the existing dual extended Kalman filter (DEKF) method [67] demonstrated the advantages of the proposed electrical circuit with hysteresis model-based condition monitoring strategy in Figure 7.1 in terms of accuracy measured by RMSE and computational cost measured by simulation time. The electrical circuit with hysteresis model-based condition monitoring strategy and the DEKF were implemented in MATLAB on a computer using Intel® Core™2 Duo CPU T6600@2.2GHz, 64-bit OS. The system parameters of the proposed algorithm and the DEKF were carefully selected to minimize the estimation error. The data of the cell voltage and current were collected from a battery tester under ambient temperature at 23 °C and then were used as the inputs for the algorithms.

### 7.5.1 Simulation Studies

The electrical circuit with hysteresis battery model is given by (3-36), and the parameters of the model are listed in Table 7.2. The initial states  $x(0)=[SOC(0) V_{ct}(0) V_h(0)]^T$  and maximum capacity  $C_{max}$  were set to be  $x(0)=[0.8 \ 0 \ 0]^T$  and 6 Ah, respectively; while the

true initial SOC and  $C_{\max}$  used in the Coulomb-counting method were 0.95 and 5 Ah, respectively. The value of  $N_0$  and  $\delta_1$  were defined as 50 and 0.995, respectively, for FUDRLS with the VF ( $\lambda_{\min} = 0.95$  and  $\lambda_{\max} = 0.995$ ). In the SVSF, the values of  $\gamma_s$  and  $\Psi$  were set to be 0.1 and 0.2. The input current was corrupted by a zero-mean Gaussian random number having the variance  $\sigma_z^2 = (0.01)^2$ . Assuming that the SOC estimation of SVSF that is the second input to RTLS achieved an accuracy of 1%, i.e.,  $\sigma_u = 0.01$ , an overall  $\sigma_u^2$  is  $2 \times (0.01)^2$ , since two estimates of SOC were required [80]. Therefore,  $\beta_w$  becomes  $(0.01)^2 / (2 \times (0.01)^2)$ . The forgetting factor  $\mu = 0.98$  was used for the RTLS. In addition, another model-based algorithm DEKF [67], which included an EKF for SOC estimation and another EKF for parameter estimation of impedance ( $R_s$ ,  $R_{ct}$ ,  $C_d$ ) and  $C_{\max}$ , was implemented to compare with the method developed. In the DEKF design, the initial state covariance, process noise covariance matrix, and measurement noise covariance matrix, used in the SOC estimation were defined as  $diag[1 \ 1 \ 1]$ ,  $diag[0.16 \ 0.16 \ 0.16]$ , and 0.25, respectively; and those for the EKF parameter estimation were specified as  $diag[10^{-13} \ 10^{-2} \ 10^{-3} \ 10^{-4}]$ ,  $diag[4 \times 10^{-13} \ 10^{-5} \ 10^{-6} \ 10^{-7}]$ , and 0.25, respectively.

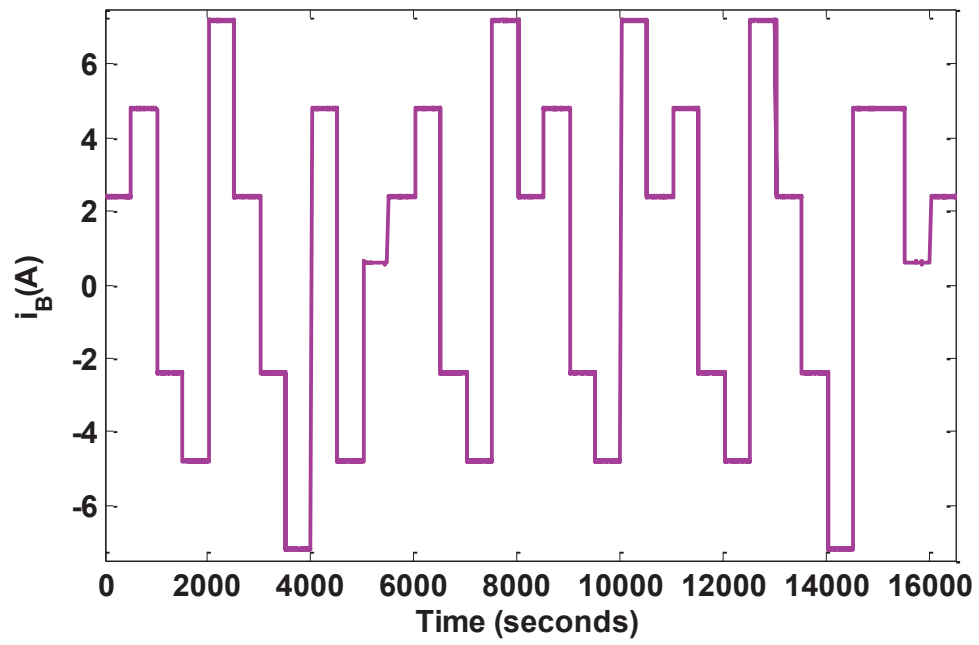
Table 7.2: Electrical circuit with hysteresis battery model parameters.

|             |        |          |                      |
|-------------|--------|----------|----------------------|
| $C_{\max}$  | 5 Ah   | $R_s$    | 0.08 ohm             |
| $C_d$       | 3000 F | $R_{ct}$ | 0.03 ohm             |
| $V_{h\max}$ | 0.01 V | $\rho$   | $2.47 \cdot 10^{-4}$ |
| $a_0$       | -0.852 | $a_1$    | 63.867               |
| $a_2$       | 3.692  | $a_3$    | 0.559                |
| $a_4$       | 0.51   | $a_5$    | 0.508                |

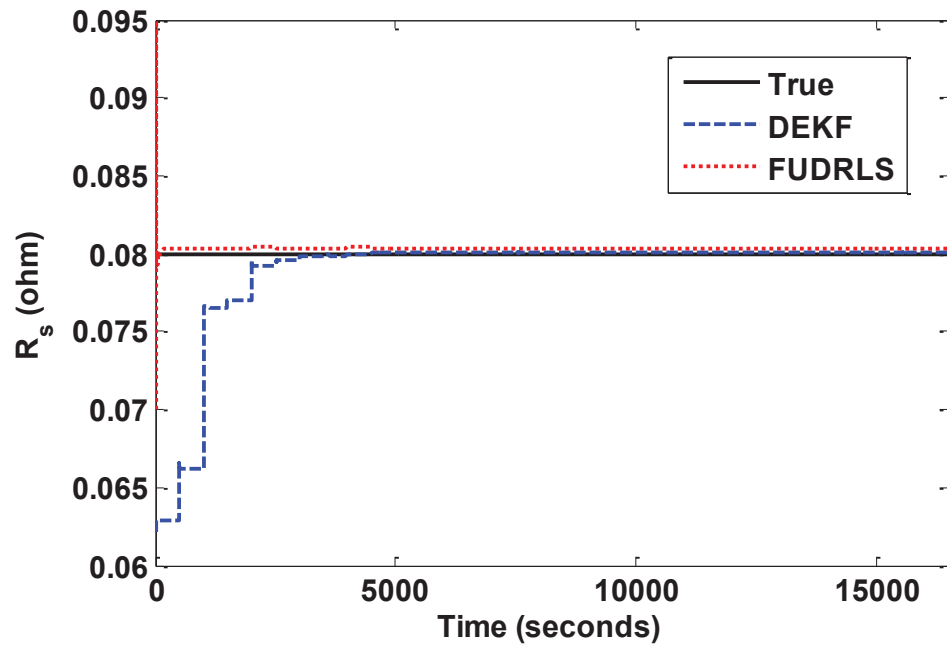
First, the FUDRLS was executed to estimate RC parameters of the electrical circuit battery model; and then SVSF was executed to estimate SOC with a small sampling period, e.g.,  $T_s = 1$  second, to keep track of the fast time-varying electrical parameters and SOC of

the cell. A large time scale, e.g.,  $T_l = 200$  seconds, was used in the execution of the RTLS for tracking the maximum capacity. The DEKF was executed with a small time scale, e.g.,  $T_s = 1$  second.

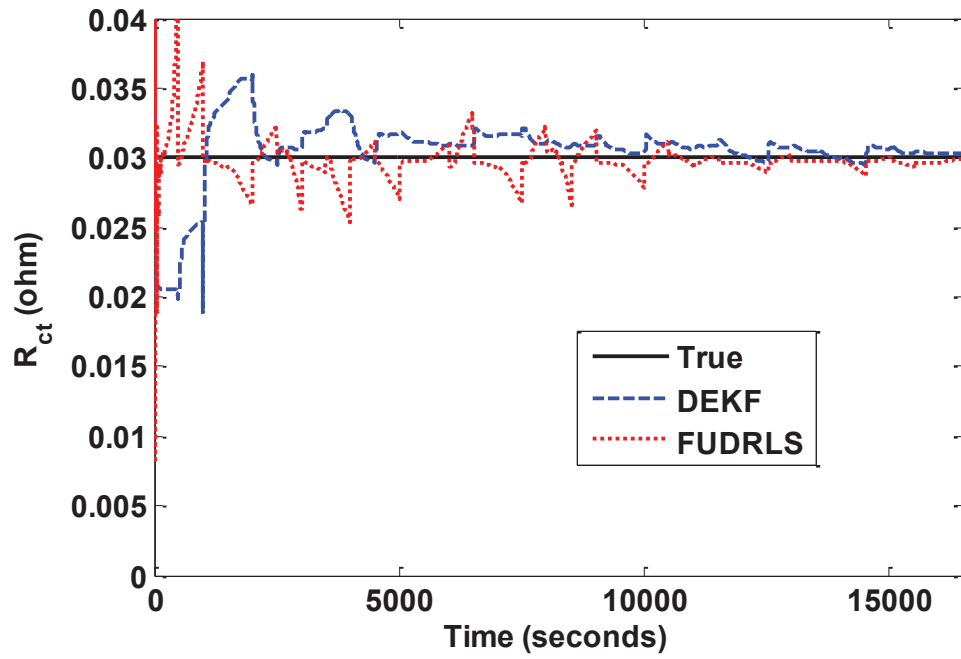
The results are shown in Figure 7.4. The battery cell was operated by a dynamic noisy current cycle, shown in Figure 7.4(a). Figure 7.4(b)-(d) shows the impedances of the battery estimated by using the online parameter identification algorithm. It has been shown that the FUDRLS with the VF converges to the true values faster than the DEKF method. Table 7.3 illustrates a comparison of the performance evaluation metrics. The results clearly indicate that the FUDRLS parameter identification algorithm works better than the DEKF in terms of accuracy and convergence speed. Figure 7.4(e) compares the estimated SOCs from DEKF and the proposed SVSF algorithm with the true SOC from the Coulomb-counting method. The SVSF algorithm converges to the true value faster than DEKF. The estimated SOC from the SVSF algorithm matched that obtained from Coulomb Counting better than those obtained from the DEKF after a certain period. Figure 7.4(f) compares the  $C_{\max}$  obtained from the RTLS algorithm and the DEKF with true maximum capacity. The result confirmed that the RTLS algorithm converged to the true maximum quickly; the DEKF method was worse than the method. Table 7.4 compares the performance evaluation matrices. The results clearly show that the electrical circuit with hysteresis model-based algorithms outperform the DEKF in terms of higher accuracy and lower computational cost.



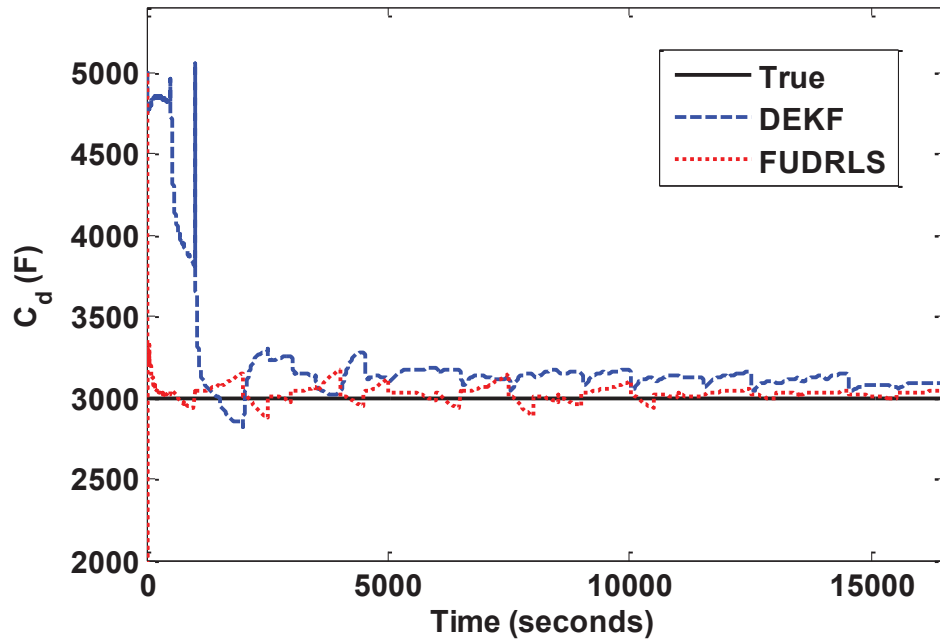
(a)



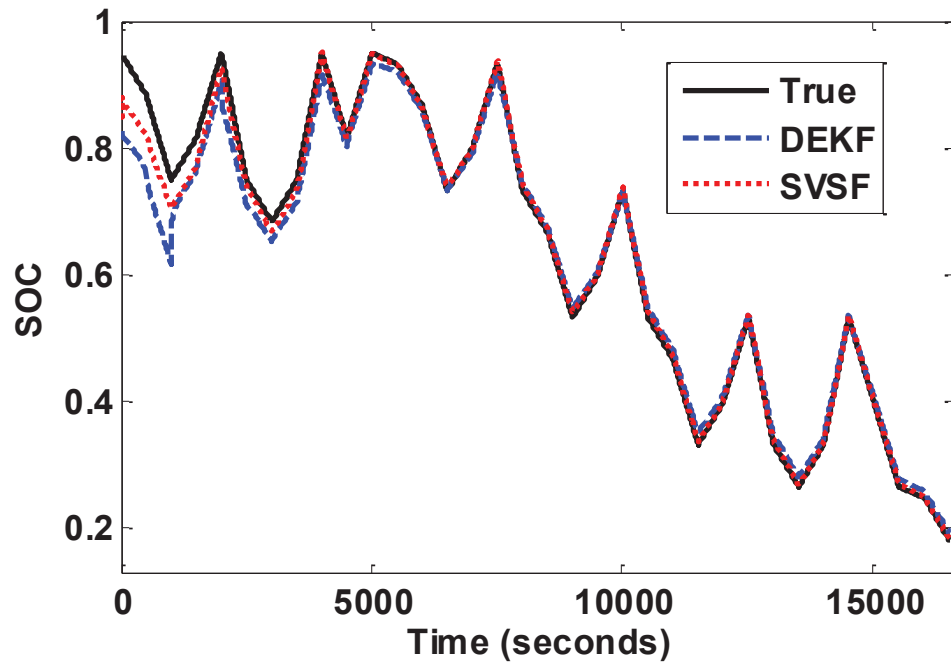
(b)



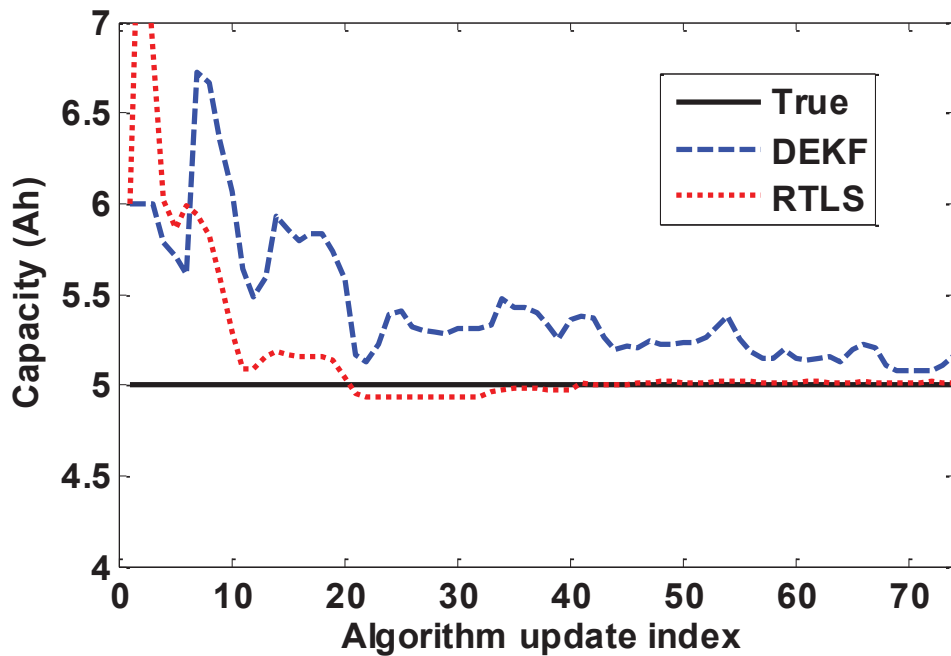
(c)



(d)



(e)



(f)

Figure 7.4: Comparison of true and estimated impedance, SOC, and maximum capacity of the battery cell from the proposed condition monitoring algorithms and DEKF: (a) input current profile; (b)  $R_s$ ; (c)  $R_{ct}$ ; (d)  $C_d$ ; (e) SOC; and (f)  $C_{max}$ .

Table 7.3: Comparison of RMSEs for the parameter identification algorithms.

| Parameter      | DEKF   | FUDRLS    |
|----------------|--------|-----------|
| $R_s$ (ohm)    | 0.0039 | 4.1559E-4 |
| $R_{ct}$ (ohm) | 0.0024 | 0.0162    |
| $C_d$ (F)      | 391.85 | 64.63     |

Table 7.4: Comparison of RMSEs and computational times for the SOC and the capacity estimation algorithms.

| Method                       | Proposed Algorithms |        |          | DEKF         |       |          |
|------------------------------|---------------------|--------|----------|--------------|-------|----------|
|                              | FUDRLS              | SVSF   | RTLS     | Impedance    | SOC   | Capacity |
| Parameter                    | Impedance           | SOC    | Capacity | Impedance    | SOC   | Capacity |
| Accuracy (RMSE)              | In Table 7.3        | 0.0191 | 0.4858   | In Table 7.3 | 0.038 | 0.5287   |
| Computational time (seconds) | 3.0822              | 11.093 | 0.0212   | 23.52        |       |          |

## 7.5.2 Experimental Studies

The model-based condition monitoring algorithms were further validated using the measured data of a lithium-ion battery cell from the Advanced Technology R&D Center, Mitsubishi Electric Corporation. The parameters of the model-based condition monitoring algorithms are shown in Table 7.5. In the DEKF design, the initial state covariance, process noise covariance matrix, and measurement noise covariance matrix, used in the EKF for SOC estimation were defined as  $diag[1 \ 1 \ 1]$ ,  $diag[0.16 \ 0.16 \ 0.16]$ , and 0.25, respectively; and those of the EKF for parameter estimation were specified as  $diag[10^{-14} \ 10^{-4} \ 10^{-5} \ 10^{-6}]$ ,  $diag[4 \times 10^{-10} \ 10^{-7} \ 10^{-10} \ 10^{-11}]$ , and 0.25, respectively. The true SOC trajectory was obtained using the Coulomb-counting method. The parameters of the OCV-SOC function of the battery cell were extracted under ambient temperature at 23 °C [95]. The initial states  $x(0)$

and maximum capacity were set to be  $x(0) = [0.4 \ 0 \ 0]^T$  and 5 Ah, respectively, while the true initial SOC and  $C_{\max}$  used in the Coulomb-counting method were 0.31 and 4.732 Ah, respectively. In order to set the test battery cell with the desired initial SOC, the battery cell was first fully charged and rested for one hour. Then the cell was discharged, using a small current, e.g., 0.2 A, to the desired initial SOC values. The true maximum capacity was extracted offline from a full discharge test with a small current, e.g., 0.2 A, at ambient temperature before testing the battery.

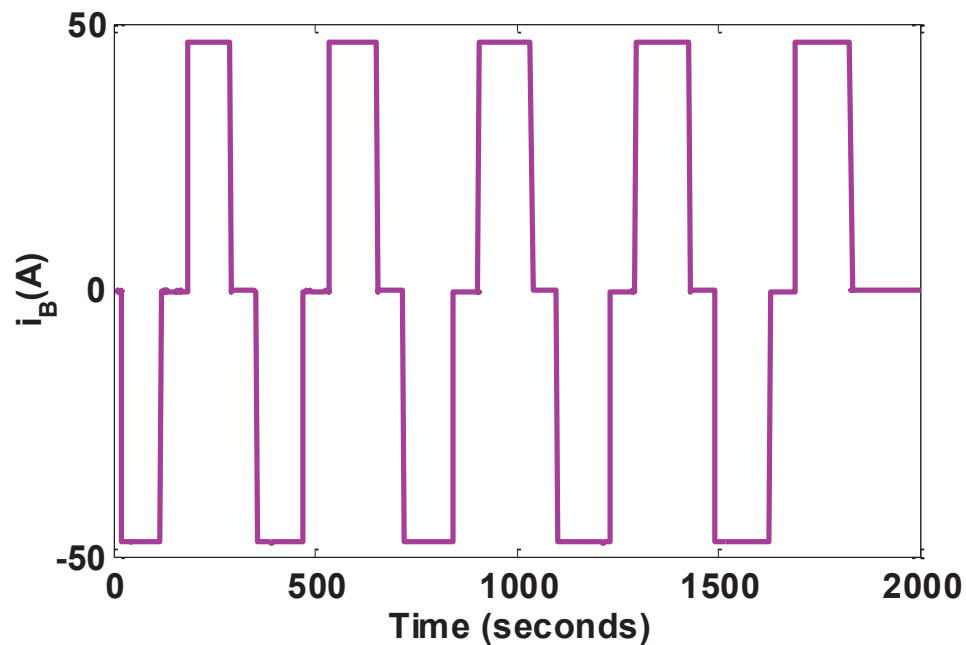
Table 7.5: Parameters of the proposed condition monitoring algorithms.

|                 |             |                 |            |        |      |
|-----------------|-------------|-----------------|------------|--------|------|
| $\lambda_{min}$ | 0.95        | $\lambda_{max}$ | 0.995      | $N_0$  | 50   |
| $\delta_l$      | 0.995       | $\gamma$        | 0.1        | $\Psi$ | 1    |
| $\sigma_u^2$    | $2(0.02)^2$ | $\sigma_z^2$    | $(0.01)^2$ | $\mu$  | 0.98 |
| $T_s$           | 1 second    | $T_l$           | 20 seconds |        |      |

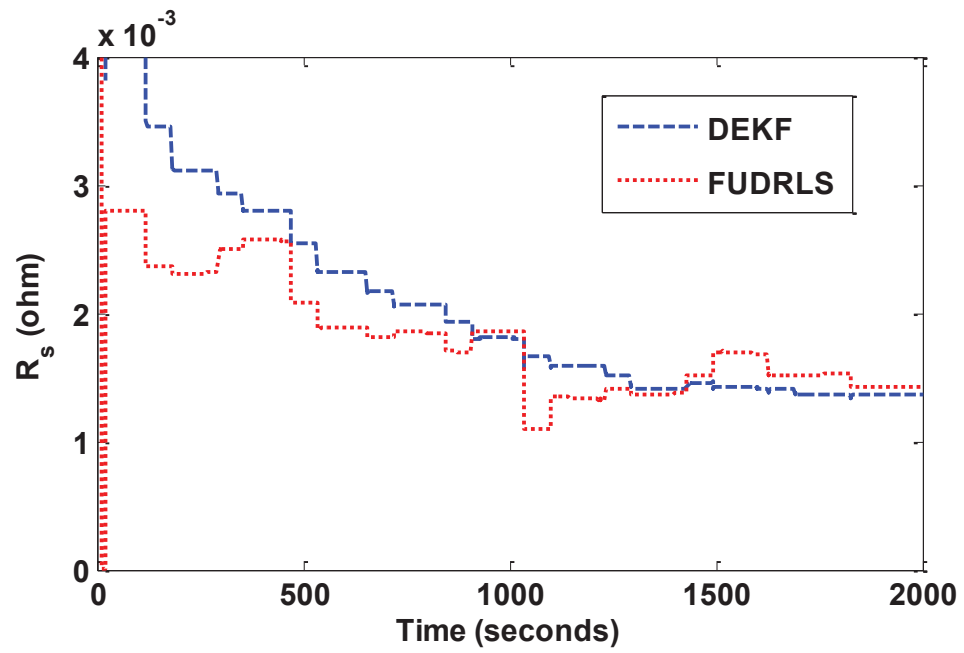
First, the FUDRLS was executed to estimate impedances (RC parameters) of the electrical circuit battery model; and then SVSF was executed after 30 seconds to estimate SOC with a small sampling period, e.g.,  $T_s = 1$  second, to keep track of the fast time-varying electrical parameters and SOC of the cell. A large time scale, e.g.,  $T_l = 20$  seconds, was used in the execution of the proposed RTLS for tracking the  $C_{\max}$ . The DEKF was executed with a small time scale, e.g.,  $T_s = 1$  second. The estimation results are shown in Figure 7.5. The battery cell was operated by a dynamic high pulse current cycle ( $i_B = 10C$ ), shown in Figure 7.5(a). Figure 7.5(b)-(d) shows the impedances of the battery estimated by using the proposed FUDRLS online parameter identification algorithm. Figure 7.5(e) compares the estimated SOC from DEKF and the proposed SVSF algorithm with the true SOC from the Coulomb-counting method. The estimated SOC from the proposed SVSF algorithm matched that

obtained from Coulomb counting better than those obtained from DEKF after a certain period. The maximum error was less than 2% after 1000 seconds. Figure 7.5(e) compares the  $C_{\max}$  obtained from the proposed RTLS algorithm and the DEKF with true maximum capacity. The RTLS algorithm converged to the true maximum quickly; while the DEKF method was worse than the RTLS algorithm, as shown in Figure 7.5(f). Table 7.6 compares the performance evaluation matrices for different methods. The results clearly show that the proposed method exceeded the DEKF in terms of higher accuracy and lower computational cost. Furthermore, the implementation of the proposed method was simpler than DEKF; and the system parameters of the proposed method were easier to tune compared with the DEKF.

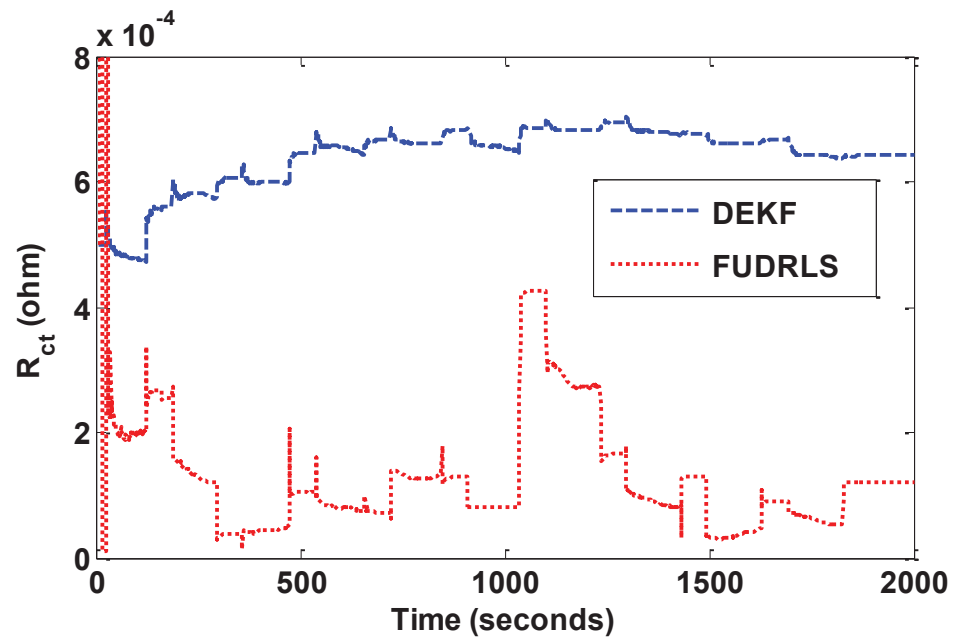
Therefore, these results again clearly show that the proposed algorithms quickly, easily, and accurately estimated impedance, SOC, and maximum capacity and, therefore, are suitable for real-time embedded BMSs for various applications.



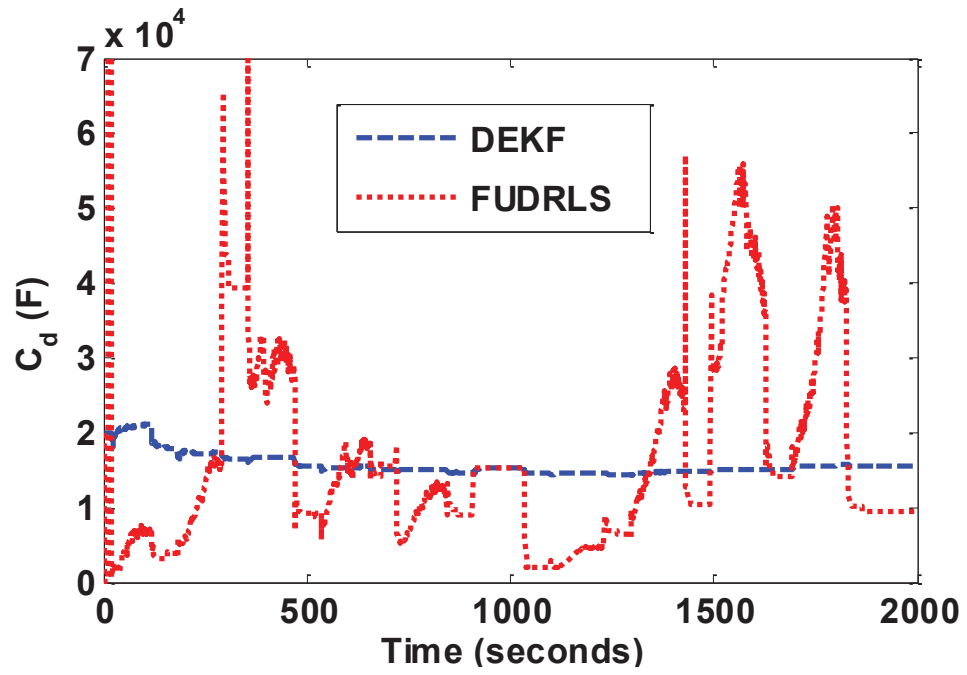
(a)



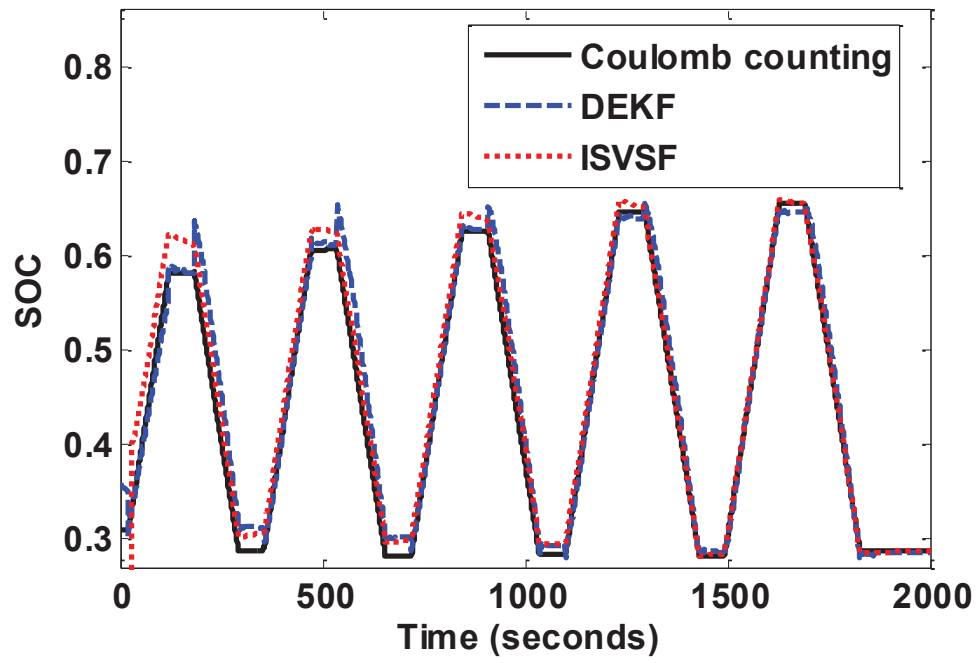
(b)



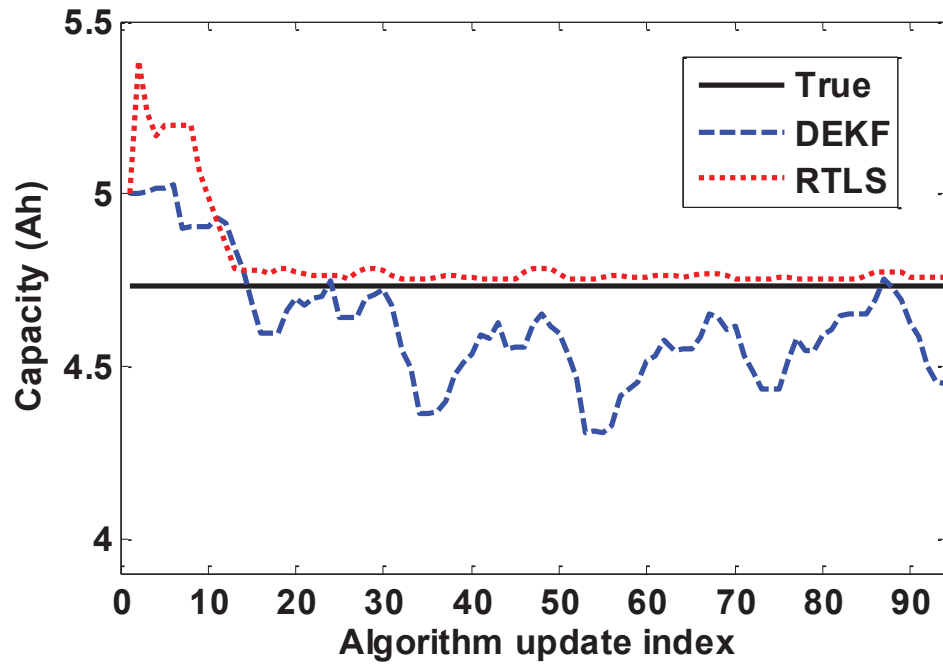
(c)



(d)



(e)



(f)

Figure 7.5: Comparison of estimated impedance, SOC, and maximum capacity from the proposed condition monitoring algorithms and DEKF on the experimental data: (a) the pulse current cycle ( $i_B = 10C$ ) applied to the battery; (b)  $R_s$ ; (c)  $R_{ct}$ ; (d)  $C_d$ ; (e) SOC; and (f)  $C_{max}$

Table 7.6: Comparison of RMSEs and computational times for the SOC and the capacity estimation algorithms on the experimental data.

| Method                       | Proposed Algorithms |        |          | DEKF      |        |          |
|------------------------------|---------------------|--------|----------|-----------|--------|----------|
|                              | FUDRLS              | SVSF   | RTLS     | Impedance | SOC    | Capacity |
| Parameter                    | Impedance           | SOC    | Capacity | Impedance | SOC    | Capacity |
| Accuracy (RMSE)              | N/A                 | 0.0171 | 0.1617   | N/A       | 0.0220 | 0.2065   |
| Computational time (seconds) | 0.1474              | 0.9070 | 0.0061   | 2.0795    |        |          |

## 7.6 Chapter Summary

This chapter introduced novel model-based condition monitoring algorithms for real-time impedance, SOC, and SOH estimation of a lithium-ion battery. The proposed algorithms have been implemented in MATLAB and validated by simulation and experimental results for a lithium-ion battery. The proposed algorithms can be applied to any type of lithium-ion battery, especially batteries having the hysteresis effect. Owing to low complexity and high accuracy, the proposed condition monitoring algorithms can be suitable for real-time embedded BMSs for various applications, such as EVs and PHEVs. In addition, the proposed condition monitoring algorithms will be extended to SOP and SOF estimation and battery prognosis and fault diagnosis research.

## CHAPTER 8: CONCLUSIONS, CONTRIBUTIONS, AND RECOMMENDATIONS FOR FUTURE RESEARCH

### 8.1. Conclusions of This Dissertation

This dissertation has presented a novel BMS for condition monitoring and power management of rechargeable multicell batteries to ensure the safety, reliability, and optimal performance of the batteries. It has addressed the following three main objectives:

- *Objective I:* Develop high-fidelity battery models for a BMS.
- *Objective II:* Develop the typology, hardware and control design for a novel power-electronics-enabled, self-X, multicell battery.
- *Objective III:* Develop condition monitoring algorithms for a BMS.

The following conclusions can be drawn based on the fulfillment of the dissertation's research. First, research was conducted on developing high-fidelity battery models for simulation and online condition monitoring of battery cells. The battery models are capable of capturing the dynamic circuit characteristics, nonlinear capacity effects, nonlinear hysteresis effect, and temperature effect of the battery cells.

Second, the research was conducted on a novel power-electronics-enabled, self-X, multicell battery design. The resulting self-X battery systems can automatically configure themselves according to the dynamic energy supply/storage demand and the condition of each battery cell, such as self-healing from failures of cells and self-balancing towards the maximum storage capacity, optimal or improved energy conversion efficiency, and prolonged battery operating time and lifespan. These features can be achieved by the

proposed self-X design and novel management systems, which are based on state-of-the-art technologies in power electronics, sensing, signal processing, modeling, control, optimization, and high-performance computation. A system-level, self-X multicell battery design for EV/PHEV applications was proposed to show the scalability of the proposed design as well as interconnection with a proposed DC/DC converter for charge, discharge, and cell balancing control of the self-X multicell battery.

Moreover, a condition monitoring algorithm is essential for a BMS. The condition monitoring of a battery involves tracking the changes in the parameters, such as maximum capacity and internal impedance, and states, such as SOC, SOH, SOP, and SOF, related to the operating and health conditions of the battery. Novel condition monitoring algorithms for lithium-ion batteries have been developed, including impedance estimation, SOC estimation, and maximum capacity estimation for SOH calculation. The main advantages of the proposed condition monitoring algorithms include high accuracy, low computational cost, and simple implementation. Therefore, the methods are suitable for use in a real-time embedded BMS.

## **8.2. Contributions of This Dissertation**

The major contributions of this research based on the three objectives are summarized. The main contribution of Objective I is that novel battery models have been proposed for battery simulation and BMS, such as model-based condition monitoring. The detailed contributions of Objective I are listed as follows:

- Developed the enhanced hybrid battery model, which is capable of accurately predicting major runtime characteristics of the batteries in the discharge and

charge modes as well as various C-rates and ambient temperatures in the operating ranges of the batteries.

- Developed simplified hybrid battery model which can be used in a real-time embedded system.
- Developed an electrical circuit battery model incorporating hysteresis which is capable of accurately predicting the dynamic circuit characteristics and the hysteresis effect of a battery. This model can be applied to any type of lithium-ion batteries, especially batteries having a strong hysteresis effect as it can be used in a real-time embedded system.

The main contribution of objective II is that self-X multicell battery architecture, where self-X stands for self-reconfiguration, self-balance, self-healing, and self-optimization, has been developed. The resulting battery system can dynamically configure itself during operation according to the load/storage demand and the condition of each cell in order to achieve self-healing from failures of single or multiple cells, self-balancing from cell state variations, and self-optimizing for optimal energy conversion efficiency. The detailed contributions are as follows:

- Developed cell switching circuits to fully control charge, discharge, and cutoff for individual cells in multicell batteries.
- Developed new gate drive circuits for controlling ON/OFF of each switch in the cell switching circuit.
- Designed a self-X multicell battery module which is connected with a DC/DC converter. Validated the self-X multicell battery module to be used as a variable voltage source and that it is possible to charge/discharge and balance the battery

module connected via the DC/DC converter using simulation and experimental studies.

- Designed a self-X multimodule battery system with a DC/DC converter for EV/PHEV applications. Validated the charge/discharge and balance of the self-X multimodule battery system with the DC/DC converter connected to an EV load via simulation studies.

The main contribution of Objective III is that new model-based condition monitoring algorithms have been developed and validated using global optimization algorithms, regressions, and nonlinear observers, filter theories, etc. The detailed contributions are listed as follows:

- Developed online parameter identification algorithms using: PSO, MWLS, and FUDRLS methods. The FUDRLS with a variable forgetting factor demonstrate better performance than existing regression methods, such as RLS and UDRLS.
- Developed SOC estimation algorithms using: PSO, ADSMO, SVSF, and ISVSF.
- Developed maximum capacity/SOH estimation algorithms using: two-point method and RTLS.

### **8.3 Recommendations for Future Research**

The recommendations for future work include:

- Develop self-X smart battery hardware to fill the need for renewable energy, electric transportation, and electric grid applications. Investigate

communication issue, efficient sensing technology, and grounding issue large-scale battery systems.

- Analyze how the reconfiguration flexibility can assist the charge scenario of the widely used lithium-ion battery systems in detail. Also, develop a DC/DC or an AC/DC charger for a self-X multicell battery.
- Develop a battery model characterizing the aging effect of battery cells. As a battery ages, its physical characteristics, such as solid electrolyte interface (SEI) resistance and other parameters, changes. To accurately capture the dynamic behaviors of a battery when it ages, some parameters of the battery model need to be adapted to the aging process of the battery.
- Improve and validate the condition monitoring algorithms using the hardware-in-the-loop test and implement them in a real imbedded system.
- Develop adaptive condition monitoring algorithms which are robust to the color noise, input error, temperature, and aging of the batteries in practical EVs and PHEVs.
- Develop fault prognosis and fault diagnosis algorithms baed on the condition monitoring algorithms.

## BIBLIOGRAPHY

- [1] H. Qian, J. Zhang, J.-S. Lai, and W. Yu, "A high-efficiency grid-tie battery energy storage system," *IEEE Trans. Power Electron.*, vol. 26, no. 3, pp. 886–896, Mar. 2011.
- [2] H. Zhou, T. Bhattacharya, D. Tran, T. S. T. Siew, and A. M. Khambadkone, "Composite energy storage system involving battery and ultracapacitor with dynamic energy management in microgrid applications," *IEEE Trans. Power Electron.*, vol. 26, no. 3, pp. 923–930, Mar. 2011.
- [3] K.-Y. Lo, Y.-M. Chen, and Y.-R. Chang, "MPPT battery charger for standalone wind power system," *IEEE Trans. Power Electron.*, vol. 26, no. 6, pp. 1631–1638, Jun. 2011.
- [4] M. Bragard, N. Soltau, S. Thomas, and R. W. De Doncker, "The balance of renewable sources and user demands in grids: Power electronics for modular battery energy storage systems," *IEEE Trans. Power Electron.*, vol. 25, no. 12, pp. 3049–3056, Dec. 2010.
- [5] L. Maharjan, T. Yamagishi, H. Akagi, and J. Asakura, "Fault-tolerant operation of a battery-energy-storage system based on a multilevel cascade PWM converter with star configuration," *IEEE Trans. Power Electron.*, vol. 25, no. 9, pp. 2386–2396, Sep. 2010.
- [6] L. Lu, X. Han, Jianqie Li, Jianfeng Hua, and Minggao Ouyang, "A review on the key issues for lithium-ion battery management in electric vehicles," *J. Power Sources*, vol. 226, pp. 272–288, Mar. 2013.

- [7] O. Erdinc, B. Vural, and M. Uzunoglu, "A dynamic lithium-ion battery model considering the effects of temperature and capacity fading," in *Proc. International Conference on Clean Electrical Power*, Jun. 2009, pp. 383-386.
- [8] N. H. Kutkut, H. L. N. Wiegman, D. M. Divan, and D. W. Novotny, "Design considerations for charge equalization of an electric vehicle battery system," *IEEE Trans. Ind. Appl.*, vol. 35, no. 1, pp. 28-35, Jan. 1999.
- [9] T. Kim, W. Qiao, and L. Qu, "A multicell battery system design for electric and plug-in hybrid electric vehicles," in *Proc. IEEE International Electric Vehicle Conference*, Mar. 2012, pp. 1-7.
- [10] V. Marano, S. Onori, Y. Guezennec, G. Rizzoni, and N. Madella, "Lithium-ion batteries life estimation for plug-in hybrid electric vehicles," in *Proc. 5th IEEE Vehicle Power and Propulsion Conference*, Sep. 2009, pp. 536-543.
- [11] D. Linden and T. B. Reddy, *Handbook of Batteries*, 3rd ed., McGraw-Hill, 2001.
- [12] Electronic Publication: MAX 11080 Datasheet, "12-channel, high voltage battery-pack fault monitor," MAXIM.
- [13] J. Cao, N. Schofield, and A. Emadi, "Battery balancing methods: A comprehensive review," in *Proc. IEEE Vehicle Power and Propulsion Conference*, Sep. 2008, pp. 1-6.
- [14] J. Shin, G. Seo, C. Chun, and B. Cho, "Selective flyback balancing circuit with improved balancing speed for series connected lithium-ion batteries," in *Proc. International Power Electronics Conference*, Jun. 2010, pp. 1180-1184.

- [15] A. C. Baughman, and M. Ferdowsi, "Double-tiered switched-capacitor battery charge equalization technique," *IEEE Trans. Ind. Electron.*, vol. 55, no. 6, pp. 2277-2285, Jun. 2008.
- [16] S. T. Huang, D. C. Hopkins, and C. R. Mosling, "Extension of battery life via charge equalization control," *IEEE Trans. Ind. Electron.*, vol. 40, no. 1, pp. 96-104, Feb. 1993.
- [17] Electronic Publication: BQ 102 Datasheet, "Power LAN dual-cell Li-ion battery monitor with power pump cell balancing," Texas Instrument.
- [18] H. Visairo and P. Kumar, "A reconfigurable battery pack for improving power conversion efficiency in portable devices," in *Proc. 7th International Caribbean Conference on Devices, Circuits and Systems*, Apr. 2008, pp. 1-6.
- [19] S. Ci, J. Zhang, H. Sharif, and M. Alahmad "A novel design of adaptive reconfigurable multicell battery for power-aware embedded networked sensing system," in *Proc. IEEE Global Telecommunication Conference*, Nov. 2007, pp. 1043-1047.
- [20] S. K. Mandal, P. S. Bhojwani, S. P. Mohanty, and R. N. Mahapata, "IntellBatt: Towards smarter battery design," in *Proc. 45th Annual ACM/IEEE Design Automation Conference*, Jun. 2008, pp. 872-877.
- [21] S. Ci, J. Zhang, H. Sharif, and M. Alahmad, "Dynamic reconfigurable multi-cell battery: A novel approach to improve battery performance," in *Proc. The Annual IEEE Applied Power Electronics Conference and Exposition*, Feb. 2012, pp. 439-442.

- [22] H. Kim and K. G. Shin, "DESA: Dependable, efficient, scalable architecture for management of large scale batteries," *IEEE Trans. Ind. Informat.*, vol. 8, no. 2, pp. 406-417, May 2012.
- [23] S. A. Gadsden, M. Al-Shabi, and S. R. Habibi, "Estimation strategies for the condition monitoring of a battery system in a hybrid electric vehicle," *ISRN Signal Processing*, vol. 2011, Feb. 2011.
- [24] B. S. Bhangu, P. Bentley, D. A. Stone, and C. M. Bingham, "Nonlinear observers for predicting state-of-charge and state-of-health of lead-acid batteries for hybrid-electric vehicles," *IEEE Trans. Veh. Tech.*, vol. 54, no. 3, pp. 783-794, May 2005.
- [25] D. Andrea, *Battery Management Systems for Large Lithium-ion Battery Packs*, Artech House, 2010.
- [26] Electronic Publication: 30016 Datasheet, "Lithium-ion battery: Li-18650 3.7V 2600mAh with PCM+Cap," TENERGY.
- [27] T. Kim, "Hybrid battery modeling capable of capturing dynamic circuit characteristics and nonlinear capacity effects," Master thesis, The University of Nebraska-Lincoln, 2012.
- [28] L. W. Juang, "Online Battery Monitoring for state-of-charge and power capability prediction," Master thesis, The University of Wisconsin-Madison, 2010.
- [29] Q. Wang, P. Ping, X. Zhao, G. Chu, J. Sun, and C. Chen, "Thermal runaway caused fire and explosion of lithium ion battery," *J. Power Sources*, vol. 208, pp. 210-224, Jun. 2012.

- [30] B. Saha, K. Goebel, S. Poll, and J. Christophersen, "Prognostics methods for battery health monitoring using a bayesian framework," *IEEE Trans. Instrumentation and Measurement*, vol. 58, no. 2, pp. 291–296, Feb. 2009.
- [31] J. Zhang and J. Lee, "A review on prognostics and health monitoring of Li-ion battery," *J. Power sources*, vol.196, no. 15, pp. 6007-6014, Aug. 2011.
- [32] J. Zhang, "Bidirectional DC-DC power converter design optimization, modeling and control," Ph.D. Dissertation, Virginia Polytechnic Institute and State University, 2008.
- [33] A. Eddahech, O. Briat, and J. Vinassa, "Real-time SOC and SOH estimation for EV Li-ion cell using online parameters identification," in *Proc. IEEE Energy Convers. Congr. Expo.*, Sep. 2012, pp. 4501-4505.
- [34] M. Doyle, T. F., Fuller, and J. Newman, "Modeling of galvanostatic charge and discharge of the lithium/polymer/insertion cell," *J. Electrochem. Soc.*, vol. 140, no. 6, pp.1526-1533, Jun. 1993.
- [35] D. Zhang, B. N. Popov, and R. E. White, "Modeling lithium intercalation of a single spinel particle under potentiodynamic control," *J. Electrochem. Soc.*, vol. 147, no. 3, pp. 831-838, Mar. 2000.
- [36] V. Subramanian, J. Ritter, and R. E. White, "Review of models for predicting the cycling performance of lithium ion batteries," *J. Power Sources*, vol. 156, no. 2, pp. 620-628, Jun. 2006.
- [37] J. Marcicki, M. Canova, A. T. Conliks, and G. Rizzoni, "Design and parameterization analysis of a reduced-order electrochemical model of graphite/LiFePO<sub>4</sub> cells for SOC/SOH estimation," *J. Power Sources*, vol. 237, pp. 310-324, Sep. 2013.

- [38] K. A. Smith, "Electrochemical modeling, estimation and control of lithium ion batteries," Ph.D thesis, Pennsylvania state university, 2006.
- [39] K. Murashko, J. Pyrhonen, and L. Laurila, "Three-dimensional thermal model of a lithium ion battery for hybrid mobile working machines: determination of the model parameters in a pouch cell," *IEEE Trans. Energy Convers.*, vol. 28, no. 2, pp. 335-343, Jun. 2013.
- [40] A. Seaman, T. Dao, and J. McPhee, "A survey of mathematics-based equivalent-circuit and electrochemical battery models for hybrid and electric vehicle simulation," *J. Power Sources*, vol. 256, pp. 410-423, Jun. 2014.
- [41] C. R. Gould, C. M. Bingham, D. A. Stone, and P. Bentley, "New battery model and state-of-health determination through subspace parameter estimation and state-observer techniques," *IEEE Trans. Veh. Technol.*, vol. 58, no. 8, pp. 3905-3916, Oct. 2009.
- [42] M. Chen and G. A. Rincon-Mora, "Accurate electrical battery model capable of predicting runtime and I-V performance," *IEEE Trans. Energy Convers.*, vol. 21, no.2, pp. 504-511, Jun. 2006.
- [43] H. Zhang and M. Chow, "Comprehensive dynamic battery modeling for PHEV applications," in *Proc. IEEE Power and Energy Soc. General Meeting*, Jul. 2010, pp. 1-6.
- [44] X. Hu, S. Li, and H. Peng. "A comparative study of equivalent circuit models for Li-ion batteries," *J. Power Sources*, vol. 198, pp. 359-367, Jan. 2012.

- [45] S. Tian, M. Hong, and M. Ouyang, "An experimental study and nonlinear modeling of discharge I-V behavior of valve-regulated lead-acid batteries," *IEEE Trans. Energy Convers.*, vol. 24, no. 2, pp. 452-458, Jun. 2103.
- [46] O. Erdinc, B. Vural, and M. Uzunoglu, "A dynamic lithium-ion battery model considering the effects of temperature and capacity fading," in *Proc. Int. Conf. Clean Electrical Power*, Jun. 2009, pp. 383-386.
- [47] J. Zhang, S. Ci, Sharif, and M. Alahmad, "An enhanced circuit-based model for single-cell battery," in *Proc. 25th Annual IEEE Applied Power Electronics Conference and Exhibition*, Feb. 2010, pp. 672-675.
- [48] D. Rakhmatov, S. Vrudhula, and A. Wallach, "An analytical high-level battery model for use in energy management of portable electronic systems," in *Proc. Int. Conf. Computer Aided Design*, Nov. 2001, pp 488-493.
- [49] J. F. Manwell and J. G. Mcgowan, "Lead acid battery storage model for hybrid energy system," *Solar Energy*, vol. 50, no.5, pp. 399-405, May 1993.
- [50] N. Hammad, "Vehicle valve regulated lead acid battery modeling and fault diagnosis," SAE Technical Paper 2010-01-0028, 2010.
- [51] J-N. Juang, *Applied System Identification*, Technology & Engineering, 1994.
- [52] M. A. Roscher, O. S. Bohlen, and D. U. Sauer, "Reliable state estimation of multicell lithium-ion battery systems," *IEEE Trans. Energy Convers.*, vol. 26, no. 3, pp. 737-743, Sep. 2011.
- [53] W. Gao, M. Jiang, and Y. Hou, "Research on PNGV model parameter identification of LiFePO<sub>4</sub> Li-ion battery based on FMRLS," In *Proc. IEEE Industrial Electronics and Applications*, Jun. 2011, pp. 2294-2297.

- [54] H. R. Eichi and M. Chow, "Adaptive parameter identification and state-of-charge estimation of lithium-ion batteries," in *Proc. 38th Annual Conference of the IEEE Industrial Electronics Society*, Oct. 2012, pp. 4012-4017.
- [55] T. Kim, W. Qiao, and L. Qu, "Online SOC and SOH estimation for multicell lithium-ion batteries based on an adaptive hybrid battery model and sliding-mode observer," in *Proc. IEEE Energy Convers. Congr. Expo.*, Sep. 2013, pp. 292-298.
- [56] X. Tang, X. Mao, J. Lin, and B. Koch, "Li-ion battery parameter estimation for state of charge," in *Proc. American Control Conf.*, Jun.-Jul. 2011, pp. 941-946.
- [57] T. R. Fortescue, L. S. Kershenbaum, and B. E. Ydstie, "Implementation of self-tuning regulators with variable forgetting factors," *Automatica*, vol. 17, no. 6, pp. 831-835, Nov. 1981.
- [58] V. Pop, H. J. Bergveld, P. H. L. Notten, and P. P. L. Regtien, "State-of-the-art of battery state-of-charge determination," *Measurement Science and Technology*, vol. 16, no.12, pp. 93-110, Oct. 2005.
- [59] W. X. Shen, K. T. Chau, and C. C. Chan, "Neural network-based residual capacity indicator for nickel-metal hydride batteries in electric vehicles," *IEEE Trans. Veh. Tech.*, vol. 54, no. 5, pp. 1705-1712, Sep. 2005.
- [60] S. Malkhandi, "Fuzzy logic-based learning system and estimation of state of charge of lead-acid battery," *Eng. Appl. Artif. Intel.*, vol. 19, pp. 479-485, 2006.
- [61] T. Hansen and C. Wang, "Support vector based battery state of charge estimator," *J. Power Sources*, vol. 141, no. 2, pp. 351-358, Mar. 2005.
- [62] J. Wang, "Estimation of dynamic battery SOC using fuzzy arithmetic and the realization on DSP," Master thesis, Jilin University, 2007.

- [63] J. Kim and B. H. Cho, "State-of-charge estimation and state-of-health prediction of a Li-Ion degraded battery based on an EKF combined with a per-unit system," *IEEE Trans. Veh. Tech.*, vol. 60, no. 9, pp. 4249-4260, Nov. 2011.
- [64] A. Vasebi, S. M. T. Bathaee, and M. Partovibakhsh, "Predicting state of charge of lead-acid batteries for hybrid electric vehicles by extended Kalman filter," *Energy Convers. Manage.*, vol. 49, no. 1, pp. 75-82, Jan. 2008.
- [65] H. Fang, Y. Wang, Z. Sahinoglu, T. Wada, and S. hara, "Adaptive estimation of state of charge for lithium-ion batteries," in *Proc. American Control Conf.*, Jun. 2013, pp. 3491-3497.
- [66] M. A. Roscher, O. Bohlen, and J. Vetter, "OCV hysteresis in Li-ion batteries including two-phase transition materials," *International Journal of Electrochemistry*, vol. 2011, Feb. 2011.
- [67] G. L. Plett, "Extended Kalman filtering for battery management systems of LiPB based HEV battery packs – Part 3. State and parameter estimation," *J. Power Sources*, vol. 134, no. 2, pp. 262-276, Aug. 2004.
- [68] G. L. Plett, "Sigma-point Kalman filtering for battery management systems of LiPB-based HEV battery packs – Part 2: Simultaneous state and parameter estimation," *J. Power Sources*, vol. 161, no. 2, pp. 1369-1384, Oct. 2006.
- [69] R. Gould, C. M. Bingham, D. A. Stone, and P. Bentley, "New battery model and state-of-health determination through subspace parameter estimation and state-observer techniques," *IEEE Trans. Veh. Tech.*, vol. 58, no. 8, pp. 3905-3916, Oct. 2009.

- [70] M. Li, W. Chen, H. Wu, and D. Gorski, "Robust state of charge estimation of lithium-ion batteries via an iterative learning observer," SAE Technical Paper 2012-01-0659, 2012.
- [71] M. Charkhgard and M. Farrokhi, "State of charge estimation for lithium-ion batteries using neural networks and EKF," *IEEE Trans. Ind. Electronic.*, vol. 57, no. 12, pp. 4178 - 4187, Dec. 2010.
- [72] N. C. Moo, Y. Chen, and Y. Hsieh, "Enhanced coulomb counting method for estimating state-of-charge and state-of-health of lithium ion batteries," *Appl. Energy*, vol. 86, no. 9, pp. 1506–1511, Sept. 2009.
- [73] M. Coleman, W. G. Hurley, and C. Lee, "An improved battery characterization method using a two-pulse load test," *IEEE Trans. Energy Convers.*, vol. 23, no. 2, 2008.
- [74] Z. Cheng, C. C. Mi, Y. Fu, J. Xu, and X. Gong, "Online battery state of health estimation based on genetic algorithm for electric and hybrid vehicle applications," *J. Power Sources*, vol. 240, pp. 184-192, Oct. 2013.
- [75] F. Huet, "A review of impedance measurements for determination of the state-of-charge or state-of-health of secondary batteries," *J. Power Sources*, vol. 70, no. 1, pp. 59-69, Jan. 1998.
- [76] Y. Lee, S. Park, and S. Han, "On-line optimal ion conductivity control of li-ion battery," in *Proc. IEEE Energy Convers. Congr. Expo.*, Sep. 2012, pp. 4493-4500.
- [77] S. Samadani, R. Fraser, and M. Fowler, "A review study of methods for lithium-ion battery health monitoring and remaining life estimation in hybrid electric vehicles," SAE Technical Paper 2012-01-0125, 2012.

- [78] I. Kim, "A technique for estimating the state of health of lithium batteries through a dual-sliding-mode observer," *IEEE Trans. Power Electron.*, vol. 25, no. 4, pp. 1013-1022, Apr. 2010.
- [79] C. Hu, B. D. Youn, and J. Chung, "A multiscale framework with extended Kalman filter for lithium-ion battery SOC and capacity estimation," *Appl. Energy*, vol. 92, pp. 694-704, Apr. 2011.
- [80] G. L. Plett, "Recursive approximate weighted total least squares estimation of battery cell total capacity," *J. Power Sources*, vol. 196, no. 4, pp. 2319-2331, Feb. 2011.
- [81] E. Meissner and G. Richter, "Battery monitoring and electrical energy management precondition for future vehicle electric power systems," *J. Power Sources*, vol. 116, no. 1-2, pp. 79-98, Jul. 2003.
- [82] H. Blanke, O. Bohlen, S. Buller, R. W. Doncker, B. Fricke, A. Hammouche, D. Linzen, M. Thele, and D. U. Sauer, "Impedance measurements of lead-acid batteries for state-of-charge, state-of-health and cranking capability prognosis in electric and hybrid electric vehicles," *J. Power Sources*, vol. 144, no. 2, pp. 418-425, Jun. 2005.
- [83] L. W. Juang, P. J. Kollmeyer, T. M. Jahns, and R. D. Lorenz, "Implementation of online battery state-of-power and state-of-function estimation in electric vehicle applications," in *Proc. IEEE Energy Convers. Congr. Expo.*, Sep. 2012, pp. 1819-1826.
- [84] S. Wang, M. Verbrugge, J. S. Wang, and P. Liu, "Multi-parameter battery state estimator based on the adaptive and direct solution of the governing differential equations," *J. Power Sources*, vol. 196, no. 20, pp. 8735-8741, Oct. 2011.

- [85] G. L. Plett, "High-performance battery-pack power estimation using a dynamic cell model," *IEEE Trans. Veh. Tech.*, vol. 53, no. 5, pp. 1586-1593, Sep. 2004.
- [86] E. Meissner and G. Richter, "Battery monitoring and electrical energy management: Precondition for future vehicle electric power systems," *J. power sources*, vol. 116, no. 1-2, pp. 79-98, Jul. 2003.
- [87] T. Kim, W. Qiao, and L. Qu, "Real-time state of charge and electrical impedance estimation for lithium-ion batteries based on a hybrid battery model," in *Proc. The Annual IEEE Appl. Power Electron. Conf. and Expo.*, Mar. 2013, pp. 563-568.
- [88] T. Kim, W. Qiao, and L. Qu, "An enhanced real-time hybrid battery model," *IEEE Trans. Energy Convers.*, in review.
- [89] Y. Yamaguchi, M. Shiota, M. Hosokawa, Y. Nakayama, N. Hirai, and S. Hara, "Study of charge acceptance for the lead-acid battery through in situ EC-AFM observation: Influence of the open-circuit standing time on the negative electrode," *J. Power Sources*, vol. 102, no. 1-2, pp. 155-161, Dec. 2001.
- [90] S. S. Zhang, K. Xu, and T. R. Jow, "Study of the charging process of a LiCoO<sub>2</sub>-based Li-ion battery," *J. Power Sources*, vol. 160, no. 2, pp. 1349-1354, Oct. 2006.
- [91] T. Kim, Y. Wang, Z. Sahinoglu, T. Wada, S. Hara, and W. Qiao, "A Rayleigh quotient-based recursive total-least-square online maximum capacity estimation for lithium-ion batteries," *IEEE Trans. Energy Convers.*, accepted for publication.
- [92] J. F. Manwell, J. G. McGowan, U. Abdulwahid, and K. Wu, "Improvements to the hybrid2 battery model," in *Proc. Windpower Conf.*, May 2005, pp 1-22.
- [93] T. Kim, Y. Wang, Z. Sahinoglu, T. Wada, S. Hara, and W. Qiao, "Fast UD factorization-based RLS online parameter identification for model-based condition

- monitoring of lithium-ion batteries,” in *Proc. American Control Conf.*, Jun. 2014, pp. 4410-4415.
- [94] M. Verbrugge and E. Tate, “Adaptive state of charge algorithm for nickel metal hydride batteries including hysteresis phenomena,” *J. Power Sources*, vol. 126, no. 1-2, pp. 236-249, Feb. 2004.
- [95] F. Haugen, Discrete-time signals and systems, Tech. Rep. TechTeach, pp. 39-49, 2005.
- [96] G. L. Plett, “Results of temperature-dependent LiPB cell modeling for HEV SOC estimation,” in *Proc. 21st Electric Vehicle Symposium*, Apr. 2005.
- [97] T. Kim, W. Qiao, and L. Qu, “Power electronics-enabled self-X multicell batteries: A design toward smart batteries,” *IEEE Trans. Power Electron.*, vol. 27, no. 11, pp. 4723-4733, Nov. 2012.
- [98] T. Kim, W. Qiao, and L. Qu, “A multicell battery system design for electric and plug-in hybrid electric vehicles,” in *Proc. IEEE Int. Electrical Veh. Conf.*, Mar. 2012, pp. 1-7.
- [99] T. Kim, W. Qiao, and L. Qu, “A series-connected self-reconfigurable multicell battery capable of safe and effective charging/discharging and balancing operations,” in *Proc. 27th Annual IEEE Appl. Power Electron. Conf. and Expo.*, Feb. 2012, pp. 2259-2264.
- [100] C. Bonfiglio and W. Roessler, “Cost optimized battery management system with active cell balancing for lithium ion battery stacks,” in *Proc. Vehicle Power and Propulsion Conference*, Sept. 2009, pp. 304-309.

- [101]R. Matte, L. Turner, and H. Mettlach, "Voltec battery system for electric vehicle with extended range," *SAE Int. J. Engines*, vol. 4, no.1, pp. 1944-1962, Apr. 2011.
- [102]T. Kim, W. Qiao, and L. Qu, "Series-connected reconfigurable multicell battery," in *Proc. The Annual IEEE Appl. Power Electron. Conf. and Expo.*, Mar. 2011, pp. 1382-1387.
- [103]T. Kim, W. Qiao, and L. Qu, "Online state of charge and electrical impedance estimation for multicell lithium-ion batteries," in *Proc. IEEE Transportation Electrification Conference and Expo*, Jun. 2013, pp. 1-6.
- [104]D. Noren and M. Hoffman "Clarifying the Butler-Volmer equation and related approximations for calculating activation losses in solid oxide fuel cell models," *J. Power Sources*, vol. 152, pp. 175-181, Dec. 2005.
- [105]J. Jiang and Y. Zhang, "A revisit to block and recursive least squares for parameter estimation," *Comput. Electr. Eng.*, vol. 30, no. 5, pp. 403-416, Jul. 2004.
- [106]S. Lee, J. Kim, J. Lee, and B. H. Cho, "State-of-charge and capacity estimation of lithium-ion battery using a new open-circuit voltage versus state-of-charge," *J. Power Sources*, vol. 185, no. 2, pp. 1367-1373, Dec. 2008.
- [107]T. Kim, Y. Wang, Z. Sahinoglu, T. Wada, S. Hara, and W. Qiao, "Model-based condition monitoring for lithium-ion batteries," *J. Power Sources*, 2015, accepted for publication.
- [108]J. M. Jover and T. Kailath, "A parallel architecture for Kalman filter measurement update and parameter estimation," *Automatica*, vol. 22, no. 1, pp. 337-346, Jan.1986.

- [109]R. Fortescue, L. S. Kershenbaum and B. E. Ydstie, "Implementation of self-tuning regulators with variable forgetting factors," *Automatica*, vol. 17, no. 6, pp. 831-835, Nov. 1981.
- [110]bq2750x Datasheet, "Theory and implementation of Impedance Track™ battery fuel-gauging algorithm," Texas Instrument, Dallas, Jan. 2008.
- [111]K. K. Parhi, *VLSI Digital Signal Processing System: Design and Implementation*, John Wiley & Sons, 2007.
- [112]S. R. Habibi, "The smooth variable structure filter," *Proceedings of the IEEE*, vol. 95, no. 5, pp. 1026-1059, May 2007.
- [113]M. S. Farag, R. Ahmed, S.A Gadsden, S. R. Habibi, and J. Tjong, "A comparative study of Li-ion battery models and nonlinear dual estimation strategies," in *Proc. IEEE Transportation Electrification Conference and Expo*, Jun. 2012, pp.1-8.
- [114]T. Kim, Y. Wang, Z. Sahinoglu, T. Wada, S. Hara, and W. Qiao, "State of charge estimation based on real-time battery model and iterative SVSF," in *Proc. IEEE Innovative Smart Grid Technologies Conf.*, May 2014, pp. 132-137.
- [115]X. Tang, X. Mao, J. Lin, and B. Koch, "Capacity estimation for Li-ion batteries," in *Proc. American Control Conf.*, Jun.-Jul. 2011, pp. 947-952.
- [116]G. C. Goodwin and K. S. Sin, *Adaptive Filtering, Prediction and Control*, Englewood Cliffs, NJ: Prentice-Hall, 1984.
- [117]I. Markovsky and S. V. Huffel, "Overview of total least-squares methods," *Signal Process.*, vol. 87, no. 10, pp. 2283-2302, Oct. 2007.

- [118]K. Yang, J. An, X. Bu, and G. Sun, “Constrained total least-squares location algorithm using time-difference-of-arrival measurements,” *IEEE Trans. Veh. Tech.*, vol. 59, no. 3, pp. 1558-1562, Mar. 2010.
- [119]D. Z. Feng, X. D. Zhang, D. X. Chang, and W. X. Zheng, “A fast recursive total least squares algorithm for adaptive FIR Filtering,” *IEEE Trans. Signal Process.*, vol. 52, no. 10, pp. 2729-2737, Oct. 2004.
- [120]C. E. Davila, “Efficient recursive total least squares algorithms for FIR adaptive filtering,” *IEEE Trans. Signal Process.*, vol. 42, no. 2, pp. 268–280, Feb. 1994.

## APPENDIX

The parameters of the power MOSFETs used in the simulation and experimental studies in Chapter 3 and Chapter 6 are listed as follows.

1) n-channel MOSFET ( $S_{ij}$ ): AON6400L,  $V_{DSS} = 30\text{V}$ ,  $I_{D\text{MAX}} = 85\text{ A}$ ,  $R_{DS(\text{on})} = 1.8\text{ m}\Omega$ ,  $V_{\text{th}} = 1.7\text{V}$ .

2) p-channel MOSFET ( $S_i$ ): IPD90P03P4L-04,  $V_{DSS} = -30\text{V}$ ,  $I_{D\text{MAX}} = -90\text{ A}$ ,  $R_{DS(\text{on})} = 4.1\text{ m}\Omega$ ,  $V_{\text{th}} = -1.5\text{V}$ .

The parameters of the lithium-ion battery cells are listed as follows.

1) Polymer lithium-ion cell pl-383562 2C; nominal voltage: 3.7V; nominal capacity: 860 mAh; discharge cutoff voltage ( $V_{\text{limit\_discharge}}$ ): 3V; charge cutoff voltage ( $V_{\text{limit\_charge}}$ ): 4.2V; and maximum discharge current: 2C (1.72 A).

1) Tenergy 18650; nominal voltage: 3.7 V; nominal capacity: 2.6 Ah; discharge cutoff voltage ( $V_{\text{limit\_discharge}}$ ): 3 V; charge cutoff voltage ( $V_{\text{limit\_charge}}$ ): 4.2 V; maximum discharge current: 1C (2.6 A) used in Chapter 4 and Chapter 5.

2) Samsung ICR18650-28A; nominal voltage: 3.75 V; nominal capacity: 2800 mAh; discharge cutoff voltage ( $V_{\text{limit\_discharge}}$ ): 3 V; charge cutoff voltage ( $V_{\text{limit\_charge}}$ ): 4.3 V; maximum discharge current: 2C (5.6 A) used in Chapter 3 and Chapter 6.